ISTANBUL TECHNICAL UNIVERSITY ★ GRADUATE SCHOOL OF SCIENCE ENGINEERING AND TECHNOLOGY

MAGNETOTAIL SHAPE, FLOW AND MAGNETIC FIELD STRUCTURE AT LUNAR DISTANCES USING ARTEMIS OBSERVATIONS

Ph.D. THESIS

İklim GENÇTÜRK AKAY

Department of Aeronautics and Astronautics Engineering

Aeronautics and Astronautics Engineering Programme

JUNE 2019

ISTANBUL TECHNICAL UNIVERSITY ★ GRADUATE SCHOOL OF SCIENCE ENGINEERING AND TECHNOLOGY

MAGNETOTAIL SHAPE, FLOW AND MAGNETIC FIELD STRUCTURE AT LUNAR DISTANCES USING ARTEMIS OBSERVATIONS

Ph.D. THESIS

İklim GENÇTÜRK AKAY
(511102109)

Department of Aeronautics and Astronautics Engineering

Aeronautics and Astronautics Engineering Programme

Thesis Advisor: Prof. Dr. Zerefşan KAYMAZ

JUNE 2019

ISTANBUL TEKNİK ÜNİVERSİTESİ ★ FEN BİLİMLERİ ENSTİTÜSÜ

DÜNYA'NIN MANYETİK KUYRUĞUNUN ŞEKİL, PLAZMA AKIŞI VE MANYETİK ALAN YAPISI AÇISINDAN AY MESAFESİNDE ARTEMİS UYDU VERİLERİ İLE İNCELENMESİ

DOKTORA TEZİ

İklim GENÇTÜRK AKAY
(511102109)

Uçak ve Uzay Mühendisliği Anabilim Dalı

Uçak ve Uzay Mühendisliği Programı

Tez Danışmanı: Prof. Dr. Zerefşan KAYMAZ

HAZİRAN 2019

İklim Gençtürk Akay, a Ph.D. student of ITU Graduate School of Science Engineering and Technology student ID 511102109, successfully defended the dissertation entitled "MAGNETOTAIL SHAPE, FLOW AND MAGNETIC FIELD STRUCTURE AT LUNAR DISTANCES USING ARTEMIS OBSERVATIONS", which she prepared after fulfilling the requirements specified in the associated legislations, before the jury whose signatures are below.

Thesis Advisor :	**Prof. Dr. Zerefşan KAYMAZ** İstanbul Technical University	.....
Jury Members :	**Prof. Dr. Zafer ASLAN** Istanbul Aydin University	.....
	Assist. Prof. Dr. Cuma YARIM Istanbul Technical University	.....
	Prof. Dr. Adnan ÖKTEN Istanbul University	.....
	Prof. Dr. Kazım Yavuz EKŞİ Istanbul Technical University	.....

Date of Submission : 17 May 2019
Date of Defense : 20 June 2019

To my beloved family,

FOREWORD

Space Physics, specifically magnetospheric physics is a subject that I intended to start studying instantly after I took the first class that Prof. Z. KAYMAZ was lecturing. After my masters' degree on Aerospace Engineering in US, I knew that I wanted to go back and study space physics.

Now, I understand that from the first day at the UZB 441E Space Environment course, space physics was my thing and you, Prof. Z. KAYMAZ are my supervisor. You are not only my advisor, but also my mentor. You give me courage and advice whenever I needed to. You always believed in me and this work would not have been possible without your scientific guidance and participation. Under your guidance, I productively overcame many problems and learned a lot. Seeing your passion and courage inspires me and I just would like to continue learning, carry the torch of teaching Space Physics to any enthusiast. For all these, I am truly grateful to you.

I greatly appreciate and acknowledge the support received from Dr. SIBECK. Your insight and the time that I spent at NASA Goddard Space Flight Center improved me a lot.

My special thanks goes to my friends, Room 320 lights with joy and laughs that can be heard from couple of floors down; thanks to you. Filiz, you are a beautiful soul and very special for me. Your positive energy is always right there to share with us; Ceren, Banu, and me. You girls create the most enjoyable and memorable times during the coffee hours. Thank you all from the bottom of my heart.

Some special words of gratitude go to my family. My mother, you are a very special woman. You can do all, you can do the best. I learned not to give up from you. My dad, my sister and my grand mother, you are always with me by my side, encouraging and helping to me. I am very lucky to have such a good family. Thank you.

A very special word of thanks goes to my husband, my best friend, my office mate and my travel and life companion, Erdem. You are always there for me. Thanks for the continual support, courage and all the help. We learned a lot with and from each other. I love you.

The last word goes for Parla, my daughter. You have been the light of my life for the last five years. You lit my face whenever I come back to home and gave me the extra strength to live and fight, if needed. I know that you will be a strong and educated woman. This thesis is dedicated to her.

June 2019

İklim GENÇTÜRK AKAY
(Research Assistant)

TABLE OF CONTENTS

Page

ABBREVIATIONS

ACE : Advanced Composition Explorer
AE : Auroral Electrojet
AL : Auroral Electrojet Lower
AU : Auroral Electrojet Upper
AU : Astronomical Unit
aSWGSE : aberrated Solar Wind corrected Geocentric Solar Ecliptic
aSWGSM : aberrated Solar Wind corrected Geocentric Solar Magnetospheric
BATS-R-US : Block-Adaptive-Tree-Solarwind-Roe-Upwind-Scheme
BBF : Bursty Bulk Flow
CME : Coronal Mass Ejection
CPLEE : Charged Particle Lunar Environment Experiment
CPS : Central Plasma Sheet
CS : Current Sheet
C02 : Chao et al., (2002) analytical magnetopause model
DST : Disturbance Storm Time
DNL : Distant Neutral Line
EFI : Electric Field Instrument
ESA : Electrostatic Analyzer
eV : Electron Volt
FGM : Flux Gate Magnetometer
FGS : Flux Gate Magnetometer Spin-resolution
FTE : Flux Transfer Event
GSE : Geocentric Solar Ecliptic
GSM : Geocentric Solar Magnetospheric
HB72 : Howe and Binsack (1972) analytical magnetopause model
HLBL : High Latitude Boundary Layer
ICME : Interplanetary Coronal Mass Ejection
IMF : Interplanetary Magnetic Field
LLBL : Low Latitude Boundary Layer
L11 : Lui et al. (2011) analytical magnetopause model

MAG **:** Interplanetary Magnetic Field Instrument

MHD **:** Magneto Hydro Dynamic

MC **:** Magnetic Cloud

MOM **:** On board Moments

MP **:** Magnetopause

MS **:** Magnetosheath

NENL **:** Near Earth Neutral Line

NS **:** Neutral Sheet

nT **:** Nano Tesla

PR96 **:** Petrinec and Russell (1996) analytical magnetopause model

PS **:** Plasma Sheet

PSBL **:** Plasma Sheet Boundary Layer

$\mathbf{R_E}$ **:** Radius of the Earth

$\mathbf{R_{MP}}$ **:** Magnetopause stand-off distance from the Earth

RMS **:** Root Mean Square

S97 **:** Shue et al. (1997) analytical magnetopause model

S98 **:** Shue et al. (1998) analytical magnetopause model

SST **:** Solid State Telescope

SW **:** Solar Wind

SWEPAM **:** Solar Wind Electron Proton Alpha Monitor

SYMBOLS

a	**:** semi-major axis
b	**:** semi-minor axis
B	**:** Magnetic Field
Bx, By, Bz	**:** Magnetic Field components in x,y,z direction
Dp	**:** Dynamic Pressure as used in Shue et al. (1997)
e	**:** Eccentricity
E	**:** Electric Field
V	**:** Velocity
$\mathbf{V_x, V_y, V_z}$	**:** Velocity components in x,y,z direction
Pdyn	**:** Dynamic Pressure
Pmag	**:** Magnetic Pressure
α_e	**:** Aberration angle due to Earth's orbital Motion around the Sun
α_{sw}	**:** Aberration angle due to non-radial velocity component of solar wind
α_{total}	**:** Total aberration angle due to non-radial velocity component of solar wind and Earth's orbital motion around the Sun
β	**:** Aberration angle due to displacement of the tail axis in z-direction
μ	**:** Statistical mean
θ	**:** Clock angle
φ_{fl}	**:** Flaring angle
ρ	**:** Density
σ	**:** Resistivity

LIST OF TABLES

Page

LIST OF FIGURES

Page

MAGNETOTAIL SHAPE, FLOW AND MAGNETIC FIELD STRUCTURE AT LUNAR DISTANCES USING ARTEMIS OBSERVATIONS

SUMMARY

When the solar wind reaches the Earth, it interacts with the Earth's dipole magnetic field, confining it to a region known as the magnetosphere. The magnetosphere extends from the dayside to nightside and has several regions. One of these regions is the magnetopause, which is the boundary between the shocked solar wind and magnetosphere. In the anti-sunward direction, the geomagnetic field lines are stretched by the solar wind, forming Earth's magnetotail that occupies the nightside magnetosphere. The magnetotail is a very active region with its length nearly reaching $1000R_E$ ($1\ R_E$ = Radius of the Earth) distances.

Geomagnetic tail is one of the least investigated regions of the magnetosphere on the nightside of the Earth owing to the limited number of spacecraft and observations. Near-Earth tail, at about $-30\ R_E$ down the tail, has been investigated in detail by using IMP-8 observations (e.g. Kaymaz, et al., 1994; Hammond, et al., 1994, Ohtani et al. 1991). However, the magnetotail at mid ($-60\ R_E$) to distant regions ($\leq -200\ R_E$) was only studied based on the scarce data obtained from the very limited number of traversals by Explorer series and ISEE-3 in 1970s to 80s, and Wind and Geotail missions in 1990s, from which the present knowledge has been derived on the global character of the magnetotail (Fairfield, 1992; Fairfield, 1993; Reader, et al., 1995; Slavin, et al., 1985; Sibeck, et al., 1985; Tsurutani, et al., 1984). Especially, mid to distant tail is one of the most interesting regions where distant reconnection line appears to be and is expected to control the internal distant tail dynamics. The main advantage of ARTEMIS spacecraft, operating since August 2011, is to give the researchers for an extensive, comprehensive and systematic investigation of the magnetotail at the lunar distances, $-60\ R_E$.

The magnetosphere interacts with the solar wind through magnetic reconnection, which creates direct entry of the solar wind plasma and magnetic field under certain conditions and forms an open magnetosphere. The magnetic flux and the solar wind energy that drive the magnetotail dynamics flow into the magnetosphere through open magnetic field lines via reconnection process. The rate of reconnection and reconnection site appears to be depended mainly on interplanetary magnetic field (IMF) direction (Tsurutani, et al., 1984; Slavin, et al., 1983; Sibeck, et al., 1985). Especially IMF By and IMF Bz, and solar wind plasma (density, velocity and temperature) can move, fluctuate and alter the shape and location of the tail. Accordingly, the magnetotail can twist and/or flatten in different directions, shrink or expand and therefore the boundary can flare in or out. In addition to the sign of IMF By and Bz, the velocity variations in the solar wind direction, the geomagnetic activity (storms/substorms) can lead internal variations in the magnetotail structure and dynamics. Thus, reconnection changes the dynamics of the magnetotail, magnetic field topology, and the flow structure. All these variations at different spatial and time scales

make the interpretation of the measurements from satellite difficult (Reader, et al., 1995). For example, the fluctuating tail triggers spacecraft cross the magnetopause back and forth several times in such short time intervals, which will make the detection of the magnetopause boundary harder in the data.

The purpose of this thesis study is twofold. The first is to investigate the structure of the magnetopause boundary and how it varies with the changing IMF conditions using case studies and statistics as well. The second is to map the magnetic field and plasma structure within the magnetotail at the Moon's distance. The primary objective in the magnetotail study is to reveal the plasma, namely velocity, density, temperature and pressure structure at the Moon distance, which was not previously studied in detail using high-resolution measurements and large number of data. Secondly, even though the magnetic field structure of the magnetotail was well investigated in near Earth distances, the magnetotail's magnetic structure at Moon's distance lacks of completeness. Using the state-of-the-art magnetic field measurements from ARTEMIS, the magnetotail's magnetic field structure and its variability in response to IMF were shown using vector maps. There are several "firsts" that bring out this study forward. One is that it is the first time that the magnetotail plasma structure at the Moon distances is studied using high resolution plasma data. Second, it is the first time that the global scale structure of both plasma and magnetic field in the magnetotail at Moon distances were studied using vector mapping technique. Third, this is the first study that the magnetic field maps are accompanied by the plasma flow maps. Thus, these two complementary data sets, give us an opportunity to address on the magnetotail dynamics at the Moon's distances while revealing the global structure.

This dissertation starts with an introductory chapter, Chapter 1, that contains brief information regarding the Sun, magnetosphere, and the magnetotail which is followed by the purpose of the study and a review of the literature related to the thesis subjects.

Chapter 2 describes and explains the instruments of the ARTEMIS and the solar wind monitor spacecraft from which the observations are taken. This chapter continues with the processes applied to data including how the magnetopause crossings are identified, performing the appropriate coordinate system, correcting for solar wind flow direction and Earth's orbital motion and separation by the IMF clock angle.

Chapter 3 presents the magnetopause study at the distance of the Moon. The size, geometry and shape of the magnetotail boundary are discussed as well as the factors that affect the magnetotail's motion and its variability, e.g. different IMF orientations and solar wind dynamic pressure. On average, the magnetopause positions indicate a tail size with a radius of about 27 ± 5 R_E at lunar distance. The analytical magnetopause models (Howe and Binsack, 1972 ; Petrinec and Russell, 1996; Shue et al., 1997; Shue et al., 1998; Chao et al., 2002 and Lui et al, 2011) were compared with the observed boundary crossings. It is shown that the oldest model Howe and Binscak model predicts the average size of the tail boundary very well. Case studies of the extreme occurrences of the boundary crossings show that the magnetotail size at lunar distances is controlled by the relative magnitudes of the solar wind dynamic pressure and the strength of the IMF Bz. While the east-west IMFs result in an ellipse which is flattened from the top and bottom, the north-south IMFs cause an ellipse squeezed from sides. The tail size and dimensions at lunar distance were found to be slightly larger for southward IMFs compared to northward IMFs, as expected from the theory.

In Chapter 4, the vector and contour maps of the magnetic field and the plasma, namely velocity, density, temperature and pressure, structure of the magnetotail are presented.

Statistical analysis using histograms, and the response of the magnetotail structure to the IMF orientation are studied in this chapter as well. The magnetopause boundary crossings detected in Chapter 3 are used to obtain the magnetotail data which are then analyzed and evaluated in order to reveal the global magnetic and plasma features of the magnetotail and its variability at lunar distances. Both magnetic field and flow vector maps are performed in different planes consisting XY-, XZ-, YZ-planes as well as XBx- and YBx-planes using binning techniques.

Magnetic field vector maps reveal that the magnetotail magnetic structure follows the dipolar structure of the Earth's magnetic field at lunar distances with slightly weaker magnitudes as compared to near Earth distances. Both XZ- and YZ-planes reveal the magnetic field structure of the plasma sheet. It is shown that the plasma sheet becomes thinner with increasing down tail distance. It also appears to be thinner compared to near Earth distances but still have the gross features of the butterfly structure being thinner in the central mid-plane and thicker on the dawn-dusk sides in the YZ-plane. IMF By effects are seen clearly on the respective dawn and dusk quadrants of the northern and southern magnetotail at this distance. In the YBx-plane, a node like feature appear at Y=-3 R_E, Bx=9nT. The rotation of the node is evident in response to IMF By. For southward IMF sector, it was shown that the plasma sheet is thinner while it is seen to be thicker for northward IMFs at lunar distances. The increased size of the magnetotail due to tail's expansion when IMF is southward is also observed.

The flows are categorized into 3; fast, medium and slow using |Vx|. The slow flows (<100km/s) are dominant throughout the magnetotail as discussed by Hayakawa at al. (1982) and fast flows (>300km/sec) are rare. The dawn-dusk directed flows are only seen with the slow flow cases. The fast flows have a more tendency to occur with southward IMF sector. The plasma flow has the slowest velocities in YZ-plane since the main flow direction is in a plane orthogonal to this plane.

Three types of plasma populations are observed when density and temperature parameters are investigated when the data are separated according to IMF direction. The denser plasma is found during the northward IMFs on the average of 0.16 cm^{-3} compared to 0.12 cm^{-3} for southward IMFs. The density-temperature distributions show that the plasma is more concentrated in the case of northward IMF while it is more scatter in case of southward IMF, especially the hot, dense plasma. Discussions related to the magnetic field and plasma maps are given in detail in this chapter and compared with the literature.

The last chapter of the thesis, Chapter 5, presents the summary of the thesis and gives conclusions obtained.

This thesis study is the first study that investigates the space environment and environmental parameters and their variability at the lunar distances using a twin spacecraft of ARTEMIS with high-resolution data in the Faculty of Aeronautics and Astronautics at Istanbul Technical University. In addition, it is a leader study in its field in Turkey. The findings of this study do not only contribute to aerospace engineers to understand the environment for near lunar missions and the spacecraft will be exposed to but also will give an insight to space physicists about the global character of the magnetotail and its response to varying factors at lunar distances. Moreover, in the increasingly space dependent age of technological advancements, this study serves as an example how one can extract real and useful information from different but continuous and massive data sets by using the modern analysis techniques and make them useful for the community.

DÜNYA'NIN MANYETİK KUYRUĞUNUN ŞEKİL, PLAZMA AKIŞI VE MANYETİK ALAN YAPISI AÇISINDAN AY MESAFESİNDE ARTEMIS UYDU VERİLERİ İLE İNCELENMESİ

ÖZET

Güneş rüzgarı Dünya'ya ulaştığında, Dünya'nın çift kutuplu manyetik alanı ile etkileşime girerek manyetosferi oluşturur. Manyetosfer, hem Güneş hem de gece tarafında bir çok bölgeden oluşur. Bunlardan biri şoka uğratılmış Güneş rüzgarı plazması ile manyetosfer plazması arasındaki sınır olan manyetopozdur. Gece tarafında jeomanyetik alan çizgileri Güneş rüzgarıyla uzar ve manyetosferin gece tarafını işgal eden Dünya'nın manyetik kuyruğunu oluşturur. Magnetik kuyruk, uzunluğu neredeyse 1000 R_E (1 R_E = Dünya Yarıçapı) mesafelere ulaşan çok aktif bir bölgedir.

Jeomanyetik kuyruk, sınırlı sayıdaki uzay görevleri ve kesintili ve/veya yetersiz gözlemler nedeniyle Dünya'nın arkasındaki manyetosferin en az araştırılan bölgelerinden biridir. Dünya'ya yakın kuyruk, yaklaşık -30 R_E, IMP-8 gözlemleri kullanılarak detaylı olarak incelenmiştir (Kaymaz ve diğerleri, 1994; Hammond ve diğerleri, 1994). Bununla birlikte, şu anki manyetik kuyruğun yapısıyla ilgili bildiklerimiz, -60 R_E civarı ve daha uzak kuyruk bölgelerindeki ($\leq$-200 R_E) 1970'lerde 80'lerdeki Explorer serisi ve ISEE-3, Wind ve Geotail uzay araçlarının 1990'lardaki sınırlı sayıdaki geçişlerinden elde edilen kısıtlı verilere dayanmaktadır (Fairfield, 1992; Fairfield, 1993; Reader ve diğerleri, 1995; Slavin ve diğerleri, 1985; Sibeck ve diğerleri, 1985; Tsurutani ve diğerleri, 1984). Özellikle, kuyruk iç dinamiklerini kontrol etmesi beklenen uzaktaki birleşme noktasının (DNL) civarında olan orta-uzak kuyruk dediğimiz Ay uzaklığındaki manyetik kuyruk bölgesini önemli kılar. Ağustos 2011'den bu yana faaliyet gösteren ARTEMIS uzay araçlarının temel avantajı, araştırmacılara Ay mesafesindeki manyetik kuyruğunun kapsamlı, veri yönünden tam ve sistematik bir incelemesini sağlamaktır.

Dünya'nın manyetik alanı ile Güneş'in manyetik alanı belirli şartlar altında manyetik olarak birleşir (reconnection). Bu birleşme sonucunda Güneş rüzgarına ait parçacıklar birleşen manyetik alan çizgileri üzerinden Dünya manyetosferine girerler. Bu şartlar altında oluşan manyetosfere açık manyetosfer adı verilir. Açık manyetik alan çizgilerinin gece tarafına hareketi ile de parçacıklar manyetik kuyruğa taşınarak manyetik kuyruğun yapısını ve dinamiğini değiştirirler. Manyetik birleşme gezegenler arası manyetik alanın (IMF) yönüne bağlıdır (Tsurutani ve diğerleri, 1984; Slavin ve diğerleri, 1983; Sibeck ve diğerleri, 1985). Özellikle IMF By ve IMF Bz ve Güneş rüzgârı plazması (yoğunluk, hız ve sıcaklık) kuyruğun şeklini ve konumunu değiştirebilir ve onu hareket ettirebilir. Buna göre, IMF yönü manyetik kuyruğu farklı yönlerde döndürebilir ve / veya şeklini düzleyebilir, büzebilir veya genişletebilir ve bu nedenle manyetopoz sınırı içe ya da dışa doğru hareket ederek şekil değiştirebilir. IMF

By ve Bz'nin yönüne ek olarak, Güneş rüzgârı yönündeki hız değişimleri, jeomanyetik aktivite (fırtınalar / mikro fırtınalar) manyetik kuyruk yapısında ve dinamiklerinde içsel değişimlere neden olabilir. Böylece, manyetik birleşme kuyruğun manyetik alan topolojisini, akış yapısının dinamiklerini ve diğer plazma parametrelerini değiştirir. Değişimin ölçeğine bağlı olarak, manyetik kuyruğun hareketi, dinamiğinde ve yapısında meydana gelen değişimler uydulardan alınan ölçümlerin yorumlanmasını zorlaştırmaktadır (Reader, et al., 1995). Örneğin, Güneş rüzgarının ekvatoryal düzlemindeki hareketinden ötürü dalgalanan kuyruk, uzay aracı verisinden manyetopoz sınırından kısa zaman aralıklarla çok kez sınırın üzerinden geçip geri gelebilir ve bu hareket manyetopoz sınırını tespit etmeyi zorlaştırır.

Tezin birinci bölümünde (Bölüm 1) terimler tanıtılarak konu ile ilgili giriş niteliğinde temel bilgiler verilmiştir. Bunu takiben literatürde mevcut eski çalışmaların kapsamlı bir özeti sunulmuştur. Tezin ikinci bölümünde, (Bölüm 2), ölçümler ve ölçümlerin yapıldığı aletlerle ilgili bilgiler verilmiş, manyetopoz sınır tabaka geçişlerini incelemek için gerekli olan işlemler anlatılmıştır. Bunlar manyetopoz sınır tabakasının ölçümlerden nasıl belirlendiğini, hangi verilerin ve kriterlerin kullanıldığı açıklanarak detaylandırılmıştır. Örneğin, ARTEMIS uydularının manyetik alan, plazma yoğunluğu, hızı, sıcaklığı ve iyon enerjisi gözlemleri günlük ve saatlik ölçeklerde dikkatlice incelendiğinde manyetopoz sınırının Ay mesafesinde tanımlanmasındaki en iyi kriterin yüksek enerjili parçacık akısının varlığı veya yokluğu olduğu ve buna ek olarak, plazma sıcaklığındaki hızlı bir artışın, yoğunluk ve hızdaki bir azalmanın buna eşlik ederek manyetik kuyruk ile manyetik örtü arasındaki geçişi ve dolayısıyla manyetopoz sınırının yerini gösterdiğine karar verilmiştir. Bölüm, çveriyi yorumlamayı anlamlı hale getirecek olan uygun koordinat sisteminin belirlenmesini ve verilerin bu koordinat sistemine dönüştürülmesini, Güneş rüzgarının hızının yönünden ve Dünya'nın Güneş etrafındaki hareketinden kaynaklanan düzeltmeleri ve Güneş rüzgarının taşıdığı manyetik alanın (IMF) yönüne göre verilerin ayrıştırılmasının nasıl yapılacağını da kapsamaktadır. Bu bağlamda Güneş rüzgarı akışına hizalı yeni x- ekseni etrafında simetrik bir manyetik kuyruk elde edebilmek için bu çalışmada ARTEMIS verilerinin tüm pozisyonları, manyetik alan bileşenleri ve plazma vektörleri, anormal Güneş rüzgarı düzeltilmiş Yer merkezli Güneş Manyetosferik (aSWGSM) koordinat sistemi olarak adlandırılan yeni bir koordinat sistemine dönüştürülerek incelenmiştir.

Bölüm 3 Ay mesafesindeki manyetik kuyruğun sınır tabakasının (manyetopoz) incelenmesine ait analizleri ve bulguları vermektedir. Manyetopoz manyetik kuyruğun büyüklüğünü belirler. Bu bölümde, manyetopoz sınırının çapsal genişliği, şekli ve geometrisi, bu yapısal değerleri ve manyetik kuyruğun hareketini etkileyen IMF ve Güneş rüzgarı dinamik basıncı gibi faktörler incelenmektedir. İstatistiksel analizler sonucunda ortalama manyetopozun yarıçapı diğer bir değişle manyetik kuyruğum genişliği Ay mesafesinde 27 ± 5 R_E olarak elde edilmiştir. Sonuçlar mevcut analitik modellerle ((Howe and Binsack, 1972 ; Petrinec and Russell, 1996; Shue et al., 1997; Shue et al., 1998; Chao et al., 2002 and Lui et al, 2011) karşılaştırılmaktadır. En eski model olan Howe and Binsack modelinin ortalama manyetopoz büyüklüğünü en iyi tahmin ettiği görülmüştür. Bunun sebebi olarak Howe ve Binsack modeli dışındaki hiç bir analitik model Ay bölgesinden ve hatta -20 R_E'nin gerisindeki hiçbir bölgeden gelen veriyi baz almamışlardır. Güneş rüzgarı basıncı ve IMF'de meydana gelen çok uç (ekstrem) manyetopoz geçişleri vaka çalışması olarak ayrıca detaylı olarak incelenerek sunulmuştur. Bu vakalar için değişen koşullara bağlı olarak analik modellerin çıktıları karşılaştırılmıştır. Bu iki vaka çalışması, Ay mesafesindeki

manyetik kuyruğun büyüklüğünün, güney-kuzey yönündeki IMF'nin ve Güneş rüzgarı dinamik basıncının birlikte etkisi sonucunda belirlendiğini, her ikisinin birbirlerine göre büyüklüklerine ve hangisinin daha baskın olduğuna göre değiştiğini göstermiştir. Doğulu-Batılı IMF durumunda kuyruğun şeklinin üstten ve alttan bastırılmış bir elips, kuzeyli-güneyli bir IMF durumunda ise yanlardan bastırılmış yumurta şeklinde olduğu gösterilmiştir. Ay mesafesindeki manyetik kuyruğun büyüklüğünün güneyli IMF durumunda kuzeyli IMF durumundan biraz daha geniş olduğu görülmüştür.

Bölüm 4'de Ay mesafesindeki manyetik kuyruk verilerinin analizleri ve bulguları verilmektedir. Bu bölümde manyetik kuyruk içerisindeki manyetik alan, plazma hızı, plazma yoğunluğu, plazma sıcaklığı gibi parametreler kutulama tekniği ile vektör ve kontur haritaları oluşturularak incelenmiştir. Bu parametrelerin vektör ve skaler (kontur) dağılımları XZ, XY, ve YZ-düzlemlerinde gösterilerek, manyetik kuyruğun üç boyutlu olarak global yapısı ve mekansal değişimleri anlatılmıştır. Bunlara ilaveten nötral tabakayı daha iyi ifade eden xBx ve yBx düzlemleri de oluşturulmuştur. Ayrıca tüm bu haritalar istatistiksel olarak da incelemek amacıyla konumsal olarak ayrıştırılmış çokluk dağılımı grafikleriyle (histogramlarla) da desteklenmiştir.

Manyetik alan vektör haritaları manyetik kuyruğun manyetik yapısının Ay mesafesinde çift kutuplu dipol yapıyı koruduğunu göstermiştir. Beklendiği üzere, manyetik alan büyüklüğü bu mesafede Dünya'ya yakın mesafelerdekine göre daha zayıftır, ve ortalama 8 nT civaında olduğu görülmüştür. Manyetik kuyruğun yapısının XZ- ve YZ- düzlemlerinde, manyetik alan çizgilerinin güneyde Dünya'ya ve kuzeyde ise Dünya'dan uzağa doğru uzanan manyetik alan çizgileri arasında plazma örtüyü bir sandviç biçiminde içine alacak şekilde olduğu görülmektedir. Her iki düzlemde de plazma örtü ve plazma örtünün alt bölümleri belirgindir. Plazma örtüsünün Ay mesfesinde Dünya mesafesindekine göre daha ince olduğu ve data eskiklikleirne rağmen şeklinin YZ-düzleminde, bir kelebek şeklinde, merkezde ince, yanlara doğru daha kalınlaştığı anlaşılmaktadır. IMF By'nin etkileri plazma örtüsü içinde net bir şekilde görülmektedir. Vektör haritaları pozitif IMF By durumunda manyetik alan çizgileirnin IMF By'nin yönünde eğildiğini, node-like bölgelerin IMF By'nin yönünde kaydığını (kuyruğun kuzey kısmında Y=0 dan Y=+3) göstermektedir. İstatisksel sonuçlar, kuyruğun manyetik alanının By bileşeni manyetik birleşmeden beklenildiği gibi pozitif IMF By durumunda plazma örtüsünün kuzey+dogu ve güney+batı bölgelerinde; negative IMF By durumunda ise güney+doğu ve kuzey+batı bölgelerinde daha fazla olduğunu göstermektedir. Bu sonuçlar teoriyi ve daha önce daha yakın kuyruk mesafelerindeki sonuçları desteklemektedir. Ayrıca manyetik kuyruğun güneyli IMF durumunda kuzeyli IMF'e göre daha büyük olduğu görülmüştür.

Yine bu bölümde, plazmanın hızı Vx bileşenine göre gruplanmış ve yavaş, orta ve hızlı akışlar olarak üçe ayrılarak incelenmiştir. Hayakawa et al. (1982) tarafından da tartışıldığı üzere manyetik kuyruk içerisinde daha çok yavaş akışlar hakimdir, hızlı akışlar enderdir. Doğu-batı doğrultusundaki akışlar sadece yavaş akışlarda görülmektedir. Gızlı akışlar daha çok güneyli IMF durumunda oluşmaktadır. Plazma akışının YZ-düzleminde en yavaş oldğu görülmüştür. Hakim olan akışlar Dünya'a doğru ve Dünya'dan uzağa doru olan x-yönündeki akışlardır.

IMF yönüne göre ayrıştırma yapıldıktan sonra yoğunluk ve sıcaklık parametreleri incelendiğinde üç tip plazma popülasyonu gözlenir. Kuzeyli IMF durumunda 0.16 cm^{-3} mertebesinde daha yoğun bir plazma saptanmıştır. Güneyli IMF durumunda yoğunluk biraz daha düşük olup 0.12 cm^{-3} mertebesindedir. Ancak IMF Bz'e göre

yoğunlukta görülen bu farkların sıcaklıkda görülmediği, sıcak ve soğuk plazmanın hem kuzeyli hem de güneyli IMF durumunda mevcut olduğu görülmüştür. Yoğunluk-sıcaklık dağılımları ise kuzeyli IMF durumunda plazmanın daha konsantrik ve bir orta değere daha yakın olduğunu buna karşın güneyli IMF durumunda saçılmanın daha çok olduğu görülmüştür. Özellikle, yoğun-sıcak plazma daha dağınık, daha büyük saçılma göstermektedir. Bu konuya sonuçlar ve tartışma bu bölümde detaylı olarak verilmektedir.

Tezin son bölümü, Bölüm 5, ise tezdeki bulguları özetlemekte ve sonuçları yansıtmaktadır.

Son olarak, İstanbul Teknik Üniversitesi Uçak ve Uzay Bilimleri Fakültesi'nde yürütülen bu tez, yüksek çözünürlüklü cihazlarıyla, ARTEMIS p1 ve p2 ikiz uzay aracı kullanarak Ay mesafesindeki manyetik sınırı ve manyetik kuyruk haritasını inceleyen ilk çalışmadır. Bu çalışmanın bulguları, sadece örneğin Ay'a yakın hedeflenen bir görev için tasarlanan uzay aracı için uzay mühendislerine uzay aracının maruz kalacağı çevreye ilişkin ortamı anlamalarına katkıda bulunmayacak, aynı zamanda bu konuda çalışan uzay fizikçisi bilim insanlarına Ay mesafesindeki manyetik kuyruğun makro ölçekteki karakteri, yapısı, akışı ve farklı faktörlere verdiği tepkiler hakkında bir fikir vermekte, yol göstemektedir. Ayrıca, bu çalışma, uzay teknolojilerine giderek artan bir ihtiyacın doğduğu günlük hayatımızda, modern veri analizi teknikler kullanılarak çok büyük ve farklı veri kümelerini biraraya getirerek faydalı bilginin nasıl çıkarılıp, toplum için nasıl faydalı olabileceğini göstermek açısından da önem taşımaktadır.

1. INTRODUCTION

The Sun continuously emits a plasma flow from solar corona to the interplanetary medium called the solar wind. When the solar wind reaches the Earth, it interacts with the Earth's dipole magnetic field, confining it to a region known as the magnetosphere.

The magnetosphere has many regions both on the dayside and on nightside of the Earth one of which is the magnetopause, the boundary between the shocked solar wind plasma and magnetospheric plasma. In the anti-sunward direction, the geomagnetic field lines are stretched by the solar wind, forming Earth's magnetotail that occupies the nightside magnetosphere. The magnetotail is a very active region with its length nearly reaching 1000 R_E (1 R_E = Radius of the Earth) distances. The external effects from the solar wind, and the magnetic field structure that it carries with and the internal dynamics resulting from the storms/substorms determine the structure of and variations within the magnetotail. A brief description of the solar-terrestrial plasma environment is provided in this section.

1.1 The Solar Wind, and Earth's Magnetosphere

In 1958, Parker showed that the solar wind is streaming radially outward from the Sun (Parker, 1958). It consists of nearly equal number of electrons and protons, with some heavy ions, like helium and others. The solar wind moves supersonically throughout the solar system with an average speed varying between 350-450 km/sec. Table 1.1 gives the average characteristics of the solar wind at Earth distances, i. e. at one astronomical unit (1 AU = 149,597,870 km).

Earth's dipole field, on the other hand, is created by the dynamo within the Earth's core associated with the motion of the liquid metallic elements and together with the Earth's rotation.

Table 1.1 : Average characteristics of the solar wind at Earth's distances, 1 AU.

Solar Wind Parameters	SW Parameters Unit	Average Values
Velocity	km/sec	350 – 450
Density	#/cm^3	5 – 10
Magnetic Field Strength	nT	5
Temperature	K	$0.5x10^5$
Dynamic Pressure	erg/cm^3	$1.9x10^{-8}$
Magnetic Pressure	$dyne/cm^3$	$1.7x10^{-10}$
Gas Pressure	$dyne/cm^3$	$1.9x10^{-10}$

While moving, the electrically conducting solar wind carries the Sun's magnetic field into the interplanetary medium as if it is "frozen-in" to the plasma. The magnetic field lines in the solar wind are called interplanetary magnetic field lines (IMF). Since the footprints of the IMF are connected to the Sun, as Sun rotates the plasma and embedded magnetic field lines takes a spiral structure form seen in Figure 1.1.

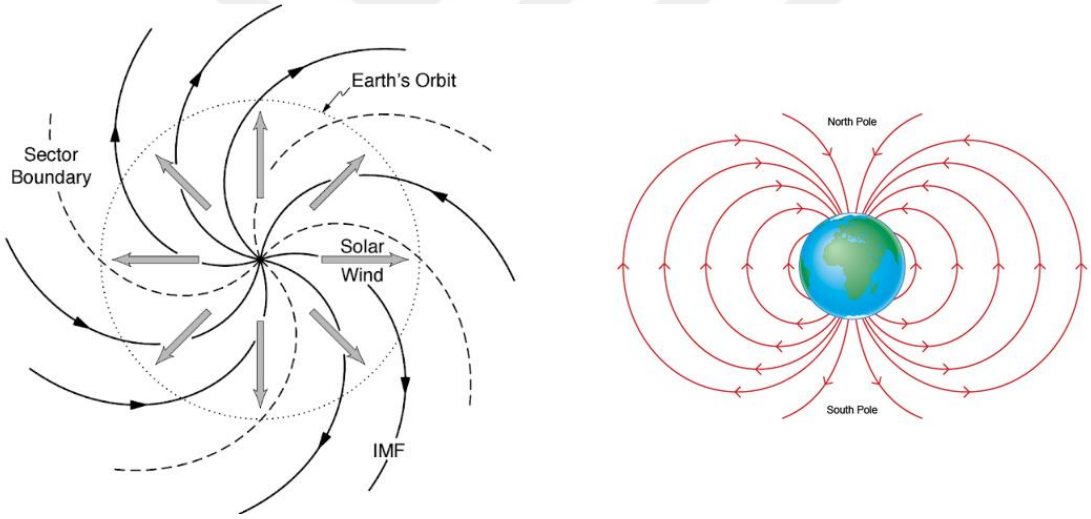

Figure 1.1 : Interplanetary Magnetic Field (IMF) Lines frozen into radially flowing solar wind on the left side (Baumjohann and Treumann, 2012) and on the right side Earth's dipole field structure.

The magnetosphere of the Earth takes its bullet like shape as a result of the interaction between the solar wind as well as the solar magnetic field with the Earth's dipole magnetic field. The magnetosphere protects the Earth from ionized particles occasionally erupting as bursts and constantly coming from the Sun and/or outside the solar system.

1.1.1 The boundary layers: the bow shock and the magnetopause

When the supersonic and superalfvenic plasma flow with Alfven Mach number and sonic Mach number higher than eight, reaches the Earth, a standing shock wave, known as the bow shock, is formed at around 14 R_E distances at the subsolar point on the dayside region. Since the density in the solar wind is very low, 5-10 #/cm^3 on average, it is a collisionless shock created by the collective effects of the electrical and magnetic effects in the solar wind. The variations in the magnetic field and plasma parameters before and after the shock are calculated via Magneto Hydro Dynamic (MHD) equations including the continuity, momentum and energy equations and Ohm's, Ampere's and Faraday's laws. In the following equations, Equations (1.1) to (1.6), ρ is plasma density, V is velocity, p is pressure, B is magnetic field, E is electric field and σ is resistivity (Bellan, 2008).

Continuity $$\frac{\partial \rho}{\partial t} + \nabla . \rho \boldsymbol{V} = 0 \quad (1.1)$$

Momentum $$\rho \frac{\partial \boldsymbol{V}}{\partial t} + \rho(\boldsymbol{V}.\nabla)\boldsymbol{V} = -\nabla p + \boldsymbol{J}x\boldsymbol{B} + \rho \boldsymbol{g} \quad (1.2)$$

Energy $$\frac{d}{dt}\left(\frac{P}{\rho^{\gamma}}\right) = 0 \quad (1.3)$$

Ohm's Law $$E = -VxB \quad (1.4)$$

Ampere's Law $$\nabla x \boldsymbol{B} = \mu_0 \boldsymbol{j} \quad (1.5)$$

Faraday's Law $$\nabla x \boldsymbol{E} = -\frac{\partial \boldsymbol{B}}{\partial t} \quad (1.6)$$

The plasma crossing the bow shock called magnetosheath (MS) with reduced solar wind flow velocity and higher plasma temperature. The solar wind speed and density vary according to the continuity law across the bow shock into the magnetosheath and thus the shocked solar wind plasma speed in this region is reduced by a factor of four while the density is increased by a factor of four at the bow shock. The magnetic field is also increased by about factor of four seen in Figure 1.2 in accordance with the Maxwell relations, given in Equation 1.5 and 1.6. Thus, the magnetosheath plasma is denser and hotter than the solar wind plasma, and the magnetic fields are higher in this

region compared to out in the solar wind. Owing to the variations at the bow shock, all the variables present turbulent structure in the magnetosheath. High fluctuations in the density, velocity, and magnetic fields parameters dominate the region. However, the plasma inside the magnetosphere is denser than the plasma in the magnetosheath. The boundary that separates these two different plasma regions with two types of dipole fields (one is belong to Sun and the other Earth) is called the magnetopause. The earliest idea of a magnetopause is proposed by Chapman and Ferraro, 1931; Chapman and Ferraro, 1940) as sketched in Figure 1.3.

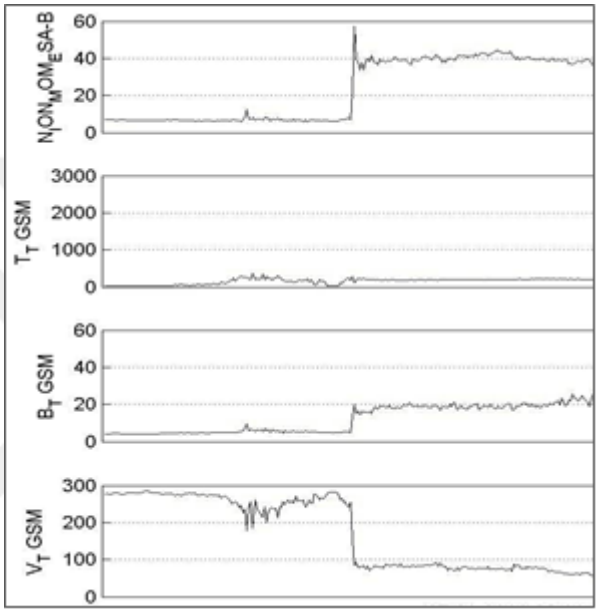

Figure 1.2 : An example Bow Shock crossing from Themis-B with density (cm^{-3}), temperature (eV), magnetic field (nT) and velocity components (km/sec).

Theoretically, the magnetopause boundary is found by the pressure balance between the solar wind plasma $P_{dyn} = \rho(V_{SW}\cos\psi)^2$ and Earth's magnetic field $P_{mag} = B^2/(2\mu_0)$. Since magnetopause is the equilibrium between the shocked solar wind and the magnetospheric field pressure, i.e. $P_{dyn} = P_{mag}$, the balance location is mainly controlled by the dynamic pressure of the solar wind since the magnetic pressure inside is due to the dipolar magnetic field of the Earth which is theoretically predictable. As the solar wind dynamic pressure increases, the angle, ψ, between the magnetopause surface and the solar wind flow direction increases and the magnetopause size widens in the dawn-dusk direction (Scherer et al., 2005). The stand-off distance of the magnetopause from the Earth's center (R_{mp}) is given in Equation (1.7). For the average values for the solar wind ($n_{sw} = 5cm^{-3}$, $V_{sw} = 400$ km/s, $B_E = 3.1x10^4$ nT, using the constant values K = 2, $m_p = 1.7x10^{-27}$ kg and $\mu_0 = 4\pi x10^{-7}$ $mkgs^{-2}A^{-2}$) the stand-off

distance is found at about R_{MP}=9.9 R_E while it can change between 6-16 R_E (Baumjohann and Treumann, 2012; Fairfield, 1971).

$$R_{MP} = \left(\frac{KB_E^2}{2\mu_0 n_{sw} m_p V_s w^2}\right)^{1/6} \quad (1.7)$$

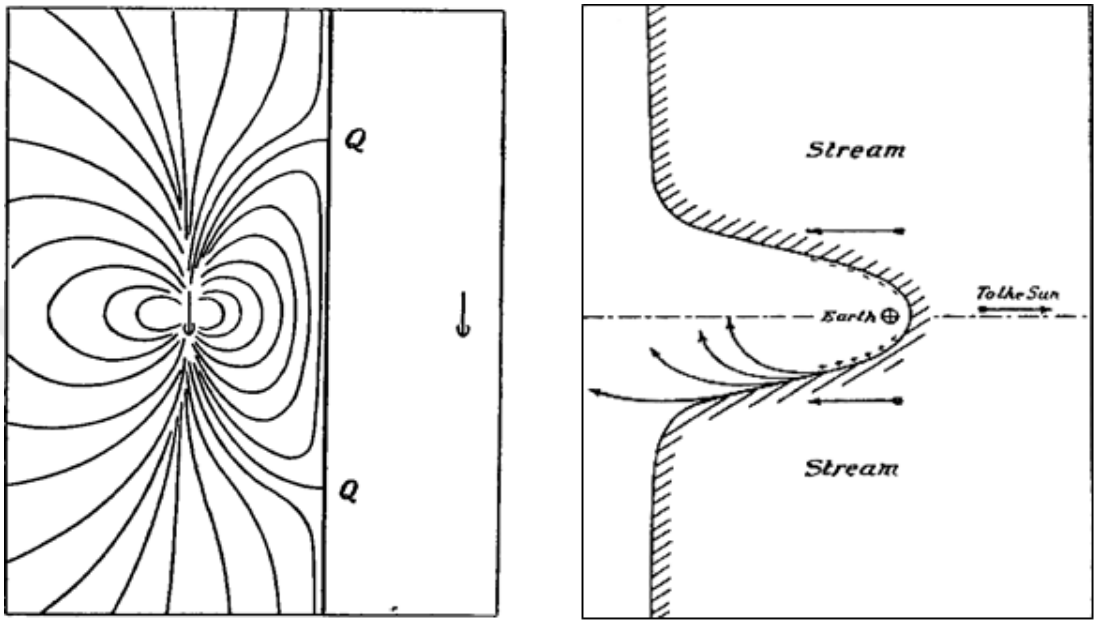

Figure 1.3 : Compressed dipole and formation of magnetospheric cavity known as Chapman-Ferraro cavity (Chapman and Ferraro, 1930; Chapman and Ferraro, 1940).

1.1.2 The geomagnetic tail

The geomagnetic tail is formed as a result of the stretching of the geomagnetic dipole field lines into a long extended tail. The tail magnetopause boundary is determined by the total of solar wind tangential force (stress) and solar wind gas pressure and the tail's magnetic and gas pressure. The magnetotail may extend beyond 1000 R_E on the nightside of the Earth (Fairfield, 1968). The magnetotail is assumed to have a cylindrical shape with a radius of 20 R_E (40 R_E diameter) under the average solar wind conditions. However, the interplanetary magnetic field direction, dynamics of the magnetosphere as well as the solar wind condition changes the shape. The magnetotail dimensions (diameter) can be ~ 53 – 59 R_E in the north-south and ~45R_E in the east-west direction (Tsurutani et al., 1984).

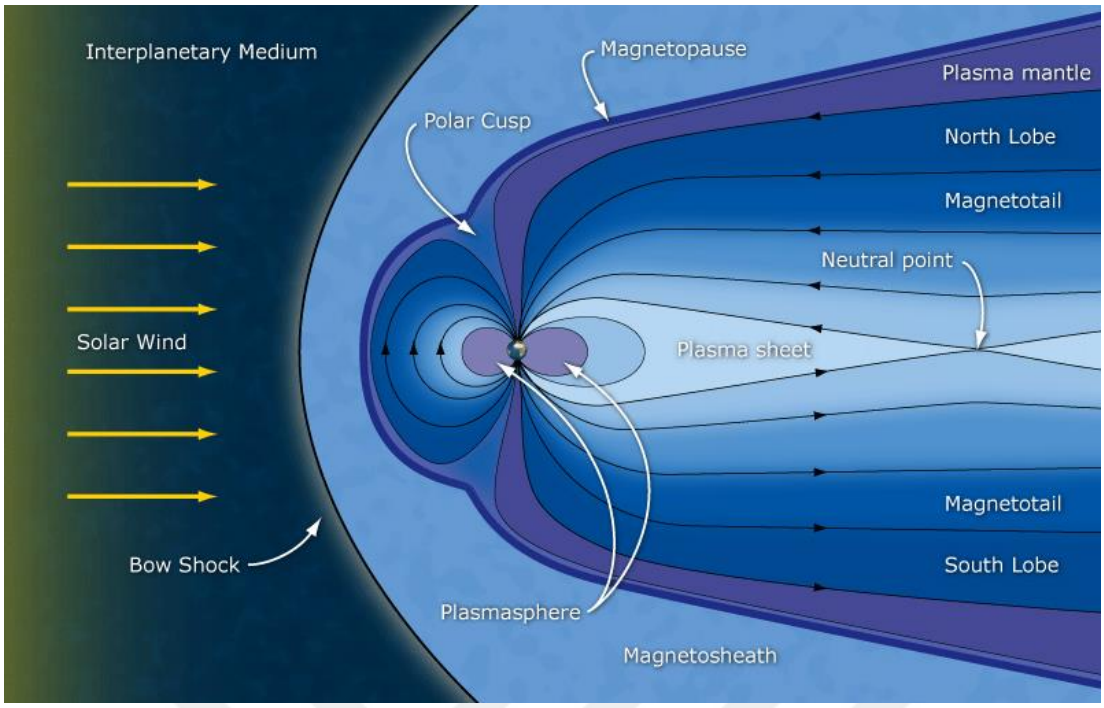

Figure 1.4 : Magnetosphere with compressed and stretched magnetic field lines after (Russell, 1972).

The XZ-plane view, noon-midnight meridian plane, of the magnetic tail regions with different plasma and magnetic structure is presented in Figure 1.4 (Russell, 1972). The tail has a two-lobe structure, with plasma sheet separating the two lobes. The nightside magnetosphere is largely occupied by the tail lobes with magnetically open-field lines, which are connected to Earth's polar caps in accordance with their hemispheres as depicted in Figure 1.5. It consists of two large bundles of nearly parallel, to the tail axis, magnetic field lines oppositely directed in the northern and southern half of the tail, which are called "northern" and "southern" lobes, i.e. directed toward/away in the northern/southern hemisphere. The tail lobes have been measured to extend beyond 220 R_E, at greater distances the tail is eventually penetrated fully by solar wind plasma (Slavin et al., 1983), (Kivelson et al., 1995). The magnetic field in the tail lobes is the strongest when compared to the tail's other regions and nearly uniform about 20 to 30 nano Tesla (nT) near Earth, diminishing to 9 to 10 nT in the distant tail (eg. Pulkkinen, 2007). The tail lobes are almost empty due to open field line configuration, with average ion densities around 0.01 cm^{-3} resulting in a low plasma-beta, β, values in this region (Koskinen, 2011).

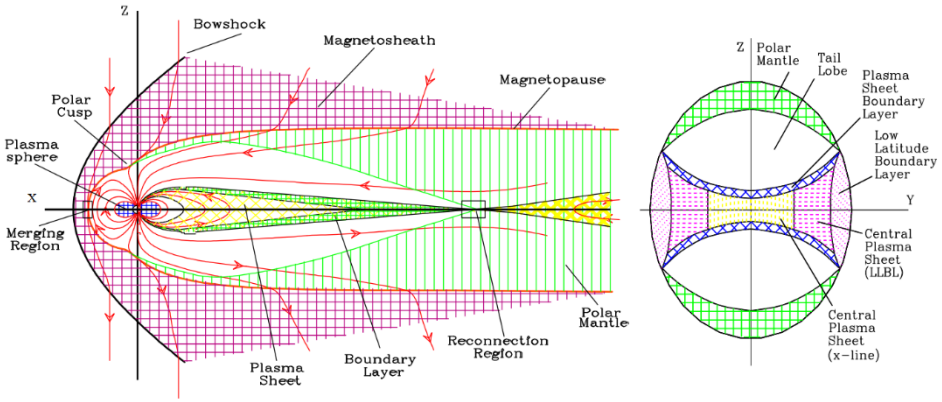

Figure 1.5 : Magnetotail regions with different plasma population in XZ- and YZ planes (Angelopoulos and Strangeway, 2009).

Between the two tail lobes is a denser plasma region called the plasma sheet (PS). The plasma sheet is a thin layer and gets thinner in the middle of the tail and expanding towards the dawn and dusk magnetopause as seen in Figure 1.5 YZ-plane view on the right side. It includes current sheet (CS), neutral sheet (NS), central plasma sheet (CPS) and it is separated from the tail lobes by plasma sheet boundary layer (PSBL). The central plasma sheet has a slightly higher density and weaker magnetic field than the PSBL as given in Table 1.2. Neutral sheet is where the magnetic field strength is very small. The magnetic fields are small but northernly (z-directed) and the x-component of the tail field (stretched component) diminishes as the magnetic field lines turn from the southern part of the tail to the northern hemisphere. Current sheet is the layer combination of the sharp turnings of the two oppositely directed magnetic field lines near the neutral line. This sudden turning creates a strong current layer at the center, called cross-tail current flowing from dawn (positive y axis) to dusk (negative y axis). Even though average plasma sheet plasma properties are given in Table 1.2, they vary with the solar wind conditions and the geomagnetic activity. The thickness of the plasma sheet gets thinner during storm conditions (Fairfield et al., 1981). The average thickness is determined as 9-15 R_E at far tail distances (Tsurutani et al., 1984).

High-Latitude Boundary Layer (HLBL), Plasma mantle, or Polar Mantle is the boundary layer that starts just inside the magnetopause and gets thinner towards the flanks as seen Figure 1.5. The HLBL (mantle) field lines are connected to the high ionospheric magnetic latitudes on The Earth's surface whereas the other ends are linked to the interplanetary magnetic field lines in the solar wind. The mantle plasma values show a transition from magnetosheath to lobe since it consists of both

magnetospheric and magnetosheath particles due to the reconnection. The plasma flows in this region are mostly in antisunward, i.e. tailward, direction.

The Low-Latitude Boundary Layer (LLBL) is a mixture of cold, dense, rapidly flowing magnetosheath and warm, tenuous, slow moving magnetospheric plasma at the flanks of magnetopause (Sibeck et al., 1985). LLBL is located inside the magnetopause and on the dawn and dusk sides of the plasma sheet separating plasma sheet from the magnetosheath with its width maximizing at dawn-dusk terminator (Mitchell, et al., 1987). The main difference between the HBLL and LLBL comes from their magnetic structure. Field lines in the HLBL are open whereas LLBL field lines are closed, i.e. field lines closes earthward (Song and Russell, 1992). Besides, the dependence on IMF is another factor to distinguish; LLBL is independent of IMF orientation while HLBL density and its thickness depends on IMF orientation (IMF By<0 or IMF By>0) (Frank, 1985), (Sibeck D., et al., 1985).

The plasma profiles of different tail regions, visualized in Figure 1.5 are tabulated in Table 1.2 in order to help us to distinguish between the different regions of the tail from the surrounding. The numbers in Table 1.2 are gathered from various sources (Lui, 1987; Sibeck et al., 1985; Angelopoulos, 2009). As shown in Table 1.2, the magnetic field magnitude is highest in the tail lobe and lowest in the plasmasheet. However, the density gives a reverse profile where it is depleted in the lobe region, increases in the plasmasheet, and maximizes in the neutral sheet. These variations in the magnetic field magnitude and plasma parameters across the regions enable us to identify their crossings along spacecraft trajectory from their data. However, the spacecraft does not have to visit magnetotail on its path during a magnetotail traversal.

Table 1.2 : Average plasma values of the different regions in the magnetosphere.

Parameters	MS	Lobes	PS	CPS	NS	HLBL	LLBL	PSBL
B (nT)	2 – 15	20 – 30	5 – 10	10	2	25	15	20
n (cm^{-3})	2 – 50	10^{-2} – 10^{-3}	10^{-1} – 1	$3x10^{-1}$	1	1	5	10^{-1}
T (K)	10^6	$<10^6$	10^6 – 10^7	10^6 – 10^7	10^7	10^5 – 10^6	10^6 – 10^7	10^3 – 10^6
V(km/sec)	200 – 500		10 – 50			300 – 400	300 – 500	

1.1.3 Solar wind – magnetosphere coupling

In space plasmas, magnetic fields and the plasma interact electromagnetically. The geometry of the magnetic field lines can be described as closed or open. While the closed fields mean that both ends of a particular magnetic field is connected to the same object, e.g. dipole field lines of the Earth, (Figure 1.6a), the open magnetic field lines refer to the field lines extending from one object but closing with another magnetic field line of a different object in space, e.g. Earth's magnetic field (Figure 1.6b). This happens under very special circumstances especially during the high solar activity times. Although the solar magnetic fields are small in magnitude and on the average lie in the horizontal plane (xy-plane), during the high solar activity, the strength of the IMF increases and IMF gains strong vertical component (z-directed) which is very crucial for the connectivity between the Sun and the Earth's environment. Until the second half of twentieth century, magnetosphere has been presumed to be totally excluded from the solar wind into a cavity. The magnetosphere in this case is called the closed magnetosphere and the magnetopause strictly separates the solar wind from the magnetospheric plasma. This is the situation expected to happen if the IMF points in the northward direction and it was long before the magnetic reconnection theories had been studied on. The ground observations of the geomagnetic field variations indicate that at special times there are particles entering the Earth's atmosphere. Following Chapman, Dungey suggested the first "open" magnetosphere concept in 1961 (Dungey, 1961). In his study, the geomagnetic field lines are connected with the solar magnetic field either on the day-side, if they are

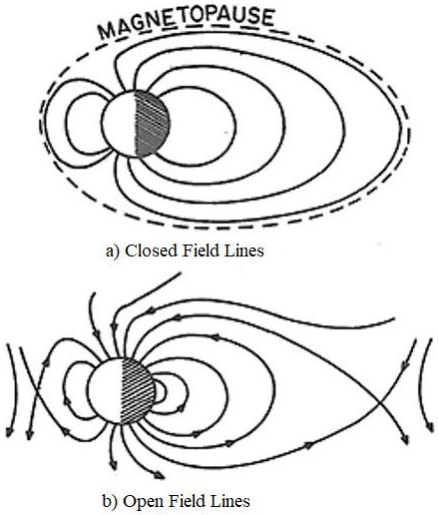

Figure 1.6 : Open and closed magnetosphere after Dungey (Dungey, 1961).

southward, or at the high latitudes of the magnetopause, if they are northward, as depicted in Figure 1.6. Thus, it is clear that the magnetic reconnection between an interplanetary magnetic field and the magnetic field of the Earth creates the open magnetosphere. This connectivity through magnetic reconnection is important because the solar wind plasma then gain access directly to the Earth's magnetosphere and atmosphere. The magnetosphere is identified as closed during pure northward IMF condition, see Figure 1.6a. The interaction between the solar wind plasma and Earth's magnetic environment is dominantly viscous as it flows along the sides of the magnetosphere while stretching the geomagnetic field lines. Current studies also suggest that the magnetosphere can be open even under the very strong northward IMFs (Kessel et al., 1996; Frey et al., 2003). There are observational evidences showing the tailward or cusp reconnection occurs during the northward IMFs as suggested by Dungey (1961). However, the situation with northward IMF is still a controversial issue and is under investigation via the numerical models and spacecraft observations. Dungey's reconnection picture with southward IMFs leads to a steady state magnetosphere as depicted in Figure 1.6b. The open magnetic flux is transported into the magnetotail via magnetic field lines opened at the reconnection site at the dayside magnetopause and they are returned back to dayside via reconnection at the distant tail. However, in reality, it is hard to find such a steady-state situation of the magnetosphere. The IMF direction is highly variable and the rate of reconnection can vary from zero which is the case for pure northward or hundred percent for the southward IMFs.

On occasion, the magnetic flux built up in the magnetotail can be carried no more and a discharge of magnetic flux and particles occur suddenly in the middle of the tail at the near Earth distances known as magnetospheric substorm (Nagai et al., 1998; Nagai et al., 2005). Magnetospheric substorms send energized particles toward the Earth into the atmosphere (Ohtani, 2004). During the substorms, magnetotail undergoes strong geometrical and structural changes as seen in Figure 1.7. As the current sheet gets thinner and a reconnection line, called X-line, forms between -15 R_E and -30 R_E distances down the tail called the Near Earth Neutral Line, NENL. Plasmoids or flux ropes are thrown away from the reconnection line, called X-line, toward the tail as seen in Figure 1.7 (Eastwood et al., 2015; Eastwood et al., 2017). Flux ropes are characterized by strong currents and spiraling of the field lines like fibers of a rope

(Slavin et al., 2003). They are formed nearly aligned and parallel to the tail axis. The strong magnetic field within the core of the flux ropes is surrounded by weaker circumferential magnetic field and they show a bipolar By magnetic field signature both of which are different than plasmoids (Sibeck et al., 1984).

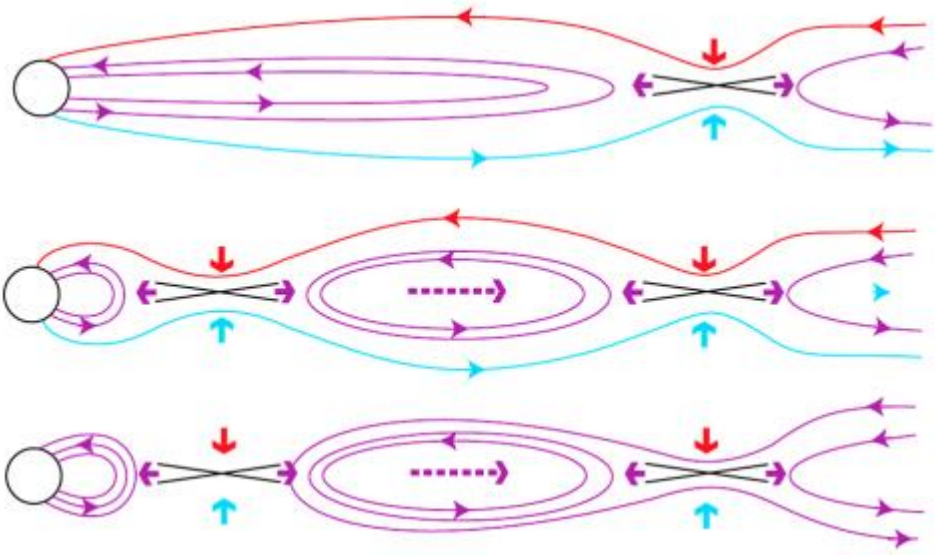

Figure 1.7 : The substorm growth phase, the substorm expansion phase, and the formation of plasmoid/flux rope release (Eastwood et al., 2015).

The Distant Neutral Line, DNL, forms at about ~ -100 R_E, and eventually the near Earth reconnection line becomes the distant reconnection point. Bursty Bulk Flow events (BBFs) occur in the center of the tail and accelerated flows are observed both earthward and tailward of the reconnection site around -25 R_E. Bursty bulk flows carry large amount of energy into the ionosphere. Other complex structures, e.g. Flux Transfer Events (FTEs), are sporadically observed mostly in geomagnetically active times. Magnetic field magnitude and plasma parameters of these structures differ from magnetosheath values. In general, these events are significantly important since they carry substantial amount of flux and energy from dayside to magnetotail (Cowley, 1982). The first studies based on FTEs indicate that FTEs are the formations caused by the merging of the magnetosheath and the magnetosphere magnetic field, as seen in Figure 1.8 (Russell and Elphic, 1978; Cowley, 1982; Sibeck and Siscoe, 1984). They are characterized by strong magnetic field, and density and temperature values between magnetosphere and magnetosheath (Sibeck and Siscoe, 1984). Majority of FTE observations have been made on the dayside magnetopause and so the evolution of FTEs as they are transported into magnetotail is poorly understood besides that they

are stretched due to tailward advection (Eastwood, et al., 2012). These interval structures like BBFs, FTEs, flux ropes and plasmoids are typical indicators of the substorm occurring near tail (Imber, Slavin, Auster, & Angelopoulos, 2011). Since the dynamics of substorm events are highly variable and spatially distributed, THEMIS mission with a primary objective to investigate these events and collect multi-point measurements reveals the mystery of substorm evolution (Angelopoulos V. , 2009). The variations in the area of the mid to distant magnetotail are primarily related with the magnetic flux escape from the tail and how much energy is stored inside (e.g. Hones, 1985).

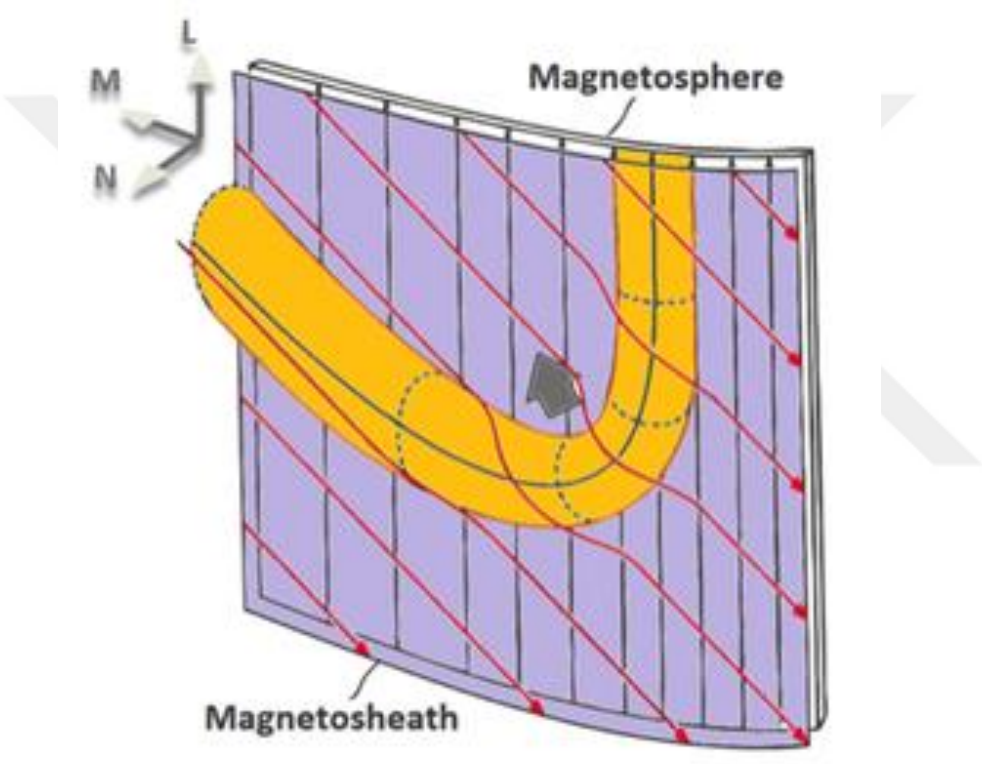

Figure 1.8 : Flux Transfer Event Formation (Russell and Elphic, 1978).

1.2 Purpose of Thesis

The Earth's magnetotail structure has been an area under discussion for decades. Luna 10, Explorer 33, Explorer 35, Pioneer 7, Pioneer 8, Geotail, WIND, ISEE 3 and IMP 8 crossed the tail at different distances down the tail (Dolginov et al., 1966; Gringauz et al., 1966; Ness, 1967; Mihalov and Sonett, 1968; Behannon 1968; Meng and Anderson, 1974; Wolfe et al., 1967; Ness et al., 1967; Fairfield, 1968; Walker et al., 1975; Slavin et al., 1983; Tsuturani et al., 1984; Sibeck et al., 1985; Kaymaz et al.,

1994; Kaymaz et al., 1995; Sanchez et al., 1992). Despite large number of spacecraft visited geomagnetic tail, owing to very brief passes, single spacecraft observations, lack of instrumentation, low-resolution data sets, etc., we are still far from fully understanding many of the phenomena that control the structure of the magnetotail and the dynamics at several distances from the Earth. The many of the both global scale features and especially the microphysical phenomena and their consequences require simultaneous observations from multiple spacecraft. The need for two-spacecraft measurements is crucial in order to separate temporal from spatial effects. ARTEMIS probes are one such spacecraft-in-pair to perform the first systematic, two-point observations of the mid-to-near distant tail, the solar wind, and the lunar environment while orbiting around the Moon. This continuous set of observations at $\sim -60R_E$ help us to understand how the tail dynamics vary at lunar distances, what are the connection to the near earth tail, what is the geometry, flow and magnetic structure of the tail and how it is controlled, how much of the information is known based on the limited number of observations taken before and how much is not, what is confirmed and what is not. Although there have been several spacecraft visits, even though brief, distant tail, distance larger than 100 R_E, ARTEMIS is the first mission launched to study the magnetotail at lunar distances. Our purpose in this study is, by taking the state of the art instrumentation and twin spacecraft measurements of the ARTEMIS probes to reveal;

- Magnetopause shape and size,
- Magnetotail topology (geometry),
- Magnetic field structure,
- Plasma flow morphology,
- Plasma characteristics (i.e. density, temperature, pressure etc.), and
- How they relate to external and internal structures (e.g. IMF By, IMF Bz)

at lunar distances.

This dissertation is the first study, which investigates the map of magnetotail at $-60R_E$ distance using a twin spacecraft, ARTEMIS p1 and p2, with high resolution instruments. ARTEMIS spacecraft spends most of their time, (80%), in the solar wind while orbiting around the Moon (Sibeck, et al., 2011). However, every once a month

the Moon moves around the Earth and passes through the Earth's magnetosheath and magnetotail for 2.5 – 4.5 days so that the magnetopause boundary and the magnetotail itself can be studied by ARTEMIS observations. Figure 1.9 presents fifty ARTEMIS trajectories from August 2011 to August 2013 in (a) xy-, (b) xz-, and (c) yz- GSE planes to illustrate the coverage of the tail crossings. The orbit of the Moon is plotted with orange-dashed line in xy-plane and the average magnetopause and the bow shock positions are presented using Roelof and Sibeck study (Roelof & Sibeck, 1993). Given the low inclination of ARTEMIS orbits, better coverage in the equatorial plane is achieved as seen in detail in Section 4.1.1.

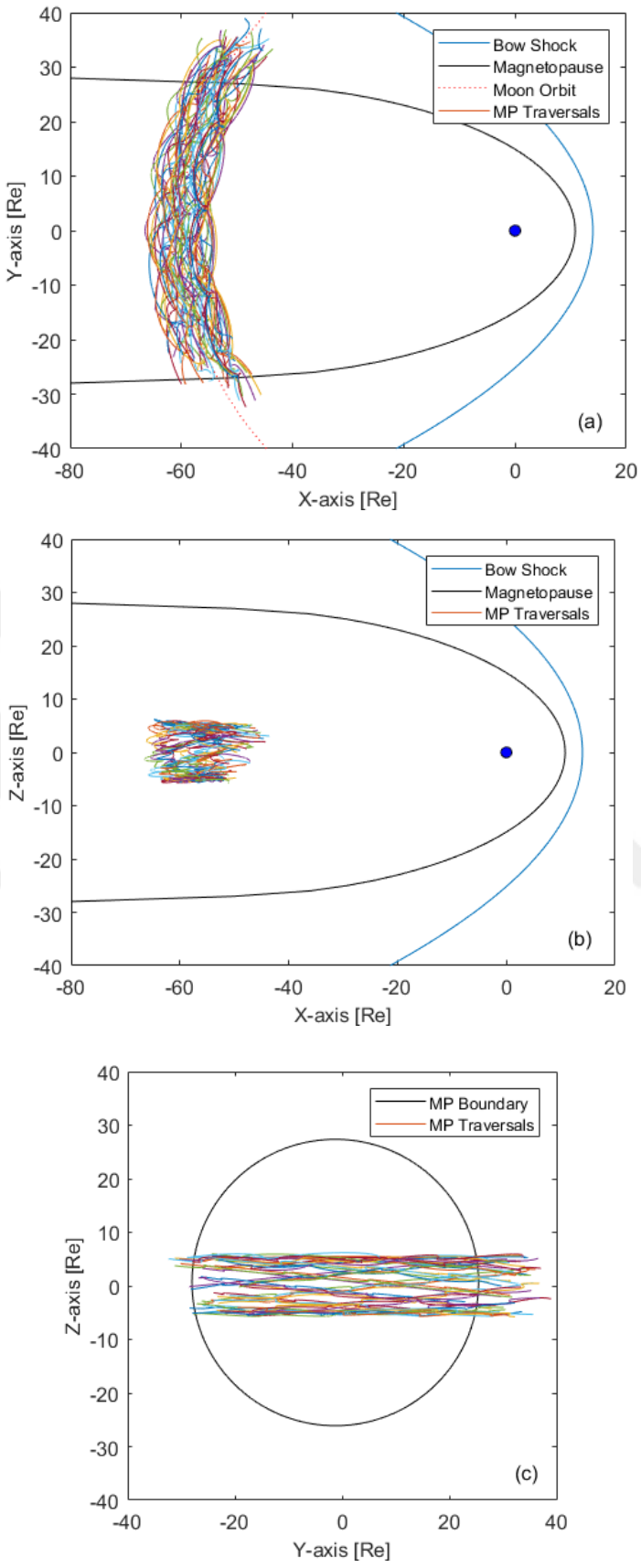

Figure 1.9 : ARTEMIS trajectories in GSE coordinates (a) xy-, (b) xz- and (c) yz-planes. The average magnetopause and the bow shock positions are plotted using Roelof and Sibeck (1993) study.

1.3 Literature Review

There have been many studies of the magnetotail since its discovery during 1960s. The studies related to our concern, analyzing the shape and structure of the tail, have been observed by Explorer 33-35, ISEE 3 and Geotail for the distant-tail ($x \geq 200R_E$). These studies are summarized according to their influences.

The studies related to magnetic field topology, magnetic flow morphology, and other parameters are presented in details in Section 3. 4.1, 4.2 and 4.3, respectively.

1.3.1 Magnetotail shape and size

The structure of the nightside magnetotail had also been in discussion; either it has a filamentary structure or not. Several dated studies had pointed out that tail may be filamentary especially after several hundred R_E distances whereas the successor ones established two-lobe tail structure with plasmasheet embedded in center (Tsurutani et al., 1984). The IMF dependence of the magnetotail shape, structure and dynamics has been studied for northward and southward IMF cases, using ISEE 3 observations by many researchers (Fairfield, 1992; Chen et al., 1993; Fairfield, 1993; Raeder et al., 1995). In the average tail configuration, in Figure 1.10, the last closed field line crosses equatorial plane at about $-100R_E$ but tail structure extend beyond $-200R_E$, whereas for strong northward IMF cases the last closed field line is found at around $-150R_E$ distances, leaving a short tail (Fedder and Lyon, 1995). High latitude reconnection may affect the length of the tail since it can convert open interplanetary field lines to closed ones (Fairfield, 1993). Observations of magnetosheath at ecliptic regions can be explained by non-radial solar wind, solar wind streams and closing of the polar cap field lines earthward (Fairfield, 1993). The north-south dimension of the distant magnetotail is also found to be related with the interplanetary magnetic field direction. The cross-sectional area of the mid to distant magnetotail is primarily related with the magnetic flux escape from the tail, either through the magnetopause boundary or via connection across the neutral sheet. This area may change according to the external effects.

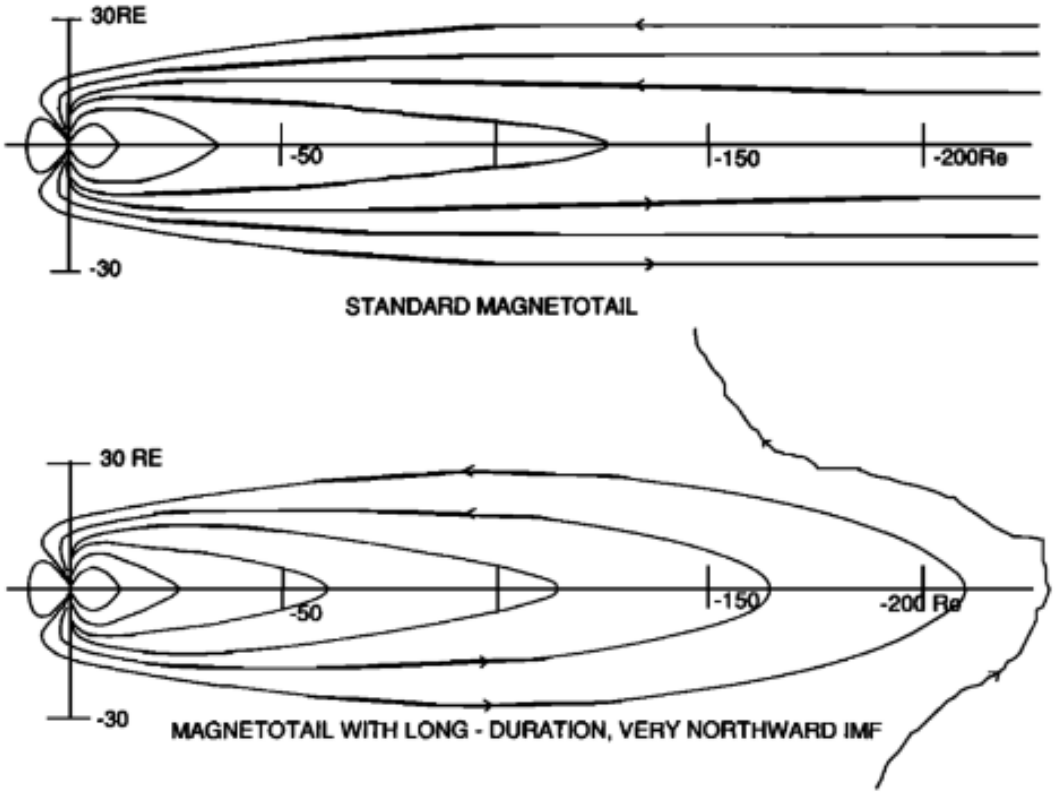

Figure 1.10 : Average configuration of the magnetotail (top) and magnetotail under very strong northward IMF condition (bottom) with high latitude field lines closing earthward < −200R_E following Fairfield (Fairfield, 1993).

Table 1.3 : The average magnetotail size in YZ-plane from various studies from mid-to Distant-tail distances following (Sibeck et al., 1986).

Distance (X) [R_E]	Tail Size [R_E]	Reference Study
−40:−80	40x60	(Behannon, 1968; Behannon, 1970)
−40:−100	56x56	(Howe, 1971; Fairfield, 1971; Howe and Binsack, 1972
−50:−70	40x60	(Behannon, 1968; Behannon, 1970)
−50:−80	56 – 56±2	(Howe, 1971; Howe and Binsack, 1972; Fairfield, 1971)
−60	20x30	(Behannon, 1970)
−60	52x52	(Howe and Binsack, 1972; Reiff and Reasoner, 1975)
–60	50x50 ±0.8	(Mihalov, 1970; Siscoe, 1972)
< −100	Quiet: 70x46 Disturbed: 52x68, 56x74	(Nakamura et al.,1997)
−130:−225	60x60 ±5	(Slavin et al., 1985)
< −200	45x53 – 59	(Tsurutani et al., 1984)
< −200	48x48 ±4	(Fairfield, 1992)
−200:−220	75.6x37	(Sibeck et al., 1986)

The early studies on magnetotail cross section assume the shape as a circle (Behannon, 1970; Fairfield, 1971; Howe & Binsack, 1972). The following researches agree on slightly elliptical cross-section while differentiating in the elongation direction; either on the y or z direction (Tsurutani et al., 1984; Hill, 1985; Sibeck et al., 1986). The Table 1.3 gives the tail size observations at different distances down the tail following (Sibeck et al., 1986).

1.3.2 IMF control of the nightside magnetotail

The magnetopause structure is often indicated either as a tangential or as a rotational discontinuity (Matzner, 2001). The research on magnetopause crossings tested the models to understand the reason why and how magnetosheath plasma enters magnetosphere. The reconnection model suggests that the interconnected tail and sheath field lines leave the magnetotail through a long, narrow "window" (Cowley, 1981; Sibeck et al., 1985; Sibeck et al., 1986).

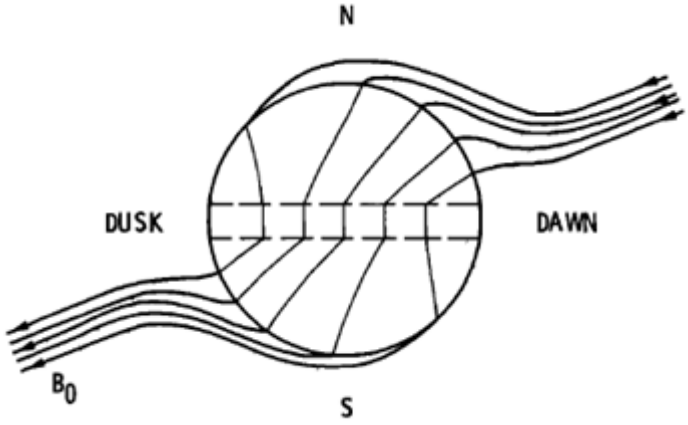

Figure 1.11 : IMF $B_Y > 0$, interconnection in north-dawn & south-dusk quadrants following (Tsurutani et al., 1984).

Due to sharp plasma parameter changes during magnetopause crossings, they can be described as tangential discontinuities over the most of its surface. However, magnetopause is a rotational discontinuity where the magnetotail and magnetosheath field lines leave and enter tail via a narrow (5 R_E) "window". The quadrant of the windows may change according to the sign of the B_Y and B_Z (Sibeck et al., 1985). Existence of a positive or negative IMF By in the magnetosphere determines where tail field lines cross the magnetopause and in which quadrant of the tail, the interconnection takes place (Cowley, 1981; Tsurutani et al, 1984). Depending on in which quadrant the interconnection will take place, an unequal flux transfer will be

created over the magnetopause. This asymmetry in Figure 1.11 with magnetic field lines in the dawn and dusk side of the northern and southern hemispheres, twist the tail accordingly (Cowley, 1981; Tsurutani et al., 1984).

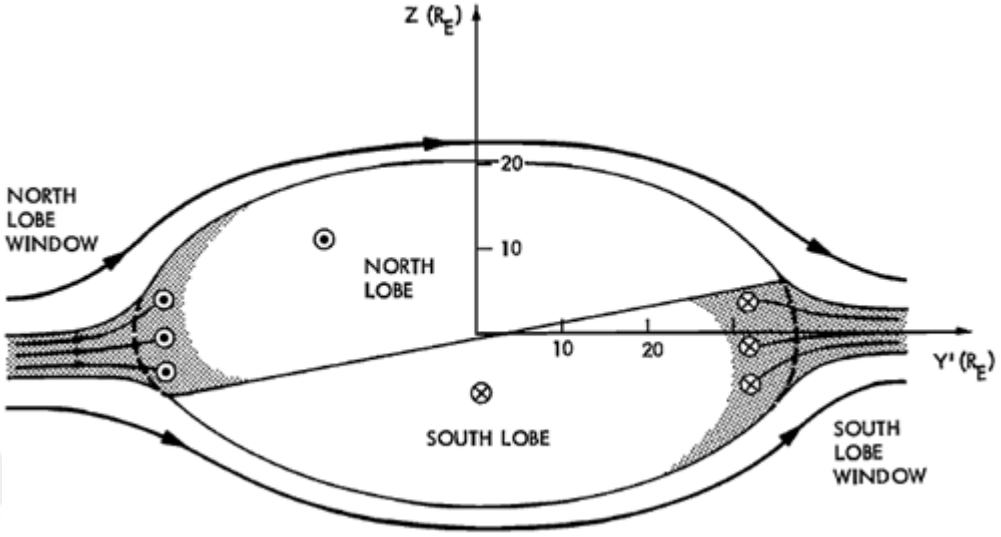

Figure 1.12 : The tail cross-section at around −200 R_E, as seen from Earth following Sibeck's study (Sibeck et al., 1985).

A strong B_Y case with twisted magnetotail where north lobe is encountered below the ecliptic plane investigated by Sibeck et al. (1986). The effect of this IMF condition on plasma is well-defined as flattening, bending and twisting. The anisotropic pressure of draped magnetosheath field lines causes tail cross-section to flatten in the z-direction. The interconnected magnetosheath and magnetotail field lines bent in the IMF direction to pass through the windows. The newly formed merged magnetic field lines exert a torque upon the tail and bring the north lobe below ecliptic as seen in Figure 1.12 (Sibeck et al., 1985). Therefore, models incorporating merging between dayside magnetosheath and magnetospheric field lines predict the location of the magnetotail layer and bending of magnetotail field lines in the direction of the IMF (Sibeck et al., 1985).

1.3.3 Substorm effects on the magnetotail

Observations show that the tail grows at the geomagnetically quiet times (Fairfield, 1992; Hill, 1985). The smaller radius measurements have been caught by ISEE 3 at 225R_E distances associated with high K_P and high-pressure values. The average radius of the tail near lunar distances is approximately 25 R_E (Mihalov et al., 1970; Hardy et al., 1979) and increases with the distance (Slavin et al., 1985). Tail radius sizes are

approximately observed as $15R_E$, $22R_E$, $25R_E$ and $30R_E$ at distances of terminator, 25−35 R_E, $60R_E$ and $200R_E$ down the tail. The radius increase trend slows down after mid-tail distances due to flaring effect (Coroniti and Kennel, 1972; Slavin et al., 1983). Tail radius can be determined either by marking the magnetopause crossings or by considering the frequency distributions of the east-west and north-south occurrences of the tail (Fairfield, 1992). Down the tail, as the solar wind and other effects increase, the determination of the magnetopause location gets complicated (Slavin et al., 1993).

1.3.4 Plasma flow at lunar distances

ARTEMIS is the first multi-spacecraft mission with the comprehensive and high-resolution magnetic field and particle instrumentation required to study the mid-to-distant tail, i.e. lunar distances. ARTEMIS probes are located between the two magnetotail reconnection regions, the Near-Earth Neutral Line (NENL) at about -20R_E to -30 R_E distance and the Distant Neutral Line (DNL) at about -100 R_E distances down the magnetotail. This crucial positioning of the probes is chosen on purpose (Sibeck et al., 2011) and is to be used to investigate the plasma flow characteristics, e.g. flow velocity, direction and its dependence on IMF, between these two source regions.

In the near earth magnetotail (>-30 R_E) the plasma flow direction is temporally and spatially depended on the substorm activity whereas the bulk plasma flow in the distant tail (<-100 Re) are dominantly in tailward direction (Hones and Schindler, 1979; Hayakawa et al., 1982; Bame et al., 1983; Zwickl et al., 1984). At lunar distances, the probability of the earthward/tailward direction of the plasma flow has the same occurrence rate (~50%) based on lunar swingbys of the ISEE 3 spacecraft (Scholer et al., 1984). Thus, the flow structure at lunar distances is expected to be affected from both structures and will be a mixture of two effects.

In the study by Rich et al. (1973), the average quiet-time plasma characteristics are presented as $n = 0.1 cm^{-3}$, Te = 0.20keV, $P_{plasma} = 4.3x10^{-11}$ N/m^2 and the plasma sheet thickness as the $5R_E \mp 2R_E$ at lunar distances. In this study, plasma velocity vectors will be studied in all planes, as well as their statistical characteristics. Besides, the temperature, density and pressure parameters will be evaluated and compared to the findings of previous studies.

1.4 Organization of Thesis

The dissertation study starts with an introductory chapter that contains brief information regarding the Sun, interplanetary medium, and the magnetotail. Then the purpose of the thesis is given in which we point out the uniqueness and the singularity of this study. After that, a comprehensive set of background studies are presented according to how they relate to our study. After literature review, thesis organization is presented.

Chapter 2 starts with the details of on-board instruments from which the observations are taken both of the ARTEMIS and the solar wind monitor spacecraft. Then how the magnetopause crossings are determined and marked as the magnetotail boundary is given with examples of ARTEMIS crossings. After identification of the magnetopause crossings, the appropriate coordinate system is explained. The data is gathered in GSE however, the investigation should be done after various conversions to make judgements. Then, how we separate our data according to IMF direction is given since all of our findings are evaluated according to its corresponding IMF condition in which IMF sector separation is done by the use of IMF clock angle.

In Chapter 3, the magnetopause positions will be plotted in the xy-, xz-, yz- and xR-planes where we will see if the tail has a firm, stable shape or if it is moving a lot thus the magnetopause positions will be scattered. We will try to find the best fit to describe the magnetopause locations, which will give us the average shape of the tail at $-60\ R_E$. In this chapter, we will also test available analytical models of the magnetopause shape and see how they represent the tail at lunar distances or why they can not?

Chapter 4 is the core of this thesis study in which the magnetic field structure, plasma flow morphology and other parameters, e.g. temperature, density, pressure, of the magnetotail at lunar distances is mapped. The aim is to find an answer to the following questions. Do we see the tail structure as a compact structure, i.e. current sheet, plasma sheet, lobes, magnetopause boundary? Alternatively, do we see a filamentary structure where we see only part of the tail? What is the tendency for the plasma to flow, i.e. tailward/earthward direction? Can we observe the general IMF effects on the tail at lunar distances, i.e. the twisting, flattening, etc. due to IMF By and the expanding and flaring effect due to southward IMF Bz? How the temperature and density profiles look like at mid-to-distant tail? We will look at the magnetic field and plasma

signatures for this. We will first determine nearby magnetosheath characteristics and solar wind properties at -60 R_E and reveal the plasma statistics using ARTEMIS magnetic field, plasma flow, density, temperature, and pressure measurements. In addition, how all of these parameters changes with the IMF direction and within the tail, i.e. whether there is any asymmetry in dawn-dusk direction of the tail.

The last chapter covers the conclusion and recommendations for future studies.

2. DATA SET AND METHODOLOGY

In this part, first we present a brief literature survey about what have been studied related to the distant tail. The structure of the distant magnetotail, north and south lobes, plasmasheet, and boundary layers, and their response to the solar wind plasma and IMF, the studies on the size and length of the tail were reviewed. This is followed by ARTEMIS mission details, its instrumentation and its data details. Then we present our motivation in this work and highlight what we will be studying on, the research problems we will address and the tools and data we will be using.

2.1 ARTEMIS Instrument and Data

The Acceleration, Reconnection, Turbulence, and Electrodynamics of the Moon's Interaction with the Sun (ARTEMIS) mission is a "green" one in a way that it reuses two of the five THEMIS probes by repositioning them at lunar distances, about $-60R_E$. The five THEMIS satellites were launched by NASA in 2007 to explore how the sun's magnetic field and solar wind interact with Earth's magnetic field on Earth's near nightside, $< -30R_E$. As the mission objectives completed in 2010, two of the outer probes are placed to the Moon to extend their magnetic field studies farther into space as seen in Figure 2.1.

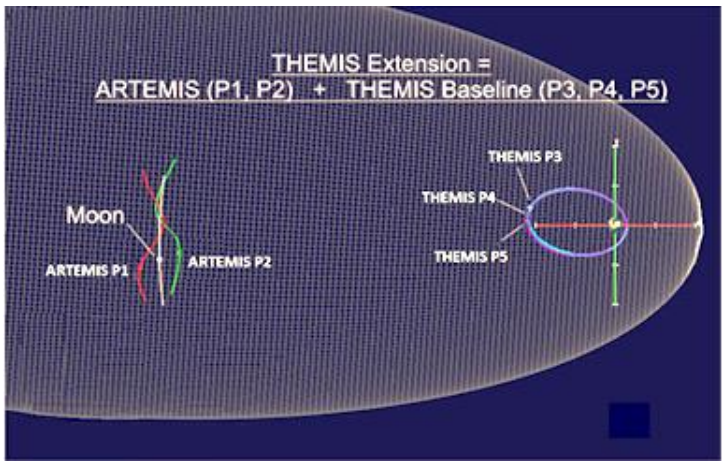

Figure 2.1 : The ARTEMIS satellites in lunar orbit and THEMIS satellites in near-Earth orbit (Angelopoulos, 2009).

To achieve this new mission, a successful set of orbital maneuvers took place for a period of 18 months (Angelopoulos, 2009). The probes are placed into temporary orbits via trans-lunar injection near the Earth-Sun Lagrange points and then into two Earth-Moon Lagrange points. After these flybys, probes are settled into a stable orbit around the Moon's equator on July 2011 since when magnetopause and magnetotail data had been collected for this study.

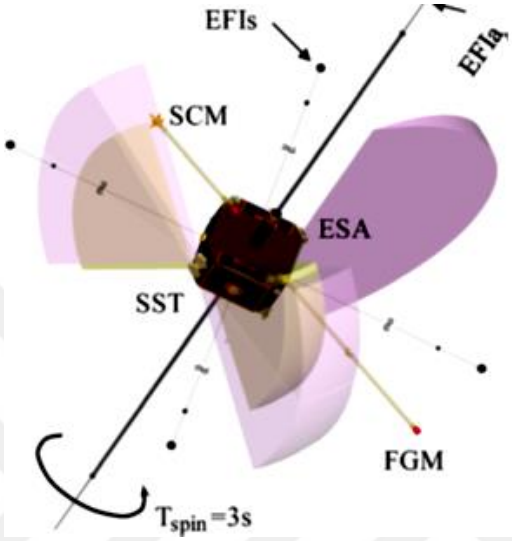

Figure 2.2 : Magnetic field and plasma instruments and their whereabouts shown on spin-stabilized ARTEMIS probe (Angelopoulos V. , 2009).

ARTEMIS probes measure magnetic and electric field with its Flux Gate Magnetometer, FGM, and Electric Field Instrument, EFI, while Electro Static Analyzer, ESA and Solid State Telescope, SST instruments measure plasma data (Auster et al., 2008; McFadden et al., 2008; Angelopoulos, 2009). The whereabouts of the instruments are shown on the Figure 2.2. ARTEMIS data used throughout this study is gathered from the Flux Gate Magnetometer (FGM-FGS), the Electrostatic Analyzers (ESA) and the plasma moments (MOM) from August 2011 to August 2013. The FGM measures magnetic field in three-dimensions while ESA data gives the density, velocity, and temperature of the plasma and the ion spectra (Sibeck and Angelopoulos, 2008).

2.2 Solar Wind Monitor Instrument and Data

Advanced Composition Explorer (ACE), launched in 1997, is a mission designed to monitor solar wind constantly in L1 Lagrange point, which is a point of Earth-Sun gravitational equilibrium about 1.5 million km (235 R_E) from Earth (Stone, et al.,

1998). ACE carries a magnetometer and a suite of charged particle instruments designed to measure the properties of ions in a wide energy range to be able to determine the change of the particle properties during quiet and active periods. In this thesis, the bulk parameters of the solar wind, i.e. position, magnetic field and velocity components are necessary in order to match magnetotail data with the solar wind information. Data from the Magnetic Field Experiment (MAG) is used with 16-sec resolution for position and the magnetic field components whereas for ion velocities Solar Wind Electron Proton Alpha Monitor (SWEPAM) instrument is used with 64-sec resolution (McComas et al., 1998; Smith et al., 1998). In the absence of ACE data, WIND spacecraft is also used since it is one of three solar monitors (ACE, WIND and DSCOVR, replacement of ACE) at L1. Data used from Magnetic Field Investigation (MFI) and Solar Wind Experiment (SWE) instruments (Lepping et al., 1995; Ogilvie et al., 1995). All validated (level 2) data from the ACE and WIND spacecraft were averaged over 1-min resolution for consistency between each other and the magnetotail data form ARTEMIS probes. Solar wind information is publicly available through the CDAWeb portal and gathered from that source. In the analyses, the magnetic field and velocity data from ACE or WIND were in GSM coordinates, while ARTEMIS data were converted into a new coordinate system that takes into account the non-radial components of the solar velocity and the aberration due to the Earth's motion as described in section 2.3.3.

2.3 Methodology

In our study, the time intervals when ARTEMIS probes are in lunar wake were carefully detected by visual inspection of each parameter, i.e. particle energy, energy flux, velocity, density and magnetic field, and simply deleted from our data set in order to remove the ambiguity related to this. An example of such time interval selected from UC-Berkeley's ARTEMIS website is given to show how lunar wake intervals are detected. In the Figure 2.3, the orange rectangle area indicates the period that covers the lunar wake. In this example taken on 2012/08/29, probes were in the lunar wake approximately from 15:30 to 16:30, and therefore, this period was identified as lunar wake interval and the data in this interval were omitted from our data set.

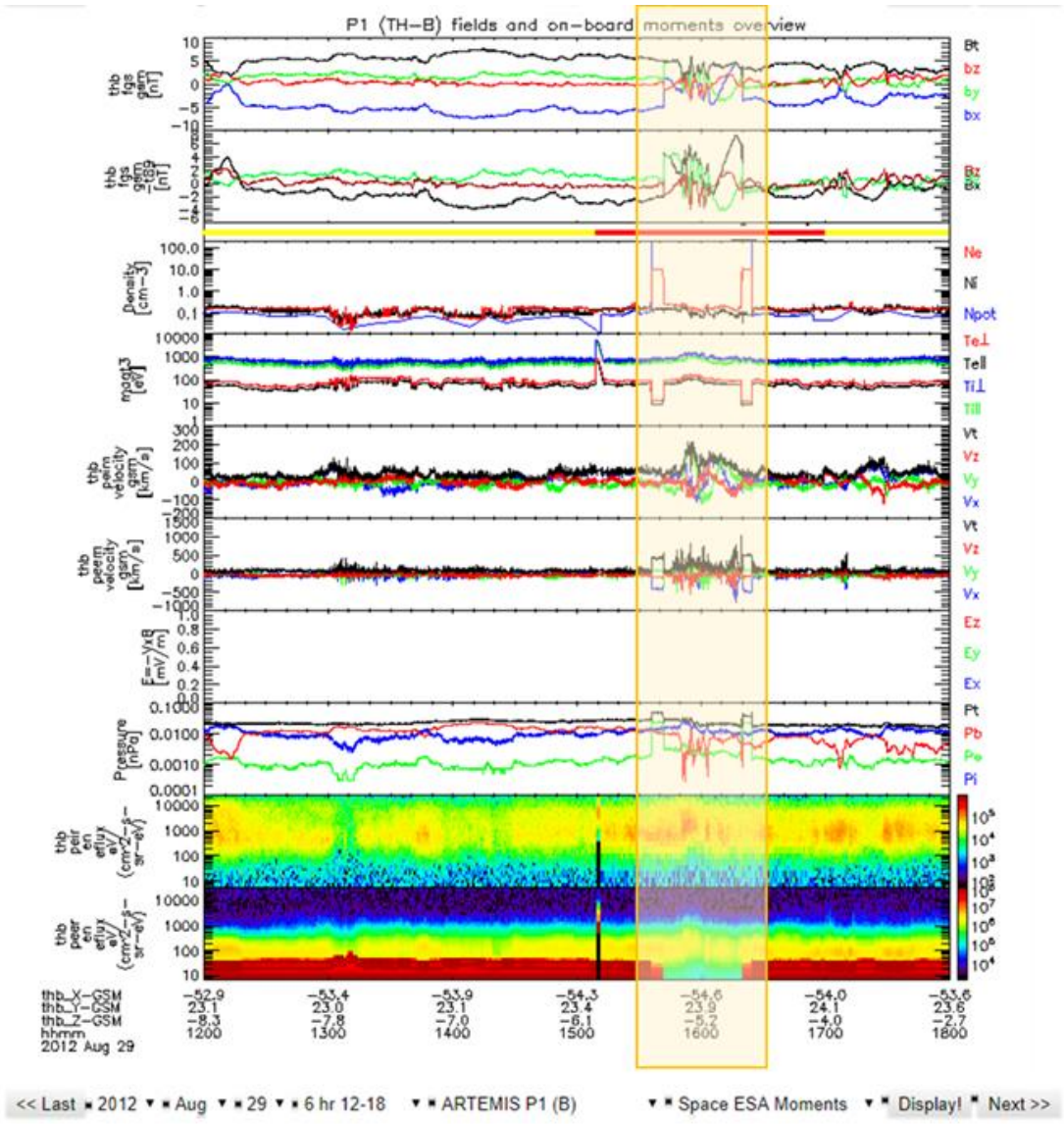

Figure 2.3 : An example interval of time when ARTEMIS probe is in lunar wake.

ARTEMIS probes encounter lunar wake at every 25-30 hours during one tail passage and each lunar wake lasts about 20-60 minutes. During a lunar wake, the energetic particle flux drops out and gives a very clear sign of the wake along the trajectory. In addition, total B and ion temperature increase while the density and velocity decrease. In Figure 2, the lunar wake effect is clearly visible as large spikes in the density, temperature and velocity panels. These intervals were carefully detected and excluded from the data set.

Multiple crossings are quite often in our database, one of which is shown in Figure 2.6.

2.3.1 Matching ARTEMIS and ACE information

When we match each 888 magnetopause crossings to corresponding ACE time for solar wind information, the delay time is different for each crossing. A pie chart in Figure 2.4 shows that depending on the solar wind velocity, the delay time (MP Crossing Time from ARTEMIS – Anchor Time at ACE) can be as low as 40 minutes, or as high as 120 minutes. Another percentage discussion is about the accuracy of matching ARTEMIS time to ACE time procedure. When calculating the delay time and finding the ACE time (anchor time), there might be a gap in the data, or it can converge so that the "nearest" time is taken for matching with solar wind information which corresponds to a maximum of 5 min. For example, 91% of our crossings data were combined within 1 min with ACE/WIND data, i.e. the closest time between the two data set was found within 1 min (exactly concurrent matching for near 1-min data resolution of both spacecraft), and while 2% were combined within 5 min interval. In this last case, we find that ARTEMIS data are concurrent with ACE/WIND data within maximum 5 min.

$$\Delta t_j = \frac{X_{ace_i} - X_{art_j}}{|V_{x_{ace_i}}|} \tag{2.1}$$

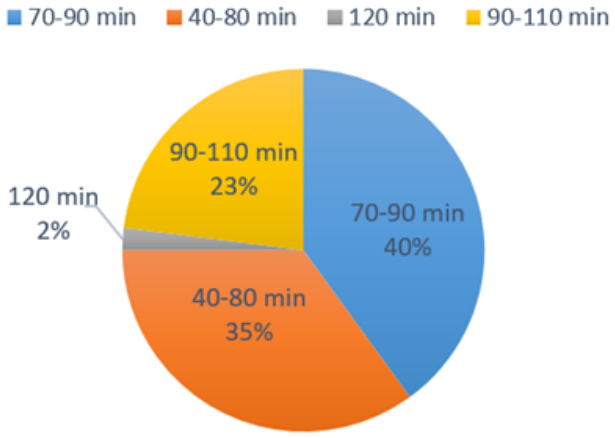

Figure 2.4 : ARTEMIS-ACE Delay time distribution.

2.3.2 Identification of the boundary

At lunar distances, the boundary layers do not look as definitive as the dayside or near Earth tail magnetopause owing to the decreasing geomagnetic field strength by distance down the tail and the trajectory of the ARTEMIS in the xy-plane. One of the

best signatures of the magnetopause definition is the magnetic field direction and strength within the tail.

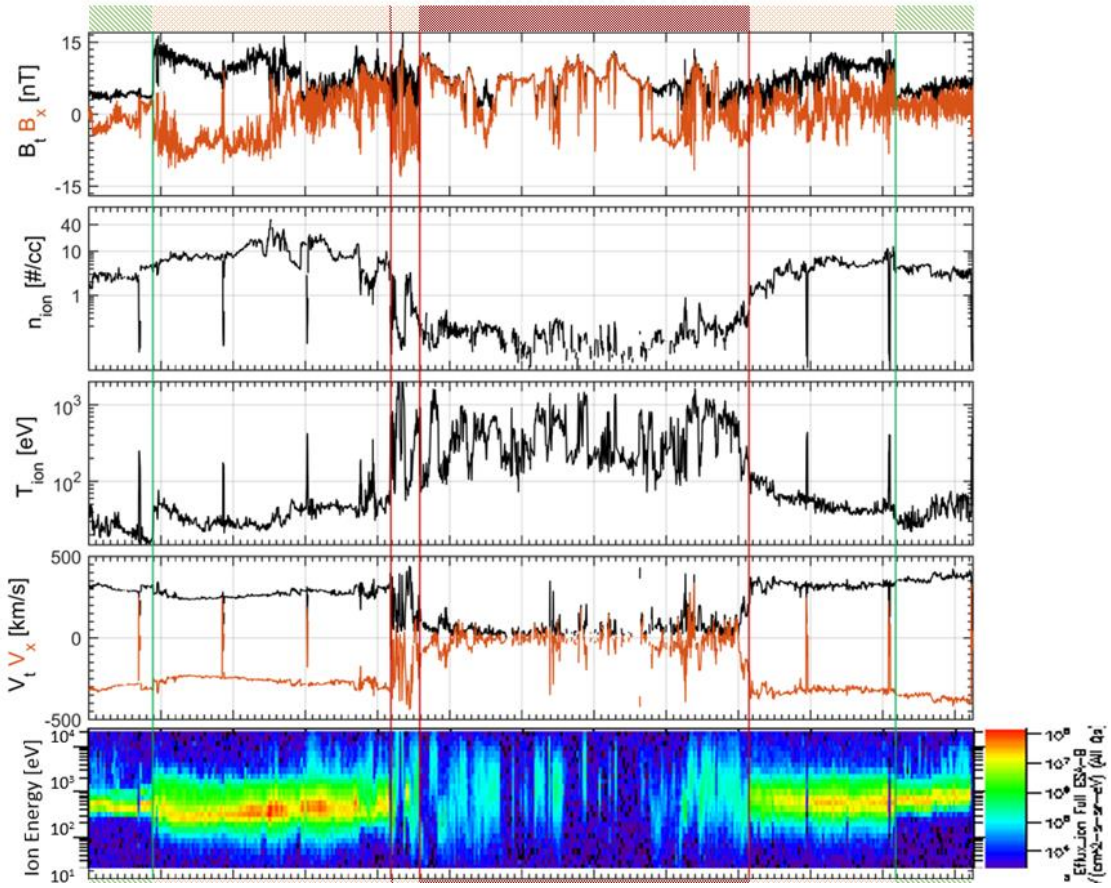

Figure 2.5 : An example of magnetotail pass at -60 R_E from ARTEMIS-B on the day of July 10, 2011. The bow shock and magnetopause were shown in red and green respectively. The panels from top to bottom represent density, temperature, and total magnetic field, speed and x-component of velocity (Vx) data.

We will first determine where the magnetopause crossings occur. For this purpose magnetic field, density, velocity, temperature and ion energy observations are visually investigated in macro (daily) and then micro (hourly) scales from ARTEMIS-UC Berkeley's website. This is a very tedious process. The best criteria in defining the magnetopause boundary at lunar distance is decided. The plasma parameters show a gradual increase/decrease between magnetosheath to lobe values as seen in Figure 2.5. The probes passes through the solar wind, magnetosheath into the geomagnetic tail, then continue to magnetosheath, and leave the magnetosphere to interplanetary medium. The hypersonic flows can be seen in the tail center.

To identify the exact position of the magnetopause crossing, the variations in all magnetic field, density, temperature, velocity, ion energy, ion flux, and derived

quantities such as pressures were carefully examined. The particle energies in the magnetosheath are found to range from a few 100s eV to a few 1000 eV but being lower than those in the adjacent plasma sheet region that are typically higher than 1000 eV. In the lobes, on the other hand, high-energy particles do not exist. Therefore, the presence or absence of high-energy particle flux indicates the spacecraft entry/exit to/from the magnetotail, and thus the location of the magnetopause boundary. In addition, the change in the high-energy particle flux is accompanied by a rapid increase in plasma temperature and decrease in density and velocity during an inbound pass, and vice versa for an outbound pass. We emphasize that if not all above quantities show clear signatures at the spacecraft position; the position was not included as magnetopause position in our list.

The magnetotail is not a stable structure. As a result of its motion in response to internal and external causes, the spacecraft often encounters the tail boundary multiple times. While presenting stimulating dynamics of the tail boundary at -60 R_E, accurate detection of these multiple crossings is a very tedious and lengthy process. The time interval between the multiple crossings can vary from minutes to a day at the lunar distance. In our search, the multiple crossings occurred within 5 minutes were not included in the analysis. 5 min threshold was chosen somewhat arbitrarily to optimize between maximizing the number of crossings and the time to spend in identifying each crossing. Consequently, this selection imposes only the temporal variations of the magnetopause boundary larger than 5 min to be considered. The shorter time variations of the boundary known to be caused by the substorms, wave activities etc. were ignored. The exception for this, however, as dual spacecraft, there are instances that both ARTEMIS spacecraft may encounter the boundary at about the same time or within 5 min of each other. Another point to mention is that the magnetopause crossing positions in our data set are not consecutive entry-exit pairs of the boundary. As a result, the number of total boundary crossings obtained from the 50 tail passages of both ARTEMIS probes during two years from 2011 to 2013, including the multiple crossings, is 888. Figure 1.9 presents all ARTEMIS trajectories (50) in (a) xy-, (b) xz, and (c) yz- GSE planes to illustrate the coverage of the tail crossings. The Moon's orbit is plotted in xy-plane and average magnetopause and the bow shock positions are presented using Roelof and Sibeck (1993) study. Given the low inclination of ARTEMIS orbits, better coverage in the equatorial plane is achieved. It should be

indicated here that the years covered by our crossings (2011-2013) correspond to low solar activity period.

Figure 2.5 illustrates one of the magnetotail passages of ARTEMIS-P1 from Nov. 4, 2011 to Nov. 16, 2011 for a 12-day stretch to show an example of the magnetotail regions traversed by the spacecraft at the lunar distance. The regions that the spacecraft travelled through were indicated using colored hatched lines on the top of the first panel. The panels from top to bottom are B_x (orange) and B_{tot} (black), density, temperature, V_x (orange) and V_{tot} (black), the ion energy (left) and ion flux (right). These signatures locate the magnetopause position at 05:00, 05:30, 06:00, 09:30 and 11:30 UT on November 8, 2011 during the inbound and at 03:50 UT on Nov. 13, 2011 during the outbound magnetotail passage of the spacecraft in this example. The red and green vertical lines indicate the magnetopause and the bow shock encounters respectively.

The interval covers the initial transition from solar wind to magnetosheath on the dusk flank to the final crossing of the bow shock on the dawn flank to demonstrate the full magnetotail environment of the spacecraft at $-60R_E$; namely magnetosheath, magnetopause, and magnetotail. This figure demonstrates an example of a magnetotail pass with relatively few multiple magnetopause crossings. The spacecraft spends, on the average, about 3.5 days within the magnetotail during each orbit. Figure 2.5 presents one of the longest magnetotail traversals, lasting about 4.5 days. In order to locate the magnetopause correctly, it helps to look for the successive order of the regions seen in this figure as the spacecraft transits back and forth between different regions.

As any statistical study based on years there will be bias according to solar cycle and other contributing factors. To our knowledge, there were two major CMEs occurred throughout our time interval, one on March 2012, one on Jan 2013.

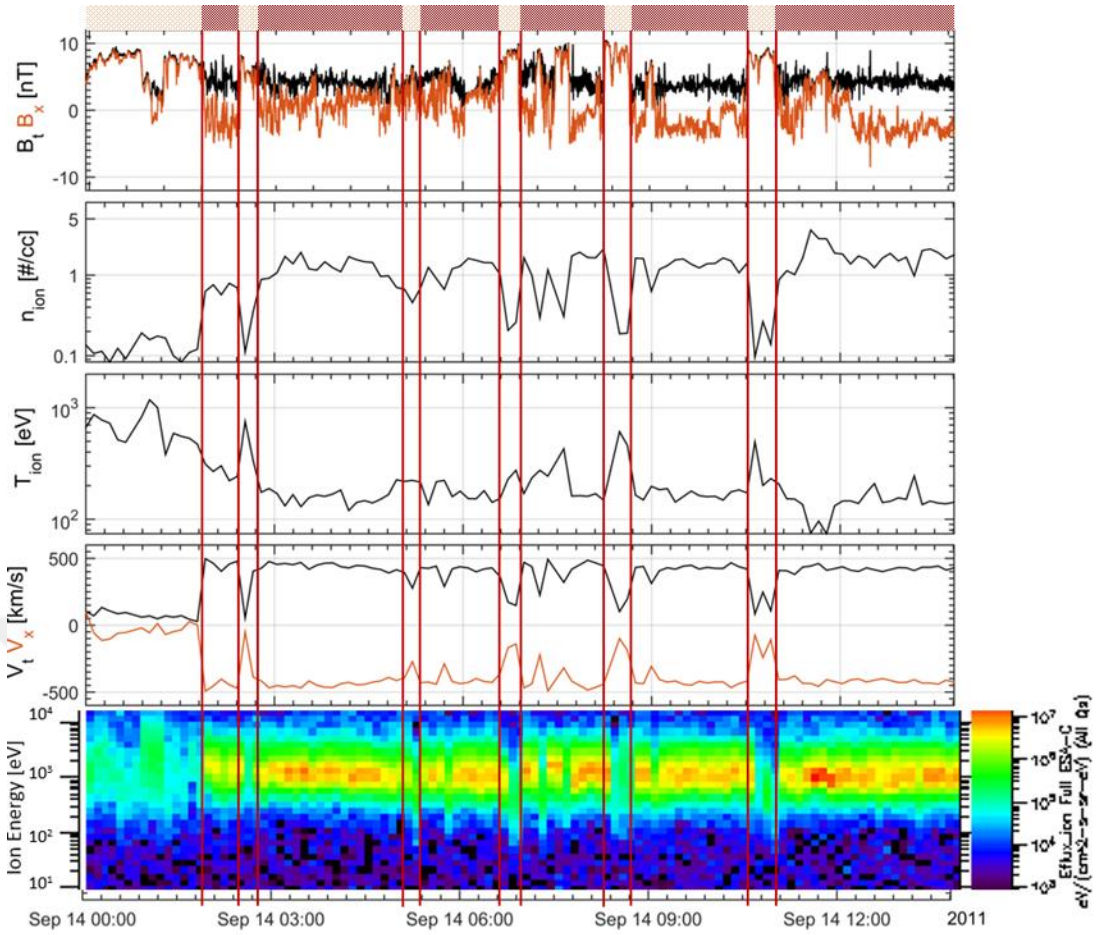

Figure 2.6 : Multiple crossing example from ARTEMIS probe B on 09/14/2011 from 00:00 to 15:00.

Below in Figure 2.7 is our magnetopause crossing-times, and how many data points we collected at that month. On average magnetopause is encountered 36 times. We did not collect more magnetopause crossing points than usual around those extreme events but as expected, their radial size is not on average. However, one thing to mention the bias is always there since it is done by human eye, and as one can see from table as time spent with data increases, the number of magnetopause encounter increases as well. So, as our experience increase, we feel more comfortable pinpointing the magnetopause crossings, so more data is collected after 2013.

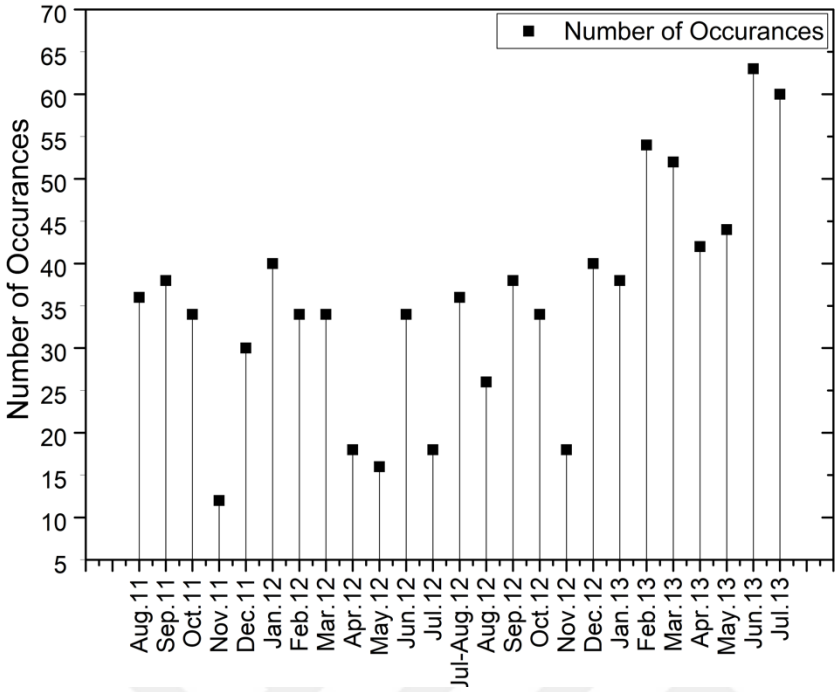

Figure 2.7 : Number of magnetopause encounters per total of inbound and outbound passes.

2.3.3 Coordinate systems and aberration correction

As the magnetotail moves in response to the internal and external factors, the magnetopause boundary positions need to be transformed into the most appropriate coordinate system. The procedure defined here is also presented as a flow chart in Appendix (Figure A.1). The plots giving the satellite orbits in Figure 1.9, use Geocentric Solar Ecliptic (GSE) coordinates since it is easier to visualize with its x-axis pointing sunward, z-axis towards the ecliptic north pole and y-direction is in the ecliptic plane pointing towards dusk according to the right-hand-rule. In Geocentric Solar Magnetic (GSM) coordinates, the X-axis is directed from Earth to Sun as GSE but Z-axis is aligned with the north magnetic pole and Y-axis is perpendicular to the Earth's magnetic dipole so that the XZ-plane contains the dipole axis (Russell, 1971; Hapgood, 1992). The positions, magnetic field components and all plasma vectors will be depicted in aberrated solar wind corrected Geocentric Solar Magnetospheric (aSWGSM) coordinate throughout the study. The aim using the aberrated solar wind corrected GSM coordinate system is that solar wind flow will be aligned with the new x-axis. The Earth's motion around the Sun at 30 km/sec introduces a deflection of the magnetotail axis away from the Sun-Earth line. For an average radial solar wind speed

of 400 km/sec, the Earth's rotation alone will cause an aberration angle of 4° which deviates the magnetotail axis clockwise (as viewed from above) by about $4R_E$ in the positive y-direction at $X = -60R_E$. The solar wind data measured by ACE and WIND spacecraft is corrected via removing Earth's orbital motion around the Sun, about 30 km/sec, from the Vy component in GSE coordinate system. Therefore, the equations used for the aberration include the correction for the Earth's orbital motion given in eq. (2.2), and eq. (2.4). eq. (2.3) calculates how the solar wind velocity in the y-direction (Vy) will increase or decrease the aberration caused by the Earth's motion depending on the sign of the Vy component. In this study, the aberration effects resulting from both Earth's rotation and non-radial solar wind (Vy) were corrected using concurrent upstream solar wind velocity from ACE spacecraft according to the procedure described by Dmitriev et al. (2003). Their approach includes both the displacements of the tail axis in y- and z-direction due to the variations in the z-component of the solar wind (Vz). The equations for the aberration angles, shown in Figure 2.8 and the conversion matrix from GSE to aberrated Solar Wind corrected GSE (aSWGSE) are shown below in Equations (2.2) to (2.6), adopted from (Dmitriev, et al., 2003).

$$\alpha_{earth} = \tan^{-1}\left(\frac{30}{|V_x|}\right) \tag{2.2}$$

$$\alpha_{sw} = \tan^{-1}\left(\frac{V_y}{|V_x|}\right) \tag{2.3}$$

$$\alpha_{total} = \tan^{-1}\left(\frac{V_y + 30}{|V_x|}\right) \tag{2.4}$$

$$\beta = \tan^{-1}\left(\frac{V_z}{\sqrt{V_x^2 + (V_y + 30)^2}}\right) \tag{2.5}$$

$$\begin{bmatrix} x_{aswgse} \\ y_{aswgse} \\ z_{aswgse} \end{bmatrix} = \begin{bmatrix} \cos\alpha\cos\beta & -\sin\alpha\cos\beta & -\sin\beta \\ \sin\alpha & \cos\alpha & 0 \\ \cos\alpha\sin\beta & -\sin\alpha\sin\beta & \cos\beta \end{bmatrix} \begin{bmatrix} x_{gse} \\ y_{gse} \\ z_{gse} \end{bmatrix} \tag{2.6}$$

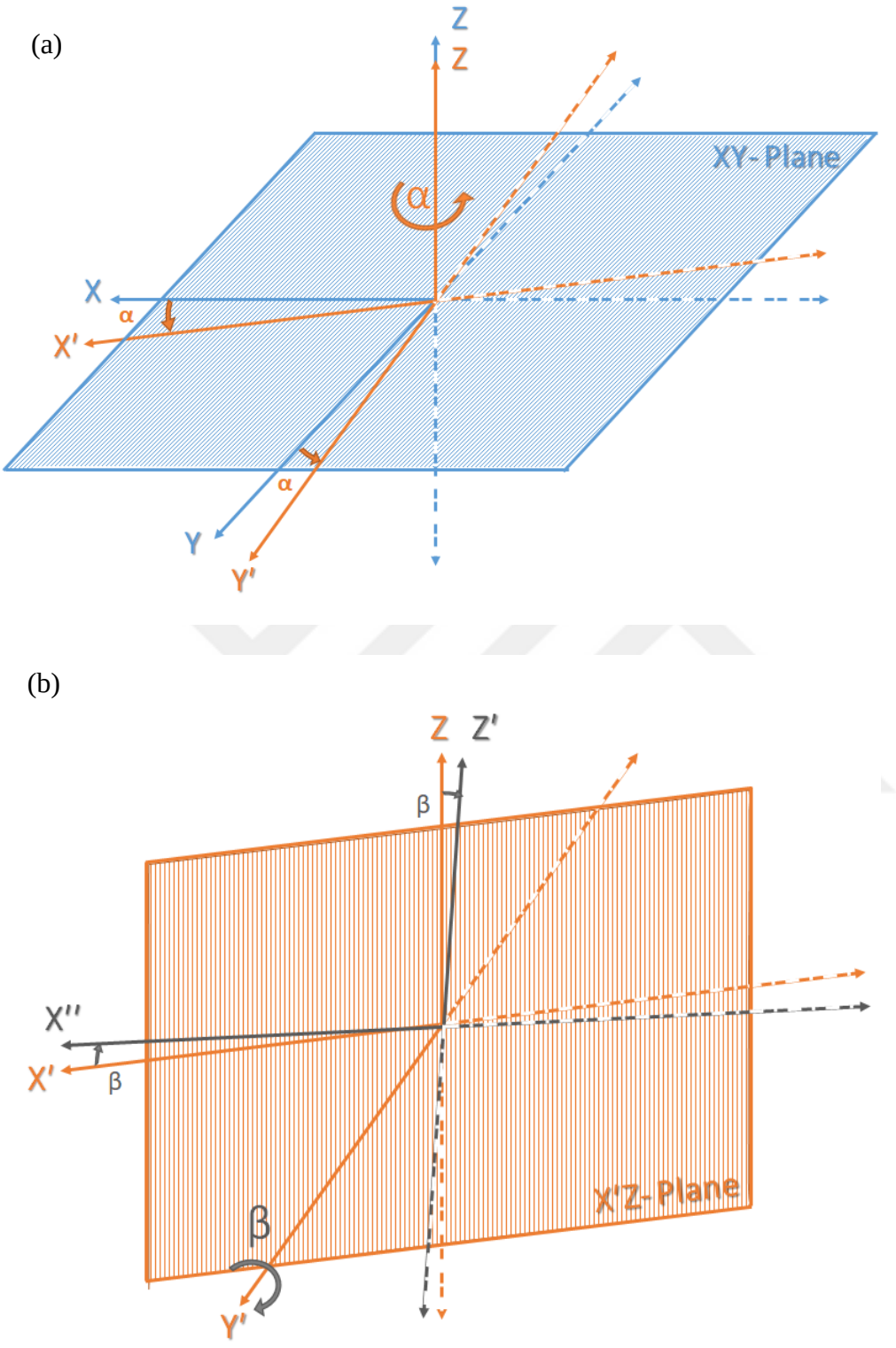

Figure 2.8 : Applied Euler Transformation with aberration angles, (a) α and (b) β, defined in XY and X′Z planes.

The magnetotail is symmetric around the x-axis of the GSM coordinate system while the observations are taken in GSE. Therefore, the last coordinate conversion applied

converted the data from aSWGSE to aberrated Solar Wind corrected GSM (aSWGSM) using Tsyganenko's subroutines that rotates the system about X-axis (available at http://geo.phys.spbu.ru/~tsyganenko/Geopack-2008.html). Figure 2.9 displays the magnetotail displacement at -60 R_E resulting from both Vy and Vz components and the Earth's motion using all 888 boundary crossings. The panels illustrates (a) the occurrence rate of the total dawn-dusk aberration (α_{total}) due to non-radial solar wind and Earth's motion, (b) the displacement of the tail axis in the north-south direction from the dawn-dusk aberrated tail axis. We can see that the absolute average angle (β_{total}), 2.7^o, varies around zero. Figure 2.9b also indicates that the tail axis can move up to 10^o above or below the ecliptic plane. These large flapping angles correspond to solar wind velocities in the z-direction of about 100 km/sec. Comparing Panel a and Panel b shows that the dawn-dusk displacement of the magnetotail is larger than its north-south displacement. However, for an accurate representation of the tail boundary, it is clear that both should be implemented in especially distant tail studies. Panel (b) in Figure 2.9 illustrates the variations in the aberration angle resulting from only non-radial velocity component of solar wind, Vy, (red), only Earth's rotation (blue), and total (black). The tail displacement caused by the non-radial Vy component (red) in Figure 2.9b was added to or subtracted from that due to the Earth's rotation (blue) to produce the total aberration (α_{total}, black) in y-direction. As seen from the figure, there are cases when the absolute total aberration angle is as large as 20^o and as small as 0^o, with an average of 5.7^o. These unusual occurrences of aberration angles correspond to strong non-radial Vy components of the solar wind velocity being added to or subtracted from the displacement caused by the Earth's rotation. Red dots in Panel b show that the Vy component of the solar wind in our data set varies from -70 km/sec to 140 km/sec which results in an aberration in y-direction ranging from -6^o to 23^o . Total aberration angles (black) being zero or near zero in Panels a and c indicate that Vy component of solar wind cancels the speed of the Earth's orbital motion. An angular shift of the magnetotail's axis from 0^o to 20^o corresponds to a displacement of the tail axis up to 20 R_E in the dawn-dusk direction at -60 R_E. In several distant tail studies (e.g. Mihalov et al., 1970; Howe and Binsack, 1972; Fairfield, 1968), it was shown that the aberration can cause deviations of the tail axis as large as its radius in the dawn-dusk direction at large distances in the magnetotail (Fairfield et al., 1968, Mihalov et al., 1970; Howe and Binsack 1972). Blue dots in Panel b, plotted at the corresponding Vy component of the solar wind, are given to show the range of

aberration due only to Earth's orbital motion. The variations in the aberration angle in this case result purely from the variations in the Vx component. The panel indicates that the magnetotail's aberration can be as small as 2^o and as large as 7^o for the range of Vx changing from 250 to 850 km/sec in our data set if only the Earth's motion is considered.

2.3.4 Sector separation

Once determining the magnetopause locations, and transform them into appropriate coordinate system, the data will be studied with respect to IMF orientation. IMF direction affects the magnetotail even at lunar distances towards the dominancy. Therefore, data is evaluated with respect to its IMF direction. To examine the IMF effects, in other words to be able to correlate magnetotail response at lunar distance to dayside or high latitude reconnection, IMF Bz negative or positive cases or the tilt of the magnetotail in the positive or negative y direction, IMF clock angle is used throughout this thesis. To accomplish this, IMF data is taken from ACE spacecraft at the L1 Lagrangian point. It is defined as the inverse tangent of the ratio of the interplanetary magnetic field components in y- and z- direction, in Equation (2.7). The clock angle, θ, is measured from north, lies in the YZ-plane, and is used to divide IMF direction. The sectors, given in Figure 2.10, are assigned such that clock angles from −45^o to +45^o of the positive z-axis as 'northward' (or +IMFBz) sector; clock angles greater than +135^o or less than −135^o represent 'southward' (−IMFBz) sector; clock angles within ±45^o of the positive y-axis as 'eastward' (duskward, +IMFBy) sector, and clock angles within ±45^o of the negative y-axis as 'westward' (dawnward, −IMFBy) sector.

$$\theta = \tan^{-1}\frac{\text{IMF B}_y}{\text{IMF B}_z} \tag{2.7}$$

Throughout this study, both the boundary crossings study in Chapter 3 and the magnetotail data investigation in Chapter 4 are examined with respect to IMF characteristics using these four primary clock angle sectors.

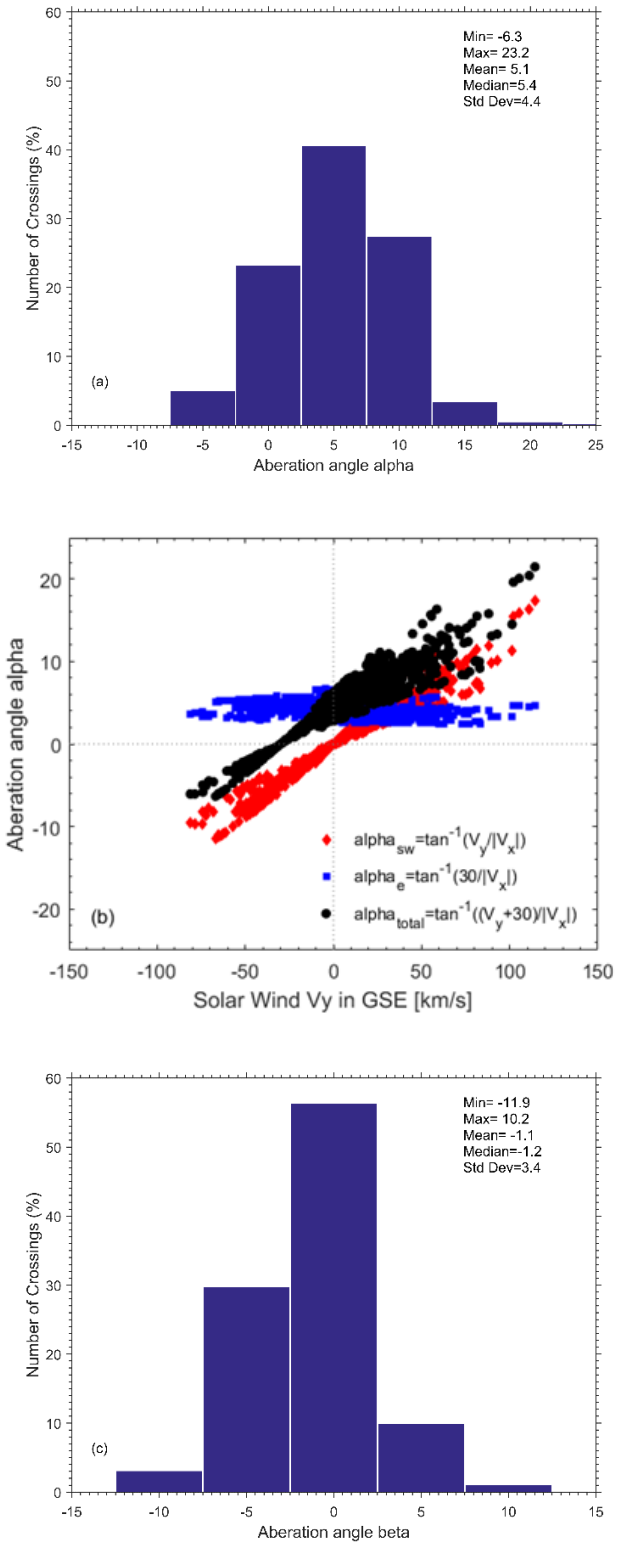

Figure 2.9 : (a) Percentage occurrence of total aberration angle (αTOTAL) in the dawn-dusk direction. (b) Percentage occurrence of aberration angle (β) in the north-south direction. (c) Dawn-dusk component of solar wind velocity versus aberration angles in the dawn-dusk direction. In red is the solar wind Vy component while the black is the total Vy resulting from both Earth's motion and non-radial solar wind and the blue is the aberration due to the Earth's orbital motion.

IMF statistics for each clock angle range in Table 2.1 bring out several facts related to the distribution of the IMF By and IMF Bz that will affect the characteristics of the magnetotail at lunar distances. The occurrence of IMF Bz (361 crossings) sectors is smaller when compared to the occurrence of dominant IMF By (526 crossings) sectors, indicating the fact that the IMF lies mainly in the equatorial plane, which is called the Parker spiral pattern.

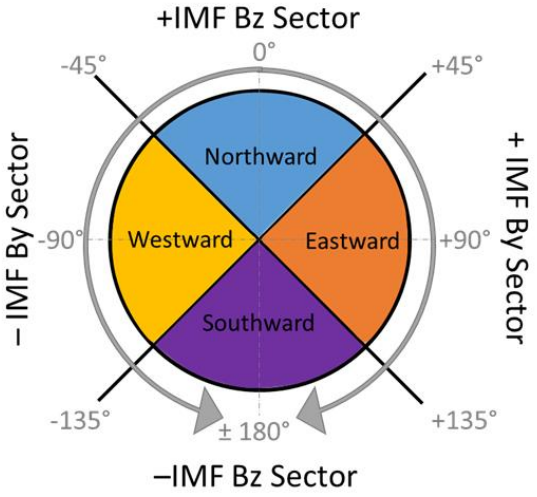

Figure 2.10 : The clock angle sectors, assigned as northward (+IMF Bz), southward (-IMF Bz), eastward (+IMF By) and westward (-IMF By), respectively.

Table 2.1: Number of data points in each sector and the average values for magnetopause boundary crossing data.

Sectors	Eastward + IMF By	Westward - IMF By	Northward + IMF Bz	Southward - IMF Bz
Number of data	139	387	158	203
$(+By)_{ave}$ [nT]	4.41	-	1.52	1.97
$(–By)_{ave}$ [nT]	-	-4.00	-2.00	-1.63
$(+Bz)_{ave}$ [nT]	1.85	1.56	3.88	-
$(–Bz)_{ave}$ [nT]	-2.18	-1.62	-	-4.50

In terms of magnetotail data, presented in Chapter 4, IMF By effect is dominant again, i.e. 44% of the data points correspond to the –IMF By (westward) sector out of 61% of the total IMF By sectors as tabulated in Table 2.2. At an early stage of magnetotail study, a stricter criterion for dividing the sectors was also tried so that the effects of IMF can be seen on the magnetotail more purely or abruptly. To minimize the effects

of neighbor sectors when around the border, we limited the clock angle from 45 degrees to 30 degrees. Another approach was to eliminate all data with IMF By and IMF Bz magnitudes lower than 5 nT to remove the weak IMF data. An increased signature of the tail twisting (dawn/dusk IMFs) and/or the reconnection site (northward/southward IMFs) would create dominant effects on the tail at lunar distances. However, increasing the criterion conditions resulted in about 1/3 and 4/5 reduction of the number of data since most of the data are cumulated in $| IMFB_{yz} |<$ 5nT for the latter condition. In Figure 2.11, these three conditions are applied to ARTEMIS magnetotail data and resulting magnetotail maps for -IMF By condition is given in the second row. Those magnetic field line maps are presented in detail in Chapter 4. The main point here in cross-sectional plane maps in Figure 2.11 is that three options give similar results with decreasing coverage with sticker criterion. For that reason, it was eventually decided to divide all data with 45-degree angles.

Table 2.2 : Number of data points in each sector for three clock angle criterions for sector separation in mapping study.

Criterion	Eastward + IMF By	Westward - IMF By	Northward + IMF Bz	Southward - IMF Bz	All sectors
Clock angle = 45°	14114 (17%)	36241 (44%)	18003 (22%)	14511 (17%)	82869 (100%)
Clock angle = 30°	9510	25920	11544	8841	67%
$\| IMFB_{yz} \| < 5nT$	4456	7070	3218	3817	22%

2.3.5 Flaring

The tail flaring is an important parameter that defines the configuration of the magnetotail and affects the tail size at large distances. For this purpose, ARTEMIS magnetic field vectors at the location of each magnetopause crossing were considered. A magnetopause boundary with a finite thickness will consist of mixture of magnetic field vectors within the magnetopause as those on the tail side of the boundary (tail-like) and those on the sheath side of the boundary (sheath-like). Based on the magnetic field components, it may be possible to separate the tail-like and sheath-like magnetic fields. A clear, consistent pattern of magnetic field vectors was investigated for to determine a criterion for sorting the magnetic field vectors as tail-like and sheath-like based on ARTEMIS Bx, By, and Bz components. Using trial-and-error method, we found that $|Bx|>3.5$ nT separates the magnetic field vectors at the magnetopause positions reasonably well as tail-like and sheath-like. The result of this process is given

in Figure 3.5 that show tail-like and sheath-like vectors respectively in the XY-plane. In this process, the tail-like vectors were assumed to lie parallel to the tail axis, and thus present more orderly pattern with larger vectors while the sheath-like vectors present more random, irregular direction and magnitude in appearance. We note that this assumption will fail when the magnetosheath field lines are draped around the magnetopause as the draping may create large sheath-like vectors parallel to the tail's axis depending on the IMF direction. However, statistically those cases, when occur, will not pose any major global effect and will not change the average tail flaring degree obtained here. The vector pattern is given for an expanding tail in the northern hemisphere (Bx>0) in order to avoid the overlapping crashing of the vectors. As expected, in this figure, we see that the sheath-like field vectors are more disordered and random in appearance, and smaller in size, while on the contrary, the tail-like magnetic field vectors are larger, ordered, stable and more like stretched dipole like appearance as illustrated. We note that we have the same pattern for also southern hemisphere. The result is the same with only Bx components of the fields pointing away from the Earth. We used tail-like magnetic field vectors separated this way to determine the flaring angle of the boundary. The flaring angle can be found using $\tan^{-1}$(By/Bx) in the dawn-dusk direction in XY-plane. Considering that, the magnetopause boundary in aSWGSM is symmetric and parallel to the tail axis as in a cylinder. Magnetic field vector deviations from the boundary in aSWGSM XY-plane can be used to refer to the degree of tail boundary flaring at lunar distances (Kaymaz et al., 1994). In other words, the angle between the tail-like magnetic field vectors and the tail axis in aSWGSM will define the orientation of the boundary. Tail-like magnetic field vectors are, thus, expected to lie parallel to tail axis in the absence of flaring, and when they are not, the angle will indicate degree of flaring. The flaring angle was calculated this way at each magnetopause position and the mean with the standard error was found to be $13.0^{o} \pm 0.4^{o}$ and the median to be 10.6^{o}. Here, only the cases for outward flaring were considered. One other point we note is that even though the outward flaring vectors dominate, the vectors that indicate a tail moving toward the tail axis exists and give approximately the same angle around 11^{o}. This indicates that the tail moves outward slightly more than it moves inward in the dawn-dusk direction. Studies that quantify tail flaring at lunar distances or in the distant tail are not available to our knowledge.

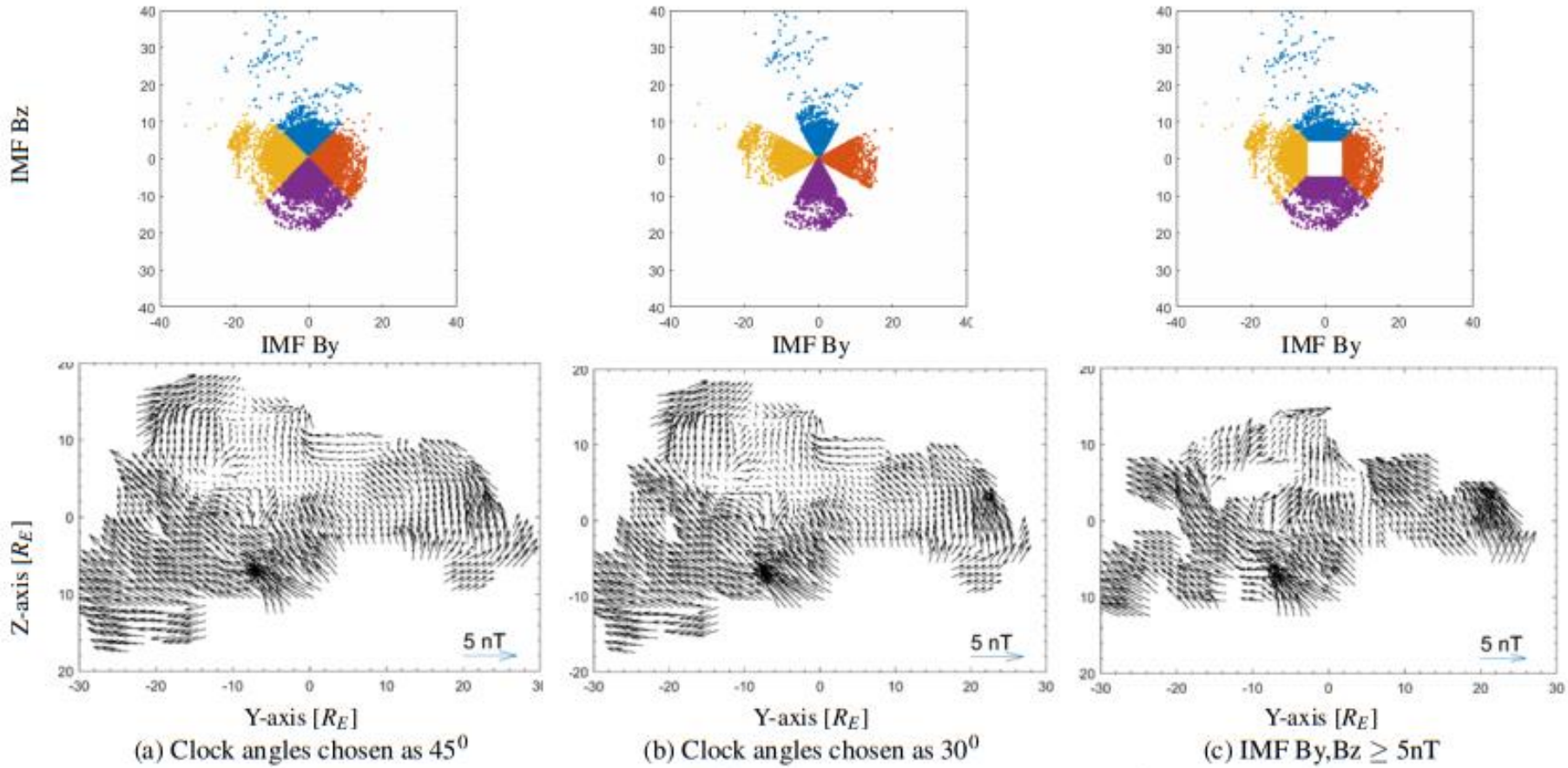

(a) Clock angles chosen as 45^0 (b) Clock angles chosen as 30^0 (c) IMF By,Bz $\geq$ 5nT

Figure 2.11 : Three sector seperation types in (a) clock angle is 45^0, in (b) clock angle is decreased to 30^0 and in (c) $|IMFByz| <$ 5nT are omitted from data. In the second row the magnetotail maps of the corresponding criteria are presented in YZ plane for -IMF By cases.

3. MAGNETOTAIL BOUNDARY CROSSINGS

With the insertion of two THEMIS spacecraft, TH-B and TH-C, into lunar orbit as ARTEMIS-P1 and P2, the tail of the Earth's magnetosphere has become one of the focus points to understand its structure and dynamics at these distances. These two spacecraft have provided the most complete, continuous, and high resolution magnetic field and plasma measurements of the magnetotail at lunar distances since the 2010s. Together with the advanced observations of concurrent solar wind and Interplanetary Magnetic Field (IMF), this set of spacecraft are used to address many of the open-ended problems such as the behavior of the magnetotail at lunar distances under the varying solar wind and IMF conditions, its boundary and variations resulting from solar wind and substorms, plasma and the magnetic field structure, issues in association with the distant and near Earth tail reconnection processes, and how these modify the flow and magnetic structure of the magnetotail at lunar distances. Several books describe the investigations of the magnetotail since the era of the Explorer series in 1960s (e.g. Lui 1987; Nishida et al., 1998; Keiling et al., 2015). In the past, the studies on the Earth's magnetotail suffered from a lack of continuous measurements at great distances from the Earth beyond -30 R_E. The first observations of the geomagnetic tail were made by the Luna 10 spacecraft, which lasted only 56 days in orbit around the moon (Dolginov et al., 1966; Gringauz et al., 1966; Ness, 1967). This was followed by the Pioneer 7 and 8 spacecraft in 1966 and 1967. More comprehensive measurements in the geomagnetic tail at lunar and farther distances were performed by the Explorer (IMP) spacecraft series, especially Explorer 18, 33 and 35 in late 1960s and early 1970s (Behannon et al., 1967; Behannon, 1968; Sonnett et al., 1968). Later, several passes of ISEE 3 spacecraft on its way to a comet through Earth's magnetotail at lunar distances were utilized in late 1982 and early 1983 (Tsurutani et al. 1984; Slavin et al., 1983). Just prior to ARTEMIS, two more spacecraft that provided observations at far distances larger than 200 R_E and around 60-80 R_E distances in the magnetotail had been WIND and GEOTAIL spacecraft, launched in 1994 and 1992 respectively. Despite their limited instrumentation and sparse coverage, these early

missions provided the observations that our understanding of the general structure and behavior of the tail beyond -30R_E is based upon. Starting with Pioneer observations, the magnetotail's existence had been shown at distances -500 R_E and -1000 R_E behind the Earth and that its structure is filamentary (Ness et al., 1967; Wolfe et al., 1967; Fairfield, 1968; Walker et al., 1975). Explorer 18 spacecraft indicated a tail structure with a plasma sheet separating the regions of stretched magnetic field lines within the northern and southern lobes (Speiser and Ness, 1967; Bame et al., 1967). Strong electrical currents flows from dawn to dusk in the center of the tail's plasma sheet and returns over the northern and southern boundary. This creates a well-known "Theta" shape of the magnetotail at near Earth distances (Ness et al., 1967, Walker et al., 1975; Kaymaz et al., 1994a, Siscoe and Kaymaz, 1999). The early studies of the distant tail structure suggested that the magnetotail loses its coherence and may not preserve its well–defined theta structure beyond -200 R_E (Ness et al., 1967; Walker et al., 1975). Using Explorer 18, 28, 32 and 35, the magnetotail boundary was shown to be highly variable in response to both solar wind and IMF variations (Ness et al., 1967; Behannon, 1967, 1968; Mihalov et al., 1968). The magnetotail axis lies aligned with the direction of the solar wind velocity, which results in north/south and east/west flapping motions depending on the variations in the direction of the solar wind velocity. The amplitudes of these motions become larger with downtail distance. This was first considered in Howe and Binsack (1972) and a new coordinate system called a "solar wind aligned coordinate system" was introduced. The response of the geomagnetic tail to the varying solar wind velocity direction could also be the cause of the multiple magnetopause crossings at these great distances. In addition, Howe and Binsack (1972) gave the first analytical expression of the magnetotail boundary that defines the average boundary at these spacecraft distances and showed that the average radial size of the tail at these distances is 26.5 R_E. Based on extensive magnetopause boundary crossings from Explorer 33 and 35 spacecraft, the tail boundary was shown to move over great distances as large as 39 R_E and as small as 12 R_E away from the tail axis beyond -40 R_E (Howe and Binsack, 1972). In addition, most of these early spacecraft observations suggested that the cross-section of the magnetotail was a circle. Similar studies at different tail distances using the Explorer series demonstrated that the magnetotail size varies from 18 R_E to 20 R_E between -50 R_E and -70 R_E with an elongated shape (Ness et al., 1967). ISEE 3 observations indicated that the magnetotail radius varies from 24 to 30 R_E at about -220 R_E from Earth (Slavin et al.,

1985; Sibeck et al., 1986; Fairfield, 1992). In the past, the magnetotail modelling studies were hindered by insufficient spacecraft data at great distances. This problem persists. Many of the tail models do not include data at tail distances beyond 40 R_E, which is one of the main reasons for the model-data discrepancies at these distances. Most of the empirical boundary models so far available (e.g., Sibeck et al., 1991; Roelof and Sibeck, 1993; Petrinec and Russell, 1996; Shue et al. 1997; Kawano et al. 1999) adopted the hypothesis that the near-Earth magnetotail is symmetric about the aberrated x-axis and assumed a circular cross section. Several other studies on the tail modelling proposed slightly elliptical cross-section with an elongation along either y- or z-axis depending on the IMF orientation and the solar wind dynamic pressure (Sibeck et al., 1986), and some others assumed a parabolic function for the shape (e.g. Kuznetsov and Suvorova, 1998). The elliptic or parabolic functions are generally found to be inappropriate for describing the distant nightside magnetopause, because the ellipses close with the increasing down tail distance while parabolas flare too much at the large distances. Petrinec and Russell (1996) overcame this problem by using inverse trigonometric functions to describe the nightside magnetopause. Another approach for the fitting was introduced by Shue et al. (1997, 1998) that produces an open or a closed magnetopause by changing the level of tail flaring, and is generally considered appropriate for the distant nightside magnetopause. The magnetotail's response to variations in the IMF orientation is another subject that was widely studied using spacecraft data and magnetohydrodynamic (MHD) models (e.g. Sibeck et al., 1986; Slavin et al., 1985; Maezawa et al., 1998; Nishida et al., 1995). These studies showed that both IMF By and IMF Bz have important effects on the structure of the magnetotail at lunar distances. The improvements in MHD modelling and supercomputing made it possible to study both the geometry and the structure of the distant tail, its boundaries, and the dynamics in response to various solar wind and IMF conditions. IMF By flattens the tail cross-section in the north-south direction and stretches it in the east-west direction, creating an elliptical shape (e.g. Kaymaz et al., 1995). At the same time, the entire magnetotail including the neutral sheet twists by an amount that depends on the distance and the magnitude of the IMF By (Cowley, 1981; Sibeck et al., 1985, Kaymaz et al., 1994b). Elliptical tail boundary rotates clockwise or anticlockwise depending of the sign of the IMF By. This rotation moves open magnetic field lines asymmetrically on the tail cross-section creating boundary regions which are partially closed and partially open (Kaymaz et al., 1994b; Kaymaz

and Siscoe, 1998), which causes difficulties in the detection of the tail magnetopause boundary. All these effects due to IMF By were also supported by the MHD simulations at lunar distances (Fedder and Lyon, 1995; Kaymaz et al., 1995; Sibeck and Lin, 2014). In case of a dominant north-south IMF, the size and shape of the magnetotail, as well as the structure of the boundary, are distinctively different. Using IMP 8 boundary crossings at -25 R_E, Sanchez and Siscoe (1990) indicated that sometimes the tail boundary is a rotational discontinuity that lets IMF and the solar wind plasma in, at other times it is a tangential discontinuity, and thus it is closed to the solar wind plasma and IMF. By analyzing IMP 8 magnetic field vectors on both sides of the boundary from -15 R_E to -40 R_E, Ohtani and Kokubun (1990) showed that the high latitude boundary locations strongly depend on the solar wind dynamic pressure as well as the IMF Bz. Using magnetic field vector maps in the magnetotail and surrounding magnetosheath using IMP-8, Kaymaz and Siscoe (1998) demonstrated that the tail is totally open during southward IMF while it is partially open when the IMF was dawn-dusk oriented. The northward IMF tail, on the other hand, displays a totally closed magnetotail. That the tail is larger during southward IMF and comparatively smaller for northward IMF was shown to be associated with the open magnetic field lines dragged into the tail resulting in magnetic flux built up during southward IMF (Cowley, 1981; Gosling et al., 1990; Kaymaz et al., 1991; Kaymaz et al., 1994b). The MHD simulations of the mid- and distant tail display a larger tail boundary during southward IMF Bz and smaller tail boundary for northward IMF Bz (e.g. Kaymaz et al., 1995). Simulations also indicate a prolate geometry of the tail cross section for both IMF Bz at these distances (Sibeck and Lin, 2014). The tail motion and multiple crossings of the tail boundary can result from several external and internal reasons. Earth's motion around the Sun causes the magnetotail central axis to rotate westward by about 4-5^o under average solar wind conditions. The amount of deviation varies with the downtail distance. The solar wind's non-radial velocity in the dawn-dusk direction amplifies or reduces this effect in the distant tail. The north-south velocity component of the solar wind flow, on the other hand, tilts the tail axis out of the ecliptic plane. In addition, solar wind disturbances propagated within the solar wind and IP shock structures associated with ICMEs can modulate the solar wind velocity and give rise to large non-radial component that may ultimately alter the magnetotail's motion (Oliveira and Samsonov, 2018; Safrankova et al., 2002). These authors found no effect of perpendicular components of the solar wind velocity (Vy,

and Vz) by using a solar wind aligned coordinate system. Similarly, Grygorov et al. (2014) argued that tail might not align itself with the solar wind velocity after studying an IP shock event and its interaction with the distant tail at -230 R_E. However, Hones et al. (1986), also Fairfield et al. (1979), showed the appropriateness of a coordinate system aligned with the solar wind flow by taking into account effects of Vy component at distances beyond -100 R_E. They indicated that the solar wind aligned coordinate system defined the tail regions better as opposed to a coordinate system using only aberration due to Earth's motion. Several other studies including dayside, and near Earth magnetotail, used solar wind aligned coordinate system in their analysis (Suvorova et al., 2004; Kaymaz et al., 1998; Shodhan-Shah et al., 1996). Kaymaz et al. (1995) also investigated the response of the tail to the variations in the non-radial solar wind velocity (Vy) and concluded that the tail responds to the solar wind velocity like a windsock, and the undisturbed concurrent solar wind propagation velocity is appropriate to account for the effects. In this study, the tail was considered to be deflected as a whole in response to the changes in the non-radial component of the solar wind and thus, the effects of the non-radial components of the solar wind velocity and the aberration due to the Earth's motion were removed by using a solar wind aligned coordinate system. Other tail configuration that may develop as response to non-radial components, increased in the presence of IP shocks, as discussed in Grygorov et al. (2014) is not present in our events (Oliveira, 2015; Oliveira and Raeder, 2015). Among the solar wind disturbances, Alfven waves or the Alfvenic fluctuations are also known to affect the solar wind velocity by introducing a non-radial component. Crooker et al. (1982) showed that the magnetic fields observed by an upstream monitor at L1 were highly correlated with those measured by a near-Earth upstream spacecraft. They emphasized that as the magnetic field variance increases at L1, the magnetic fields near the Earth correlate better. Through Walen relationship between the velocity and magnetic field disturbances, the deviations in the flow velocity may be determined on the orders of 10-20 km/sec, which may be neglected in distant tail studies. Another external effect that causes motion of the magnetopause boundary is the angle between the geomagnetic dipole and z-axis, which is referred as the dipole tilt. The magnetotail moves above or below the central plane depending on the dipole pointing towards the Sun (summer solstice case) and away from the Sun (winter solstice case) respectively. Using a large number of IMP-8, IMP-7 and ISEE-2 data, Hammond et al. (1994) demonstrated that at about -25 R_E, the tail

magnetopause boundary was shifted in the z-direction in order to balance the magnetic flux within the magnetotail lobes by keeping the lobe areas constant in response to the variations in dipole tilt angle. They showed that the shift in the magnetopause boundary position increased as the dipole tilt angle increased and the highest shift of about 2 R_E occurred for dipole angles larger than 30o. The shape of the magnetotail boundary in their analysis was determined to be an ellipse on average for dipole tilt angles larger than 30^o. For very small dipole tilt angles, less than 5^o, it presented a circle. Additionally, their results indicated that as the dipole tilt angle increases, the shape of the boundary did not change and the size of the north-south and east-west dimensions of the tail stayed the same. Similar effects were also shown by Tsyganenko (1998) while studying the global configuration of the geomagnetic tail using large numbers of spacecraft data collected from -20 to -40 R_E in the tail. Tsyganenko (1998) places the tail's center about 3 R_E away from the equatorial plane. The uncertainties in Tsyganenko (1998) study is large, especially for dipole tilt angles larger than 20^o. They especially cautioned on their findings for a large negative dipole tilt angles because of the insufficient number of data that fell into this category and thus the error is larger. On the shape, their results do not strongly conclude that the tail's boundary shape changes with the dipole angle even though they found the shape of the tail boundary is close to circle for large negative and low dipole tilt angles while the shape becomes elliptical for the dipole angle is strongly positive. They noted that the shift is expected to decrease with the distance in the tail. Therefore, we do not expect to see much of this effect in our study at lunar distances and we did not look at dipole tilt effects on the shape or size of the magnetotail at lunar distances. In addition, temporal variations of the boundary on shorter time scales may result from substorms and boundary waves (Nakamura et al., 1996; Ho and Tsurutani, 1997; Nikolaeva et al., 2006). Magnetic flux from the dayside stored in the magnetotail was released during the substorms in the form of plasmoids that produce travelling compression regions (TCRs) in the distant tail. As they move downtail, the size of the tail expands and shrinks (e.g. Slavin, 1998). The magnetotail also expands and contracts because of substorm loading and unloading that creates brEarthing motion of the near Earth tail (Shodhan-Shah et al., 1996). Tail boundary is also expected to vary by the effects of the large-scale wave motions on the boundary through Kelvin Helmholtz instability (Fairfield et al., 2000). Studying the magnetotail boundary is difficult when the magnetotail is open because of the difficulties in determining the exact location of the boundary. In the absence of

reconnection, the boundary is sharply defined and thus easily detectable in both magnetic field and plasma data. However, the tail boundary becomes indistinct when the tail is open and it is challenging to detect the boundary with high accuracy. The motion of the magnetotail in response to the variations in the solar wind, including solar wind disturbances and structure such as coronal mass ejections (CMEs), interplanetary CMEs (ICME), interplanetary shocks (IP shocks), High Speed Streams (HSS) etc., and the occurrence of substorms adds to the complexity of determining the exact location of the boundary. Therefore, identifying the location of the magnetotail magnetopause requires both high resolution magnetic field and concurrent plasma data. The same observations are needed to determine why the magnetotail moves in response to variations in the solar wind and IMF and to the internal dynamics. In this study, taking advantage of the state-of-the-art instrumentation and spacecraft placement, we study the crossings of the magnetotail magnetopause at the lunar distances in order to determine the size and the shape of the magnetotail, their variations, as well the dependence on IMF and solar wind plasma using ARTEMIS magnetopause crossings concurrently with ACE or WIND solar wind and IMF data. In the next section, we describe the data and the coordinate system that were used in our analyses. Then, we present the results followed by the summary and conclusions.

3.1 Magnetopause Observations

Figure 3.1 demonstrates all boundary crossing positions including the multiple crossings in the aberrated coordinate system, aSWGSM. Panels from left to right are the xy-, xz-, yz-plane views of the tail boundary crossings. These magnetopause-crossing positions mark the magnetotail boundary and thus approximate the size of the magnetotail. Under the assumption that the tail is symmetric and its cross-section is a circle, $R_{aSWGSM} = \sqrt{y^2 + z^2}$ will then define the tail's boundary in the yz-plane, where y and z are the spacecraft's magnetopause crossing positions in aSWGSM. Hereafter, R_{aSWGSM} will be referred as the magnetopause distance, which alternatively gives the magnetotail size. Solid lines indicate the average magnetopause position. The width of the magnetotail demarcated by the innermost (x=-41 R_E) and outermost (x=-64 R_E) crossing points in xy-plane is defined by the spacecraft's orbit around the moon. In the y-direction, on the other hand, the innermost (10 R_E) and outermost (39 R_E) boundary crossings are due to the tail's motion in the east-west direction in response

to the external and internal causes such as solar wind and IMF as well as substorms. In the north-south direction, Panels b and c show that the outermost magnetopause positions were seen around 21 R_E. The crossings close to the central tail axis in xz-view have large y-positions. In all planes, it is seen that there is a large scatter of the crossing points, which is an indication of a highly dynamic magnetotail at -60 R_E. In addition, when compared to dusk, the magnetotail crossings at dawn present larger scatter in Figure 3.1c. A similar dawn-dusk asymmetry in the variability of magnetopause positions were observed in Explorer 35 observations at lunar distances and the differences were attributed to the varying solar wind conditions. While this also holds for the large spread in the z-direction seen on the dawn magnetopause in Panel c, this apparent asymmetry towards dawn in the variability of magnetopause positions can also be due to the pressure variations from the foreshock convected downstream of the bow shock to the magnetotail at lunar distances. Using data in Figure 3.1c, for a possible shape of the magnetotail boundary at this distance down the tail, a circle and an ellipse fit were implemented. The average of the magnetopause distance in this figure was obtained as 26.3 R_E with a standard deviation of 5.5 R_E.

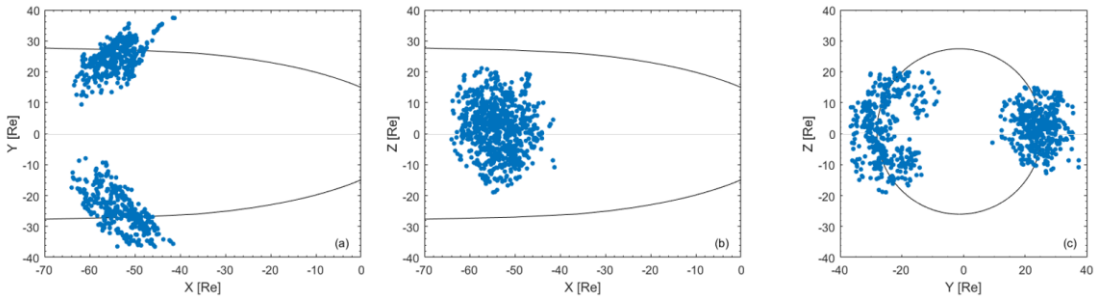

Figure 3.1 : ARTEMIS magnetotail boundary crossings for two years in the aberrated Solar Wind corrected GSM coordinate system (aSWGSM). (a) xy-, (b) xz-, and (c) yz-plane. The circle in panel (c) has a radius of 26.3 R_E, the average size of the magnetopause crossing positions.

Using an algebraic fit to a circle as described in (Taubin, 1991), the radius of the circle was found to be 26.74 R_E with a root mean square (RMS) error of 4.94 R_E. The parameters of the ellipse, on the other hand, was obtained with a=29.56 R_E as the semi-major axis, and b=20.96 R_E as the semi-minor axis with an RMS error of 5.02 R_E. In the absence of high latitude boundary crossings, both fits are possible for the shape of the tail for all upstream solar wind that correspond to average IMF Bx, By, Bz, and solar wind density and speed of 1.8 nT, -1.1 nT, -0.5 nT, and 3.4 #/cm^3 and 418.5 km/sec respectively. Based on RMS errors, we will use the circle fit to represent the

boundary shape at this distance. Seasonal distribution of the magnetopause crossings between equinox and solstice is that 440 crossings are for equinox months (Aug-Sept-Oct, and Feb-Mar-Apr) while they are 235 and 200 for summer and winter solstices. This suggests that the dipole effects will be negligible. Both Hammond et al. (1994) and Tsyganenko (1998) indicated that the solstice shift of the position of the central tail axis with the dipole tilt angle will decrease with distance in the tail. Therefore, we expect that the shift would be smaller at -60 R_E than that in both studies. In addition, both studies indicate a circular cross-section for the equinoctial tail. Taken together, these imply a circle for the average shape of the tail at lunar distances as well, which is depicted by a circular line with a radius of 26.7 R_E in Figure 3.1c.

3.2 Model Comparisons

Figure 3.2 presents both the radial positions of the magnetopause crossings from the aberrated tail axis in the xR-plane and also compares with those predicted by the empirical models. While exposing the spatial variability in the size of the magnetotail boundary, it demarcates the span of the radial size of the magnetotail boundary between 10 R_E and 39 R_E. These two extremities of the magnetopause boundary occur when IMF Bz and solar wind dynamic pressure show unusual variations and are R_E in detail further in Section 3.4. The statistics in Figure 3.3 illustrates the range of the distribution that the tail's magnetopause distance varies. Here we can see that the magnetopause distance between 25-30 R_E occurs at a rate of about 37%, while a magnetopause distance 15 R_E is rarely seen (about 1%), and a magnetopause distance 35 R_E is encountered 4% of the time. The majority of magnetopause positions are seen to be slightly larger than the average magnetopause distance with an occurrence rate corresponding to about 53%. This indicates that the probability of observing a larger tail is slightly higher (by about 6%) than observing a smaller tail at these distances. The solar wind disturbances such as Alfven waves or Alfvenic fluctuations may cause variations in the flow direction in the solar wind and ultimately it is expected that they may shift the tail axis and thus make the determination of its center difficult. Nevertheless, through Walen relationship, it may be shown that the velocity perturbations on the order of 10-20 km/sec corresponding to the standard deviations of 1-2 nT in the magnetic fields of the solar wind will result in an error on the order of 1 to 3 R_E on the estimated magnetopause distance at X=-60 R_E. Figure 3.2 evaluates

the performance of the models using six empirical models at lunar distances as well. These models are Howe and Binsack (1972) (HB72), Petrinec and Russell (1996) (PR96), Shue et al. (1997) (S97), Shue et al. (1998) (S98), Chao et al. (2002) (C02), and Lu et al. (2011) (L11) models shown in red, purple, orange, dark gray, blue and green lines, respectively. The models differ because the magnetopause observations cover different epochs (thus different average solar wind and IMF conditions), and sampling x-range behind the terminator. As a result, the functional forms of the model equations and the model coefficients that produce magnetotail radii are different (Petrinec et al. 1991; Sibeck et al 1991; Petrinec and Russell 1993; Roelof and Sibeck 1993; Petrinec and Russell, 1996; Shue et al. 1997 and 1998; Chao et al. 2002; Lu et al., 2011). Most of these models seen in Figure 3.2, the S97, the S98, the C02, and the L11 use the same functional form that includes subsolar standoff distance (ro) and tail flaring (φ_{fl}) with different coefficients. In order to distinguish from the aberration angle, we use fl to refer to the flaring angle. The major disadvantage of all models is that their magnetopause data do not extend beyond -20 R_E in the tail and to the high latitudes.

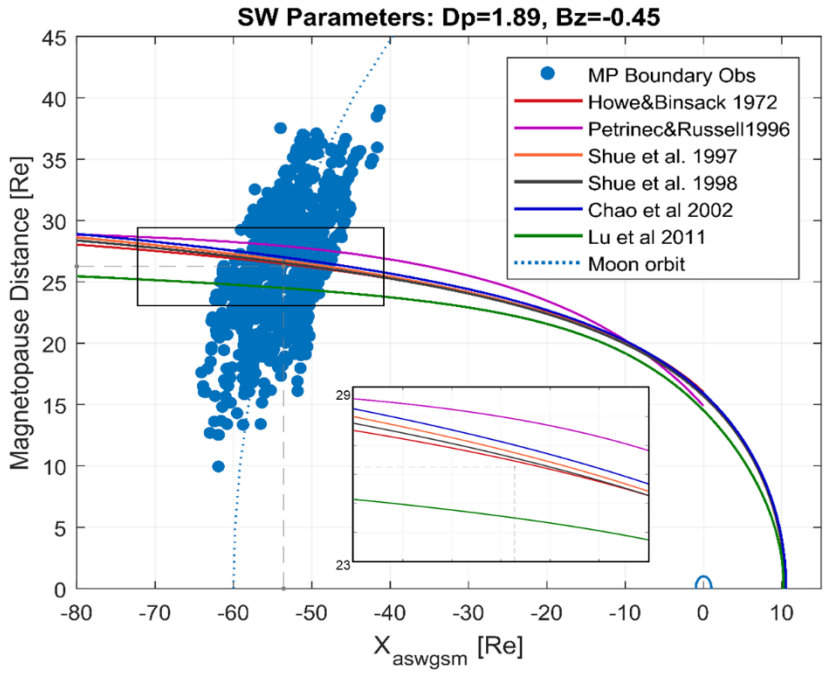

Figure 3.2 : Magnetopause crossing positions in xR-plane and their comparison with the empirical models. The inset is the expansion of the region from x=-70 R_E and x=-40 R_E. Dashed line shows the average position of ARTEMIS while dotted line is the orbit of the Moon.

In Figure 3.2, the only model that extends beyond -40 R_E in the distant tail is the Howe and Binsack (1972) model, which is based on Explorer 33 and 35 observations. Their model is a static model and uses an inverse trigonometric function to describe the nightside magnetopause boundary as a function of distance in the tail. No dependence on the solar wind conditions or IMF was included. The Petrinec and Russell (1996) model, on the other hand, was developed for the near Earth magnetotail and takes tail flaring into account using the pressure balance at the boundary from -10 to -20 R_E while conserving the magnetic flux within the tail. Tail flaring in their model is a function of tail distance, solar wind dynamic pressure, and IMF Bz. The empirical function including flaring angle was used to determine the tail radius. The model was validated using ISEE 2 magnetospheric IMP 8, solar wind, and IMF observations. The model gives a good estimate of the average size and shape of the near Earth magnetotail, which are consistent with ISEE magnetopause positions for the range of their solar wind, IMF Bz and magnetotail position data. The Shue et al. (1997) model is an empirical model for the size and shape of the magnetopause as a function of magnetopause standoff distance (r_o), position defined by the polar angle (θ) and tail flaring (φ_{fl}) which depends on the solar wind dynamic pressure and IMF Bz. The Shue et al. (1998) model is an extension of Shue et al. (1997) model with adapted parameters for more extreme solar wind and IMF Bz conditions. Both models were based on mainly ISEE 1 and 2, and AMPTE/IRM magnetopause crossings and derived optimal parameters for various solar wind dynamic pressure and IMF conditions. The majority of their data is from sunward of -10 R_E and include only 20 magnetopause crossings between -18 R_E and -32 R_E. These models assume symmetry about the solar wind velocity vector and a circular boundary and use the aberrated coordinates as well as an average time shift to advance the solar wind from their upstream monitor to the dayside magnetopause. Chao et al. (2002) improved Shue et al. (1997) by using solar wind measurements specific to each boundary crossing instead of using an average time shift in order to associate the variations in the solar wind correctly with the magnetopause positions. Therefore, the coefficients they obtained in their model and the range of the upstream variables differ from Shue et al. (1997). Accurate calculations of the time shift are especially important in the distant tail when compared to the near-Earth tail and dayside since the distant tail magnetopause moves continually in response to the variations in the upstream solar wind. The last model that we used for comparisons is a more recent study by Lu et al. (2011) and

methodically is slightly different from the others. These authors improved Shue et al. (1997) model using the magnetopause current as the boundary signatures in a large number of MHD simulations covering a variety of solar wind and IMF conditions. Their equations that describe the magnetopause parameters are different for the dayside and nightside magnetopause and the model does not have any presumption about the magnetopause boundary shape, i.e. circular and symmetric. The models presented in Figure 3.2 were run using average concurrent solar wind dynamic pressure, Dp= 1.89 nPa, and average IMF Bz, IMF Bz=-0.45nT as given in Table 3.1 and were compared at the average ARTEMIS magnetopause position, x=-54 R_E, marked with a dashed line. In general, the figure displays several distinct features about the model predictions. The first is that all models give close predictions for the magnetopause on the tailside of the terminator, except the PR96 and the L11 models.

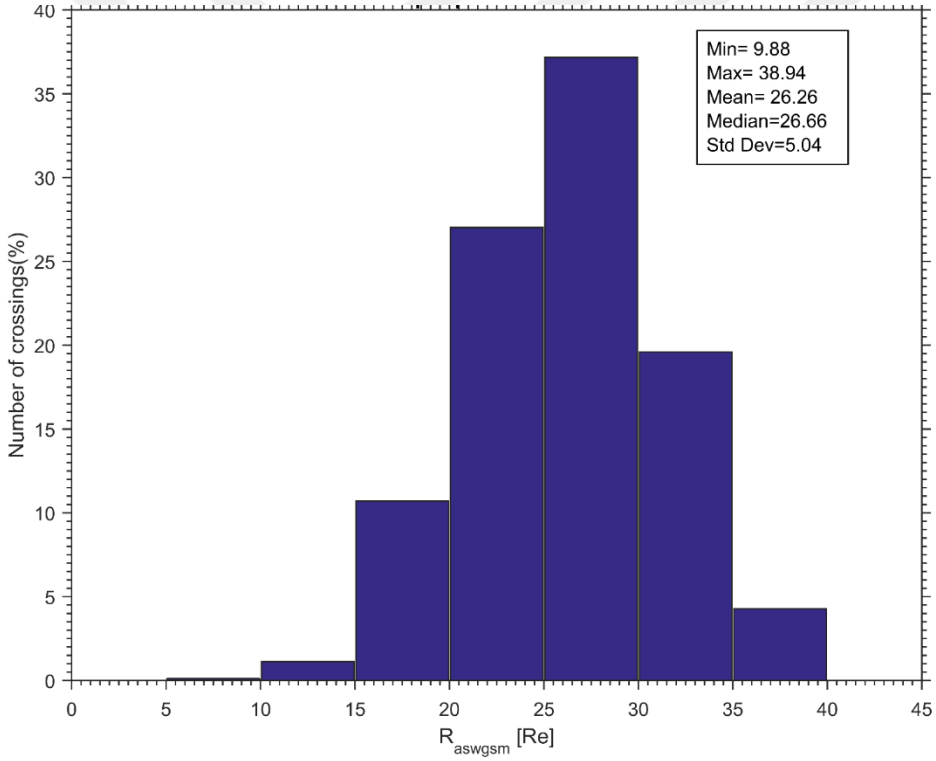

Figure 3.3 : Occurrence frequency of magnetopause crossing positions.

These two models are markedly different from each other such that while one gives the largest magnetopause size, the other gives the smallest, respectively. The second is that there is virtually no difference between the magnetopause predictions of Shue et al. based models, the S97, the S98, and the C02. The third is that the differences between the model predictions become larger at far tail distances. The figure displays that the predicted model magnetopause positions at the average ARTEMIS position,

x=-54 R_E, range from 27.9 to 24.5 R_E for the average upstream solar wind conditions. At this distance, all models differ within 0.2-1.6 R_E from the average size of the tail boundary (26.3 R_E). The HB72 model gives the closest prediction with 26.5 R_E and it is followed by the S98 with 26.6 R_E and by the S97 with 26.7 R_E. The C02 places the tail magnetopause at 27.0 R_E, which is a slightly larger prediction than those of the S97 and the S98. The size of the magnetopause in the PR96 model was obtained as 27.9 R_E at x=-54 R_E and is the largest predicted magnetopause among the models compared here. One last feature that this figure exposes is that while all models slightly expanding beyond x=-54 R_E, the expansion of the tail boundary in the PR96 model ceases slowly and the PR96 boundary approaches to those predicted by the S97, S98 and C02 models. The larger size of the PR96 magnetopause at x=-54 R_E can be traced back to the boundary at about x=-10 R_E where the PR96 starts diverging from the other models. On the contrary, the L11 model yields a magnetopause boundary at 24.5 R_E, which is about 0.9 R_E, smaller than the average magnetopause. Being the smallest prediction of the tail boundary at x=-54 R_E, the L11 model, in fact, gives a few R_E smaller magnetopause size starting from the dayside when compared with the predictions of the other models but its difference increases with the tail distance. Figure 3.4 compares the model predictions at the smallest and largest magnetopause positions (9.8 R_E and 38.9 R_E) that were observed when unusually strong/weak solar wind dynamic pressure exists together with an unusually strong northward and southward IMF Bz respectively. For both cases, the IMF Bz and dynamic pressure data were taken from WIND. For these cases, the models were run with the concurrent solar wind and IMF conditions given in Table 3.1. The left panel in the figure is the case when the smallest magnetopause distance (Case-1) was observed at 9.8 R_E and the right panel corresponds to the case when the largest magnetopause was encountered at 38.9 R_E (Case-2). The large dots in both panels mark these positions at x=-61 R_E and x=-41 R_E on the left and right panels, respectively. First we examine the left panel for Jan. 25, 2013 event. We see that all models are away from producing the observed magnetopause location. The most notable features are the predictions by the HB72 and the L11 models. While the HB72 model gives, the largest magnetopause prediction at 27 R_E, the L11 model predicts the smallest magnetopause position at 13.4 R_E. Among Shue et al. models, the S97 model prediction is the closest prediction at 17.4 R_E while the S98 and the C02 models predict a magnetopause of about 19.6 R_E and 22.1 R_E. The PR96 model gives a prediction at 20.5 R_E, which is much closer to the observed

magnetopause than its prediction for the average case in Figure 3.2. Similarly, the L11 model, which predicts the farthest magnetopause for the average solar wind conditions, presents the closest approximation to the observed magnetopause for these unusual solar wind and IMF Bz conditions. Lastly, we compare the down tail evolution of the models and the flaring of the predicted magnetopause. The flaring angles in this figure may be inferred simply by using the angle between the tangent line to the boundary at the observed position and the x-axis in the figure plane. The magnetopause distance predicted by the S97 and the C02 models stays almost constant beyond the position of the small magnetopause at x=-62 R_E. These models introduce almost zero tail flaring at this down tail distance and beyond. The PR96 model introduces a very small expansion of the tail boundary, indicating an outward flaring, by about 1.8^o. The model predictions of the magnetopause start to be larger beyond x=-18 R_E than those of the S97 model and beyond x=-40 R_E than those of the S98 model. The L11 model produces a tail boundary tilted toward x-axis as well, beyond x=-12 R_E where it starts to differ the most from the other models. The model gives a tail boundary tilted inward by about 3.2^o during this event. In addition to a better prediction of the size of the tail boundary at x=-62 R_E, the model produces a boundary which is consistent with the model inputs of solar wind and IMF Bz, which were 11.5 nT and Dp=4.1 nPa. The agreement between the observed and the L11 prediction of the tail magnetopause boundary give support to the occurrence of the smallest tail as a result of the unusually high solar wind dynamic pressure and strong northward IMF Bz which we will see in Section 3.4. The right panel in Figure 3.4 presents the second event (Case-2) which was observed in 28 August 2012 as associated with an unusually small dynamic pressure (0.41 nPa) and a slight southward IMF Bz (-0.17 nT). The plot indicates that under these upstream conditions, all models, except the PR96 model, underestimate the magnetopause size at x=-41 R_E. The PR96 model gives the best prediction (39.7 R_E) close to the observed magnetopause (38.9 R_E) while the poorest prediction (25.4 R_E) was made by the HB72.

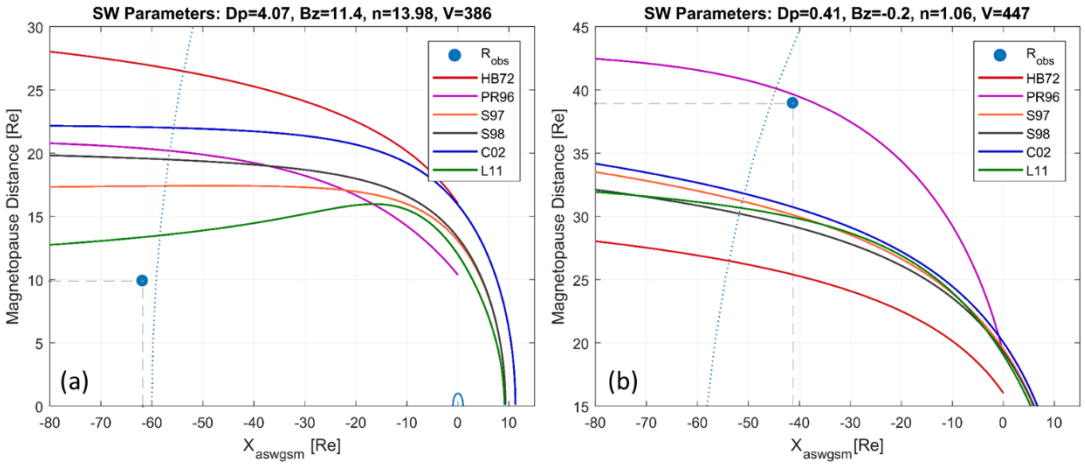

Figure 3.4 : Predictions of the emprical models in xR-plane for the smallest and largest magnetopause crossing cases. (a) Case 1 at R_{obs}=10 R_E, January 25, 2013 pass and (b) Case 2 at R_{obs}=39 R_E, August 28, 2012 pass.

Other models, the C02, the S97, the L11, and the S98, follow with magnetopause predictions at 30.7 R_E, 30.1 R_E, 29.9 R_E, and 29.2 R_E. The S97 and the L11 models yield almost identical boundary as far as x= -41 R_E and differ beyond this distance. As seen, between Shue et al. models, prediction by the S97 is closer to the observed magnetopause. The S97 and the S98 models diverge beyond the terminator point. Being in the same group, the C02 model predicts a larger magnetopause compared to S97 and S98. Comparing the tail evolution and flaring of the boundary as seen in this figure, all models predict an outward expansion of the tail magnetopause boundary x=-41 R_E and beyond. The approximate flaring using the figure may be obtained (the PR96, the C02, the S97, the S98, the L11, the HB72) as 7.6º, 6.6º, 7.2º, 7.2º, 7.2º, 4.4º, that indicates an average of about 7º outward flaring at this distance. Evaluating together with Case-1, the PR96 model agrees better with the observations for these upstream conditions dominated by weaker dynamic pressure and very weak southward IMF Bz when compared to Case-1 with the high dynamic pressure and relatively strong northward IMF Bz. Similarly, even though the S98 is the version of the S97 improved for extreme solar wind and IMF conditions, here we see that the S97 agrees better with the observed magnetopause. Table 3.2 quantifies the differences between the models magnetopause predictions and boundary flaring presented in Figure 3.2 and Figure 3.5 and gives the percent errors. These comparisons emphasize the sensitivity of each model to the highly variable upstream solar wind conditions, especially to extreme variations in the dynamic pressure and IMF Bz, at lunar distances. The models seem to differ in the detail while the error ranges depend on the solar wind conditions.

The weaker upstream conditions give rise to models' underestimation of the observed magnetopause distance while the stronger upstream conditions produce overestimated magnetopause distance in the models.

Table 3.1 : Upstream solar wind and IMF conditions for all magnetopause crossings and crossings with the smallest and largest magnetopause distances.

Upstream Solar Wind Parameters	All data average	Case 1	Case 2
MP Distance (R_E)	26.3	9.9	38.9
X-distance (R_E)	-54	-62	-41
IMF Bz (nT)	-0.45	11.4	-0.17
n_{sw} (cm^{-3})	5.2	14.0	1.1
V_{sw} (km/sec)	419	386	447
V_y (km/sec)	7.4	-15	-30
V_z (km/sec)	-8.5	16	-16
D_p (nPa)	1.89	4.07	0.41

In the models (the S97, the S98, the CH02 and the L11) the level of tail flaring was introduced via parameter φ_{fl}. In these papers, the tail boundary expands if the parameter $\varphi_{fl} > 0.5$, closes in if $\varphi_{fl} < 0.5$, and lies parallel to the ail axis if $\varphi_{fl} = 0$. It is a coefficient of the least square curve fit that was obtained from the relationship between the magnetopause distance and the polar angle under various dynamic pressure and IMF Bz. The degree of flaring is difficult to compare between these four models and our observations, as it does not have a physical unit in the Shue et al. models. However, qualitatively models indicate that the tail flares slightly outward at this distance as seen in the Figure 3.2. A hand derivation of flaring in Figure 3.2 gives an angle varying from 2.6° to 5.3°. In case of the PR96, the flaring is explicitly a function of solar wind dynamic pressure and IMF Bz and measured in degrees from the tail axis. The model gives 3.3° flaring corresponding to average upstream solar wind conditions at average x-position, $x = -54R_E$, which is much smaller than 13° we obtained above. The flaring in the model decreases with downtail distance as expected. Their Figure 7 in Petrinec and Russell (1996) indicates a flaring of about 4° for P_{dyn}=2nPa and IMF Bz =0 at x=-54 R_E which is the closest case to average upstream P_{dyn} (1.16 nPa) and IMF Bz (-0.45nT) in Figure 3.2. Even though the difference between two cases is small, this shows the sensitivity of the model to the solar wind dynamic pressure and IMF Bz conditions.

Overall, for the average upstream conditions given in Table 3.1, all models show slightly increased outward flaring at x=-54 R_E. This agrees qualitatively with the

dominant outward flaring pattern of the ARTEMIS field vectors at the magnetopause locations. In the absence of any quantitative measure of flaring angle in the distant tail, Figure 3.5 quantifies the flaring angle as a first approximation at lunar distances and provides means to compare with the model predictions.

Table 3.2 : Magnetopause distance predicted by the models and tail flaring at the average magnetopause position and when the smallest and largest magnetopause were encountered. First rows in the table give the magnetopause distance while the second rows are the percent errors computed using$((R_{model} - R_{obs})/Robs) * 100$ (%). In the case of all data, average magnetopause and standard deviation are given. Average Flaring parameter φ_{fl}>0.5 and φ_{fl} <0.5 indicate an outward and inward flaring tail, while φ_{fl}=0.5 is a non-flaring tail.

	X (R_E)	R (R_E)	R_{model}±Percent Error					
			HB72	PR96	S97	S98	C02	L11
All Data	-54	26.3± 5.5	26.5+ 0.8	27.9+ 6.3	26.7+ 1.9	26.6+ 1.2	27.0+ 2.9	24.5- 6.7
Case 1	-62	9.9	27.0+ 173	20.4+ 106	17.4+ 76	19.6+ 98	22.1+ 123	13.4+ 35
Case 2	-41	38.9	25.4- 35	39.7+ 2	30.1- 23	29.2- 25	30.7- 21	29.9- 23
			Tail Flaring (φ_{fl})					
All Data			-	3.3°	0.60	0.59	0.60	0.56
Case 1			-	1.8°	0.49	0.52	0.50	0.43
Case 2			-	8.6°	0.58	0.57	0.58	0.55

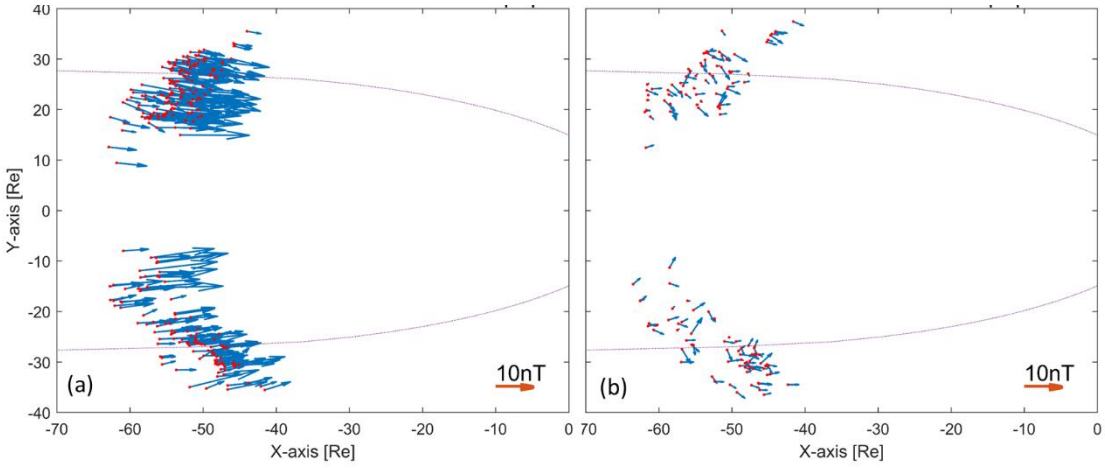

Figure 3.5 : Tail-like (a) and sheath-like (b) vectors in the xy-plane in the northern hemisphere of the magnetotail.

3.3 Magnetotail Shape and Size Dependence

In this part, the magnetotail shape dependence (i.e. circular boundary versus elliptical boundary) on the IMF By and IMF Bz will be investigated in detail as well as the magnetotail size dependence on the dynamic pressure and IMF Bz.

3.3.1 IMF By

In this part, we discuss the effects of IMF By and IMF Bz on the magnetotail boundary size and shape as well as the occurrence of the smallest and largest tail dimensions under the effect of unusually strong and persisting IMF orientations. In the absence of high latitude boundary crossings resulting from the orbital coverage of ARTEMIS given in Figure 1.9, exposing the IMF effects on the tail size and shape is difficult and limited to the low latitudes. While IMF Bz controls the size and the shape of the magnetotail in the z-direction, IMF By effects are best seen at the low latitudes (Lu et al., 2011; Sibeck and Lin, 2015). To examine the IMF effects, we first describe clock angle as $\theta_{cl}=\tan^{-1}(By/Bz)$ where θ_{cl} is measured from north. We assign clock angle sectors as below: clock angles from -45^{o} to 45^{o} of the positive z-axis as 'northward' (or +IMF Bz) sector; clock angles greater than 135^{o} or less than -135^{o} represent 'southward' (-IMF Bz) sector; clock angles within 45^{o} of the positive y-axis as 'eastward' (duskward, +IMF By) sector, and clock angles within 45^{o} of the negative y-axis as 'westward' (dawnward, -IMF By) sector. Below, we examine the boundary crossings and IMF characteristics for these four primary clock angle sectors.

IMF statistics for each clock angle range in Table 3.3 bring out several facts related to the distribution of the IMF By and IMF Bz that will affect the characteristics of the magnetotail at lunar distances. The occurrence of IMF Bz (361 crossings) sectors is smaller when compared to the occurrence of dominant IMF By (526 crossings) sectors, indicating the fact that the IMF lies mainly in the equatorial plane, Parker spiral pattern.

Table 3.3 : IMF By and IMF Bz statistics and the best fit ellipse parameters for each IMF clock angle sector.

Parameters	+ IMF By sector	– IMF By sector	+ IMF Bz sector	– IMF Bz sector
Number of data	139	387	158	203
$(+ \text{IMF By})_{ave}$ (nT)	4.41	None	1.52	1.97
$(– \text{IMF By})_{ave}$ (nT)	None	-4.00	-2.00	-1.63
$(+ \text{IMF Bz})_{ave}$ (nT)	1.85	1.56	3.88	None
$(– \text{IMF Bz})_{ave}$ (nT)	-2.18	-1.62	None	-4.50
Ellipse, a (R_E)	29.0	30.1	29.0	29.5
Ellipse, b (R_E)	20.2	21.0	26.2	26.8
Eccentricity, e	0.71	0.72	0.43	0.42
RMS ellipse (R_E)	5.12	4.86	6.00	5.79

We applied the least squares method to find the parameters of the ellipse that describes the magnetopause locations best for each clock angle sector. Average IMF statistics and the parameters of ellipse for each sector are presented in Table 3.3. Figure 3.6 presents the magnetopause positions and the best ellipse fit to these magnetopause positions corresponding to IMF By sectors, for (a) westward and (b) eastward sectors. Table 3.3 indicates the parameters of the ellipses for westward and eastward IMF By sectors are very close to each other; semi-major-axes (a) are $29.0R_E \pm 5.12$ and $30.1R_E \pm 4.86$, while the semi-minor axes (b) are 20.2 R_E and 21.0 R_E respectively. Together with an eccentricity of about 0.72, the statistical shape of the boundary is interpreted as an ellipse with major axis lying in the east-west direction for both IMF By sectors.

Sibeck and Lin (2014) studied the size and shape of the magnetotail at $–60R_E$ using magnetohydrodynamic model SWMF/BATSRUS. They ran the model for different IMF By strengths. Their Figure 2 shows that the tail dimensions enlarge in the east-west direction while shrinking in the north-south direction and the tail becomes oblate as IMF By steadily increases from 1 nT to 7 nT. The semi-major axis increases from 28 to 33 R_E while the semi-minor axis decreases from 30 to 21 R_E. This implies an elliptical shape of the boundary that at -60 R_E is smaller in the north south directions and larger in the east-west directions; which is qualitatively consistent with earlier works and theory. Rate of flattening with increased IMF By strength exceeds the east-west expansion. We compare their IMF By= 5nT case with the ellipse fit results in Panel a of Figure 3.6 for westward IMF By with an average of +4.41nT. The model in

their study indicates a tail with semi-major and semi-minor axes, a=31 R_E and b=24 R_E respectively that results in an eccentricity of e=0.63. The tail dimensions in Figure 3.6 being a=29 and b=20.20 R_E are smaller than the Sibeck and Lin results. Both indicate an oblate tail at -60 R_E but the oblateness is slightly larger in Figure 3.6.

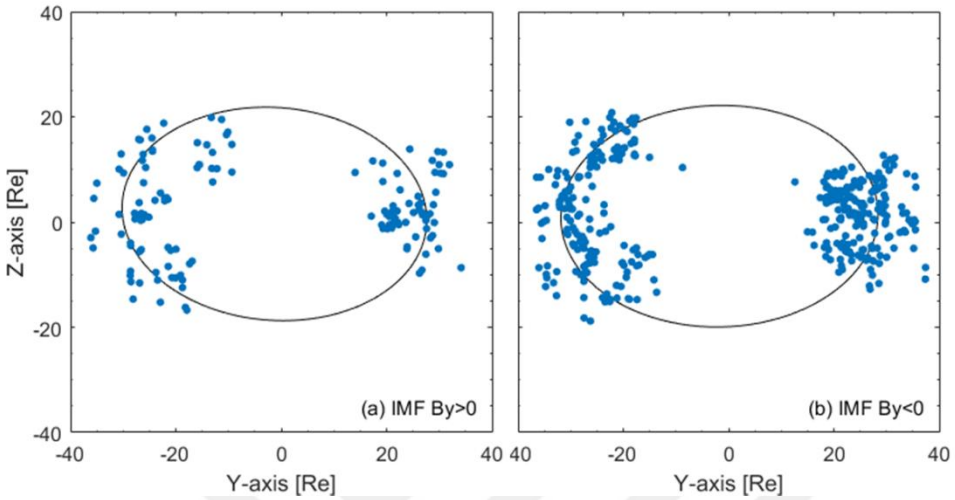

Figure 3.6 : Magnetopause crossings in yz-plane for equatorial clock angles 45<|θ|<135: (a) +IMF By and (b) –IMF By sectors. Ellipse is the least square fit to the magnetopause positions in these sectors.

3.3.2 IMF Bz

In this section, we examine the effects of IMF Bz sectors on the boundary positions, namely, the sectors with clock angles within 45^o of the positive and negative z-axis. Figure 3.7 gives the magnetopause boundary locations in yz-plane corresponding to the northward IMF Bz (a) and southward IMF Bz (b) sectors. The average strength of IMF By corresponding to northward IMF sector is small, -0.74 nT on the average while the average IMF Bz is +3.88nT. First, we investigate the shape of the magnetopause for northward case. Best fit of an ellipse indicates a boundary flattened along the east and west directions with a semi-major axis of a=29.0 R_E, semi-minor axis of b=26.2 R_E and an RMS of about 6 R_E. The RMS error for the ellipse is seen to be quiet large. In the absence of high latitude boundary crossings and based on the low eccentricity of the ellipse, we suggest a weak ellipse for the shape of the tail cross-section under northward IMFs at the lunar distances. For an IMF Bz of 7.15 nT, Sibeck and Lin (2014) obtained a prolate ellipse with a= 37 R_E and b=20 R_E using MHD model. The size of the tail in Figure 3.7 corresponds to IMF Bz= 3.88 nT. Both agree that the shape is a prolate geometry but qualitatively, the Sibeck and Lin (2014) study indicated that

the tail is larger and more prolate with an eccentricity of 0.84 than that in Figure 3.7 (e=0.43).

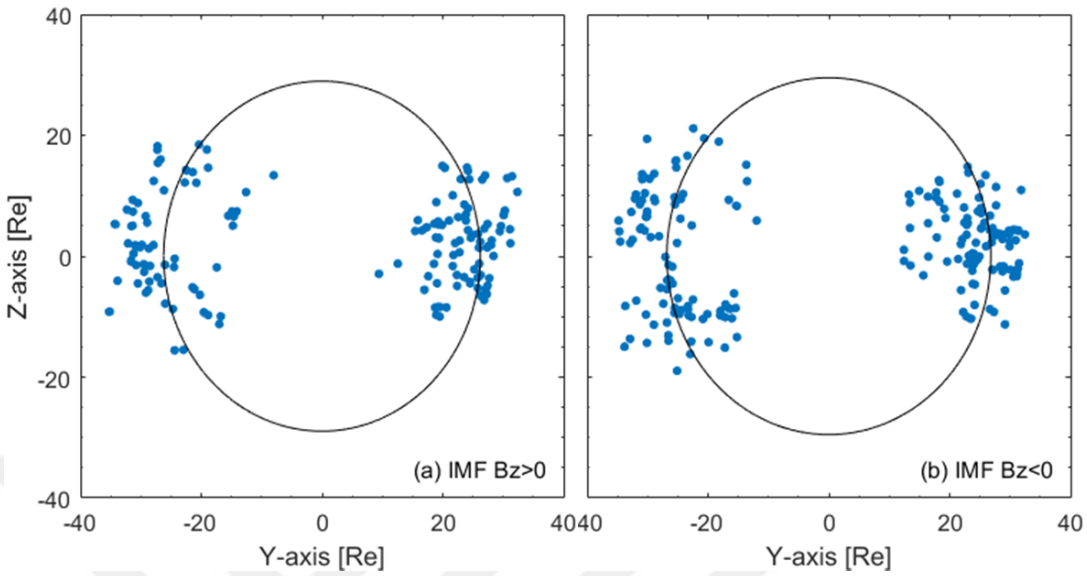

Figure 3.7 : Magnetopause crossings in yz-plane for north-south clock angles ($0 \leq |\theta| \leq 45$ and $135 \leq |\theta| \leq 180$): (a) northward IMF Bz and (b) southward IMF Bz. Ellipse is the least square fit to the magnetopause positions in these sectors.

For the southward IMF Bz sector presented in Figure 3.7b, corresponding average IMF By is +0.93 nT and average southward IMF Bz in this sector was found as -4.50 nT. In panel b, the range of the southward IMF Bz crossing positions indicate a slightly larger tail size than that of northward IMF Bz. The parameters of the ellipse were determined as a= 29.50 R_E and b=26.8 R_E with an RMS error of about 5.2 R_E and eccentricity of about 0.42. As in the case of northward IMFs, the RMS error of both circle and ellipse for southward IMF case is large as well. Based on the eccentricity, a weak ellipse was also suggested for the shape of the tail cross-section under southward IMFs.

The Sibeck and Lin (2014) study found a very small model magnetotail for southward IMF compared with that in Figure 3.7b. The model predicts a completely open magnetopause boundary with a=25 R_E and b=7.5 R_E for an IMF Bz= -7.15 nT. The small size of the tail indicates that there is too much reconnection in the model. The shape of the tail is seen to be compressed on the flanks in the east-west direction and elongated in the north-south direction. Qualitatively, both Figure 3.7 and Sibeck and Lin's study present a prolate tail, but the ellipse in Figure 3.7 is closer to a circle when compared to Sibeck and Lin's prolate boundary as in the case for positive IMF Bz. For

both northward and southward IMF Bz orientations, the tail's shape was overestimated towards more elliptical shape than predicted in our study.

3.3.3 Dynamic pressure and IMF Bz

In this part, we investigate the magnetotail size dependence on the dynamic pressure and IMF Bz in detail. Figure 3.8 shows how the magnetopause distance varies with the solar wind dynamic pressure for those magnetopause crossings when corresponding dynamic pressure data exists. The figure illustrates the inverse relationship between the tail size in the yz-plane and the dynamic pressure. It is possible to distinguish two different types of variation for those crossings less than and greater than P_{dyn}< 2 nPa. A decreasing variation with increasing dynamic pressure for those crossings P_{dyn}< 2 nPa is observed. Average solar wind velocity and Vy, and Vz components for those crossings P_{dyn} > 2 nPa are 439 km/s, 21.43 km/s, and 14.45 km/s respectively and northward IMF has an average of 5.04 nT while average southward IMF is -3.3 nT.

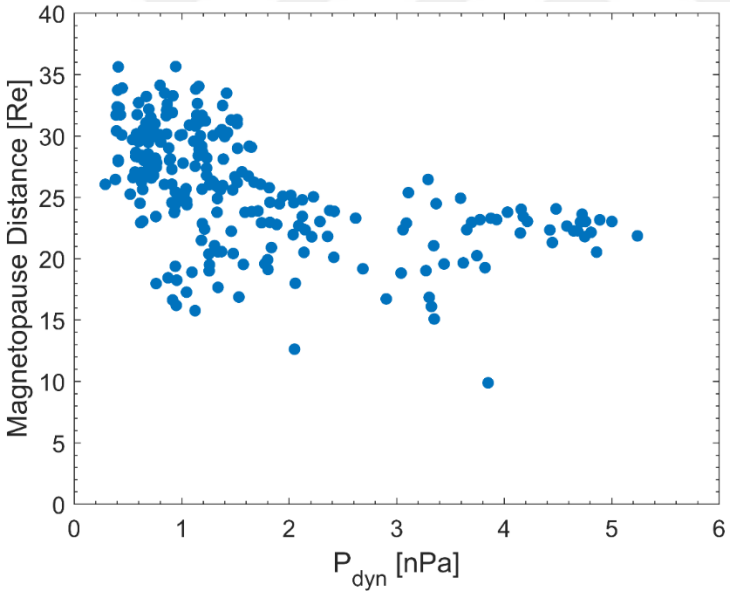

Figure 3.8 : Variations in the magnetopause distance in response to solar wind dynamic pressure. Magnetopause distance is given in aSWGSM system.

Two of the magnetopause crossings have the smallest magnetopause distance with 12.62 R_E and 9.88 R_E. These correspond to large northward IMFs, (10.22 nT and 13.46 nT), and large dynamic pressures, larger than 2nPa (2.05 nPa and 3.84 nPa). Solar wind speed for these two cases are about 380 km/s and 390 km/s, and non-radial components of the velocity (Vy, and Vz) are less than 18 km/sec. Except these two smallest crossings, the magnetopause distance for those crossings P_{dyn}>2 nPa varies

around 22.2 R_E. The northward IMF is expected to give rise to a smaller tail cross-section. The southward IMF Bz, on the contrary, is expected to give larger magnetotail size. Figure indicates that in addition to increasing dynamic pressure, it is the dynamics driven by the southward or northward IMF that cause the magnetotail shrink or expand to its final size.

Next, we investigate the IMF Bz dependence of the magnetopause distance. Figure 3.9 gives how the magnetopause distance varies with the direction of IMF Bz, i.e. northward or southward, for IMF Bz clock angle sector ($0<|\theta|<45^o$, $135<|\theta|<180^o$). Right side of the figure gives the plot for northward IMFs while the left side is for the southward IMFs. In the right side of the figure, despite the large variability in the boundary positions, it is seen that the tail size decreases as the strength of the northward IMF Bz increases, which is anticipated in the absence of dayside reconnection and its consequences. The smallest magnetopause distance was found when a large northward IMF of about 12 nT occurs. Corresponding dynamic pressure is about 4 nPa.

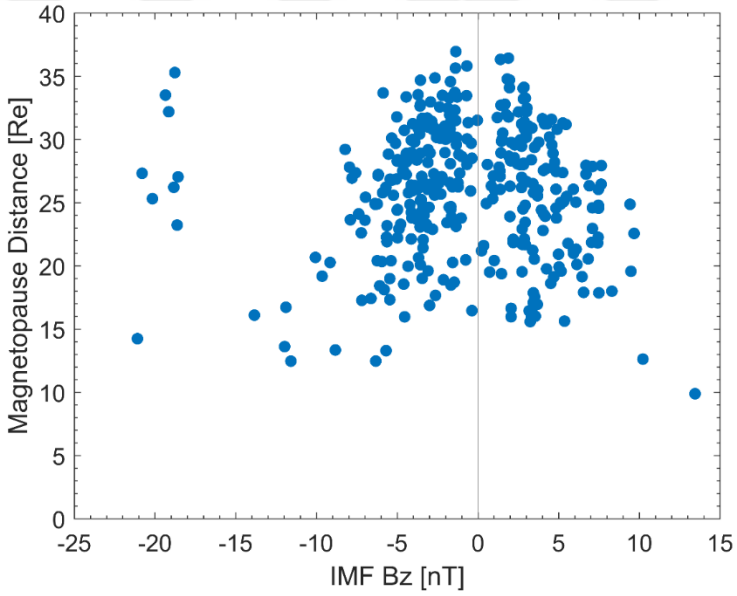

Figure 3.9 : Variations in magnetopause distance in response to IMF Bz within clock angles of $0\leq|\theta|\leq45$ and $135\leq|\theta|\leq 180$.

Southward IMF boundary crossings on the left side in Figure 3.9 shows that the tail at lunar distances becomes smaller as southward IMF Bz increases, except for the boundary crossings that are seen on the upper left part corresponding to southward IMF Bz >15 nT. This is also the result observed in the northward IMF boundary crossings on the right side and seems to indicate that the size of the magnetotail cannot

differentiate on the polarity of the IMF Bz. However, southward IMF Bz case displays large magnetopause positons seen as outliers on the upper left corner of the figure for southward IMF Bz>15nT. The cluster of these 9 points belongs to two different ARTEMIS passes. They correspond to two different ICME events in the solar wind. Close examination of ACE and WIND plasma and magnetic field data for these points indicate that four of these points correspond to the front region of the magnetic cloud (MC) while the other four are from the region just inside the MC (Kilpua et al. 2013; Gopalswamy, 2007; Cho et al., 2003). On average, in both regions, the magnetic field strength varies around 20 nT, IMF Bz is southward and strong of about -20 nT, and the speed is about 400 km/sec. Non-radial components of the solar wind, Vy and Vz, vary around 40-50 km/sec in the front region of the MC, while they are about 110 and 10 km/sec inside the MC. Similarly, the density in front of the MC is about 20 #/cc giving a dynamic pressure of about 6.5 nPa, while inside the MC, it varies around 8 #/cc indicating a dynamic pressure of about 3-4 nPa. One single point, which is from a different pass, also corresponds to the region in front of the MC with about a 20 nT magnetic field strength, southward IMF Bz with -20 nT, speed of about 490 km/sec, non-radial components (Vy and Vz) of about 130 and -100 km/sec, density around 10 #/cc and dynamic pressure of about 3-4 nPa. Overall, strong southward IMF Bz and strong dynamic pressures, larger than 3-4 nPa, typify these cluster of 9 points with mostly large non-radial components.

Occurrence of outliers in the case of southward IMF case suggests that the size of the magnetotail can be as large as 20 Re, or larger, when southward IMF Bz is stronger than 15 nT. It seems that the high dynamic pressures are not influential on the size of the tail for these cases. Compared to southward IMF Bz effects, their effects may be constrained in the determining the size of the magnetotail at this distance. The corresponding magnetotail size in these cases varies from 27 R_E to 36 R_E with an average of 27.2 R_E. Examination of magnetic indices AE (and AL/AU) index for these cases exhibit that a substorm with AE of about 400 nT occurs as a result of the ICME passage. The substorms are also expected to affect the tail's size. Partially, they may be considered as included in the southward IMF Bz effects. As being associated with the reconnected open magnetic flux, persistent strong southward IMFs or persistently increasing southward IMFs seem to limit the decreasing effect of the dynamic pressure on the tail size. Under such conditions, whether tail will grow further or not will depend

on the degree of which of these effects is more dominant. Based on the current data, it is difficult to assess the effects solely due to the large southward IMFs or due to the large dynamic pressures. However, southward IMF case outliers present such instances that the strong southward IMFs may be more dominant over high dynamic pressures on the size of the magnetotail at x=-60 R_E. In addition to these, substorms and the history of the solar wind are the other factors that can contribute on the final size of the magnetotail at lunar distances.

A further investigation of the dependence of the magnetopause distance and consequently size of the tail on the solar wind and IMF Bz parameters was studied using the smallest (10 R_E) and the largest (39 R_E) magnetopause crossings seen in Figure 3.2. Below, for these cases, the magnetopause variations along the ARTEMIS trajectory were investigated together with the IMF Bz and solar wind dynamic pressure as the spacecraft enters the magnetotail in detail.

3.4 Case Studies

In this part, the extreme observations will be investigated deeply to look for the physical conditions that can create such outcomes.

3.4.1 Case-1: January 25, 2013 pass

During this event, ARTEMIS-P2 was located on the dusk side and moving inward toward the tail. Figure 3.10a gives the variations in the solar wind dynamic pressure and IMF Bz corresponding to the boundary crossings detected during the January 25, 2013 pass when it encounters the smallest magnetopause position. In the figure, the left axes give the position of the magnetopause at lunar distances in red and IMF B_z in black while the right axis is the solar wind dynamic pressure (D_p) in blue. Here we used D_p for solar wind dynamic pressure and calculated as $D_p = 1.95nmV^2$ that takes helium contribution into account following Shue et al. (1997, 1998). In these plots, appropriately delayed WIND density, velocity, and IMF Bz data were used to obtain dynamic pressures.

In Figure 3.10a, we see that the magnetopause position gradually decreases along the spacecraft trajectory in response to the changes in IMF Bz and dynamic pressure. ARTEMIS-P2 sees the first magnetopause crossing at 28 R_E during a slightly southward IMF Bz of about -0.3 nT and a dynamic pressure of about 1 nPa. As the

IMF Bz turns slowly to northward direction and increases, the size of the magnetotail becomes smaller at about 20 R_E. During this time, the dynamic pressure shows a slight increase to 1.4 nPa. Later, the magnetopause further decreases slightly towards 19 R_E when IMF Bz becomes southward at about 3 nT and the dynamic pressure increases to 2.7 nPa at this time. After a long tail passage that lasts for about 15 hours, ARTEMIS-P2 crosses into the magnetosheath as the magnetotail contracts as a result of a strong northward IMF Bz of 11.5 nT and increased dynamic pressure to 4 nPa. It is at this time the smallest magnetopause distance was recorded at 20:05 UT as 9.8 R_E. Following this, IMF becomes strongly southward, -11.5 nT, and dynamic pressure increases further to 4.4 nPa, together that give rise to a magnetopause distance of about 14 R_E, increased again with respect to the previous one. In addition, ARTEMIS-P1 during the January 25, 2013 pass observes a decreasing magnetopause distance too, and finds a tail size of 12 R_E at the time when ARTEMIS-P2 records 10 R_E. At the time of these crossings, solar wind non-radial velocity components (Vy and Vz) are -15 km/sec and 15 km/sec respectively. All these indicate that the features emerging in this figure are the consequences of the interaction between the distant tail and a solar wind with a strong northward IMF and a strong dynamic pressure. This case corresponds to the shock sheath region of an ICME where the high fluctuating magnetic fields between north and south were seen. The maximum speed and the density following the shock region is about 550 km/sec and 30 #/cc. Ground based observations of storm and substorm indices Dst and AE indicate a moderate substorm at the near Earth distances as well.

The effect of dynamic pressure may be influenced by the IMF Bz. A strong increase in the dynamic pressure may be obscured by an increase in southward IMF or vice versa. As a result, a change in the magnetotail size may not be detected. On the contrary, a weak northward IMF Bz can cause a small magnetopause in the presence of a strong dynamic pressure. Both the duration and the magnitude of the IMF Bz and the dynamic pressure will be key factors in order to detect an observable change on the size of the magnetotail at lunar distances. The smallest magnetopause size of 10 R_E is clearly a result of the combined effects of large northward IMF Bz and strong dynamic pressure.

3.4.2 Case-2: August 28, 2012 pass

In this case, ARTEMIS-P2 is seen on the dusk side in the magnetosheath again and encounter multiple magnetopauses while moving inward. The spacecraft observes the largest magnetopause at 38.9 R_E at the beginning of the event and the magnetopause encounters following this are smaller, but still larger than 30 R_E.

In Figure 3.10b, we present the magnetopause positions and the corresponding variations in IMF Bz and solar wind dynamic pressure. This event occurs during an unusually quiet time of the solar activity. WIND densities during the event vary from 0.58 to 1.06 #/cm^3 and velocity around 450 km/sec, which result in low dynamic pressures approximately 0.3-0.5 nPa. At the time when the magnetopause distance of 38.9 R_E is registered, the pressure is about 0.41 nPa. Corresponding non-radial components of solar wind velocity (Vy and Vz) are -30 km/sec and -15 km/sec, respectively. During this inbound pass, total IMF is about 4.2 nT while IMF Bz is northward most of the time with an average of 0.58 nT. In this case, it is obvious that low solar wind dynamic pressure is the determining factor on the size of the magnetopause. Even it is very small, southward IMF Bz at the time of this crossing is consistent with large tail magnetopause but the magnitude is seen to be too small to have an effect on the size of the tail when compared to the pressure. Other encounters of the magnetopause along the same trajectory give support on the relation between northward IMF Bz and small dynamic pressures. Under similar solar wind and IMF conditions, the magnetopause variations between 32 R_E and 35 R_E were recorded by ARTEMIS-P1 as well. Also similar to the January case, the aberration angles were found to be typical. Therefore, we attribute the occurrence of large magnetopause to be due to the unusually quiet solar wind conditions. We also note that there are no storms or substorms corresponding to this event.

Extremely large magnetopause positions have often been observed before. Examining the Howe and Binsack (1972) study of distant tail magnetopause crossings using the Explorer 33 and Explorer 35 spacecraft, one can clearly see that highly scattered positions of magnetopause crossings are common at distances beyond -40 R_E and the radius of the magnetotail varied between 20 R_E to 36 R_E at X=-60 R_E. Even larger magnetotail radius values of about 42 R_E was recorded at -48 R_E. Similarly, the same authors also showed that the tail size can be as small as 11 R_E to 13R_E from 50 to 80R_E

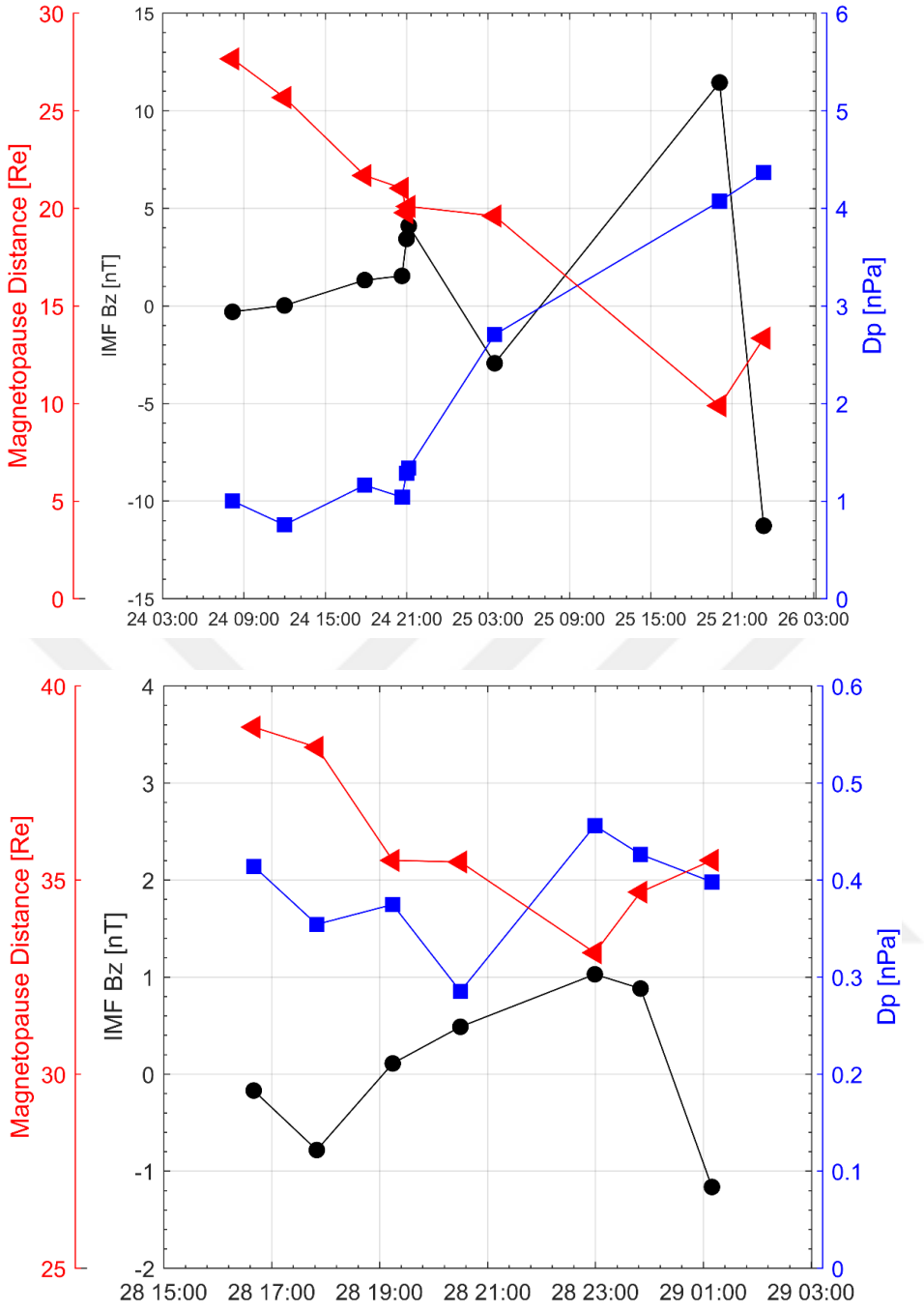

Figure 3.10 : Magnetotail distance (red), dynamic pressure (Dp, blue) and IMF Bz (black) variations along the trajectory of ARTEMIS-P2 on (a) January 24-25, 2013 and (b) August 28-29, 2012.

behind the tail. Using Explorer 33 and 35, the Behannon study (1970) recorded a tail radius of about 38R_E as well as 14R_E at distances from -40 to -70R_E in the tail. While ARTEMIS observations verify these observations, we emphasize the prevailing solar wind and IMF Bz conditions that these small (10 R_E) and large (39 R_E) dimensions of the lunar magnetopause were observed which was then not possible due to the lack of high quality measurements of both upstream and in the magnetotail.

3.5 Overview and Discussion

This chapter presents results on the size, geometry and shape of the magnetotail boundary as well as the factors that affect the tail's motion and its variability under different IMF orientations and solar wind dynamic pressure using ARTEMIS spacecraft tail observations at lunar distances. We corrected for the aberration effects resulting from Earth's orbital motion and non-radial solar wind velocity and matched each ARTEMIS magnetopause boundary crossing concurrently with ACE (or WIND) data using high-resolution data from both spacecraft. We compared our results with those found in earlier studies mostly, which had been done long ago in 1960s and 1970s. The results were also compared with the magnetopause model predictions. The effects of dipole tilt angle, IMF By, and IMF Bz on the size and shape of the magnetotail at lunar distances were addressed and discussed. Dependence on solar wind dynamic pressure and IMF Bz orientation was studied in detail on the basis of both average and unusual solar wind and IMF conditions. While our results verify the findings of the earlier works on the size and shape of the tail magnetopause, new results were obtained and demonstrated on the effects of the IMF Bz and dynamic pressure involving physics and dynamics of the magnetotail at lunar distances. We highlight our results below:

1. At lunar distances, non-radial solar wind flow deviates the magnetotail by about 6^o on the average in the dawn-dusk direction and about 3^o out of the ecliptic plane. The largest total dawn-dusk and north-south aberration was obtained to be 23.2^o and 11^o respectively. The magnetopause crossing positions should be transformed into the appropriate coordinate system for the correct interpretation of the distant tail boundary studies. It is anticipated that the Alfvenic fluctuations will have an effect on the non-radial flow velocity, which will be projected on the center of the magnetotail and thus estimated magnetopause distance at lunar distances. However, this effect was indicated to be small, on the order of 1-3 R_E for the variability seen in the near Earth magnetic fields. (see Figure 3, Section 2.2)

2. Based on the percent errors, the boundary of the magnetotail at lunar distances can be represented by a circle for all upstream conditions. A circular fit to

magnetopause positions give a tail size with radius of 26.7 R_E with an RMS=4.94 R_E. (see Figure 4c, Section 3.1)

3. The tail size and the shape for different IMF clock angle sectors were hindered by the lack of high latitude boundary crossings. An elliptical boundary is reasonable for both east-west and north-south IMFs. The east-west IMF presents an oblate ellipse while the north-south IMF indicates a prolate ellipse. The shape of the tail is more circular (e=0.47) for IMF Bz sectors compared to IMF By sectors (e=0.72). The tail size and dimensions were found to be slightly larger for southward IMF compared to northward IMF, obtained approximately equal for northward and southward IMFs at this distance. (see Figures 9,10, Sections 3.3.1, 3.3.2)

4. The magnetopause positions present a large scatter. While the average circular tail size is 26.3 R_E, the smallest (10 R_E) and the largest (39 R_E) tail dimensions were recorded. The smallest tail size was found to be associated with a strong northward IMF Bz and relatively large solar wind dynamic pressure. The largest tail size, on the other hand, corresponds to low solar wind dynamic pressure and a slightly southward IMF Bz. (see Figures 5, 6, 7, Figure 3.10, Tables 1, 2, Sections 3.1, 3.2, 3.4)

5. Magnetopause models (the HB72, the PR96, the S97, the S98, the C02, and the L11) were compared with the all boundary crossings in the xR-plane at lunar distance. The models predicted the observed positions within a range of percent errors from 0.8 % to about ±6 %. Despite being the oldest, static the HB72 model gives the best prediction of the magnetopause boundary at lunar distances corresponding to all IMF and solar wind conditions. This is considered as the result of the tail magnetopause data from lunar distances that are included in the HB72. Results from three Shue et al. based empirical models (the S97, the S98, the C02) give similar magnetopause predictions with percent error varying from 1.2 to 2.9 %. While the L11 underestimates the magnetopause size by about 7 % at lunar distance under the average solar wind conditions, the PR96 overestimates by about 6 %. (see Figure 3.2, Table 3.2, and Section 3.2)

6. The model results were also compared for the uncommon upstream conditions corresponding to the smallest and largest magnetopause observations (10 R_E and 39 R_E). All models for these cases showed large deviations from the observed boundary. The closest prediction for the smallest boundary crossing position was obtained from the L11 model. For the largest magnetopause crossing, 39 R_E, on the other hand, the PR96 model gave the best prediction. The performance of the S97 model in predicting the magnetopause under unusual conditions was better than that of the S98 model. The HB72 model, on the other hand, showed the poorest prediction for the chosen cases. The percent errors were found to be larger under the unusually weak solar wind upstream conditions. The models were found to underestimate the tail flaring for the largest boundary crossing while they, except Lu et al. (2011), failed to represent the inward flaring in the case of the smallest boundary crossing. Tail size appears to be closely associated with the tail flaring which in turn related to the evolution of the magnetopause boundary from the subsolar point, through polar cusps at the terminator, and to the tail distances. These discrepancies or agreements indicate how the models may be improved at lunar distances. (see Figures 7, Figure 3.10, Table 3.2, Sections 3.2, 3.4).

7. Dependence of the magnetotail boundary size on the dynamic pressure and the direction of IMF Bz was investigated. In general, the decreasing tail boundary are seen to be associated with the increasing dynamic pressures. However, the dynamic pressure dependence shows two groups in the distribution of the magnetopause crossing points. Those with greater than 2 nPa showed large scatter with an average magnetopause size of about 26.5 R_E while those less than 2 nPa showed a decreasing magnetotail with increased pressure. (see Figure 3.8, Section 3.4)

8. Similar results were also obtained for the dependence of the tail size on the strength of IMF Bz when IMF lies within the north-south clock angle sectors ($135 \leq |\theta| \leq 180$ and $0 \leq |\theta| \leq 45$). For both northward and southward IMF Bz, the tail size was found to decrease with the increasing strength of the northward or southward IMF Bz. The rate of decrease is slightly faster in case of southward IMF Bz.

9. Case 1 and Case 2 studies indicated that the final size of the magnetotail at lunar distances is a result of the balance between the dynamic pressure effects and IMF Bz effects. In that, compared to the nominal conditions, strong northward IMFs and large dynamic pressures resulted in the smallest tail size, while weak IMF Bz and weak dynamic pressures gave the largest tail size. Both parameters together appear to control the tail size at x=-60 R_E. (see Figure 3.9, Section 3.4)

10. The outliers in the case of strong southward IMF Bz, on the other hand, suggest that at times, when the southward IMF strength becomes larger than 15 nT, the tail size may increase despite the large dynamic pressure. The decrease in tail boundary size for southward IMF Bz appears to show a threshold at which the tail size does not continue to decrease more. A similar effect on the magnetopause distance is related to the saturation effect of the southward IMFs on the subsolar magnetopause (Yang et al., 2003), which refers to the fact that subsolar magnetopause cannot move any closer to the Earth as the southward IMF Bz strength increases more at a given dynamic pressure. As the southward IMFs become stronger than 15 nT, in spite of the increase in dynamic pressure the tail grows instead of shrinking as one would expected. The southward IMF outliers seem to indicate different dynamics associated with the strong southward IMFs when its magnitude exceeds a certain level operating in the magnetotail at lunar distances. Nevertheless, a further work in order to differentiate between the strong southward IMF effects and those of solar wind dynamic pressure in these distances in the magnetotail is needed and currently underway.

4. MAGNETOTAIL MAPPING AT LUNAR DISTANCES

ARTEMIS probes spend around 4.5 days per pass in the magnetotail at lunar distances. P1 and P2 will observe the plasma sheet from 20 to 30 hours per orbit, each collecting 100 days (2400 hours) of magnetotail data, including 20-30 days (500-700 hours) in the plasma sheet; more than enough to characterize this region of space and define its variability and with well inter-calibrated instrumentation (Sibeck, et al., 2011). The spatial coverage of the magnetotail in XY-, XZ- and YZ- planes for our study interval from August 2011 to August 2013 are presented in Figure 4.1 and the orbital coverage for each IMF condition, i.e. sector separation, is presented in Figure 4.2. As the number of ARTEMIS crossings increases, the color changes from blue to green and yellow and up to dark red. The ARTEMIS probes crosses the magnetotail from about -50 R_E to nearly -70 R_E in aSWGSM X-axis while orbiting the Moon. In the XY- plane, measurements from northern and southern tail are given both separately and mixed. There are more observations from the dusk region compared to dawn. In the XZ- plane, magnetotail data from ± 7 R_E in the azimuthal direction, where the plasma sheet particles are believed to be populated, is collected densely (Meng and Mihalov, 1972; Nishida and Lyory, 1972; Rich et al.,1973). The coverage of plasma sheet region at lunar distances is the key of this study since this region has not been investigated since Explorer 33 and 35 era and the plasma sheet is an important tunnel where the energy is transferred from solar wind to the Earth (Goertz et al., 1993). In Figure 4.2, (a)/(b) is for northward/southward IMF sector and (c)/(d) is for eastward/westward IMF sector. The dominancy of negative IMF By sector over other IMF sectors can be seen as it is also stated in Table 2.2 as in number of data point distribution for each sector.

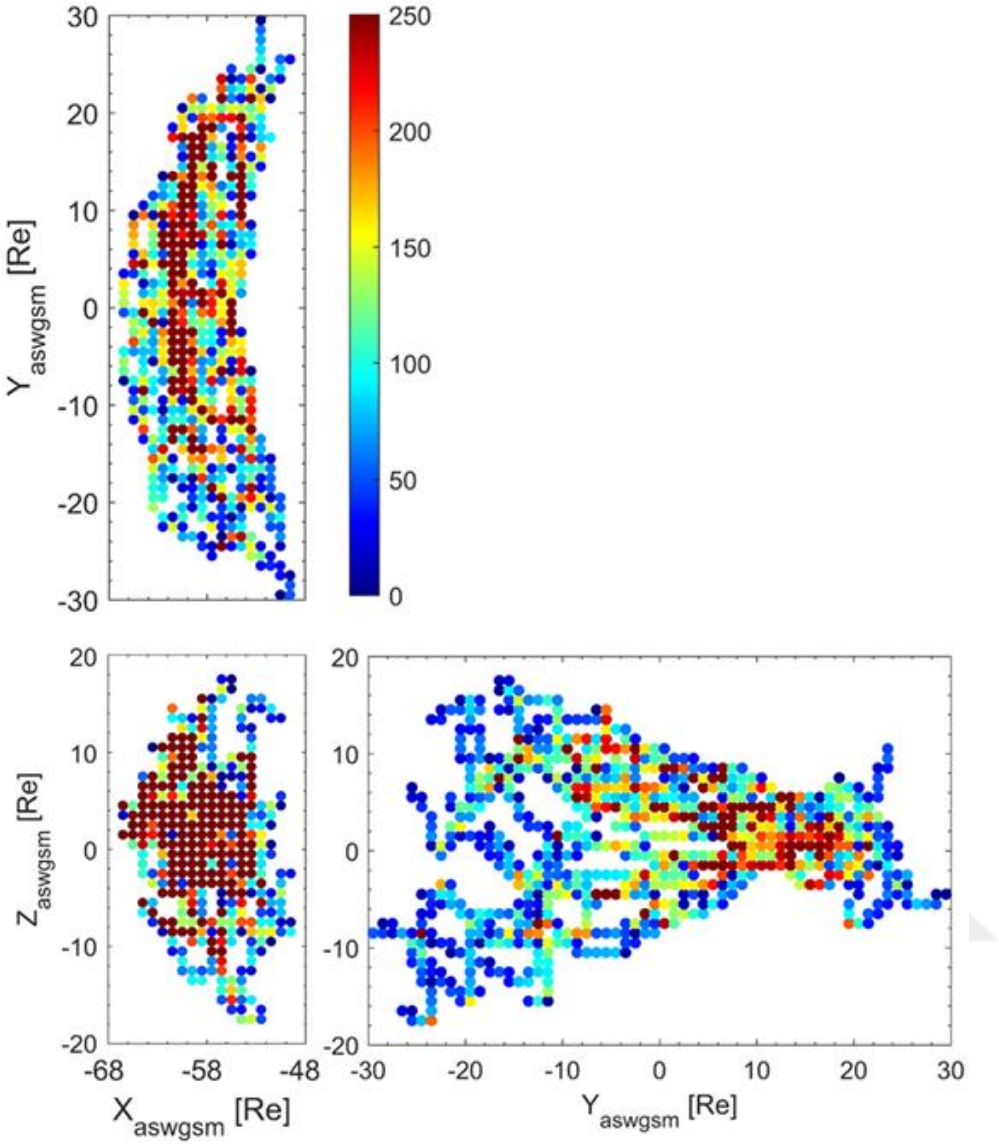

Figure 4.1: The orbital coverage of ARTEMIS probes in aberrated solar wind corrected GSM coordinate system. Red colors refer to denser coverage of the area whereas blue colors refer to less encounter of the magnetotail in that region.

ARTEMIS P1 and P2 spacecraft settled into a more stable position around the Moon and around the Earth from August 2011 after which we start collecting measurements. As described in Chapter 2.3.2, the probes travel through solar wind to magnetosheath where it spends most of its time. Then the probes starts collecting measurements from the magnetotail after which they crossed the magnetopause in the dusk side until crossing the magnetopause on the dawn side into the magnetosheath, and to solar wind again. The probes spend a minimum of 2,5 to a maximum of 4,5 days in the magnetotail only when we collect data points for this part of study.

The interval covers data from last magnetopause boundary crossing in the dusk side from magnetosheath to magnetotail to the first magnetopause boundary crossing in the dawn side. From August 2011 to January 2013, in 18 months ARTEMIS probes make 19 magnetotail traversals at -60 R_E. These 86373 data points from 19 traversals with one-minute resolution matched with 82869 data points from ACE for IMF and solar wind information.

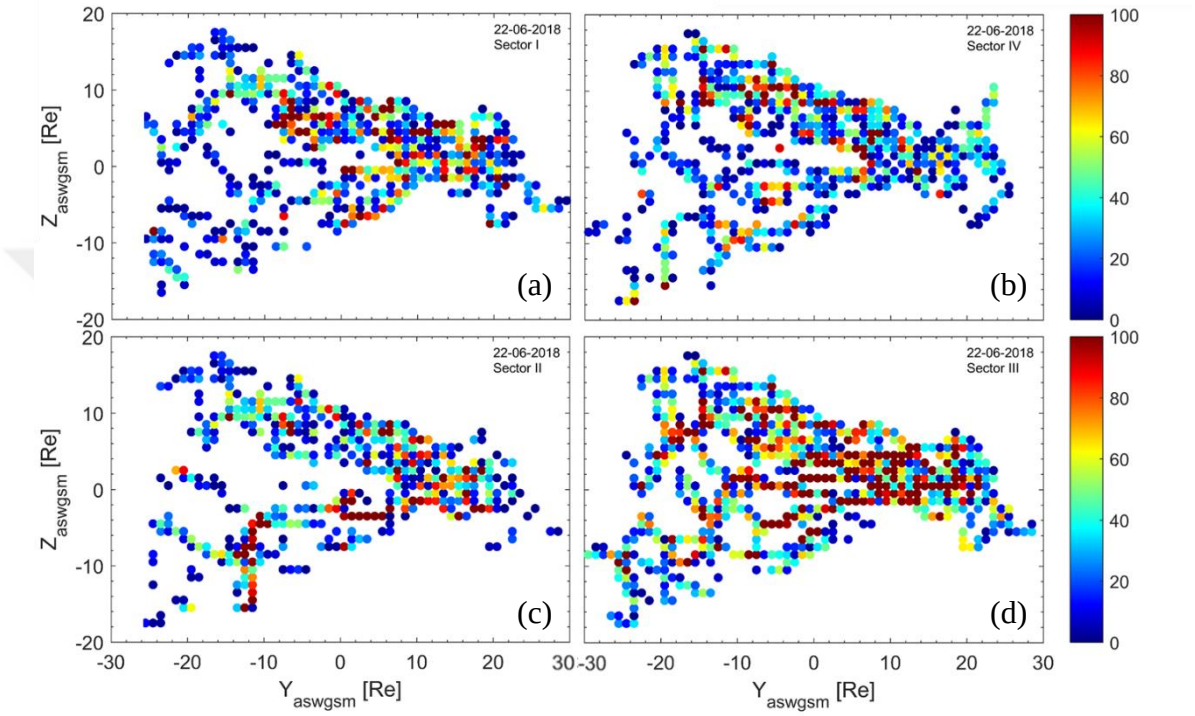

Figure 4.2 : ARTEMIS probes orbital coverage in aberrated solar wind corrected GSM coordinate system for each sector. (a) for northward (+IMF Bz), (b) for southward (-IMF Bz) , (c) for eastward (+IMF By) and (d) for westward (-IMF By) sectors.

The raw data, gathered from ARTEMIS probes, are processed such that they are binned into desired grid size, e.g. $2R_E$ x $2R_E$, $3R_E$ x $3R_E$ or $6R_E$ x $4R_E$ as seen in Figure 4.3. In YZ- planes where the observations lie within the ± 30 R_E $\pm$ 20 R_E, the grid size is chosen as 6x4 R_E to have the same dimensional scales between the Y- and Z- planes. The average of the vectors falling in each grid size is assigned to the middle point of the grid in two dimensions. Then the grid size, in which the vector averages are calculated, is moved for a determined step size (e.g. 0.5 R_E, 0.8 R_E, or 1 R_E) in both directions. The spatially moving average analyses are made if the grid has data points greater than the desired chosen value for each case and if not than that bin is left blank.

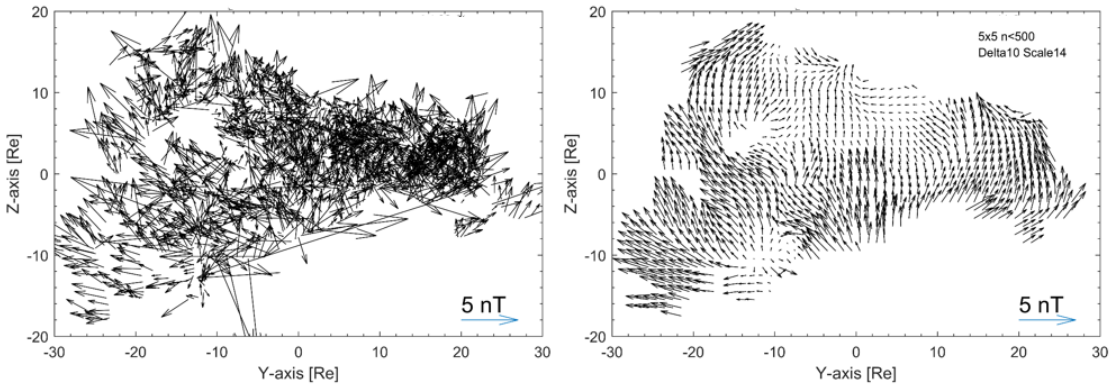

Figure 4.3 : The magnetic field vector map in YZ-plane, raw ARTEMIS data is given in left and in the right figure the magnetic field line map of the analyzed data. The bin size is $5R_E$ x $5R_E$ with at least 500 number of data points in each bin. The moving averages are calculated with $1R_E$ step size in Y- and Z- directions.

This omit number, n, corresponds to minutes of magnetotail data, either magnetic field or plasma property, and different omit numbers are used in different planes and/or sectors, e.g. n>10, n>50, n>200 or n>500 data points. However, bins with less than desired number of data points but more than the values stated in the figures left top corner are plotted in gray tones. In the Appendix part, the plots are given for every tenth unprocessed flow vector in Figure B.2 to Figure B.5.

The magnetic field line vector map is presented in Figure 4.4 for all data without any sector separation to visualize the effect of the bin size and the omit number. In (a) $2R_E$ x $2R_E$ grid size with at least 200 data points in each grid is presented. In (b) the grid size is increased from $2R_E$ x $2R_E$ to $3R_E$ x $3R_E$ with the same omit number used in (a). As the grid size increases from (a) to (b), the map becomes denser. In (c) same grid size is chosen as in (b) with increased omit number, i.e. at least 300 data points in each $3R_E$ x $3R_E$ grid. When (b) and (c) are compared, more blank spaces where the bins have less than 300 data points are seen in (c). Moreover, in (d) $4R_E$x$4R_E$ grid size is used with the same omit number in (c). Besides having more coverage compared to all, the transition between the grids also becomes more transparent in (d). When visually inspected the chosen grid size does not alter but smooth the pattern and the change in the grid size does not change the global structure of the magnetotail. Whereas the omit number affects the information given by the figure. After this exercise more than one omit number is chosen throughout this study and plotted black, dark and light gray with respect to its number of data points. The gray colored vectors

are also provided to have an idea of what is going on in that area instead of leaving as an unobserved space.

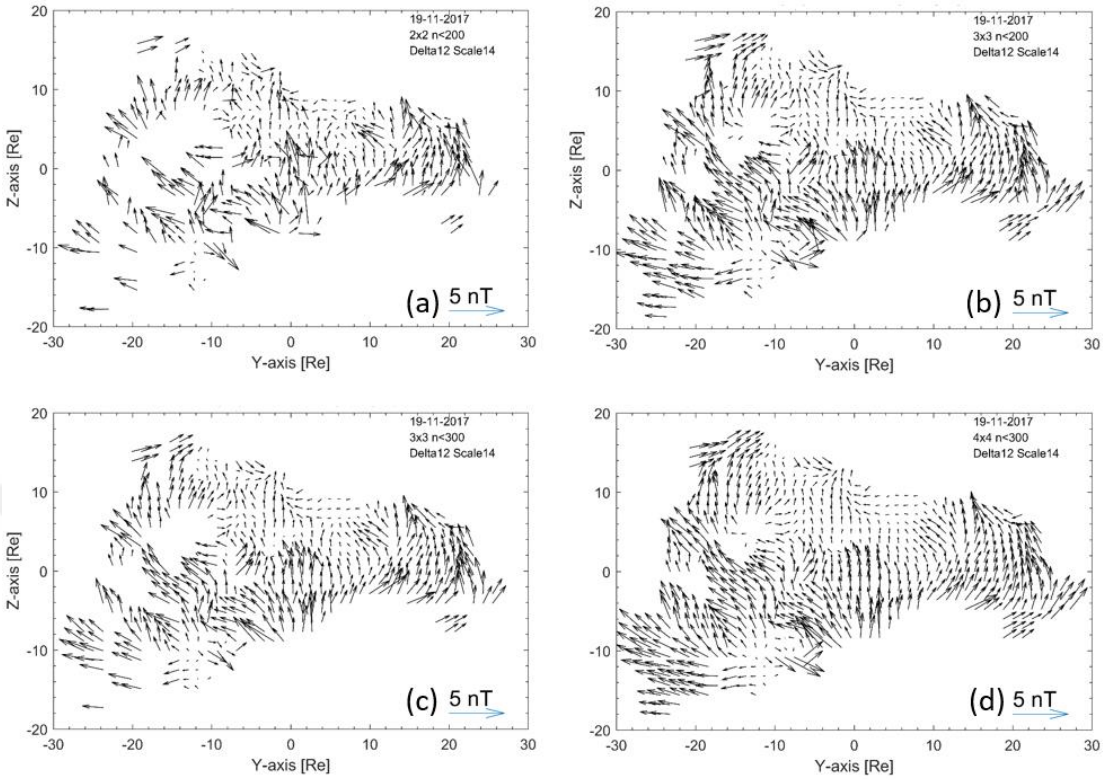

Figure 4.4 : Magnetic field line vector map with different grid size and/or omit number. In (a) $2R_E x 2R_E$ grid size with at least 200 data points in each grid is presented. In (b) $3R_E x 3R_E$ grid size is chosen with the same omit number used in (a). In (c) same grid size is chosen as in (b) with increased omit number (300 data points). And in (d) $4R_E x 4R_E$ grid size is used with the same omit number.

4.1 Magnetic Field Structure at Lunar Distances

The geomagnetic tail is one of the most dynamic regions of the Earth's magnetosphere and is probably the least understood especially at distances beyond lunar orbit due to the few number of missions, e.g. Explorer 33 and 35, ISEE 3, and Geotail, the limited time spent and the scarcity of the observations in that region. In spite of the unsteadiness of the magnetotail and difficulties related to observations, a number of studies based on theory, models, and/or observations evaluate data with a statistical point of view or via case studies. Our aim in this section is to present some of the valuable information here with a quasi-chronologic order.

During the 1960s, especially after Explorer 33 spacecraft completed a couple magnetotail traversals at around $-80R_E$ distances down the tail, the research based on

the Explorer-33 observations published and most of which showed similar results to IMP-1 satellite at half the distance to the Moon. The neutral sheet with earthward or tailward oriented tail field lines above and below it, is a thin layer, about 0.1 R_E to 1 R_E thickness, but still well defined at about -80R_E (Ness et al., 1967). The plasma sheet, surrounding the magnetically neutral sheet is shown to be 4-6 R_E thick in the center while flaring out near the dawn-dusk boundaries.

The effect of geomagnetic activity was studied by comparing the average configuration of the magnetotail during quiet times at lunar distances with disturbed times. The increase in the magnetotail field magnitudes, in the orders of 1:4, found to be correlated with the increase in the geomagnetic activity (Behannon and Ness, 1966). The magnitudes of about 10-18 nT at -50 R_E distances during quiet times, and 40 nT magnetotail magnitudes during active times had been observed (Ness et al., 1967). The average magnetotail field magnitudes was found to be 16 nT at -30 R_E, 13 nT at -40 R_E and about 7 nT at -80 R_E distances (Behannon and Ness, 1968).

Studies based on Explorer 35 findings are the only systematical observations that are collected from the same region as the ARTEMIS probes. One such study was published by Meng and Mihalov (1972) in which the writers investigated the spatial distribution of the magnetotail field magnitude in GSM coordinate system near lunar distance. Similar to this study, they divided the observations into bins, $3R_E x 3R_E$, in the cross-sectional plane and calculated the averages of Explorer 35 magnetometer data with 10-minute resolution. They found that the magnetic field magnitudes decrease in the region below and above the neutral sheet due to the diamagnetic effect of the plasma sheet, especially in the geomagnetically quiet times. The average magnetic field magnitudes range between 7 nT to 12 nT with higher values distributed adjacent to the magnetopause. Fairfield (1970) commented that there is a positive correlation between the tail field magnitudes and magnetic activity at distances $-65R_E < Xgsm < -55R_E$. The magnetic field medians increases from 8nT to 10.3nT during active times.

Meng and Mihalov (1972) also commented that the neutral sheet coordinate system sorts magnetotail data better than GSM coordinate system in YZ-plane (Russell and Brody, 1967). They found that the mosaic like pattern, i.e. magnetic field magnitudes are not changing in a uniform trend, still exists but the mid-range magnetic field averages, 7nT - 8.5nT, lie more in the northern hemisphere than southern hemisphere in neutral sheet coordinate system.

A global topology of the magnetotail at lunar distances was presented by Meng and Anderson (1974) from the 34 traversals of Explorer 35. They commented that the magnetotail neutral point is generally located beyond lunar orbit. The lobe and plasma sheet spatial distribution is different from the geometrical locations in the cross sectional plane of the magnetotail. The lobes can be encountered sporadically across almost all Y values and even though the percentages of lobe plasma detection is highest for larger Z values, one still can observe lobe plasma near the expected neutral sheet location at Zgsm=0 R_E (Russell and Brody, 1967; Meng and Anderson, 1974; Hardy et al., 1979a). In the lobe region, the magnetic field lines directed parallel to the neutral axis while inside the plasma sheet, the magnetic field lines deviate from the neutral plane (average By=2.1 nT and Bz=1.1 nT) and fluctuate a lot (e.g. Ness et al., 1967; Meng and Anderson, 1974). In the cross-sectional plane, the average magnetic field magnitude is about 10.8 nT in the lobe region independent of the geomagnetic activity and 7-8 nT is the plasma sheet region. The distribution of the magnetic field magnitudes is higher in southern hemisphere than northern hemisphere and decrease towards the magnetotail flanks, $|Y|>9$ R_E.

Hardy et al. (1976) is one of the first studies to our knowledge that correlates position of the plasma data at lunar distances with the orientation of the IMF at the time of a case event. They divided the cross-section of the tail into four quadrants to seek for magnetic merging at the magnetopause and found that the lobe plasma is strongly correlated with the y-component of the interplanetary magnetic field as was suggested by Stern (1975). Their follow up study, Hardy et al. (1979) also tested the correlation between the observations with the IMF Bz component since the plasma thickness increases with increasing negative IMF Bz magnitude. They found that the probability to encounter lobe plasma increases with the increasing negative Bz values of the IMF.

After ISEE-3 placement in orbit, studies in 1980s are mainly based on ISEE-3 observations of magnetic field and particle measurements in the distant magnetotail between $X=-60R_E$ and $X=-238R_E$. The magnetic field and plasma characteristics of the distant tail structures are important for this study since they are found to be very similar to the plasma at lunar orbit (Artemyev et al., 2017b). The theta structure, the northern and southern lobes with an embedded plasma sheet in between them lying parallel to Earth-Sun line is still valid at that distance down the tail. The lobes have a magnetic field magnitudes of about 7-8 nT whereas in the plasma sheet region, about 9-15 R_E

thick, the magnetic field values decrease due to the diamagnetic effect of plasma sheet at ISEE-3 distances (Slavin et al., 1983; Tsurutani et al., 1984).

Not only magnetic field related but also plasma flow related research has been accomplished using ISEE-3, as presented in Section 4.2.

The magnetotail is sensitive to not only plasma conditions in the magnetosheath but also the direction of the interplanetary magnetic field. The IMF By related asymmetries in the magnetotail cross-sectional plane is studied by many (Hardy et al. 1979; Cowley, 1981; Tsurutani et al., 1984; Gosling et al., 1985). This effect is due to the "penetration" of the y- component of the interplanetary magnetic field into the magnetotail in the preferred quadrants. This asymmetric addition of the magnetic flux to the tail lobes causes the mantle to be thicker on northern dawn and southern dusk quadrants of the magnetotail for positive IMF By and northern dusk and southern dawn quadrants for negative IMF By sector. Tsurutani et al. (1984) presented results using two ISEE 3 deep tail passes. They found that for positive sector IMFs 13% of the IMF penetrates into the aberrated north-dawn and south-dusk lobe quadrants at x=-150 R_E to -238 R_E. Under the same IMF sector conditions, the IMF By correlated asymmetry was also observed as an increase in the chance of observing mantle plasma in the preferred quadrants as well as, increased plasma density values compared to other quadrants (Gosling et al., 1985; Huang, 1987). A recent study based on ARTEMIS probes, in both hemispheres, gave consistent results with the strong negative IMF By condition. In the northern hemisphere, one of the probes observed a dense ($n\sim0.5cm^{-3}$), low-energy ($\sim10^2$ eV) mantle plasma whereas in the southern hemisphere, probe spotted a low density ($n<0.04\ cm^{-3}$), high-energy ($\sim10^3 – 10^4$ eV) mantle (Hietala et al., 2017).

One of the main studies of the IMF By effects on the magnetotail is on the twisting, flattening and magnetic field line bending by Sibeck et al. (1985) using ISEE 3 observations. In the northern hemisphere, the merged magnetosheath and magnetotail field lines bent in the direction of the interplanetary magnetic field direction, e.g. positive By, are pulled toward the dawnside while being pulled tailward by the magnetosheath flow. Thus twists the tail such that the north lobe can be observed in the southern hemisphere and the reconnected filed lines in the southern hemisphere are pulled toward the duskside of the tail. The magnetosheath plasma penetration is described as it takes place from a "window" in the study. The increase in the density

creates an anisotropic pressure in the magnetotail, which flattens the magnetotail cross-section. Not only has the cross-section of the tail but also the plasma processed inside the tail change in case of a dayside reconnection with a positive y-component of the IMF. The magnetic flux would be added to the preferred quadrants, e.g. for positive IMF By, northern dawn and southern dusk quadrants, and therefore magnetic and particle pressures increase and the plasma convects from those quadrants toward the plasma sheet as well as the opposite quadrant, e.g. duskward flow in the northern hemisphere for positive IMF By (Khurana et al., 1996). Additionally, the tail lobes and the neutral sheet twist around in response to the IMF By associated torque especially at downstream magnetotail where dipole effect starts to disappear. In this case, a non-uniform cross tail By field will occur (Cowley, 1981). However, the magnetotail does not act as a rigid body and IMF By effect does not expected to rotate the whole structure but skews the internal structure (Maezawa et al., 1997).

From the reviewed works, the study by Kaymaz et al. (1994a, 1994b) are the closest ones to this one. They show the average picture of the magnetotail via magnetic field vector maps using 16 years of IMP 8 magnetometer data in cross-sectional plane and noon-midnight meridional plane at -33 R_E. Being close to the Earth, the dipole effect is a major contributor at that distance, creating a symmetric dipolar pattern in YZ-plane resembling iron fillings on a paper sitting over the poles of a horseshoe magnet. They also study the IMF related effects on the magnetotail using IMF sector separation technique similar to this study. The field nodes are 18 R_E apart, above which the magnetic field lines flares outward. The magnetotail exhibits a more elliptic dipolar configuration for positive IMF Bz than in negative IMF Bz. For positive IMF By condition, the separation of the nodes skews clockwise about 2 R_E in y-direction. In the XZ- plane, the reversal of the x- component of the weak magnetic field line vectors along the current sheet, sandwiched in a thin neutral sheet, is observed to twist counterclockwise for positive IMF By condition in cross-sectional plane. The effect of the y-component of the interplanetary magnetic field found to be asymmetrical as its twisting effect increases from center (26%) to the flanks (35%) of the plasma sheet (Kaymaz et al., 1994b).

While the tilt in the current sheet purely depends on the sign of the IMF By, regardless of the sign of the IMF Bz, the degree of this tilt increases with the northward IMF than in southward IMF. The cold, dense mantle plasma adjacent to the magnetopause is

observed closer to the neutral line because of the location of the reconnection site that is at the high-latitude cusp region for northward IMF.

For northward IMF, the reconnection takes place at the tailward of the cusp region, which results in the small tail. Tail closes in the earthward of the lunar distance in the nightside region (Sibeck and Lin, 2014), and at the dayside region the surface of the boundary opens at lower latitudes on the dawn and dusk sides in the northern and southern hemispheres, respectively (Maezawa et al., 1997; Hasegawa et al., 2002). In the presence of a southward IMF, the reconnection happens in the dayside subsolar magnetopause, the reconnected field lines are pulled toward higher latitudes by the field tension as they convect tailward with the magnetosheath flow and the high latitude magnetopause becomes open type boundary (Hasegawa et al., 2002). The open surface is more in the southward IMF than in northward IMF so as the mantle plasma. A recent study based on BATS-R-US MHD model shows that the location of the mantle plasma is also seen to move to lower latitudes as IMF By increases (Wang et al., 2014). At the same year, Sibeck and Lin (2014) run a BATS-R-US MHD model and the model shows that the rotation of the plasma sheet increases as IMF By increases from 1 nT up to 3 nT, after which the skewness does not change and the tilt remains to be same as in 3 nT.

The use of MHD models in understanding the magnetotail's response to extreme solar wind and IMF conditions is useful since the models run for all territory, not like spacecraft observations from a limited region and for any desired condition. Raeder et al (1995) studied the evolution and dynamics of the magnetotail with a 400 R_E long tail during extended periods of northward IMF condition. The configuration of the regions and their proportions are different for northward IMF that in southward IMF but remains nearly the same as a function of distance down the tail. The tail lobes, the region of open-field lines, suppressed by the closed field line region but still exists at high latitudes even after almost four hours of steady northward IMF. Another three-dimensional MHD model study for understanding plasma processes within the tail under northward IMF condition is done by Fedder and Lyon (1995). The flow velocity vectors show that the flow direction is in the earthward direction in the region earthward of X=-90R_E and tailward downstream of X=-90R_E in the XZ plane. In the XY plane, the projections of the plasma velocity vectors showed the existence of the low latitude boundary layer.

A case study by Farrell et al. (2003) based on two traversals of WIND spacecraft at about -60 R_E showed an earthward moving X-line with quadrupole magnetic field configuration and a change in the direction of the fast flows, i.e. earthward to tailward flows.

The measurements of ISEE 3 spacecraft at -225 R_E showed a depression in the plasma density during periods of northward IMF orientation which they associate with high-latitude reconnection (Fairfield, 1993). For northward IMF, Wang et al. (2006) shows cold and dense magnetotail plasma observations in the dawn section of the tail. This asymmetric density distribution and the asymmetry in Bz ($Bz_{dawn} > Bz_{dusk}$) creates higher pressures at dusk (Walsh et al., 2014 and references therein).

Cowley (1981a) studied how the magnetotail respond not only to the y- component but also to the x-component of the interplanetary magnetic field in his follow-up study in the same year. He commented that the magnetic flux would be unequal in the tail lobes in which flux will be larger in the northern lobe for positive IMF Bx and southern lobe for negative IMF Bx. This IMF Bx effect is different and less obvious than IMF By associated asymmetries and does not create any difference in field strength in the two lobes. The response of the magnetotail to the x-component of the IMF results in displacement of the tail lobes so that the area occupied by the two lobes would be different. The displacement of the current sheet associated with the IMF Bx is another effect in which the current sheet must be displaced to the south for positive IMF Bx and to the north for negative IMF Bx.

For the magnetotail plasma characteristics at lunar distance, ion detectors stationed on the Apollo landing sites are the main sources of information from 200 hours of observations from 15 separate tail crossings (Hardy et al., 1976). At lunar distances, Hardy et al. (1975) studied the magnetotail plasma characteristics as Moon crosses from magnetosheath to magnetotail. They observed two kinds of crossings, one of which is direct transit from magnetosheath to lobes. For the other type of crossings, they observed plasma sheet boundary layer with plasma characteristics comparable to the near Earth plasma. Thus, they suggested that the plasma entered to the tail lobes closer to the Earth and as flowing downstream distances, the plasma convected toward center of the tail, eventually creating the distant current sheet.

The lobe characteristics are defined as bulk velocities about 60-200 km/s, plasma densities about 0.1-3 cm^{-3} and temperature about 2-80 eV, at lunar distances. In the plasma sheet region, plasma densities vary from 0.5-0.8 cm-3 to <0.1 cm-3 while plasma sheet plasma get hotter and the temperatures increase from 400-600 eV to 1000-3000 for quiet and disturbed times, respectively (Hardy et al., 1976; Hardy et al., 1979a).

The plasma parameters on average and during substorm conditions in the lobe and plasma sheet are studied as a function of downstream distance. As the x-component of the velocity and density increases the temperature decreases in the lobes. Strong density and weak velocity and temperature gradients were observed from the center of the lobes to near the magnetopause (Slavin et al., 1985). The density increases as spacecraft moves from the center of the tail ($|Y|<10\ R_E$) and toward the dawn-dusk portions of the tail ($|Y|>20\ R_E$).

The lobe magnetic field intensity falls from about 15 nT at $X=-50\ R_E$ to 8-10 nT at $X=200\text{-}220\ R_E$ (Slavin et al., 1985). The plasma density and the magnitude of the x-component of the velocity parameter increase from 0.02 cm^{-3} and 150-200 km/s at $X=-50\ R_E$ to 0.1-0.2 cm^{-3} and 200-250 km/s at $X=-220\ R_E$ whereas the plasma temperature decreases from about $1x10^6$ K to $5\text{-}8x10^5$ K at the same down tail distances.

At $X=-60R_E$ to $-100R_E$ the mean magnetic field value is 4.9 nT. The particle density increases gradually from 0.2 cm^{-3} at $X=-30\ R_E$ to 0.3 cm^{-3} at $X=220\ R_E$. The magnetotail Bz distribution is predominantly positive with a mean of 1.5 nT at $|X|<100\ R_E$. In the same region, the preference of the direction of the flow is about the same with a mean of -106 km/s. At $X=-60\ R_E$ the plasma sheet Bz was observed positive (Slavin et al., 1985).

Khurana et al. (1996) applied a simple assumption for distinction of the tail regions based on x- component of the magnetotail magnetic field vector. They assumed that the data from Galileo's Earth 1 flyby between $X= -43\ R_E$ to $-87\ R_E$ is gathered from north lobe if Bx>5nT, from south lobe if Bx<-5nT and from plasma sheet region if -5nT<Bx<5nT. There are number of studies creating their own criteria for distinguishing the mantle, lobe and plasma sheet plasma using its characteristics. Maezawa et al. (1997) differentiate magnetotail lobes by $Vx/V_{SW} < 0.8$ and plasma

sheet by $T>3.10^6$ K. Kaymaz et al. (1999) created the table below, Table 4.1, from IMP 8 observations at -30 R_E. They used magnetotail to solar wind monitor parameter ratios, i.e. IMP 8 plasma parameter value/ISEE3 time lagged parameter value, as well as the plasma density and temperature parameters of the magnetotail from IMP 8 in differentiation of the regions.

Table 4.1 : Magnetotail Region Identification Criteria adopted from Kaymaz et al. (1999).

	Velocity Ratio	Density Ratio	Tail plasma Density	Tail plasma Temperature
Mantle	≤0.6	≤0.7	>0.3	≤800eV
Lobe	-	-	<0.01	-
Plasma Sheet	-	-	-	>2000eV

As the distance from the Earth increases, the dipole effect loses its major effect on the topology and other factors become to play roles in the distant tail. One such effect will be IMF By effect; as one go downstream along the magnetotail, the structure of the magnetic field lines is expected to be more dependent on the IMF By than the near-Earth region. The relationship between the y- component of the IMF and the magnetic field direction in the four quadrants of the magnetotail lobes, i.e. north-dusk, north-dawn, south-dusk and south-dawn is studied. As a first step in our statistical analysis of the Earth's magnetotail at lunar distances, magnetic field vectors are mapped in XY, XZ-, YZ- planes as it is most commonly work out in the past (Kaymaz et al., 1994b). Bx parameter is also used to separate the north and south parts of the magnetotail or as the neutral sheet denominator since it better excludes north and south magnetotail compared to Z- parameter. Thus, addition to three planes XBx- and YBx- plane maps are also provided within the text. Then sector separation analysis is performed by dividing the data set according to IMF direction.

4.1.1 XY plane

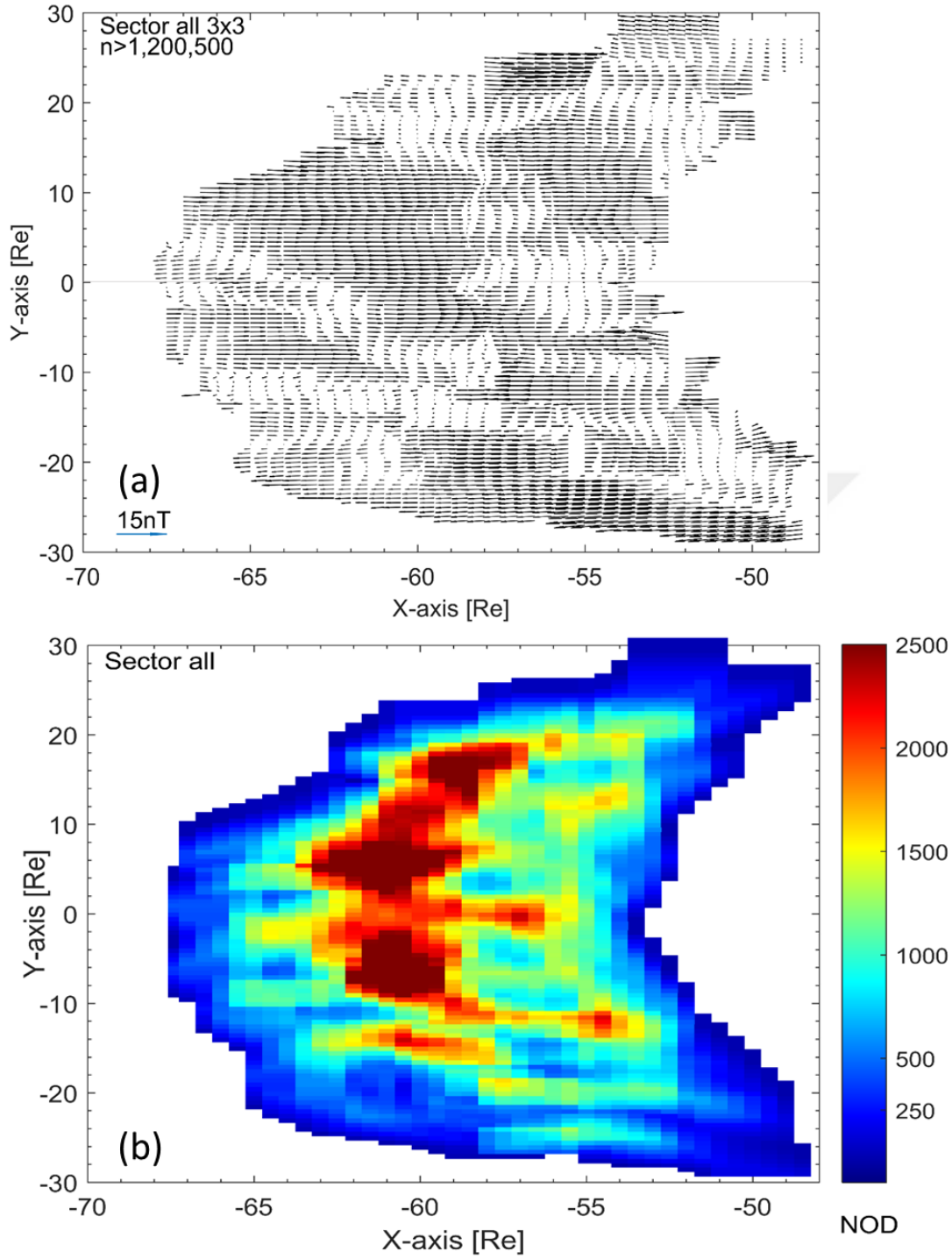

Figure 4.5 : (a) Magnetotail magnetic field projection onto XY- plane for all ARTEMIS observations with $3R_E x 3R_E$ bin size. The meridional cut, Y=0 is set with a gray solid line. (b) The color bar is the number of data points for all available observations in the XY- plane from ARTEMIS probes. The dark red color indicates at least 2500 number of data in that region.

In the Figure 4.5a, the magnetic field vectors are plotted onto XY-plane for all values of Z, i.e. magnetic field observations are gathered from both northern and southern hemispheres. The vectors are calculated by averaging magnetic field values within bins of $3R_E x 3R_E$ size. The meridional cut, Y=0 R_E, where we expected to see the neutral line is plotted with a gray solid line. Vectors are colored either in light, dark gray or in black color corresponding to the number of observations gathered from that area. Additionally, a coverage map is given with a color bar in Figure 4.5b to be able to visualize how much information is collected from that region by ARTEMIS probes. The dark red color indicates the number of data in that bin is more than 2500 minutes, which is a substantial amount of magnetotail information.

Table 4.2 : Statistical values of magnetotail magnetic lines in x- and y- direction.

	Mean Bx [nT]	Mean By [nT]	Max Bx [nT]	Max By [nT]	Min Bx [nT]	Min By [nT]
All	0.2	-0.2	11.0	2.1	-11.5	-2.6
Dawn Y<0	0.6	-0.4	10.6	1.4	-11.5	-2.6
Dusk Y>0	1.1	0.0	11.0	2.1	-9.6	-2.2

The average configuration in the XY plane is such that the magnetic field line distribution in the x-direction is nearly equal (1050 number of data vs 1320 number of data). The reason behind the average Bx value being positive (0.2 nT, as seen in Table 4.2) is due to the higher number of observations from the northern hemisphere, seen in Figure 4.7b.

The magnetic field vectors in the tailward direction is stronger in the dawn section (-11.5 nT) compared to the dusk region (-9.6 nT). The average Bx is 0.6 nT for the dawn region whereas the average Bx is 1.1 nT for dusk region and the average Bx for tailward directed magnetic field vectors is -4.0 nT in dawn and -3.4 nT in the dusk region (not shown in the table).

The magnetic field component in the y- direction is tilted in the dawn direction with the average By being negative (-0.2 nT) due to the higher amount of observations correspond to the negative IMF By sector which causes negative IMF By penetration

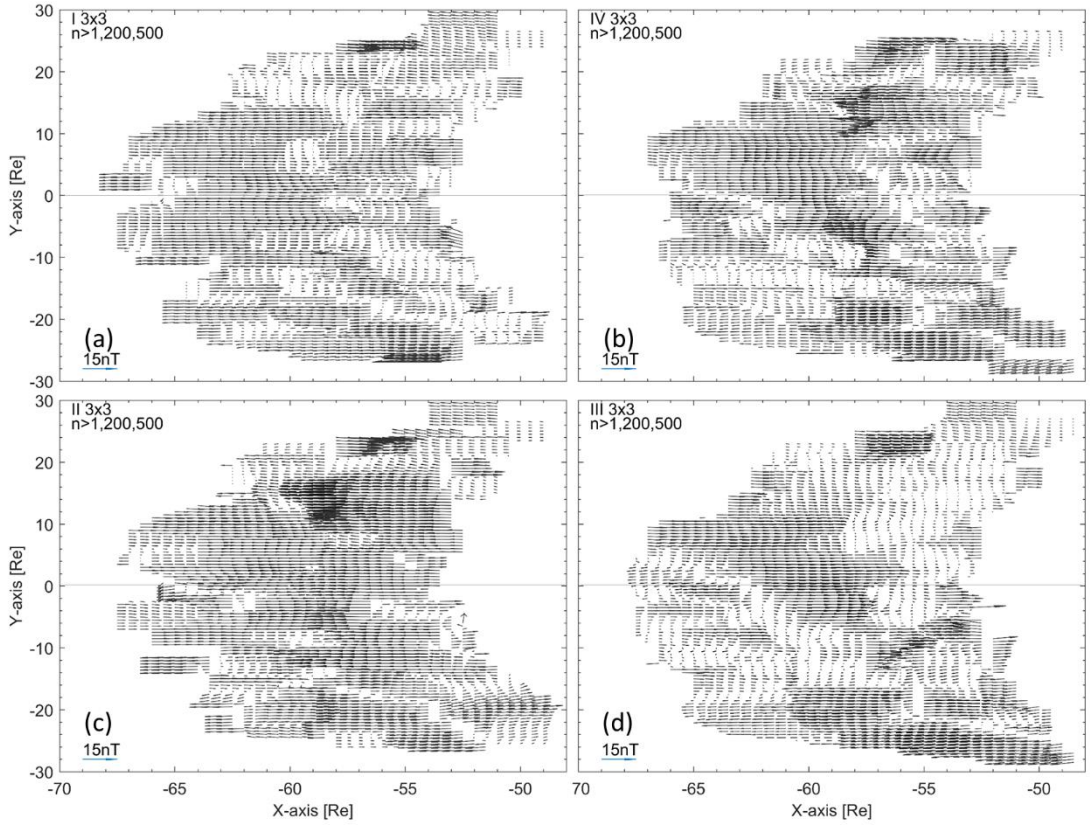

Figure 4.6 : Magnetotail magnetic field vectors in XY plane for (a) northward (+IMF Bz), (b) southward (-IMF Bz), (c) eastward (+IMF By), and (d) westward (-IMF By) sectors.

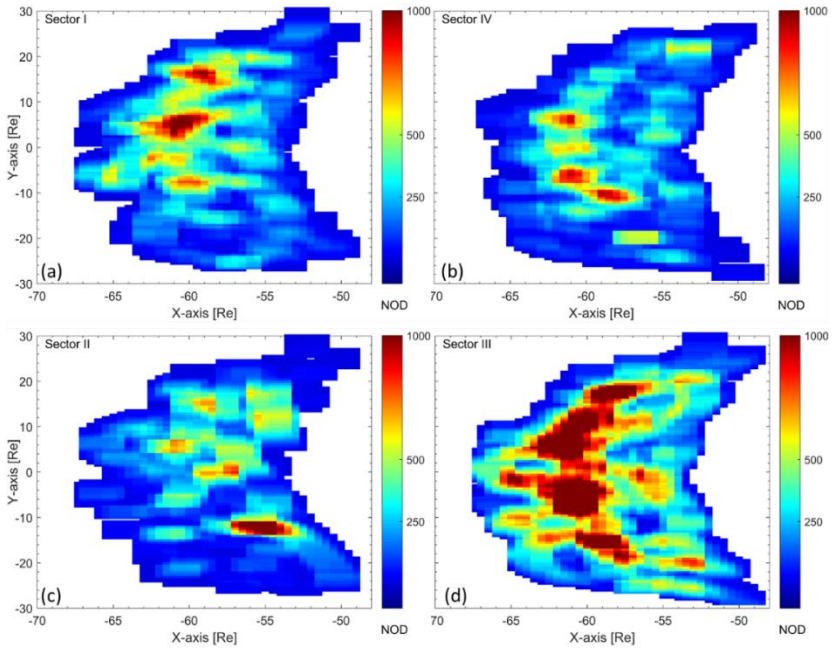

Figure 4.7 : The color scale is for number of data points XY plane for (a) northward (+IMF Bz), (b) southward (-IMF Bz), (c) eastward (+IMF By), and (d) westward (-IMF By) sectors. The dark red color indicates the number of data more than 1000.

into the magnetotail. This influence is more effective in the dawn region of the tail (average By value decrease from 0.0 for dusk region to -0.4 nT for the dawn).

Figure 4.6a and Figure 4.6b shows the magnetic field observations from all Z-values in XY-plane during northern and southern IMF conditions and Figure 4.6c and Figure 4.6d shows the positive and negative IMF By conditions with the same bin size. In addition, the color maps in the Figure 4.7 gives the number of magnetotail encounters from the ARTEMIS probes for each sector case. The distribution of the observations are more or less evenly distributed for northward and southward sectors with densely visited regions lie within the dawn-dusk direction of ±20 R_E at about X=-55 R_E to -65 R_E. The eastward IMF (-IMF By) dominancy is valid throughout this study, as it can be seen from the Figure 4.7d.

From these figures and the Table 4.3, below, we can see that the x-component of the magnetic field vector is larger in either direction, earthward and/or tailward for southward IMF case as expected from the reconnection theory. For northward IMF case, the magnetic field values are smaller and distributed more evenly in the dusk and dawn regions.

Table 4.3 : Statistical values of magnetotail magnetic field lines in the x- direction for north-south IMFs.

	+ IMF Bz Sector			+ IMF Bz Sector		
	Mean Bx [nT]	Max Bx [nT]	Min Bx [nT]	Mean Bx [nT]	Max Bx [nT]	Min Bx [nT]
Dawn Y<0	4.8	7.9	1.2	0.6	10.1	-8.7
Dusk Y>0	3.1	8.6	-5.7	8.3	10.4	-1.5

The IMF By effect is observed such that the averages of magnetic field data in y-direction is positive for positive IMF By sector and negative for negative IMF By sector independent of the y-value. Table 4.4 gives the statistical values of magnetotail magnetic field lines in y- direction for the equatorial IMFs, positive and negative IMF By. The strongest magnetic field value in y direction is observed as 2.7 nT in the dusk side while the strongest in the reverse direction, -2.7 nT, is encountered in the dawn

region. However, in order to draw some detailed conclusions, we should investigate the magnetotail observations separately for northern and southern hemispheres.

Table 4.4 : Statistical values of magnetotail magnetic field lines in y- direction for equatorial IMFs.

	+ IMF By Sector			- IMF By Sector		
	Mean By [nT]	Max By [nT]	Min By [nT]	Mean By [nT]	Max By [nT]	Min By [nT]
Dawn Y<0	0.3	0.8	-0.1	-0.6	1.0	-2.7
Dusk Y>0	0.9	2.7	-0.1	-0.6	1.3	-2.0

4.1.1.1 Bx positive

The use of x- component of the magnetic field vector as a separation for north and south hemispheres is a known technique (Khurana et al.,1996). By doing so, we can expect to see the magnetic field lines directed in the earthward direction in the northern hemisphere and tailward direction in the southern hemisphere.

Figure 4.8a shows the magnetic field line vectors for the northern part of the tail and Figure 4.8b shows the how much data is collected by ARTEMIS probes that meet the conditions mentioned. The region between X=-52 R_E and X= -66 R_E is covered with substantial amount of magnetotail observations. In dawn-dusk territory, in spite of the fact that the tail dimensions reach near to Y=±30 R_E, the region in between Y=±20 R_E is the region where we can draw conclusions for average tail.

In the northern part of the magnetotail in XY-plane, the toward vectors are seen with an average of about 4 nT in the x-direction. The vectors adjacent to the magnetopause boundary are weaker in x- but more tilted in y- direction than in the interior regions since near boundary regions are more prone to IMF By effects.

After separating the observations using IMF sector separation, seen in Figure 4.9, northward and southward IMF conditions are given in (a) and (b) whereas positive and negative IMF By conditions are given in (c) and (d). The average magnetotail By gets the IMF By sign (-0.1 nT for all data in the northern part, +0.2nT for +IMF By sector, and -0.4nT for –IMF By sector). For north tail, we expect +IMF By penetration from the dawn region and –IMF By penetration from the dusk.

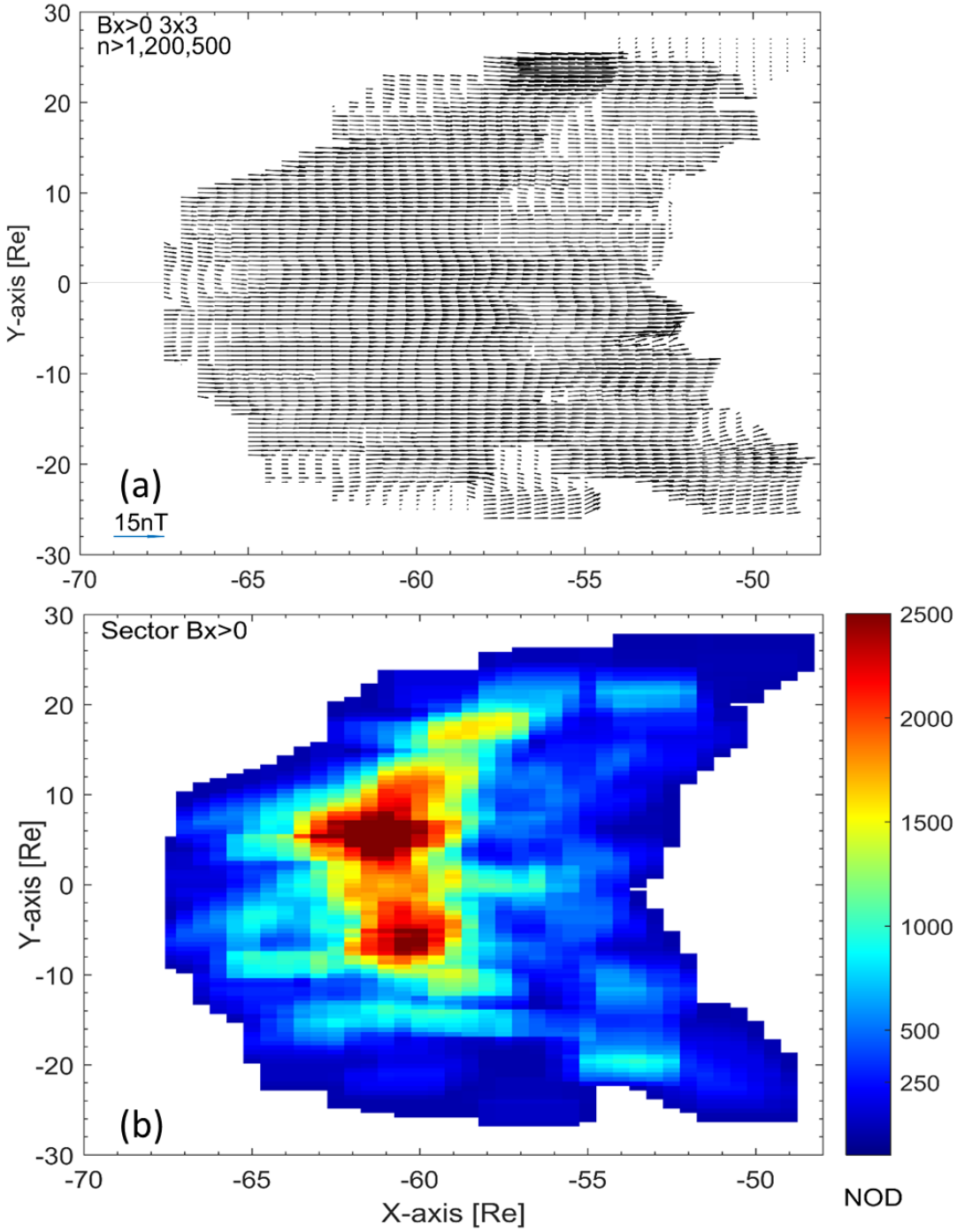

Figure 4.8 : Magnetotail magnetic field line vectors in XY- plane (a) for northern part of the tail with $3R_E x 3R_E$ bin size. Bins with measurements less than 500 are plotted in gray tones. The meridional cut, Y=0 is set with a gray solid line. The color bar (b) is the number of magnetic field observation data points from ARTEMIS probes at lunar distances in XY-plane. The dark red color indicates the number of data more than 2500.

In Figure 4.9c, at about X=-52 R_E and Y=-18R_E in the dawn region, the magnetic field vectors get +y component due to the intrusion region of the magnetosheath plasma. In

Figure 4.9d, the magnetotail magnetic field vectors in the dusk region behind the X=-65R_E has more -By value than the other regions.

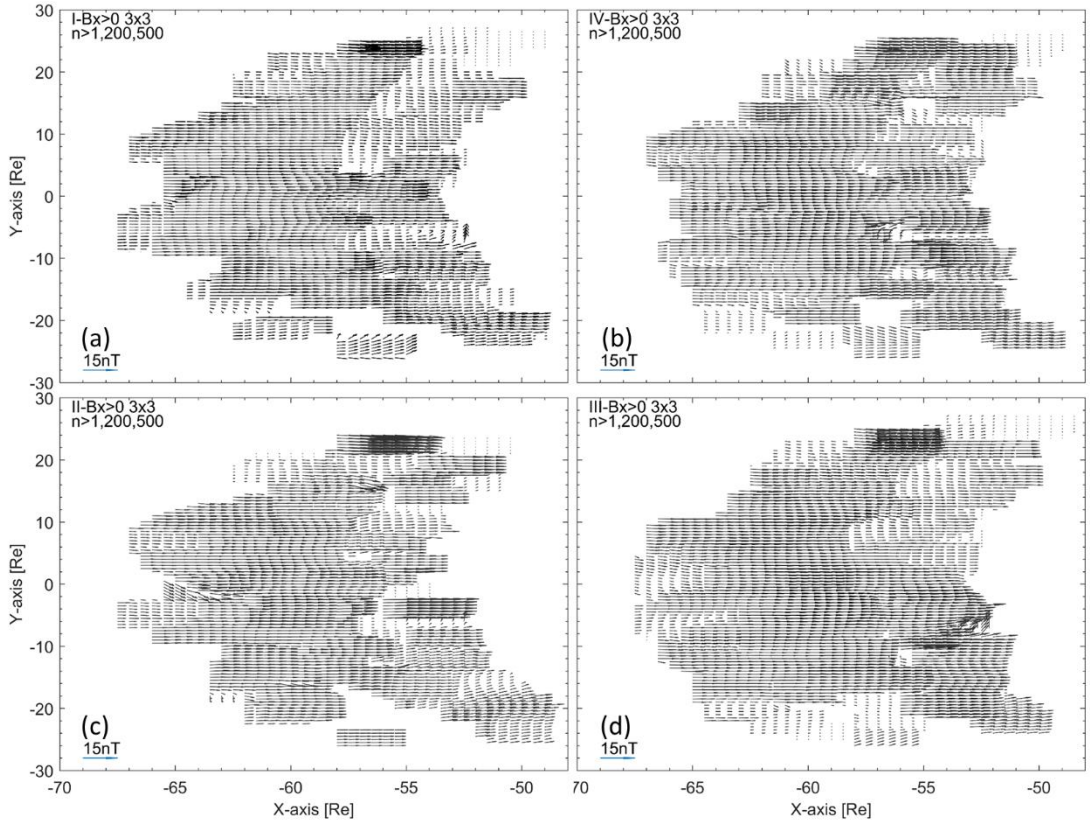

Figure 4.9 : Magnetotail magnetic field vectors in northern part of the tail in XY plane for (a) northward (+IMF Bz), (b) southward (-IMF Bz), (c) eastward (+IMF By), and (d) westward (-IMF By) sectors.

In addition, the IMF Bz effect can be seen when Figure 4.9a and Figure 4.9b is compared. The magnetic field vector sizes increase during the dayside reconnection case, i.e. –IMF Bz, southern sector. Moreover, the distribution of the sizes of the magnetic field vectors are more scattered during northward IMF condition. The color scale plot, Figure 4.10, is given immediately after sector separation plot as in each magnetotail magnetic field; plasma vector or IMF separated versions of these plots. For the northern part, in the XY plane the observations during northern and southern IMF conditions are about the same, Figure 4.10a and Figure 4.10b whereas the –IMF By sector is dominant in every case, Figure 4.10d.

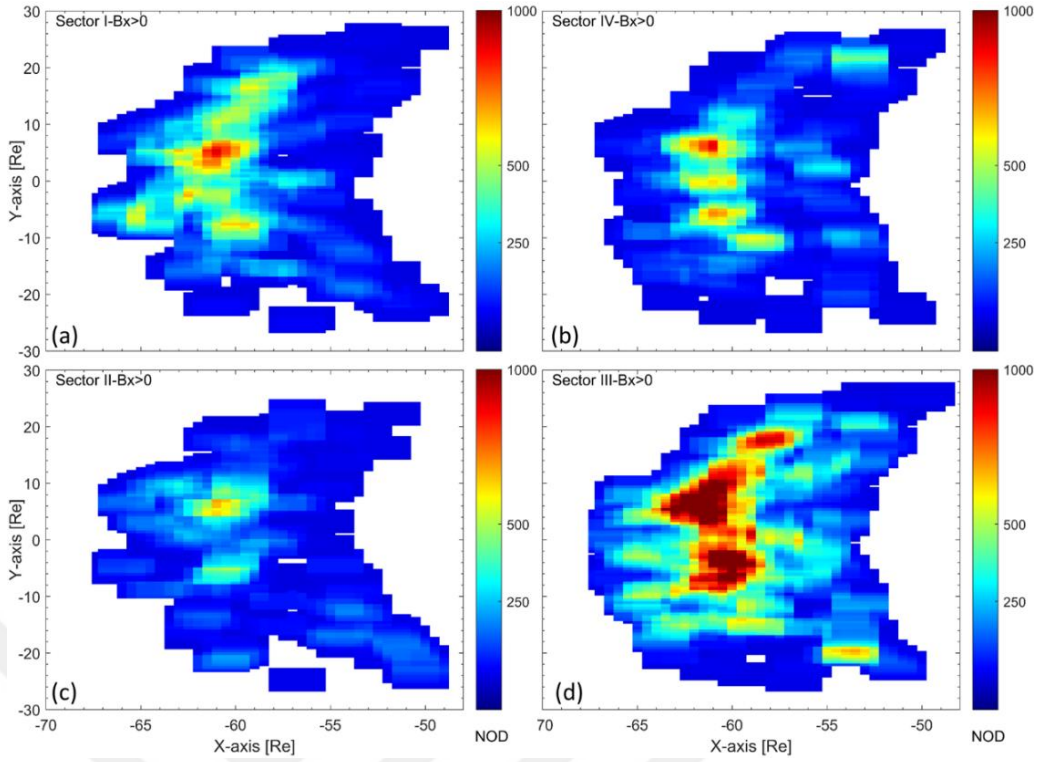

Figure 4.10 : The color scale is for the number of data points in XY plane for the northern part of the tail for (a) northward (+IMF Bz), (b) southward (-IMF Bz), (c) eastward (+IMF By), and (d) westward (-IMF By) sectors. The dark red color indicates the number of data more than 1000.

4.1.1.2 Bx negative

Magnetotail magnetic field vectors in the XY- plane for the southern part of the tail is given in Figure 4.11a using $3R_E x 3R_E$ bin sizes to evaluate the moving averages. The color bar limit in the Figure 4.11b is same as in the northern part of the tail as well as the all observations case in Figure 4.5b. These plots indicate that there are more observations gathered in the northern part of the magnetotail than the southern part when using Bx as a separator of the regions.

Nonetheless, all vectors are directed tailward as expected. The average of the x-components of the away vectors are about -8 nT with a maximum of 20 nT absolute value.

After sector separation, not only the magnitudes of the magnetic field observations but also the y-components are increased for the dusk region for positive IMF By and dawn region for negative IMF By (see Figure 4.12c and Figure 4.12d). The color maps are given in Figure 4.13 and alphabetized for the corresponding IMF condition.

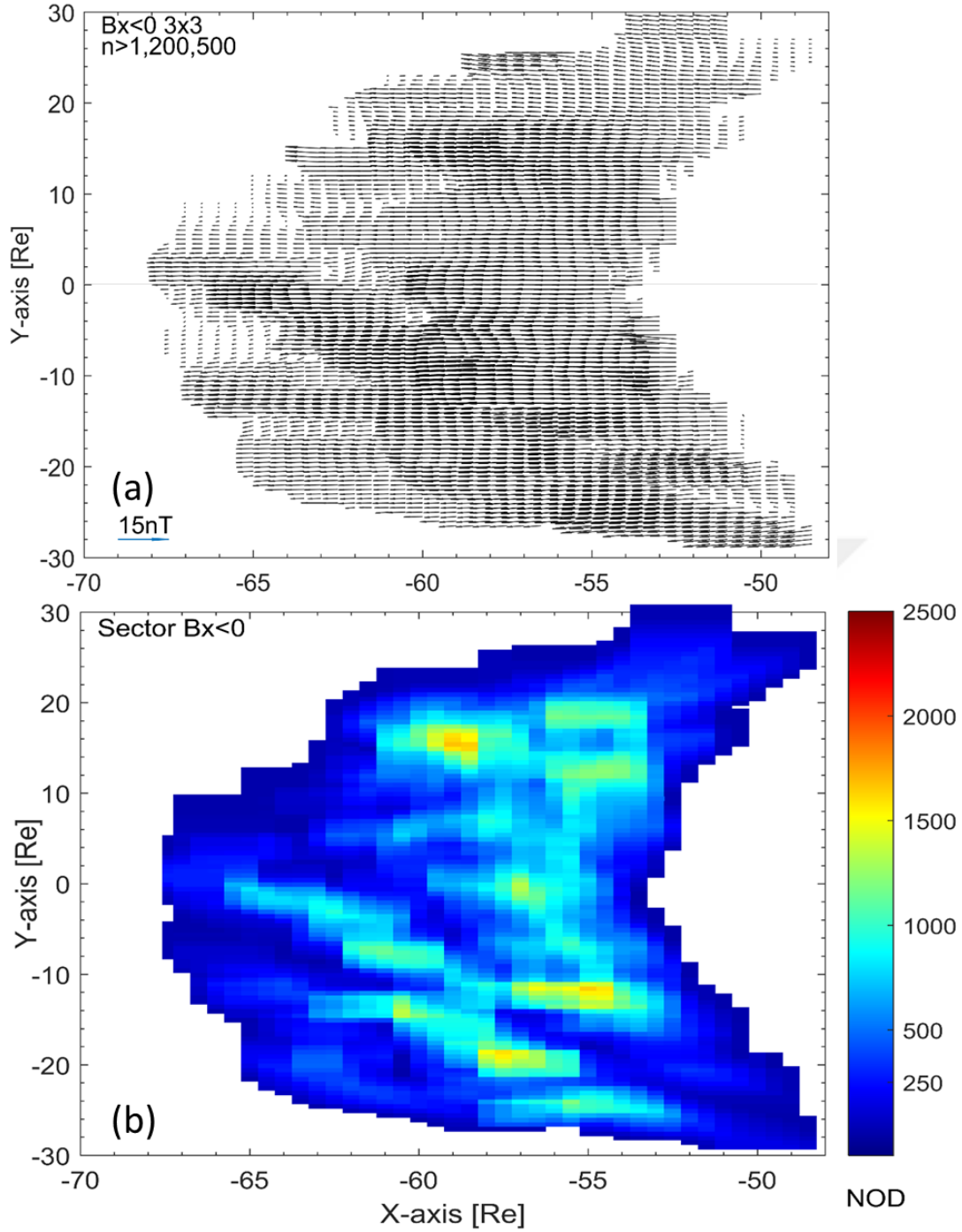

Figure 4.11 : Magnetotail magnetic field line vectors in XY- plane (a) for southern part of the tail with $3R_E x 3R_E$ bin size. Bins with measurements less than 500 are plotted in gray tones. The meridional cut, Y=0 is set with a gray solid line. The color bar (b) is the number of magnetic field observation data points from ARTEMIS probes at lunar distances in XY-plane. The dark red color indicates the number of data more than 2500.

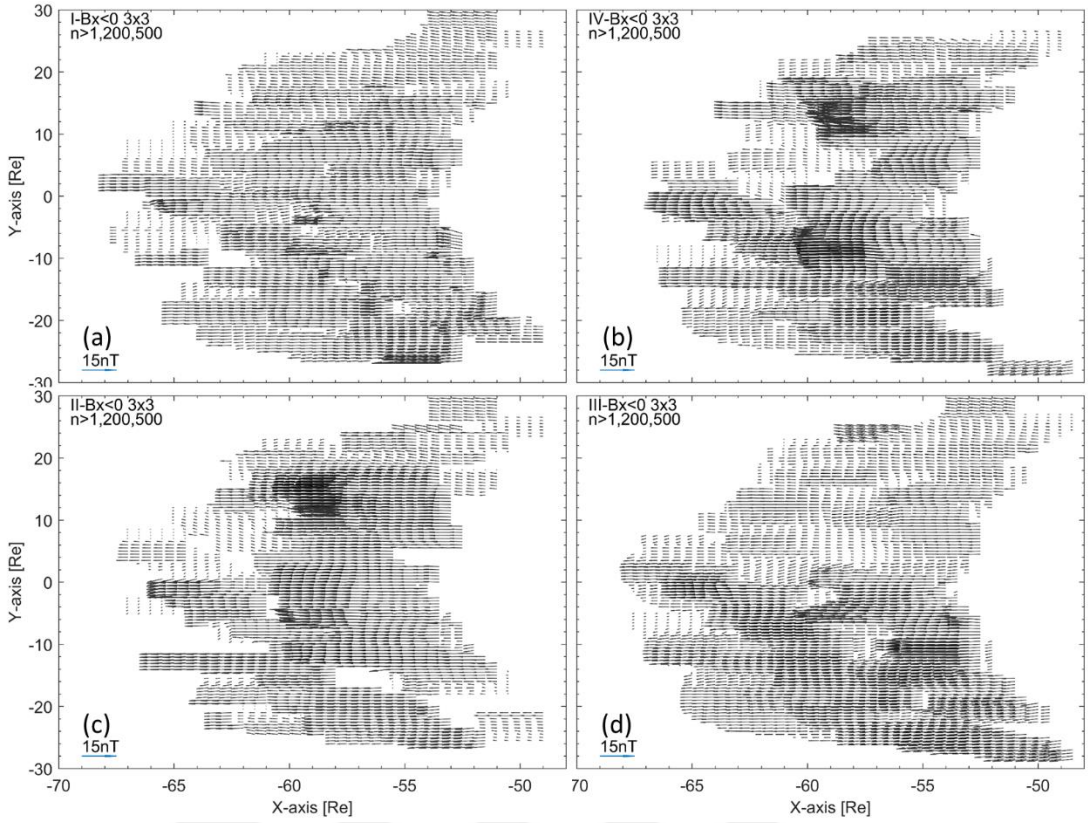

Figure 4.12 : Magnetotail magnetic field vectors in southern part of the tail in XY plane for (a) northward (+IMF Bz), (b) southward (-IMF Bz), (c) eastward (+IMF By), and (d) westward (-IMF By) sectors.

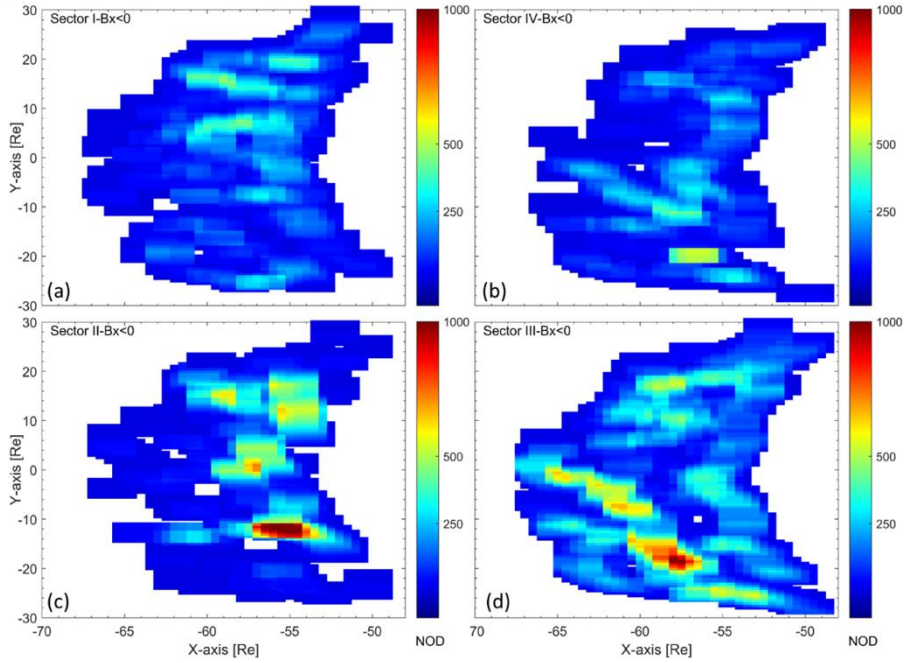

Figure 4.13 : The color scale is for the number of data points in XY plane for the southern part of the tail for (a) northward (+IMF Bz), (b) southward (-IMF Bz), (c) eastward (+IMF By), and (d) westward (-IMF By) sectors. The dark red color indicates the number of data more than 1000.

4.1.2 XZ plane

In the XZ- plane, the magnetic field lines at nightside region are stretched in the x-axis and directed earthward in the northern and tailward in the southern part of the magnetotail, as can be seen in Figure 1.5a. Figure 4.14a shows the averaged magnetic field vectors using a $3R_E x 3R_E$ bin size. All data is plotted onto XZ-plane while the bins that has less than 500 observations are plotted in gray color. The equatorial cut, Z=0 is set with a gray solid line. The current sheet region can be seen as the reversal of the magnetic field line direction. The observations show that the current sheet is not fully aligned with the Earth-Sun direction. The current sheet, sandwiched inside the neutral sheet region between the $\pm 7R_E$ across the Z-axis is seen to be on the move.

The stretched dipolar field lines in the XZ-plane have an average value of 8nT ($|Bx|_{ave}$). This value is very close to the average magnetic field value of 7 nT stated in the study by Behannon and Ness (1968) based on Explorer 33 findings at $X= -80R_E$. While the maximum Bx of 11.1 nT is observed in the northern tail, the minimum Bx of -16.2 nT is observed in the southern tail.

The diamagnetic effect observed by the even very early studies such as Meng and Mihalov (1972) can be observed by ARTEMIS measurements. The authors and the other studies on the diamagnetism at distant tail, e.g. Slavin et al, 1983; Tsurutani et al., 1984, showed that the average magnetic field is about 7 nT in the lobe region, and decreases in the plasma sheet. Here in this study, the average magnetic field vector in the x-direction is smaller in the plasma sheet region as seen in previous works, i.e. about 4nT at $|Z|<7R_E$, than the regions outside the plasma sheet (for $|Z|>7R_E$, average Bx= ~8nT).

The lack of data seen in Figure 4.14b as the little white bin in the middle of darkest blue region where $X=-56R_E$ meet the $Z=11R_E$. This gap creates a turbulent like instability feature in the B vector map at the same region. Other than that, the magnetic field vectors are uniformly distributed in the magnetotail.

Bx parameter is also used to separate the north and south parts of the magnetotail or as the neutral sheet denominator since it better excludes north and south magnetotail compared to Z- parameter. Thus, XZ- plane is also investigated using Bx instead of Z-

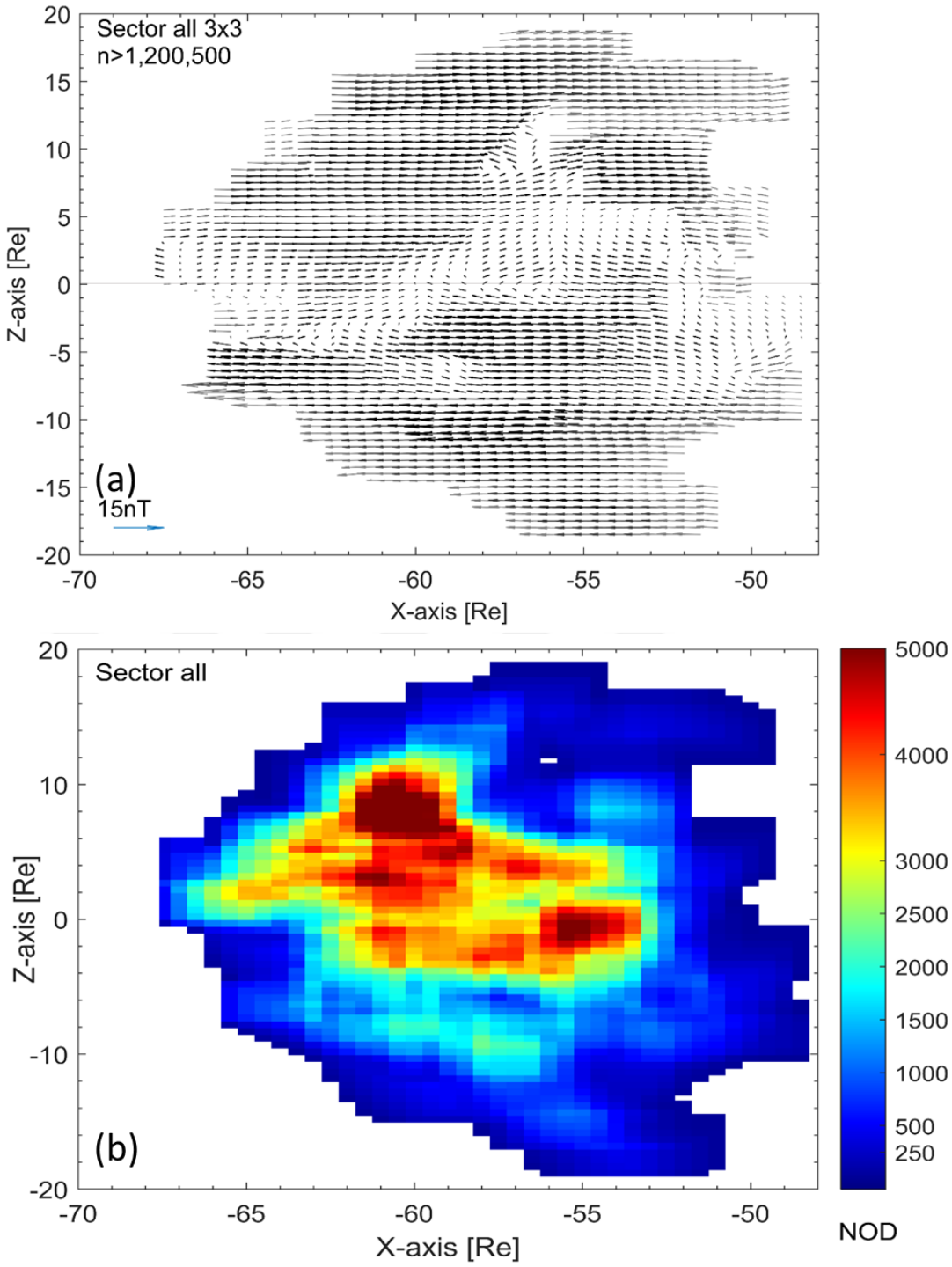

Figure 4.14 : (a) Magnetotail magnetic field line vector projection onto XZ- plane for all ARTEMIS observations with $3R_E x 3R_E$ bin size. Bins with measurements less than 500 are plotted in gray tones. The equatorial cut, Z=0 is set with a gray solid line. (b) The color bar is the number of magnetic field observation data points from ARTEMIS probes at lunar distances in XZ-plane. The dark red color indicates the number of data more than 5000.

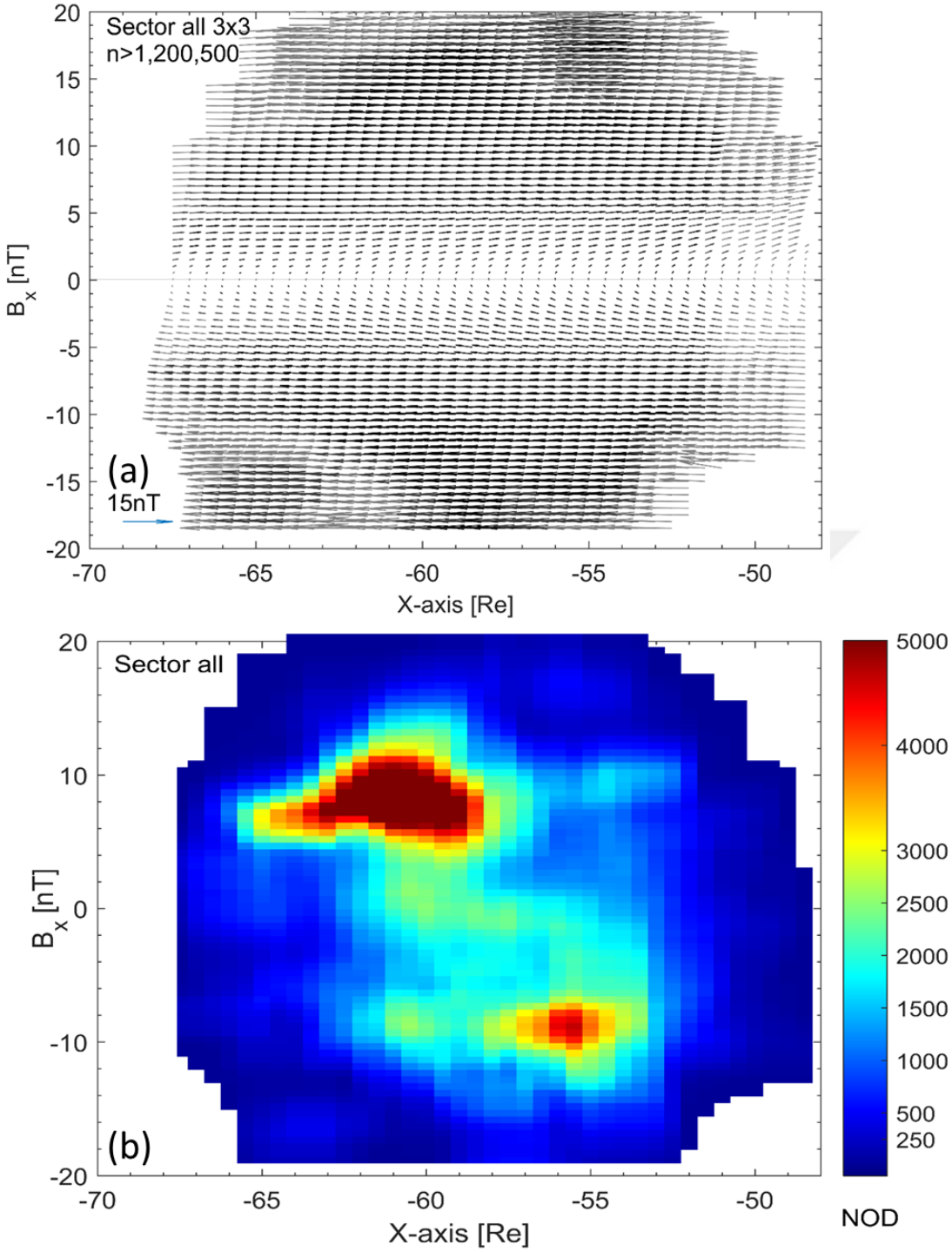

Figure 4.15 : (a) Magnetotail magnetic field line vector projection onto XBx- plane for all ARTEMIS observations with $3R_E$x$3R_E$ bin size. Bins with measurements less than 500 are plotted in gray tones. The estimated neutral sheet position where Bx=0 nT is set with a gray solid line and is only used for position purposes, Bx and Bz components are plotted onto XBx coordinates. (b) The color bar is the number of magnetic field observation points from ARTEMIS probes at lunar distances in XBx-plane. The dark red color indicates the number of data more than 5000.

value in the Figure 4.15. The magnetotail field vectors in the XBx- plane are in order consisting of two lobes with higher magnetic field vectors separated by a diamagnetized plasma sheet in which the magnetic field magnitudes decrease and embedded neutral sheet where the field lines change sign. Usage of Bx, sort the observations such that the dynamic neutral sheet region seems now to be aligned with the x-axis. The coverage map in Figure 4.15b is different from the Figure 4.14b since the Bx value is used as the hemisphere separation. Most of the Bx is populated around the positive and negative 10 nT region.

To investigate the effect of IMF direction on the XZ-plane, the magnetic field line observations split into categories in according to the interplanetary magnetic field direction as seen in Figure 4.16. One of the main motivation in sector separation is to look for thick, cold and dense plasma sheet during northward IMF condition as mentioned in previous studies, e.g. Nishida et al., 2000. The number of observations gathered especially from the expected plasma sheet region is more than enough to draw conclusions from as seen in Figure 4.17.

The increase in the thickness of the plasma sheet is observed for northward IMF case such that the magnetotail magnetic field lines get a vertical component nearly equal to the x-component. The average value of |Bz| is 2.8 nT for the northward IMF condition while for southward IMF the |Bz| average is 1.1 nT. In addition, during southward IMF condition the magnetic field lines stretched in the x-direction (Nishida et al., 2000; Petrukovich et al., 2003). The average value of the |Bx| is about 15 nT for southward IMF whereas for northward IMF case is |Bx| average is 0.2 nT. Thus, we not only see expansion in the plasma sheet region during northward IMF but also we observe the stretching of the magnetotail magnetic field lines as previous theoretical and observational studies do.

The same sector separation in the XZ- plane, in the Figure 4.16, applied to the XBx-plane and plotted in Figure 4.18. Bins with measurements less than 500 are plotted in gray tones. If one concentrate on the black lines vectors only, which has at least 500 observations from that region, one can see that the tail itself is enlarged during southward IMF case when compared to northward IMF case. The color map for the same plane is attached below in Figure 4.19.

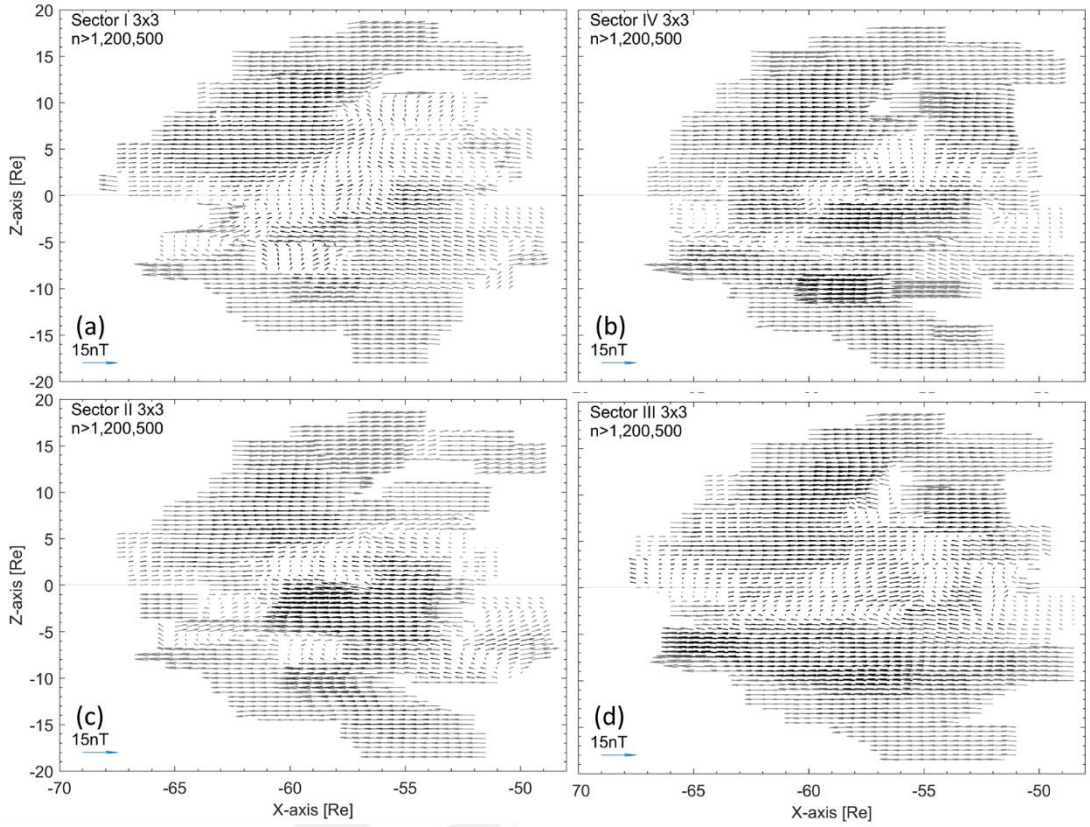

Figure 4.16 : Magnetotail magnetic field line vectors in XZ- plane for (a) northward (+IMF Bz), (b) southward (-IMF Bz), (c) eastward (+IMF By), and (d) westward (-IMF By) sectors.

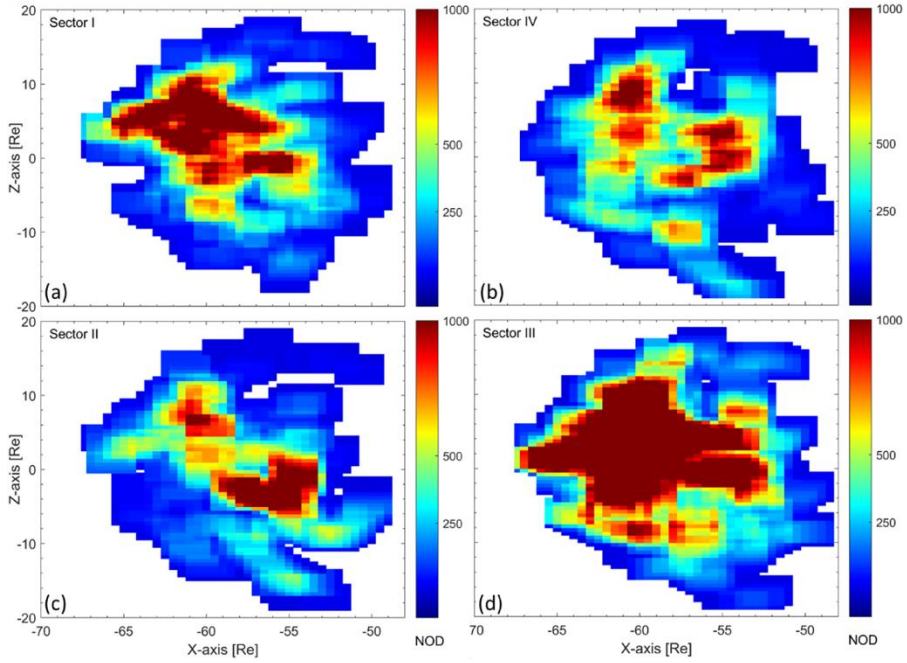

Figure 4.17 : The color scale is for number of data points in XZ- plane magnetic field line vectors for (a) northward (+IMF Bz), (b) southward (-IMF Bz), (c) eastward (+IMF By), and (d) westward (-IMF By) sectors. The dark red color indicates the number of data more than 1000.

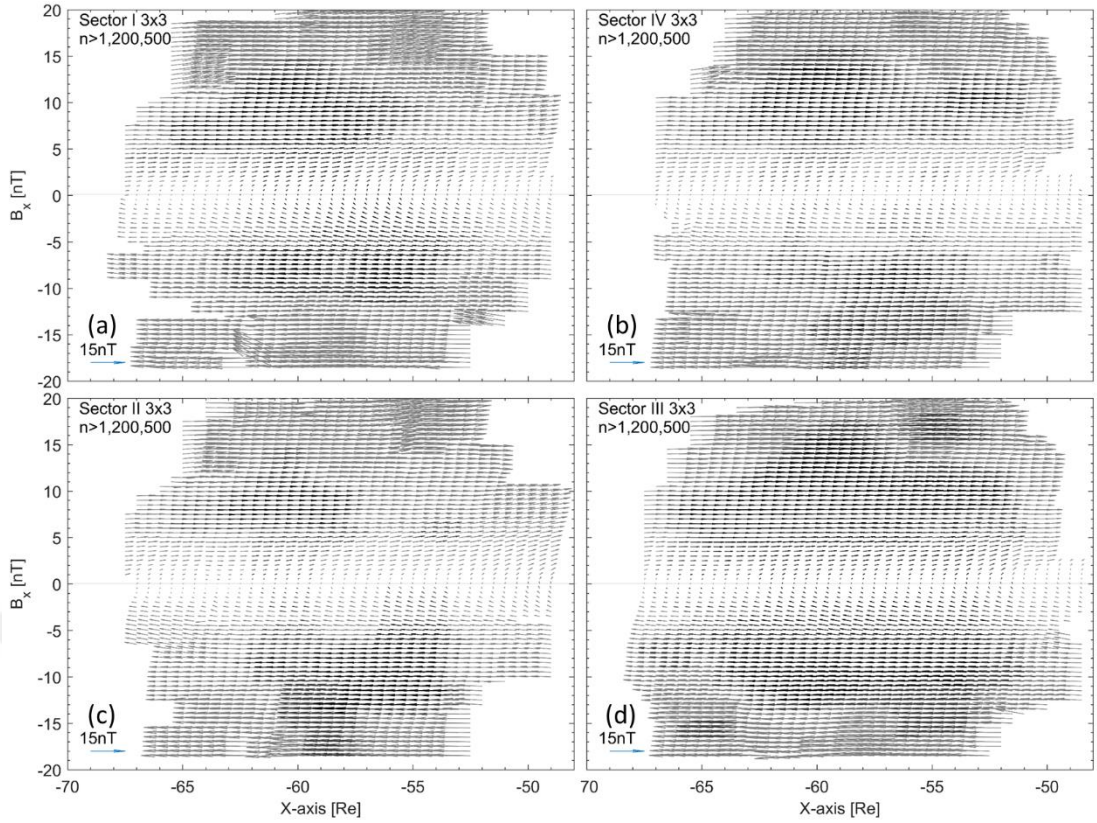

Figure 4.18 : Magnetotail magnetic field line vectors in XBx- plane for (a) northward (+IMF Bz), (b) southward (-IMF Bz), (c) eastward (+IMF By), and (d) westward (-IMF By) sectors.

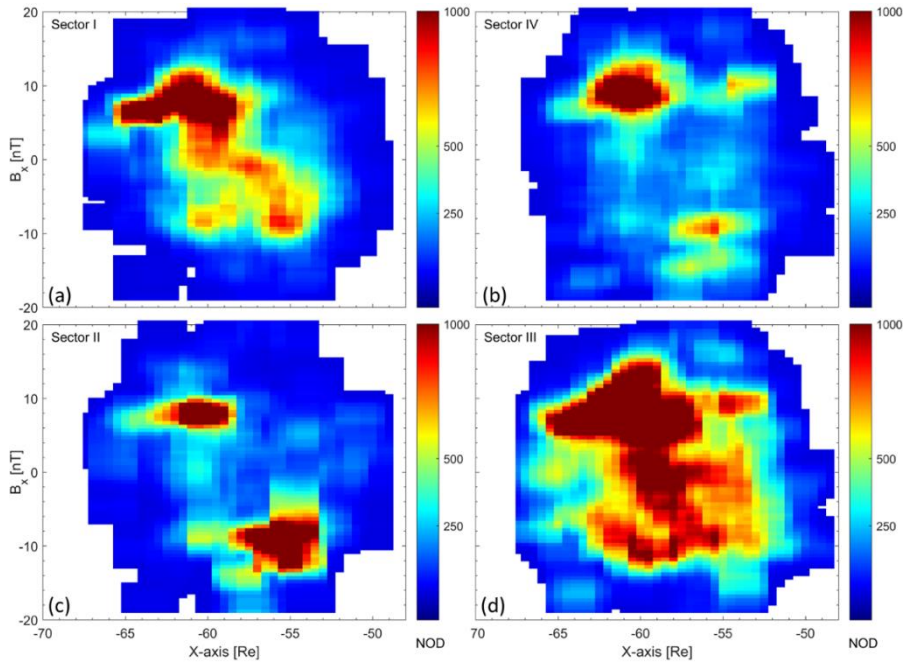

Figure 4.19 : The color scale is for number of data points in XBx- plane magnetic field line vectors for (a) northward (+IMF Bz), (b) southward (-IMF Bz), (c) eastward (+IMF By), and (d) westward (-IMF By) sectors. The dark red color indicates the number of data more than 1000.

4.1.3 YZ plane

In the plane perpendicular to Earth-Sun line, the average configuration of the magnetotail magnetic field line vectors at -33R_E is studied by Kaymaz et al. (1994a) using 16 years of IMP-8 observations. Their Figure 3 shows that the dipole effect is very dominant at half Moon distance with two nodes, located at ±9 R_E in north-south direction and the magnetic field lines merging and flaring out to and from north and south nodes, respectively. When there is a negative interplanetary By component acting on the magnetotail, the authors showed that the nodes which were aligned with Z=0, skewed about 2 R_E.

The ARTEMIS magnetic field vector projections onto YZ-plane is seen in Figure 4.20a and the collected observations can be seen in Figure 4.20b as a color map. First of all, the general pattern is not fully covered due to about 2-years of information whereas the referenced study by Kaymaz et al. used 16 years of spacecraft information. However above all, ARTEMIS trajectory has a low inclination orbit which creates the gap at |Z|>15 R_E. The observations are not evenly distributed with higher amount of time spent in the duskward of the plasma sheet. Nevertheless, it does show the dipolar effect especially in the dusk region. The general pattern seems to be distorted at about Y=-13R_E and Z=+5R_E due to limited information gathered from that region as seen in Figure 4.20b and the change of the direction of the magnetic field vectors before and after that bin creates such a form. Besides that, the curl like configuration at about Y=-8R_E and Z=-10R_E is due to one crossing when happens on March 2012 during a 52nd biggest CME eruption in history at that time.

The average IMF conditions with Bx= -1.7 nT, By=-1.1 nT and Bz= 0.1 nT, the inputs nearly create a Parker spiral model in which Bx=By and Bz~0 nT. Since the penetration of the negative IMF By would be through patchy magnetopause boundary, the near flank region is expected to be affected more than the interior plasma sheet region. The average By within the plasma sheet (within |Z|<7R_E) is negative, -0.3 nT, due to the –IMF By control on the tail. However, the effect is more significant near the lobes, |Z|>7R_E. The average magnetotail By is more than -1.0 nT for |Z|>7R_E. On the other hand, we expected to see strong vertical magnetic field vectors directed from south node to north from the reference study and we see the Bz components in the same direction. The average Bz decreases from +1.2 nT to +0.5 nT from plasma sheet region to near flanks.

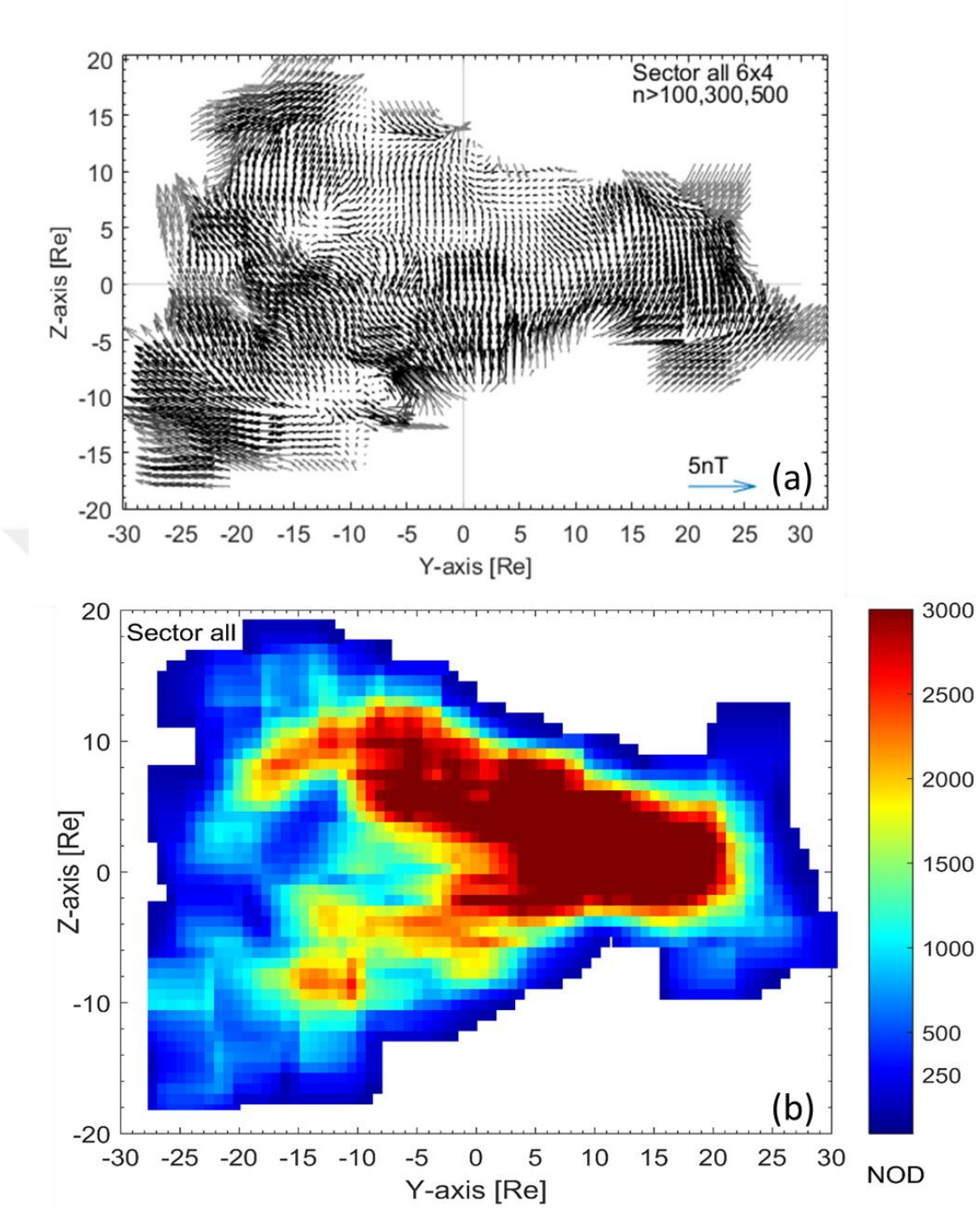

Figure 4.20 : (a) Magnetotail magnetic filed line vector projection onto YZ- plane for all ARTEMIS observations with $6R_E x 4R_E$ bin size. Bins with measurements less than 500 and higher than 100 number of data points are plotted in gray tones. Y=0 and Z=0 is set with a gray solid line. (b) The color bar is the number of data points for all available magnetic field observations from ARTEMIS probes at lunar distances in YZ-plane. The dark red color indicates the number of data more than 3000.

When the same By and Bz vectors in the figure above, are plotted onto YBx- plane, Figure 4.21, the general pattern is seen to be more evenly distributed. The dominancy

of negative IMF By effect is clear again especially in the preferred quadrants, i.e. north-dusk and south-dawn regions.

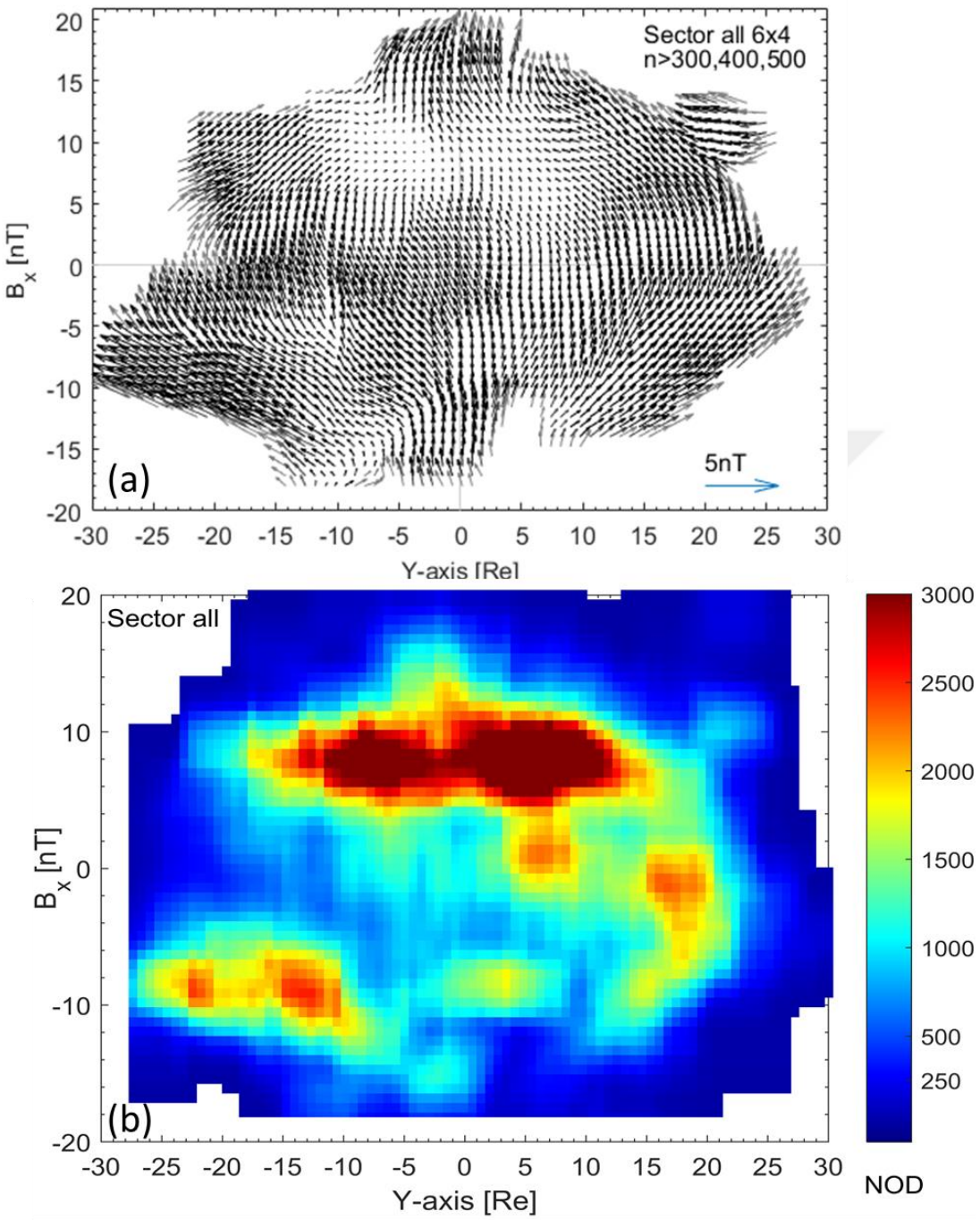

Figure 4.21 : (a) Magnetotail magnetic filed line vector projection onto YBx- plane for all ARTEMIS observations with $6R_E x 4R_E$ bin size. Bins with measurements less than 500 and higher than 300 number of data points are plotted in gray tones. Y=0 and Bx=0 is set with a gray solid line. (b) The color bar is the number of data points for all available magnetic field observations from ARTEMIS probes at lunar distances in YBx-plane. The dark red color indicates the number of data more than 3000.

When we separate the measurements for corresponding IMF sectors, the magnetotail magnetic field lines in the cross-sectional plane is given in Figure 4.22. Figure 4.23 shows that for all sectors the dusk region is mapped fuller than the dawn region as well as the region between the $Z=\pm 10R_E$. For northward IMF, the stronger Bz vectors are observed which corresponds to plasma sheet. In the dusk region, the thickened plasma sheet due to northward IMF condition is encountered while expanding towards the flanks. The magnetotail at -60 R_E is bigger in size during periods of southward IMF orientation due to expansion of the tail after dayside reconnection compared to smaller tail with more dipolar signatures during northward IMF as estimated from the theory. The pattern seems to be patchier for –IMF Bz which might be due to passages of temporal events, i.e. plasmoid or flux rope like structures. Besides, March 2012 event is observed during southward IMF at about Y=-7 R_E and Z=-10 R_E.

When equatorial IMF cases are compared, the positive IMF By effect can be observed in the favored regions, i.e. north-dawn and south-dusk. When dusk regions are compared from Figure 4.22c and Figure 4.22d, positive By is dominant in south for +IMF By sector and in north for –IMF By sector as expected. Besides, the south-dawn region is also mapped where –IMF By penetration is expected to be most effective. In Figure 4.22d, the average By distribution shows the increased diffusion of negative IMF By in the preferred quadrants; -1.5 nT in south-dawn, -0.6 nT in north-dusk compared to -0.5 nT and -0.1 nT in south-dusk and north-dawn parts of the tail, respectively. And the average By distributions for each quadrant of the tail is as follows for the positive IMF By; +1.2 nT and +0.7 nT in the south-dusk and north-dawn, and +0.2nT and +0.4 nT in the south-dawn and north-dusk. One can see that the IMF By effect can be observed in all quadrants as the magnetotail magnetic field having the same sign of the interplanetary magnetic field in all four quadrants with more emphasized effect in the preferred regions even at lunar distances.

The ARTEMIS observations are separated for corresponding IMF sectors using Bx instead of Z in Figure 4.24. Dipolar structure with smaller, closed magnetotail can be seen in northward IMF whereas bigger tail with patchy pattern is observed during southward IMF. The equatorial IMF effect is evident in the expected quadrants. The corresponding coverage map is presented in Figure 4.25.

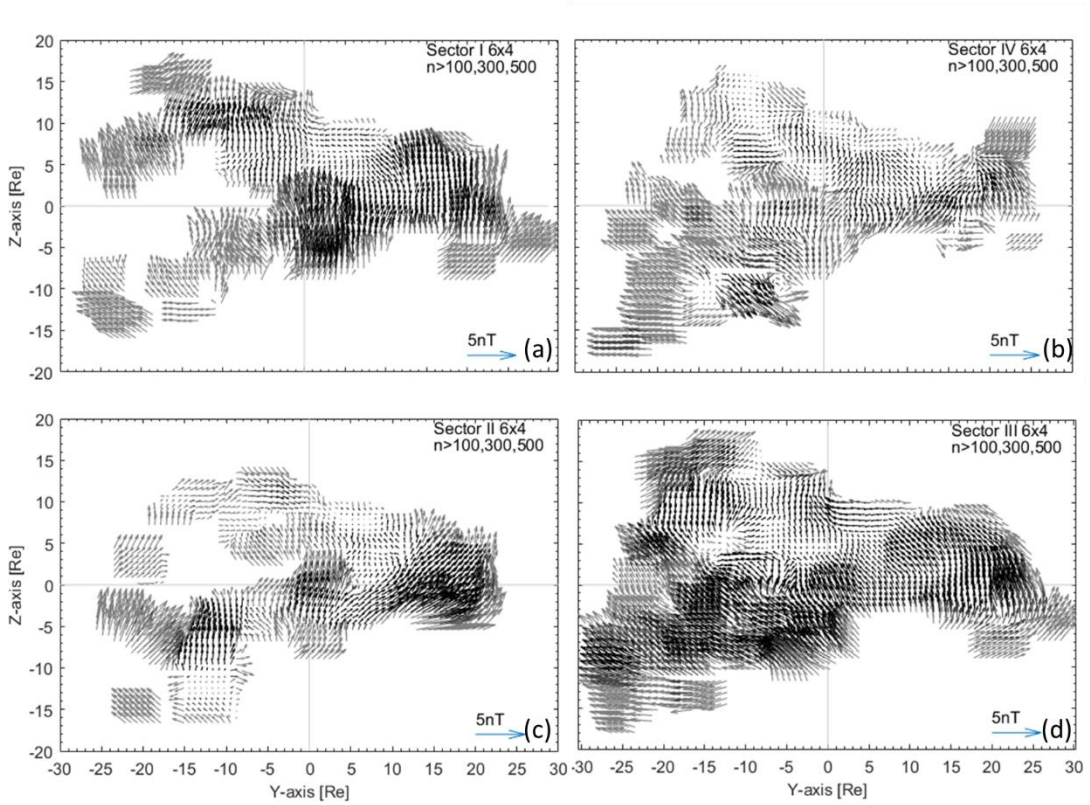

Figure 4.22 : Magnetotail magnetic field line vectors in YZ- plane with 6 R_E x4 R_E bins for (a) northward (+IMF Bz), (b) southward (-IMF Bz), (d) eastward (+IMF By), and (d) westward (-IMF By) sectors.

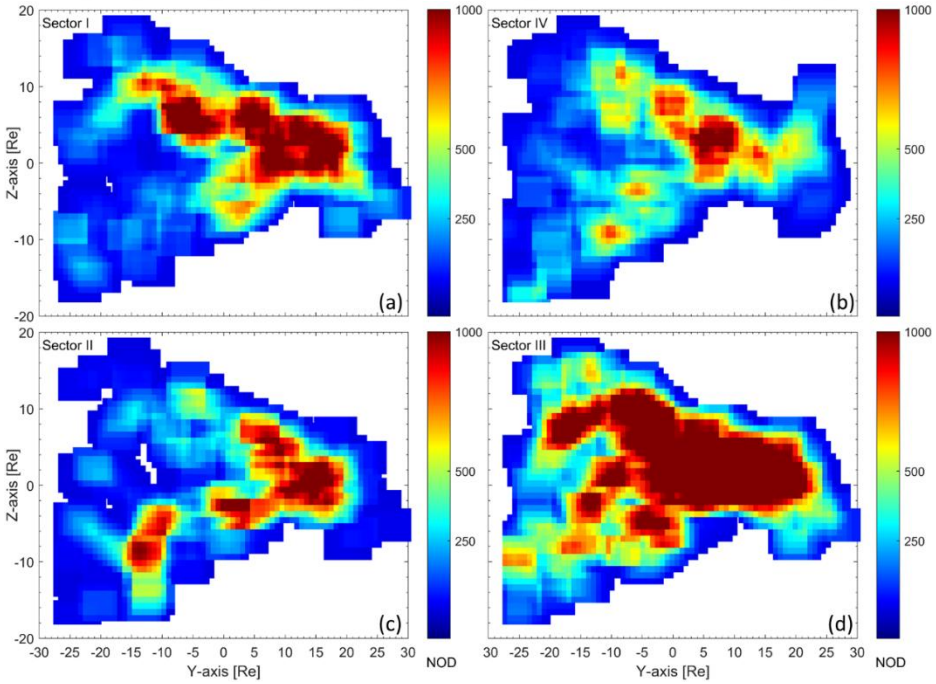

Figure 4.23 : The color scale is for number of data points in YZ- plane magnetic field line vectors for (a) northward (+IMF Bz), (b) southward (-IMF Bz), (c) eastward (+IMF By), and (d) westward (-IMF By) sectors. The dark red color indicates the number of data more than 1000.

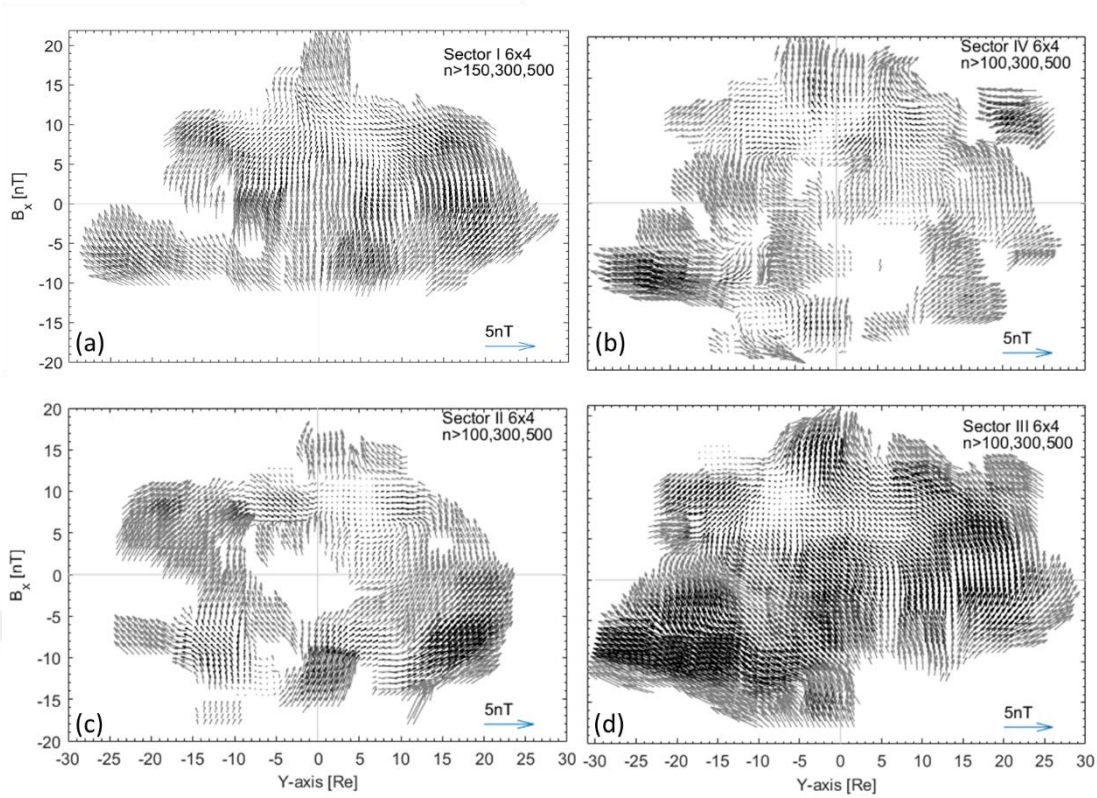

Figure 4.24 : Magnetotail magnetic field line vectors in YBx- plane with 6 R_E x4 R_E bins for (a) northward (+IMF Bz), (b) southward (-IMF Bz), (d) eastward (+IMF By), and (d) westward (-IMF By) sectors.

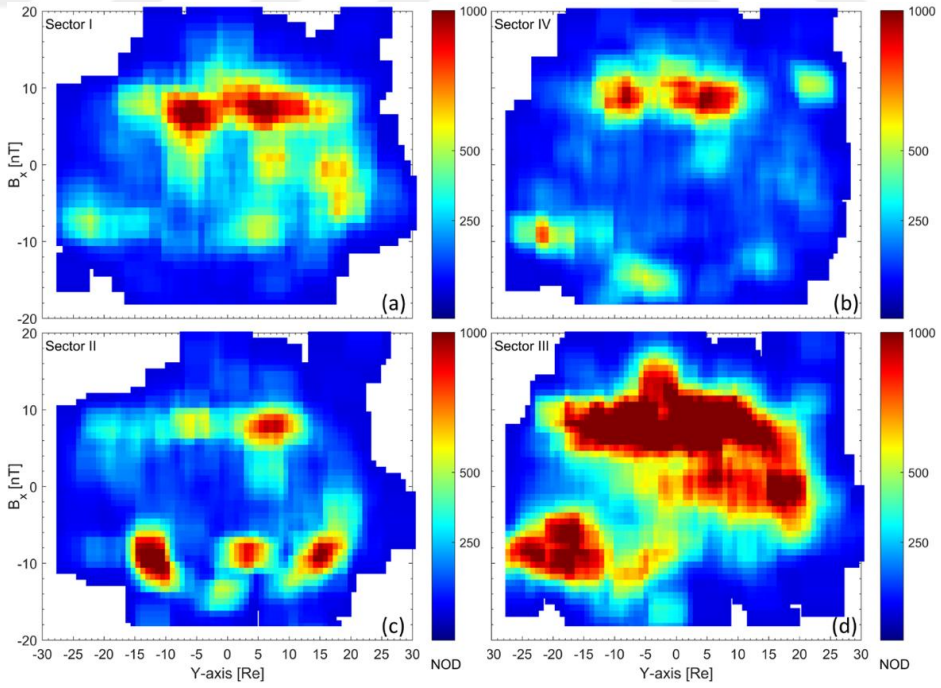

Figure 4.25 : The color scale is for number of data points in YBx- plane magnetic field line vectors for (a) northward (+IMF Bz), (b) southward (-IMF Bz), (c) eastward (+IMF By), and (d) westward (-IMF By) sectors. The dark red color indicates the number of data more than 1000.

4.2 Magnetotail Flows at Lunar Distances

ARTEMIS is the first multi-spacecraft mission with the comprehensive and high-resolution magnetic field and particle instrumentation required to study the mid-to-distant tail, i.e. lunar distances. ARTEMIS probes are located between the two magnetotail reconnection regions, the Near-Earth Neutral Line (NENL) at about -20R_E to -30 R_E distance and the Distant Neutral Line (DNL) at about -100 R_E distances down the magnetotail. This crucial positioning of the probes is chosen on purpose (Sibeck et al., 2011) and is be used to investigate the plasma flow characteristics, e.g. flow velocity, direction and its dependence on IMF, between these two source regions.

In the near earth magnetotail (>-30 R_E) the plasma flow direction is temporally and spatially depended on the substorm activity whereas the bulk plasma flow in the distant tail (<-100 Re) are dominantly in tailward direction (Hones and Schindler, 1979; Hayakawa et al., 1982; Bame et al., 1983; Zwickl et al., 1984). At lunar distances, the probability of the earthward/tailward direction of the plasma flow has the same occurrence rate (~50%) based on lunar swingbys of the ISEE 3 spacecraft (Scholer et al., 1984). Thus, the flow structure at lunar distances is expected to be effected from both structures and will be a mixture of two effects.

Plasma sheet is the region with the enhanced plasma associated with the neutral sheet, which is the region of magnetic field reversal (Bame et al., 1967). The plasma sheet investigation in the near earth magnetotail (-15 R_E to -20 R_E) had been studied by Vela and OGO satellites in late 1960s (Bame et al., 1967; Bame, 1968; Hones, 1969; Vasyliunas, 1968). The average plasma sheet thickness varies around 4-6 R_E (Bame et al., 1967; Borovsky et al., 1997), whereas it can get as thin as 0.5 R_E at near-earth distances especially in substorm growth phase (McComas et al., 1986; Baumjohann et al., 1992; Runov et al., 2005). Plasma sheet extends into and around the Earth's dipole while stretching at least 100 R_E down the magnetotail with decreasing density and temperature down the tail (Borosky et al., 1998).

Huang and Frank (1986) defined the different regimes of plasma at -10 to -25 R_E down the tail such that in the lobes, the X-component of the flow direction is in tailward direction and the density is less than 10^{-2} cm^{-3}, as tabulated in Table 4.5. The plasma sheet boundary layer region lies within 1.5 R_E in Z-direction (Huang and Frank, 1986) and the bulk flow velocity is higher than 150 km/s whereas much smaller scales are

stated in newer studies as 0.2-0.5 R_E (Ashour-Abdalla et al., 2008). Ion density and plasma beta (β) in PSBL remain nearly constant at about 0.1 – 0.5 cm^{-3} and 0.01 – 0.5, respectively (Baumjohann et al., 1988). The x- component of the magnetic field and the plasma flow is much higher than the other directions ($B_x/B_z > 2$) (Du et al., 2011). Plasma flow in low latitude boundary layer also has higher velocities higher than 150 km/s with flow in tailward direction with high density values. Baumjohann et al. (1990) study the region closer to earth (X<-9 R_E) and define the plasma sheet layer spatially as $|Y| = 15\ R_E$ and separate the central plasma sheet (CPS) region using magnetic field characteristics as below in Equation. The high-speed flows are mostly seen in PSBL with a tendency to occur mostly when density is low. Another study by Birn et al. (2004) showed that tailward flows are seen within the PSBL when low-density dipolarized earthward flows occur closer to Earth and the void region after earthward moving flow burst is filled by tailward flows, using 3D MHD simulations.

Table 4.5 : Near-earth magnetotail region plasma parameters (Huang and Frank, 1986).

Parameters	LLBL	PSBL	CPS	Lobe
Z-position (R_E)		>1.5		
n_i (cm^{-3})	$>10^0$		data after excluding other regions	$<10^{-2}$
V_i (km/sec)	>150	>150		
	Vx<0			Vx<0

$$\left(B_x^2 + B_y^2\right)^{1/2} < 15\ nT\ or\ \frac{B_z}{\left(B_x^2 + B_y^2\right)^{1/2}} > 0.5 \qquad (4.1)$$

At about -35 R_E, the features and the configuration of the PS are studied by many using IMP 6, IMP 8 observations (Behannon, 1970; Fairfield and Ness, 1970; Mihalov, 1970; Meng and Anderson, 1971; Hones, 1977; Hones and Schindler, 1979; Bieber et al., 1982). Predominantly, tailward directed plasma flows are observed at -15 R_E to -40 R_E distances. Geotail observations of the fast flows in the plasma sheet are investigated at X>-31 R_E with the applied criteria of $|V_{\perp x}| > 300\ km/s$ or $|V_x| > 300\ km/s$, $\beta_i > 0.5$ and $|Y_{agsm}| < 15\ R_E$ (Ohtani et al., 2004). Their 290 tailward out of 1108 fast flows are not always linked to reconnection or southward IMF Bz. The change in the magnetic field and plasma parameters in the tailward flow cases

tend to occur more gradually since there is no obstacle as Earth's dipole that compresses the plasma leading to sudden variations in plasma characteristics.

All of the plasma regimes identified at near earth magnetotail distances remain recognizable in the distant tail only in a more complex, intricate way (Bame et al., 1983). In their study, Bame et al. differentiate regions as tabulated below from -60 R_E up to -220 R_E distances based on ISEE 3 findings. As seen in Table 4.6, the fastest flows directed in the tailward direction are observed in plasma sheet region. In addition, they differentiate the LLBL region from other layers using flow direction. Tsyganenko and Mukai (2003) uses ion temperature-density ratio ($\gamma = T/n$) to separate cold-dense magnetosheath plasma and LLBL plasma from other regions. In terms of flows at distant tail, are directed tailward beyond -100 R_E; -140 R_E implicating the DNL at about -120 R_E (Zwickl et al., 1984; Slavin et al., 1985). The mantle plasma flows in the tailward direction along the magnetic field lines while drifting towards current sheet and midnight sector (Wang et al., 2014).

Table 4.6 : Plasma regime characteristics of different magnetotail regions at distant tail -60 to -220 R_E (Bame et al., 1983).

Parameters	LLBL	Mantle	PS	Lobe
n_e (cm^{-3})	1	1	0.6	0.04
V_e (km/sec)	200	-250	-500	-
T_e (eV)	70	~25	~75	70

At lunar distances, at about -60 R_E, Explorer 33 and Explorer 35 spacecraft complete magnetotail traversals in the YZ-plane and the plasma sheet and current sheet characteristics from various studies by Explorer series are tabulated in Table 4.7.

Explorer 35 findings showed that the plasma sheet extends to lunar distances (Nishida et al., 1969; Prakash and Binsack, 1971). However, studies using detectors mounted on the Moon, Charged Particle Lunar Environment Experiment (CPLEE), cannot observe plasma sheet due to lunar shadowing (Burke and Reasoner, 1972) or rapid random passage (>40 km/s) at magnetotail field lines (Rich et al., 1973).

The main finding of these studies in the 1970s was the thickness of the plasma sheet, which is found to be about 7 R_E. A recent study by Vasko et al. (2015) used 573 current sheet crossings using Geotail observations at mid- (-20 R_E to -50 R_E) and distant tail

(-80 R_E to -100 R_E). The authors defined the thickness of the current sheet as about 2 R_E as in the study by Baumjohann and Treuma (1996).

Table 4.7 : Characteristics of plasma at lunar distances from various studies.

Parameters	Plasma Sheet			Current Sheet
	Rich et al. (1973)	Meng and Mihalov (1972)	Nishida and Lyory (1972)	Tian et al. (2012)
B_x (nT)				±15
n (cm^{-3})	0.1±0.05			<0.4 (<0.1)
V (km/sec)				<1500 (200)
T (eV)	2.5±0.75			0.016:8.98 (3)
Thickness (R_E)	5±2	-7:+7	6	1-2 (Baumjohann and Treuma, 1996)

In terms of plasma velocity distribution, the convection is generally not stable neither in time nor in space. An instantaneous flow velocity measurement can be much higher than the average flow velocity and the velocity very near to that measurement point (Borovsky et al., 1997). The observations of the Vela 5, Vela 6, and IMP 6 shows that the flow within the plasma sheet, about 1-2 R_E thick, is generally directed earthward with speeds reaching 1000 km/s at the midnight sector while decreasing towards dawn-dusk regions (500 km/s) at -30 R_E distances (Hones et al., 1972; Lui et al., 1977). On the other hand, tailward flows were observed generally after substorm activity at about -15;-20 R_E (Hones et al., 1973). However, plasma flows directed in tailward direction especially flows with velocities higher than 200-300 km/s has not been studied as extensive as the earthward directed flows despite the fact that the usual convection can not fully explain this condition (Ohtani et.al, 2009). The symmetricity of the convective fast flows is studied by Walsh et al. (2014) and they show that the flows are symmetric however, there is a tendency of faster flows to be at the dusk region (Walsh et al., 2014).

The fast plasma flows inside plasma sheet, i. e. Bursty Bulk Flow (BBF)s, and their relation with substorms were investigated in detail in 1990s based on AMPTE/IRM and ISEE2 data at near earth distances (Baumjohann et al., 1990; Baumjohann et al.,

1991; Angelopoulos et al., 1992; Angelopoulos et al., 1994). The BBFs in the plasma sheet are spatially constrained within a region of 1 – 3 R_E to 1.5 – 2 R_E in cross-sectional plane (Angelopoulos et al., 1996; Nakamura et al., 2004). These high speed streams like any other local or transient events, e.g. plasmoids, flux ropes, flux transfer events (FTEs), are expected to have little or no effect on the global structure and the plasma characteristics of the magnetotail in a statistical study as this one. These structures are sporadically detected in the lobes especially during periods of geomagnetic activity with a maximum of about 3 R_E radius (Scholer et al., 1985). In this study, the magnetotail magnetic field values and plasma parameters are all averaged both temporally and spatially using "bins" with at least $3R_E$ size in one dimension. The effects of those signatures, if any, are assumed to be cancelled out in this study, therefore, the literature about those transient events will not be stated further on.

The plasma sheet consists of hot and tenuous plasma most of time. The IMF direction affects not only the magnetic field structure of the magnetotail as presented in Section 4.1 but also the characteristics of the plasma regime throughout the magnetotail. Even in course of quiet geomagnetic conditions with little or no reconnection in the dayside region, the plasma sheet may get colder and denser, with the strongest effect near the flanks at near earth distances down the tail (Fujimoto et al., 1997; Terasawa et al., 1997; Borovsky et al., 1998; Wing and Newell, 2002; Tsyganenko and Mukai; 2003). The entry of cold magnetosheath plasma entry into the magnetosphere is due to the high-latitude reconnection of the interplanetary magnetic field with the magnetic field of the north and south lobes creating the LLBL under prolonged northward IMF conditions (Song and Russell, 2002). The brief northward IMF conditions is not found enough to create the cold, dense plasma sheet as defined by Fujimoto et al. (1998). It takes at least several hours to significantly cool and densify the plasma sheet (Mata et al., 2014). Therefore, we would like to see if this kind of cold, dense plasma can be observed at lunar distances during northward IMF sector or not.

As reviewed above, most plasma flow related studies in the magnetotail are related to BBFs in which the duration of the flow is important or the case studies in which the observations are evaluated in time series. In this study, the flow measurements from ARTEMIS probes are examined as vectors plotted in XY-, XZ-, and YZ- planes with the corresponding IMF condition or in some cases according to their direction for

statistical purposes. Instead of using z-values, Bx-component is used for separating northern and southern tail magnetotail data in flow vector maps, e.g. Plasma velocity vector projections onto YZ- plane is done by plotting Vy-Vz vector couple onto Y-Bx coordinates.

In the Appendix B, for each crossing the magnetotail plasma velocity maps are presented in Figure B.6 to Figure B.10 for different planes.

4.2.1 XY plane

Figure 4.26 (a) shows the magnetotail plasma flow projected onto XY- plane for all ARTEMIS observations with $3R_E$x$3R_E$ bin size. The meridional cut, Y=0 is set with a gray solid line. Figure 4.26 (b) presents the color bar is the number of data points for all available plasma observations from ARTEMIS probes at lunar distances in XY-plane. The dark red color indicates the number of data in that bin is more than 2500 minutes about which one can say that there is substantial amount of magnetotail information. At first glance, the XY projection of the plasma flows in Figure 4.26 shows that the flows adjacent to magnetopause boundary seem to have higher speed with respect to deep interior regions of the magnetotail. Those tailward flows are expected to be seen near boundary since main plasma flow is in anti-sunward direction within the magnetosheath.

On the other hand, within the region of Y=±10 R_E, in the expected plasma sheet region, the transient fast flow events might be diminished by the temporal as well as spatial averaging.

Beyond about -63 R_E in the magnetotail, the speed of the flow with tailward direction is increased near midnight region (region between Y=-12 R_E to Y=4 R_E). These fast tailward flows in the nightside of -63 R_E are also seen in XZ-plane in Figure 4.30. These increased flows in the tailward direction might suggest that at about X=-63 R_E an X-type neutral line comes to existence due to reconnection. Thus, the increased velocity of the plasma flow might be correlated with the tailward motion of an earthward generated neutral line as stated in previous studies (Hones, 1979; Scholer et al., 1984).

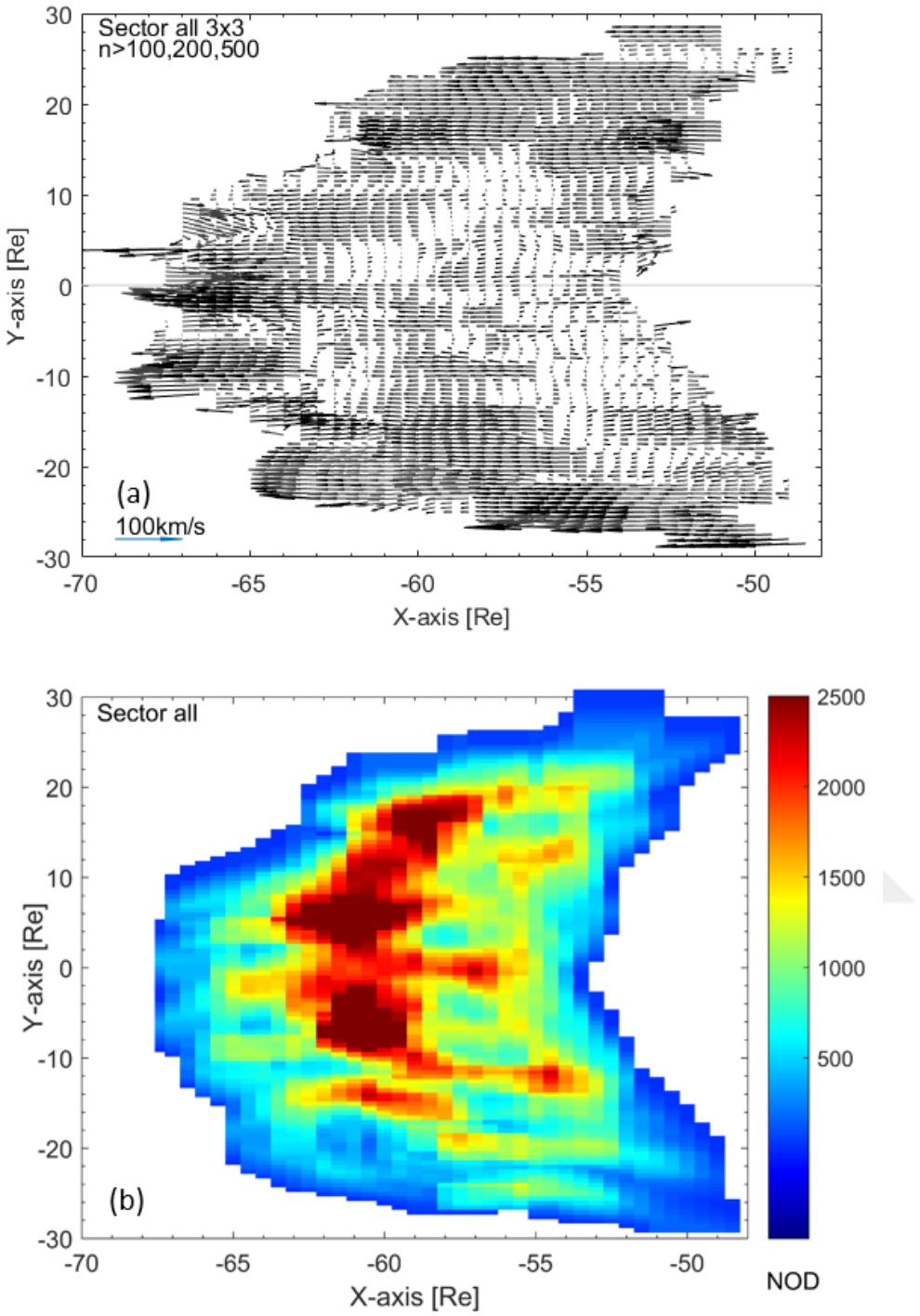

Figure 4.26 : (a) Magnetotail plasma flow projection onto XY- plane for all ARTEMIS observations with $3R_E x 3R_E$ bin size. The meridional cut, Y=0 is set with a gray solid line. (b) The color bar is the number of data points for all available plasma observations from ARTEMIS probes at lunar distances in XY-plane. The dark red color indicates the number of data more than 2500.

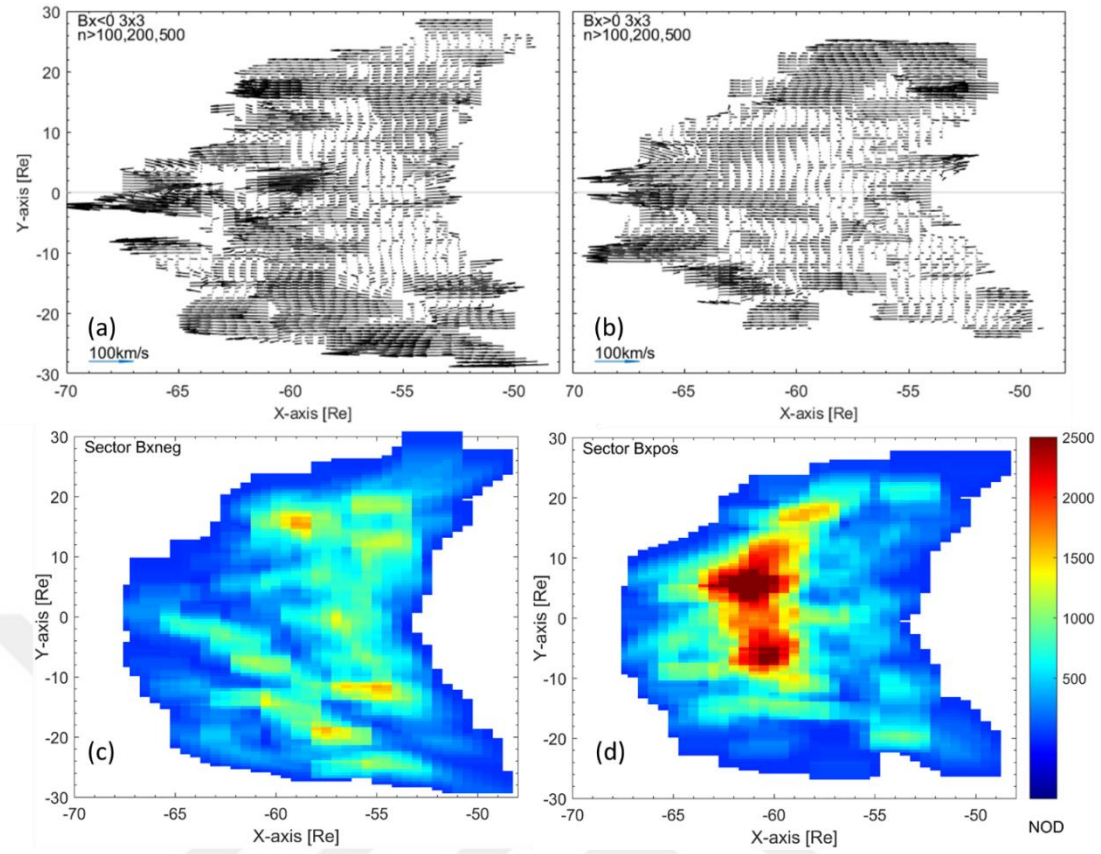

Figure 4.27 : Magnetotail plasma flow in XY- plane (a) for northern and (b) for southern tail with $3R_E$x$3R_E$ bin size. Bins with measurements less than 500 and higher than 100 number of data points are plotted in gray tones. The meridional cut, Y=0 is set with a gray solid line. The color bar is the number of data points (c) for northern and (d) for southern tail plasma observations from ARTEMIS probes at lunar distances in XY-plane. The dark red color indicates the number of data more than 2500.

In Figure 4.27, all ARTEMIS plasma flow observations are given for northern (a) and southern (b) part of the tail in XY-plane. The bin size is used same as 3x3 R_E to be able to make comparison with the mixed tail flow vectors in Figure 4.26. The distribution of the observations are more or less evenly distributed as seen in Figure 4.27 (c) and (d) with densely visited regions lie within the Y=±10 R_E at about X=~60 R_E.

IMF By effect can be seen when (c) and (d) are compared in Figure 4.28. Faster flows can be seen in the favored IMF polarity, there is a clear tendency to encounter higher flow velocities in dusk/dawn regions with positive/negative IMF By. The coverage area is presented in Figure 4.29 for each sector with color scales up to 1000 number of data points assigned to darkest red in the color bar.

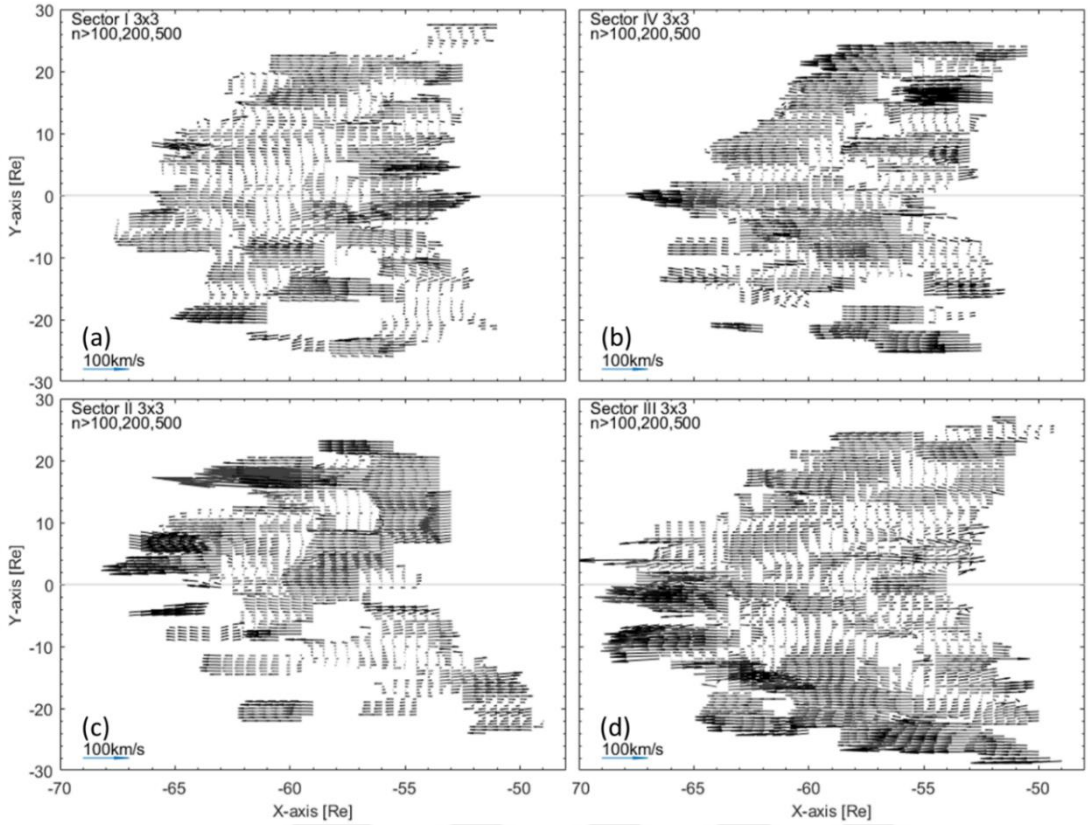

Figure 4.28 : Magnetotail plasma flow velocity vectors in XY plane for (a) northward (+IMF Bz), (b) southward (-IMF Bz), (c) eastward (+IMF By), and (d) westward (-IMF By) sectors.

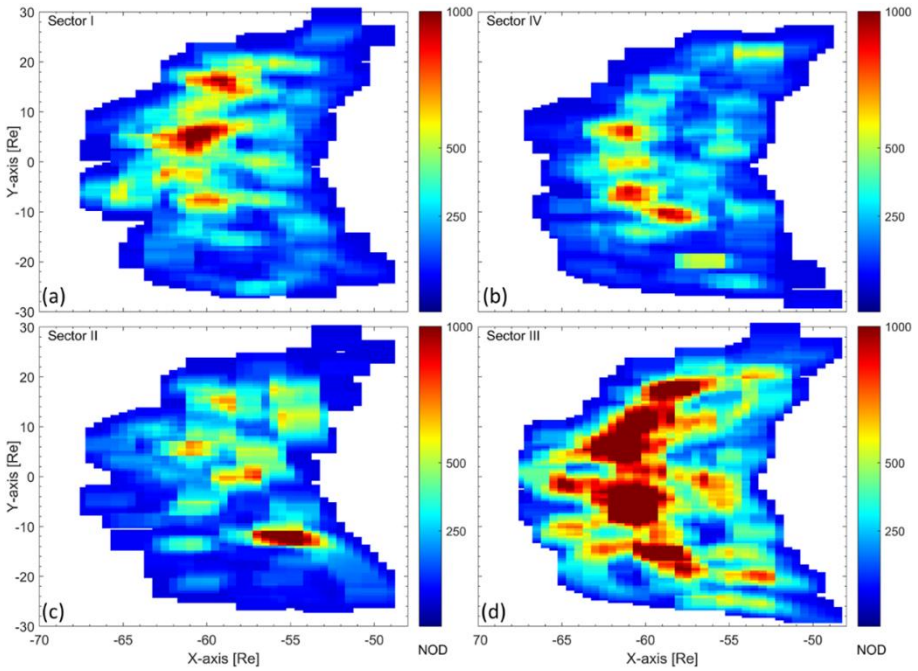

Figure 4.29 : The color scale is for number of data points XY plane for (a) northward (+IMF Bz), (b) southward (-IMF Bz), (c) eastward (+IMF By), and (d) westward (-IMF By) sectors. The dark red color indicates the number of data more than 1000.

When northward and southward IMF conditions are compared from Figure 4.28 (a) and (b), faster tailward flows can be seen when reconnection conditions are present. In contrast to that, fastest earthward flows can be seen in northward IMF sector compared to all other IMF conditions. The earthward directed flows are present within the plasma sheet region, Y=±10 R_E, in the earthward of -60 R_E.

4.2.2 XZ plane

The plasma flow projections onto XZ- plane for all available magnetotail data is presented in Figure 4.30. This distorted flow map will provide more accurate information if it is plotted onto XBx- plane as coordinates due to the fact that the even after all coordinate system transformations and solar wind corrections, neutral sheet position may not and not expected lie at Z=0 R_E.

Magnetic field x-component is a better parameter to distinguish northern and southern tail from each other. Therefore, from there on instead of Z-positions, Bx value of the ARTEMIS measurements will be used for vertical axes.

When flow patterns onto XBx- plane is investigated, two different plasma flow characteristics can be observed from Figure 4.31; in the earthward region of about -63 R_E speed of the flow is slow near to the estimated neutral sheet position and faster in other layers up to the magnetopause boundary. In the tailward region of -63 R_E, tailward flows with higher speed near to the neutral sheet and earthward directed flows at southern part of the tail are present. The increase in the flow velocity and flows in either direction, earthward or tailward may support the neutral line being at about that distance. Fast tailward flows observed within a few R_E of the estimated neutral sheet position starting at about X=-63 R_E are mainly associated with the southward polarity of the interplanetary magnetic field, as those flows are not expected to be observed with northward IMF sector (see Figure 4.32). However, Figure 4.31 (b) is attached to show that how many minutes of data is collected from that region and there is a clear drop in the number of measurements from the mentioned area. Therefore, the increase in the flow speed in the tailward direction might be a misconception due to lack of information. Nonetheless, the same increase in the tailward flow velocity is observed in XZ- plane, Figure 4.30a, with sufficient amount of magnetotail plasma flow data as seen in Figure 4.30b.

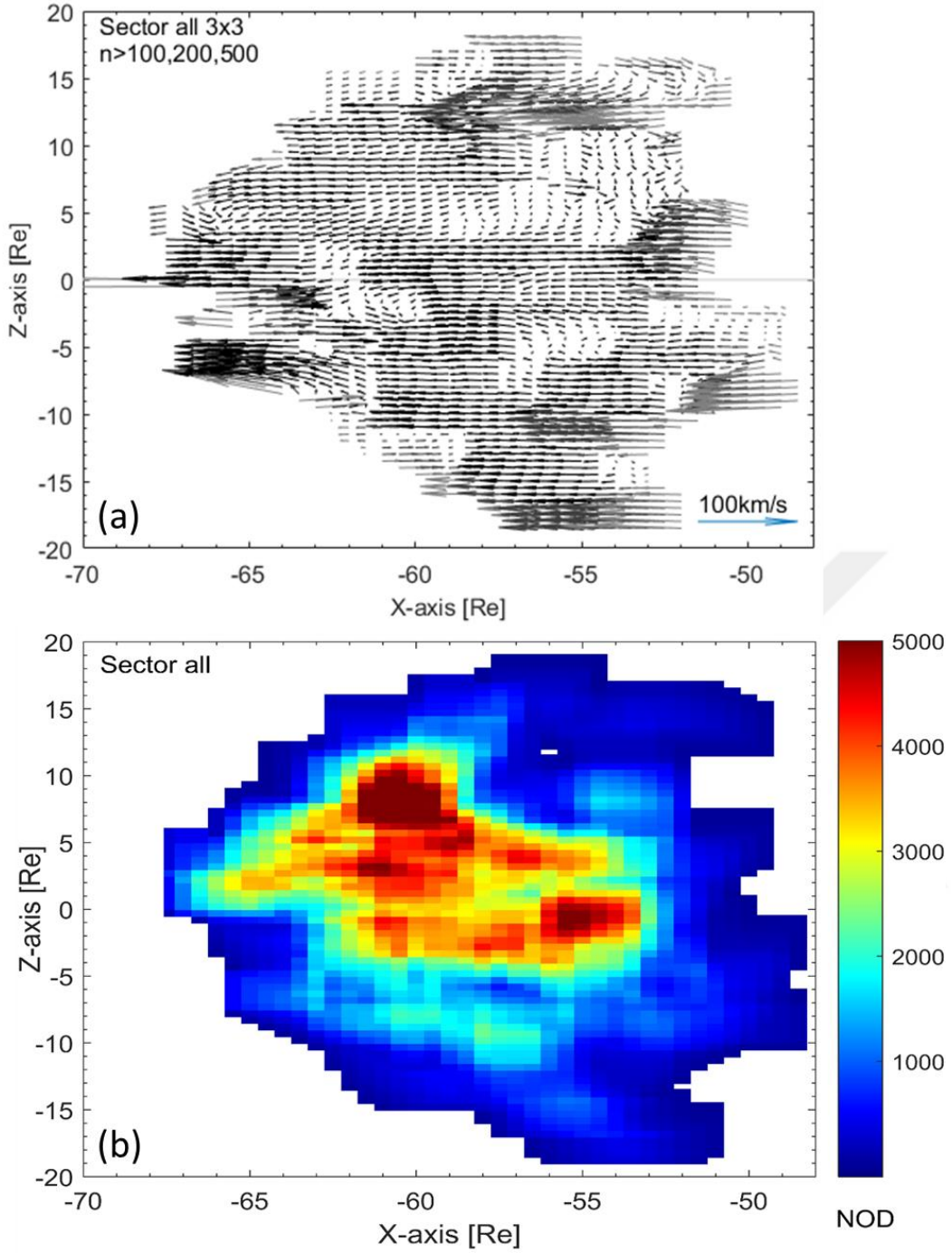

Figure 4.30 : (a) Magnetotail plasma flow projection onto XZ- plane for all ARTEMIS observations with $3R_E x 3R_E$ bin size. Bins with measurements less than 500 and higher than 100 number of data points are plotted in gray tones. The equatorial cut, Z=0 is set with a gray solid line. (b) The color bar is the number of data points for all available plasma observations from ARTEMIS probes at lunar distances in XZ-plane. The dark red color indicates the number of data more than 5000.

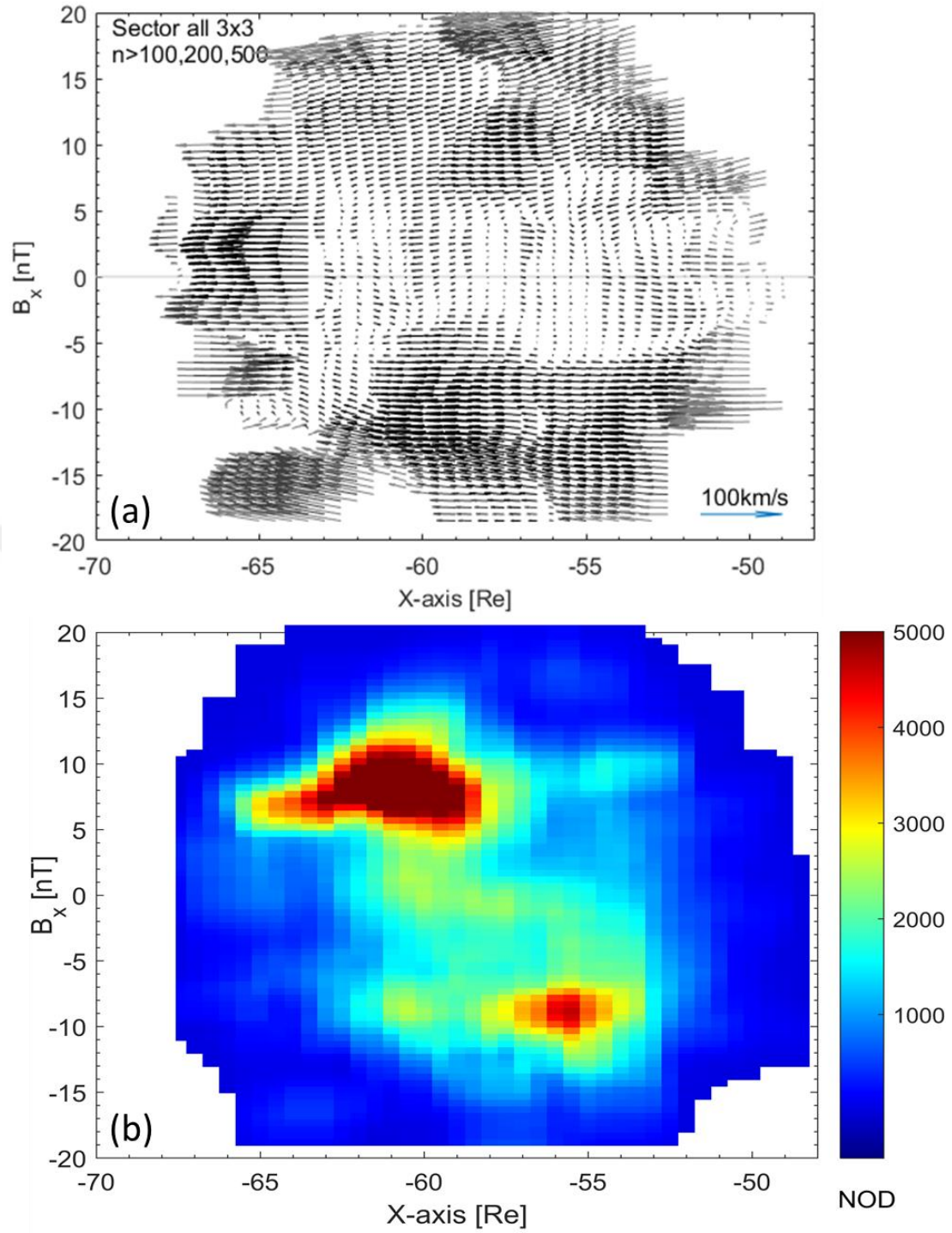

Figure 4.31 : (a) Magnetotail plasma flow projection onto XBx- plane for all ARTEMIS observations with $3R_E x 3R_E$ bin size. Bins with measurements less than 500 and higher than 100 number of data points are plotted in gray tones. The estimated neutral sheet position where Bx=0 nT is set with a gray solid line and is only used for position purposes, Vx and Vz components are plotted onto XBx coordinates. (b) The color bar is the number of data points for all available plasma observations from ARTEMIS probes at lunar distances in XBx-plane. The dark red color indicates the number of data more than 5000.

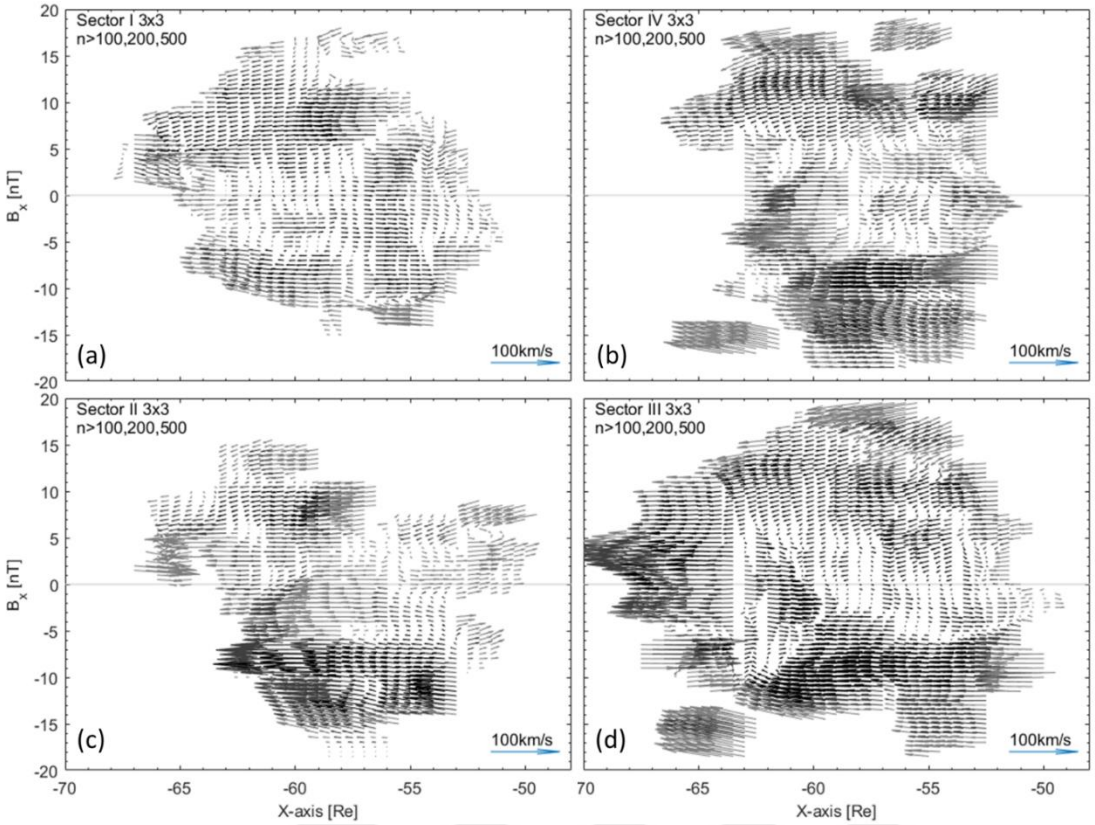

Figure 4.32 : Magnetotail plasma flow velocity vectors in XBx- plane for (a) northward (+IMF Bz), (b) southward (-IMF Bz), (c) eastward (+IMF By), and (d) westward (-IMF By) sectors.

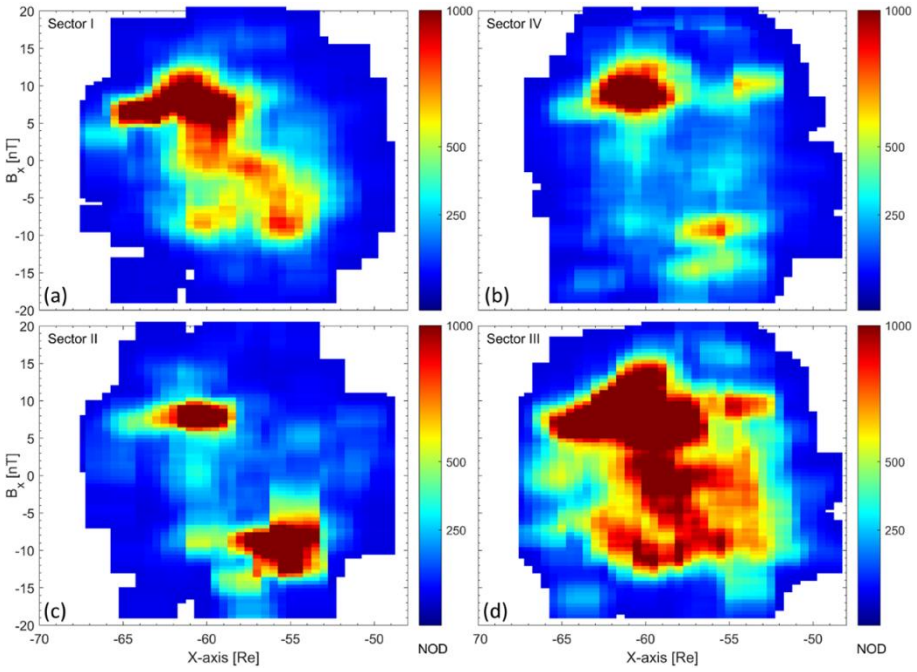

Figure 4.33 : The color scale is for number of data points XBx- plane for (a) northward (+IMF Bz), (b) southward (-IMF Bz), (c) eastward (+IMF By), and (d) westward (-IMF By) sectors. The dark red color indicates the number of data more than 1000.

Within the expected plasma sheet region of about |Bx|< 7-10 R_E, the flow velocities is much lower than the flows adjacent to lobes. The earthward to tailward flow ratio is more than the flows in the other regions. The plasma sheet boundary is seen to be on the move.

After IMF separation, there is a clear picture of flows with lower speeds during northward IMF cases compared to southward IMF cases in Figure 4.32. Additionally, the flow direction is in both ways, which might be due to flows directed earthward in the earthward of the distant neutral line formation and vice versa. In Figure 4.33, one can see how much data is gathered from each IMF sector.

4.2.3 YZ plane

Figure 4.34(a) shows the Vy, Vz vector pair in YZ- plane. We see the general flow characteristics in YZ-plane, slowest plasma velocities compared to other planes. The flow is mainly orthogonal to YZ-plane. The color map Figure 4.34 (b) shows that the region within Z=±10 R_E has more information. The flow is directed southward/northward in the north/south part of the tail. However, Bx is a better representative in dividing the northern tail from southern. Figure 4.35 is the YBx-plane projection of the plasma flow at lunar distances.

The general direction of the plasma flows in the YZ- (YBx-) plane are toward the neutral sheet (|Bx|<5nT (Runov et al., 2005)). The flow movement is more scattered and irregular in the YZ- plane than in the XY- and XZ- (XBx-) planes. The cross tail current in the dawn to dusk direction is interrupted by the flows with negative z-components (southward directed flows) at around midnight sector (Y=0). A similar dawn to dusk ion flow is also seen by Nakamura et al. (1994) in which they suggested that this dawn-to-dusk flow mechanism release the pressure build up in the near Earth region. The plasma flow speed is highest near magnetotail boundary, decreases around 10nT>|Bx|>5nT and then start to increase near neutral sheet. There are some sink regions where flow is unidirectional either in the earthward or in the tailward direction at the following y,Bx coordinates; -9R_E,-7nT; 2R_E;-6nT; 8R_E,3nT; 17R_E,-4nT. There are saddle points at around (-5R_E, -8nT) and (13 R_E, -8nT). There is a curl structure at around (-20R_E, 3nT).

The color scale in Figure 4.35 (b) is less than it is in the other planes (e.g. in Figure 4.26(b), Figure 4.31(b)) since the projection area is much wider in YBx- (or YZ-) than

other planes with horizontal axis showing the X-axis. Nonetheless, there is more than 8 hours of pure magnetotail observational information in the solid vector pairs.

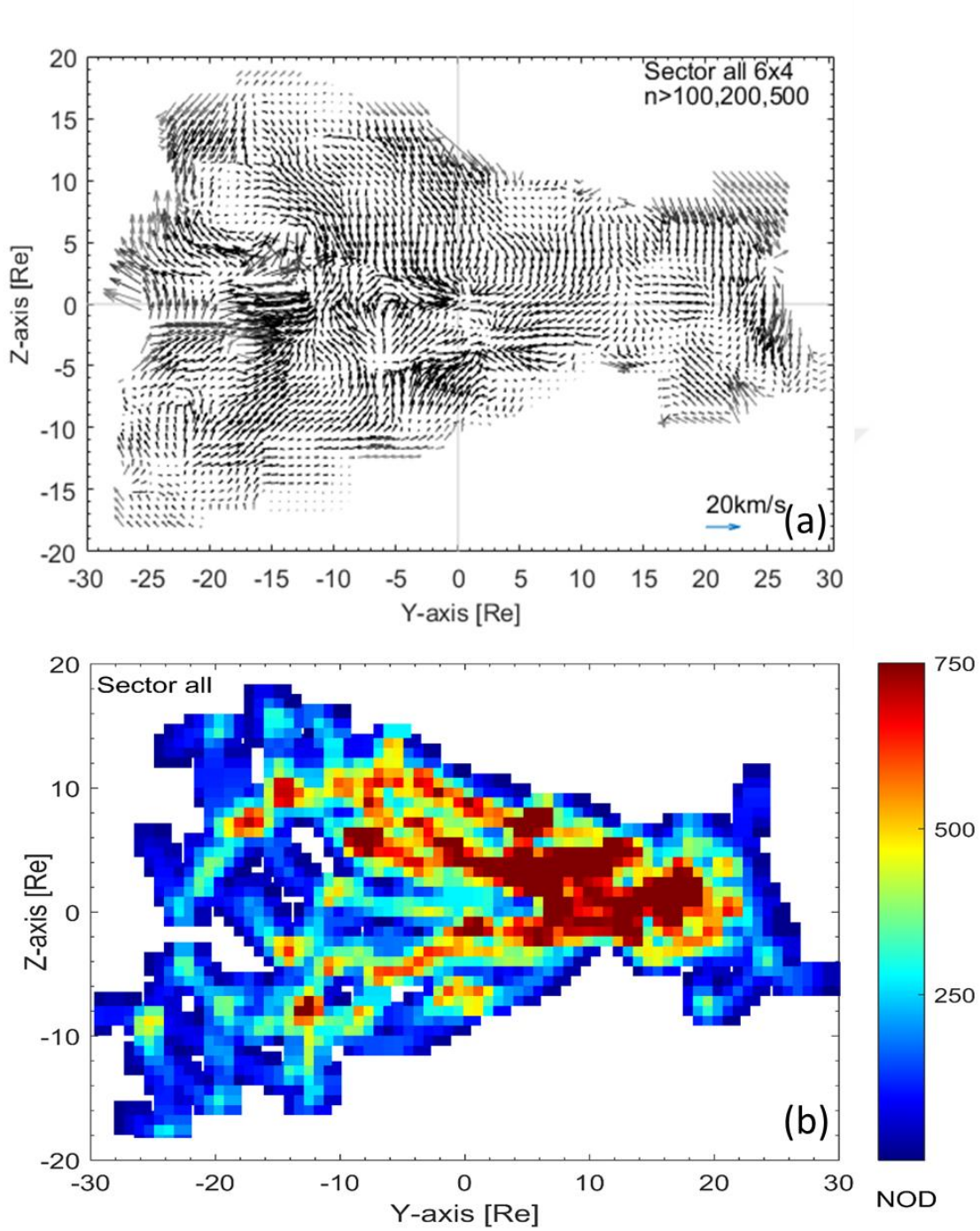

Figure 4.34 : (a) Magnetotail plasma flow projection onto YZ- plane for all ARTEMIS observations with $6R_E x 4R_E$ bin size. Bins with measurements less than 500 and higher than 100 number of data points are plotted in gray tones. Y=0 and Z=0 is set with a gray solid line. (b) The color bar is the number of data points for all available plasma observations from ARTEMIS probes at lunar distances in YZ-plane. The dark red color indicates the number of data more than 750.

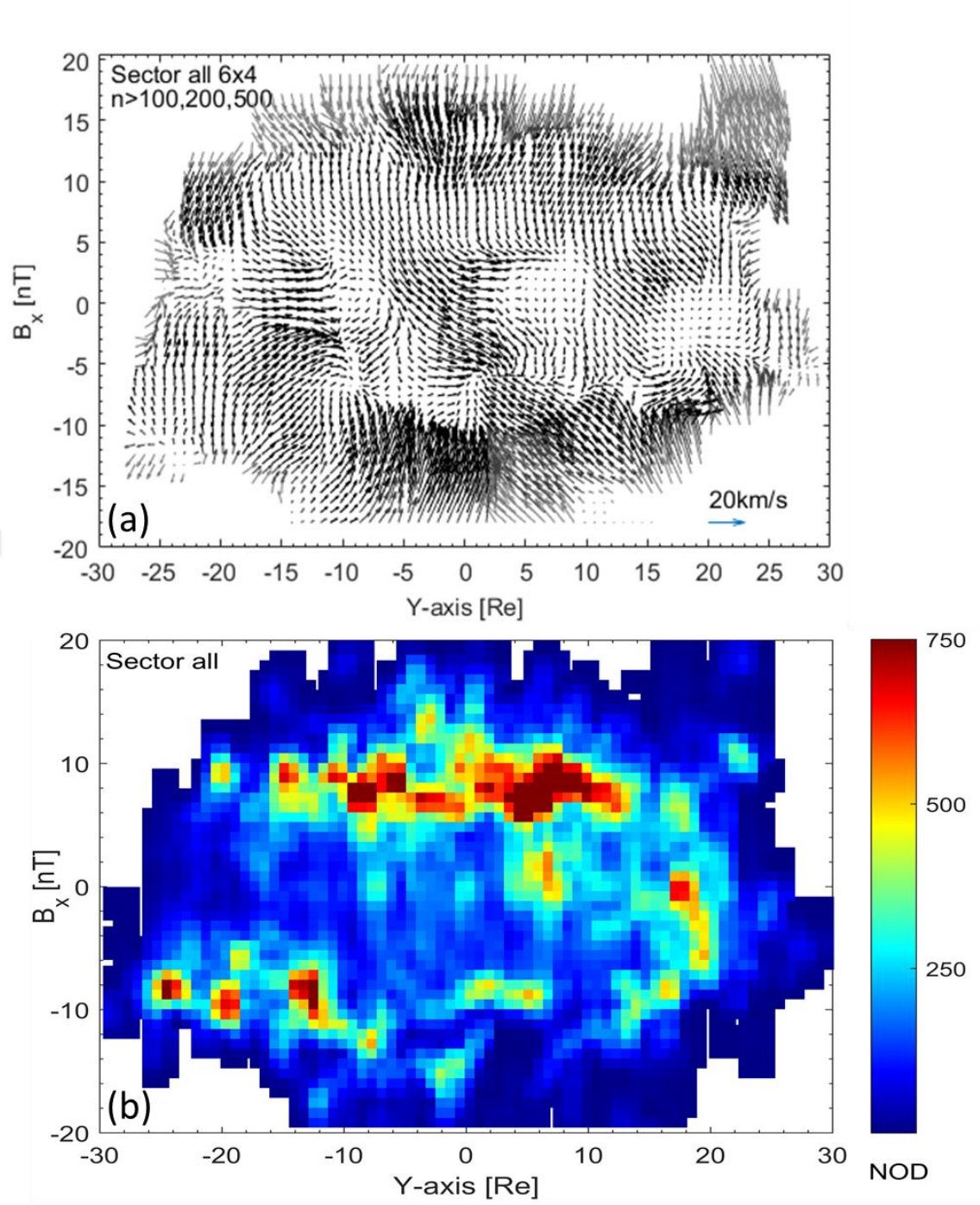

Figure 4.35 : (a) Magnetotail plasma flow projection onto YBx- plane for all ARTEMIS observations with $6R_E x 4R_E$ bin size. Bins with measurements less than 500 and higher than 100 number of data points are plotted in gray tones. The estimated neutral sheet position where Bx=0 nT is set with a gray solid line and Bx is only used for position purposes, Vy and Vz components are plotted onto YBx coordinates. (b) The color bar is the number of data points for all available plasma observations from ARTEMIS probes at lunar distances in YBx-plane. The dark red color indicates the number of data more than 750.

Figure 4.36 gives the YBx- projection of the magnetotail plasma flow after sector separation.

For comparison purposes northward and southward IMF conditions are given in (a) and (b) whereas positive and negative IMF By conditions are given in (c)and (d). Within positive and negative IMF Bz sectors; higher flow speeds can be observed during periods of southward IMF orientation compared to northward IMF directed periods. There is not an eye catching IMF By related difference in the positive/negative IMF By sector related flow maps. The number of ARTEMIS magnetotail data gathered for each bin is given in Figure 4.37 with the darkest red representing only 250 number of data points. Therefore, with data mainly less than 5 hours of magnetotail data is not expected to provide IMF effect.

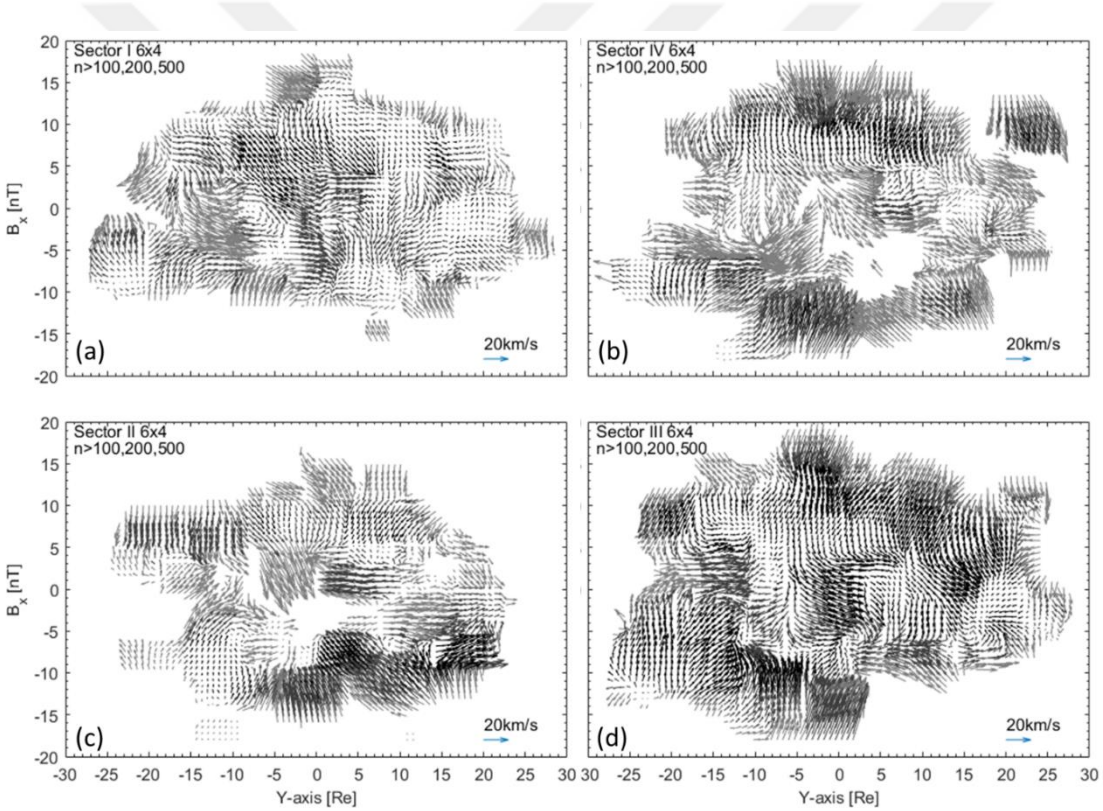

Figure 4.36 : Magnetotail plasma flow velocity vectors in YBx- plane with 6x4 R_E bins for (a) northward (+IMF Bz), (b) eastward (+IMF By), (c) westward (-IMF By), and (d) southward (-IMF Bz) sectors.

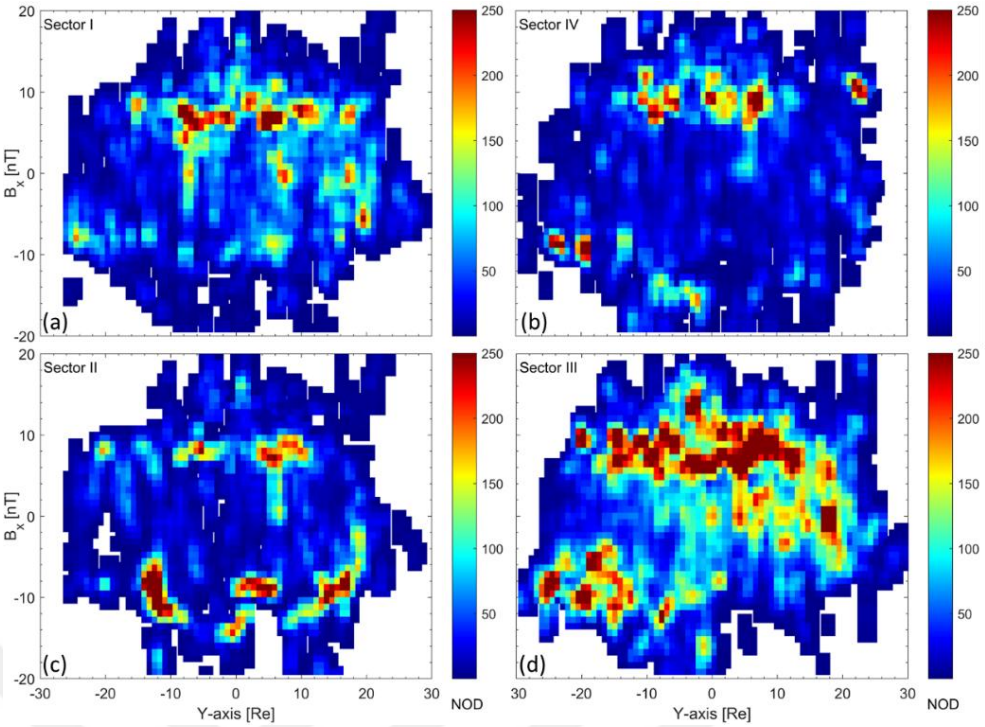

Figure 4.37 : The color scale is for number of data points YBx- plane for (a) northward (+IMF Bz), (b) southward (-IMF Bz), (c) eastward (+IMF By), and (d) westward (-IMF By) sectors. The dark red color indicates the number of data more than 250.

4.3 Density, Temperature and Pressure Distribution at Lunar Distances

For investigating average plasma properties at lunar orbit, a one-year long MHD model run shows that the density of the plasma decreases from 4 cm^{-3} adjacent to magnetopause to 0.3 cm^{-3} near the tail center, i.e. Sun-Earth line (Kallio and Facsko, 2014). The temperature of the magnetotail plasma shows reverse relation in which the temperature values vary about 10^6 K near magnetopause increase to 10^7 K near Sun-Earth line (Kallio and Facsko, 2014). For positive IMF By, an increased temperature in the northern dusk and southern dawn magnetopause is observed by IMP 8 (Siscoe and Kaymaz, 1999).

Flux rope like structures at lunar orbit, with plasma properties $n<1cm^{-3}$ and T>0.2 keV shows dawn-dusk asymmetry in a way that those events show tendency to take place in the dusk side more than the dawn side of the tail (Zhao et al., 2016). The occurrence rate of those events is higher in the tailward direction while positively correlated with the geomagnetic activity. Additionally, the events that propagates in the earthward direction has lower temperature and lower speed than tailward events.

Recent studies based on ARTEMIS observations regarding to the properties of the plasma shows that the temperature varies more than the density parameter along the magnetotail and in the north-south direction (Artemyev et al., 2017a). The plasma temperature peaks in the neutral plane and decreases toward the tail lobes. The decrease within the thin current sheet, i.e. from neutral plane to current sheet boundary, creates strong plasma temperature gradients with fast flows either in earthward or in the tailward direction (Artemyev et al., 2017a). The change in the velocity does not necessarily change the plasma properties instead there seems to be no relation with the plasma temperatures of the slow ($|Vx|<200$ km/s) and fast flows ($|Vx|>500$ km/s). However, the increase in the solar wind velocity is related to increased magnetotail temperature at lunar orbit (Artemyev et al., 2017a).

The penetration of the magnetosheath plasma into the magnetotail is observed as the increase of the plasma sheet density at lunar distances ($n\sim0.1$ cm^{-3}) to distant tail at $X=-200R_E$ ($n\geq 0.5$ cm^{-3}) (Artemyev et al., 2017b).

The plasma sheet appears to be locally homogenous in density and temperature while being very variable in time. The plasma sheet parameters, n, T are largely correlated with the solar wind density and velocity (Delapp et.al, 1995).

From this point on, the plots are based on values instead of vectors as in Section 4.1 and Section 4.2. The density-temperature relation plots are presented for all magnetotail data as well as each sector as its separation is given in Figure 2.10

For each plane, ARTEMIS plasma parameters are gathered and the averages of the values that fall into each $1R_E$ x $1R_E$ grid are calculated for the corresponding plane. In the figures below, the axes are equally scaled such that when they covers 20 R_E and 60 R_E distances in the X and Y axes, the length proportions of the axes are 1:3. I would like to point out that all density, temperature and pressure parameters in this section are evaluated together with the magnetotail magnetic field line vector maps in Section 4.1 as well as the plasma velocity vector maps in Section 4.2 for the same plane views.

Figure 4.38 shows the plasma density and temperature profiles in the XY plane. The dark red colors correspond to highest density and temperature values about 0.25 cm^{-3} and 1000 eV values. The density is highest near midnight (Y=0) and falls off toward the dawn/dusk magnetopause boundary and the density profile tends to rise where the temperature falls. The study by Tsyganenko and Mukai used Geotail observations at -

10R_E to -50 R_E distances down the tail in 2003. They explained the decrease in the temperature and the increase in the density towards the dawn/dusk regions by the entry of cold but dense magnetosheath plasma through the flank magnetopause (Wing et al., 2014; Vasko et al., 2015).

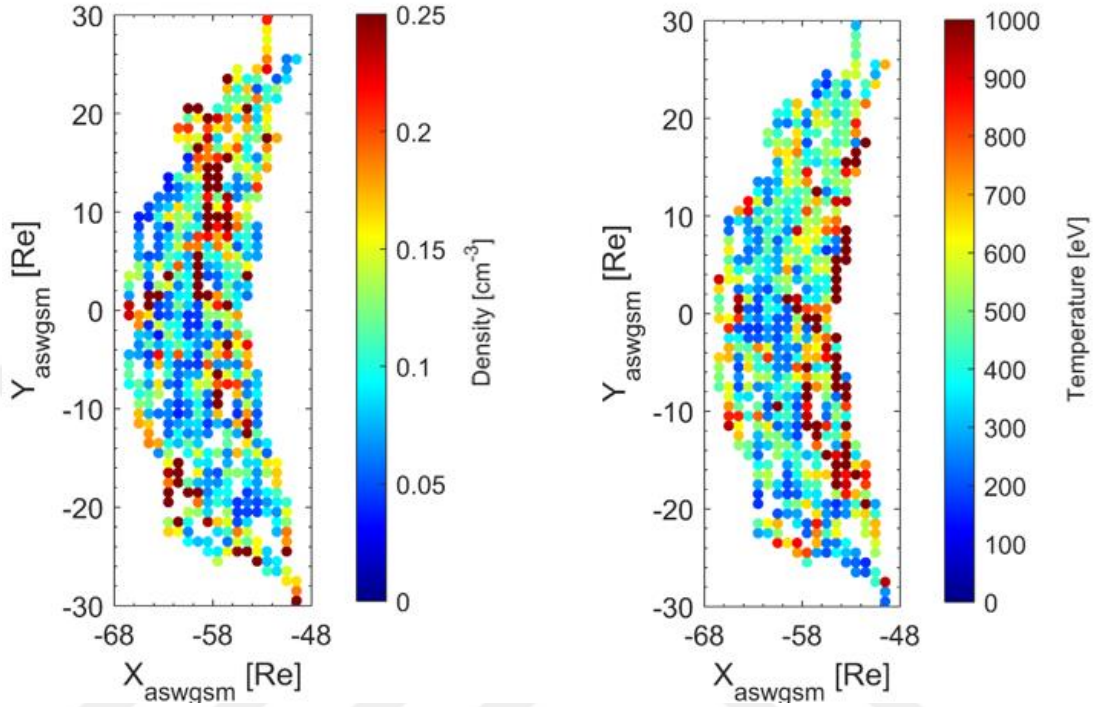

Figure 4.38 : The magnetotail plasma density (on the left) and temperature (on the right) configuration projected onto XY-plane. The X- and Y- axes covers 20R_E and 60R_E distances creating 1:3 proportion since X- and Y- axes have equal scales. The dark red colors in the equally spaced contour map corresponds to 0.25 cm^{-3} and 1000 eV for the left and right figures, respectively.

In Figure 4.39, the magnetotail plasma density (on the left) and temperature (on the right) distribution is given in the XZ plane. The ARTEMIS probes are seem to collect more observations from the northern magnetotail as seen in Figure 4.30b whereas the southern part of the magnetotail is travelled mostly within the region of Z>-5 R_E. Higher densities are observed near neutral line as well as the region at about X=-59 R_E and Z=-5 R_E to -8 R_E. The same region is also seem to have elevated temperatures. Since plasma parameters and magnetotail magnetic field configurations can give better information when evaluated together, we compared this figure with Figure 4.16 and Figure 4.30. The plasma flow does not have any signatures from that region however, the uniformity of the magnetic field vectors are interrupted in that region. The magnetic field vector maps in Figure 4.16a and c show the same decreased and earthward and/or tailward directed magnetic field vectors for positive IMF Bz and By

sectors. This can be explained by the moving out of the current sheet about 8 R_E to the southern part of the tail.

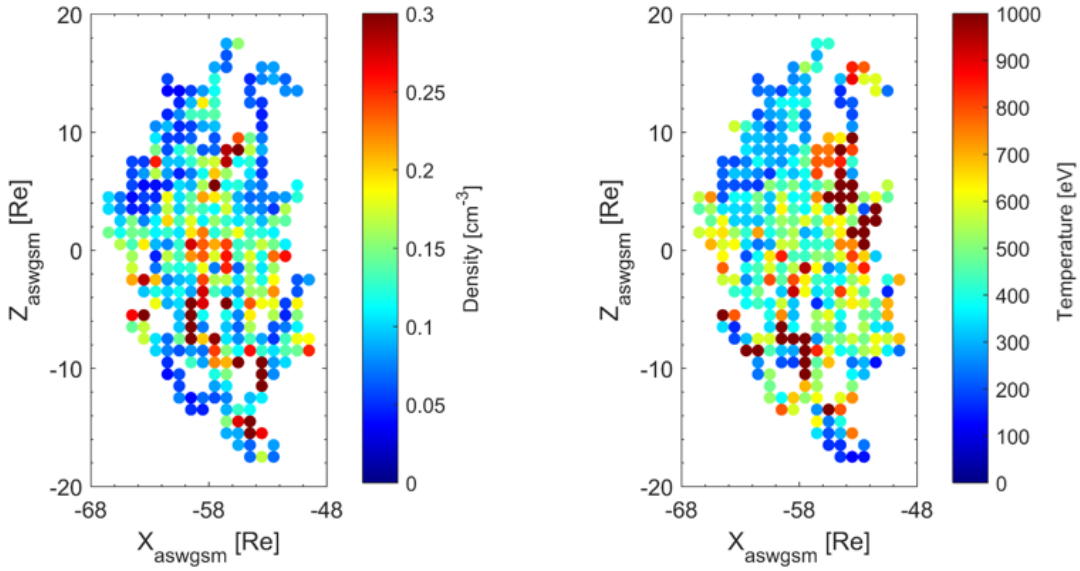

Figure 4.39 : The magnetotail plasma density (on the left) and temperature (on the right) configuration projected onto XZ-plane. The X- and Z- axes covers 20R_E and 40R_E distances creating 1:2 proportion since X- and Z- axes have equal scales. The dark red colors in the equally spaced contour map corresponds to 0.3 cm^{-3} and 1000 eV for the left and right figures, respectively.

As an alternative way to study XZ- plane, XBx- plane density and temperature distributions are given in Figure 4.40. As seen in Figure 4.15b, most of the observations are collected from the region of $-65R_E<X<-54\ R_E$ and Bx=±15nT. The current sheet where Bx=0 nT is marked with a solid, gray line is sandwiched between the plasma sheet region with denser and hotter plasma. The plasma sheet region can be defined as the region with |Bx|<7 to 10 nT. Above that region, plasma with lobe like properties are observed.

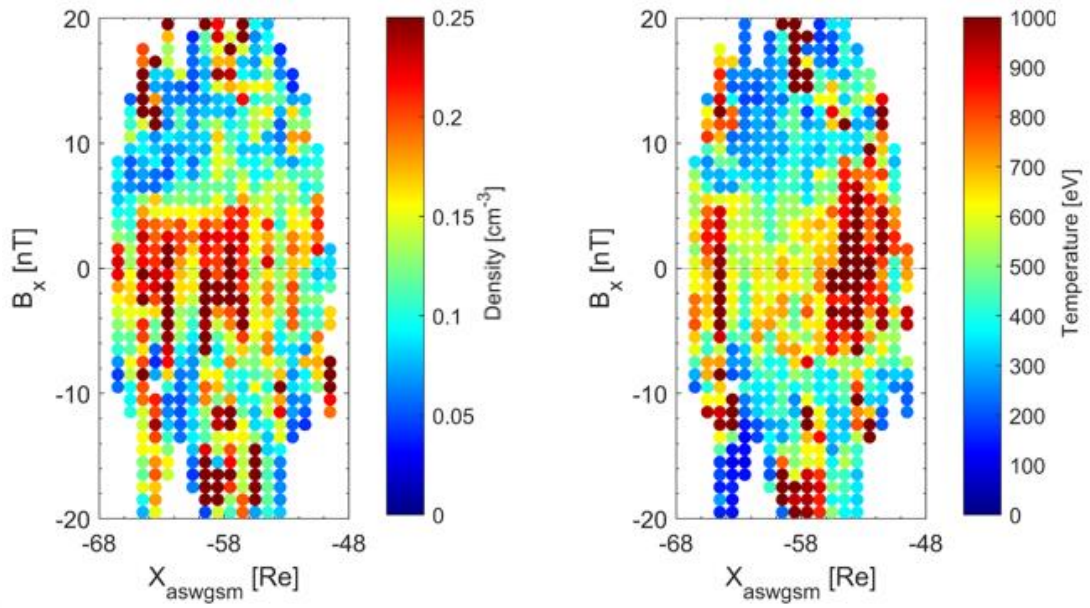

Figure 4.40 : The magnetotail plasma density (on the left) and temperature (on the right) configuration projected onto XBx-plane. This is an alternative way to study XZ-plane since Bx- is another denominator of the magnetotail hemispheres. The current sheet where Bx=0 nT is marked with a solid, gray line. The dark red colors in the equally spaced contour map corresponds to 0.25 cm^{-3} and 1000 eV for the left and right figure, respectively.

Figure 4.41 presents the magnetotail plasma density (a) and temperature (b) configuration projected onto YZ-plane, orthogonal to Earth-Sun line. The Y- and Z-axes covers $60R_E$ and $40R_E$ distances creating 3:2 proportion since Y- and Z- axes have equal scales. The unequal coverage of dawn and dusk portions of the magnetotail is due to orbital parameters of the ARTEMIS probes as seen in Figure 4.34b. The dominantly crossed region, $\pm 7R_E$, is populated with plasma sheet particles. The current sheet where Bx=0 nT is marked with a solid, gray line as well as Y=0 R_E to differentiate the dawn, dusk and north, south portions of the magnetotail from each other. The dark red colors in the equally spaced contour map corresponds to 0.3 cm^{-3} and 1000 eV for the upper and lower figure, respectively. When compared with the coverage map, denser plasma observed near Y=0 to -10 R_E and Z= $-5R_E$ to -10 R_E have very less observations gathered. Therefore, that region is not taken into consideration due to insufficient observations. Besides that, the denser regions are in the north-dusk and south-dawn regions since negative IMF By is influencing the overall magnetotail structure with an average IMF By of -1.1 nT. Under the influence of –IMF By, the magnetosheath field lines merges with magnetotail magnetic field lines in north-dusk and south-dawn regions.

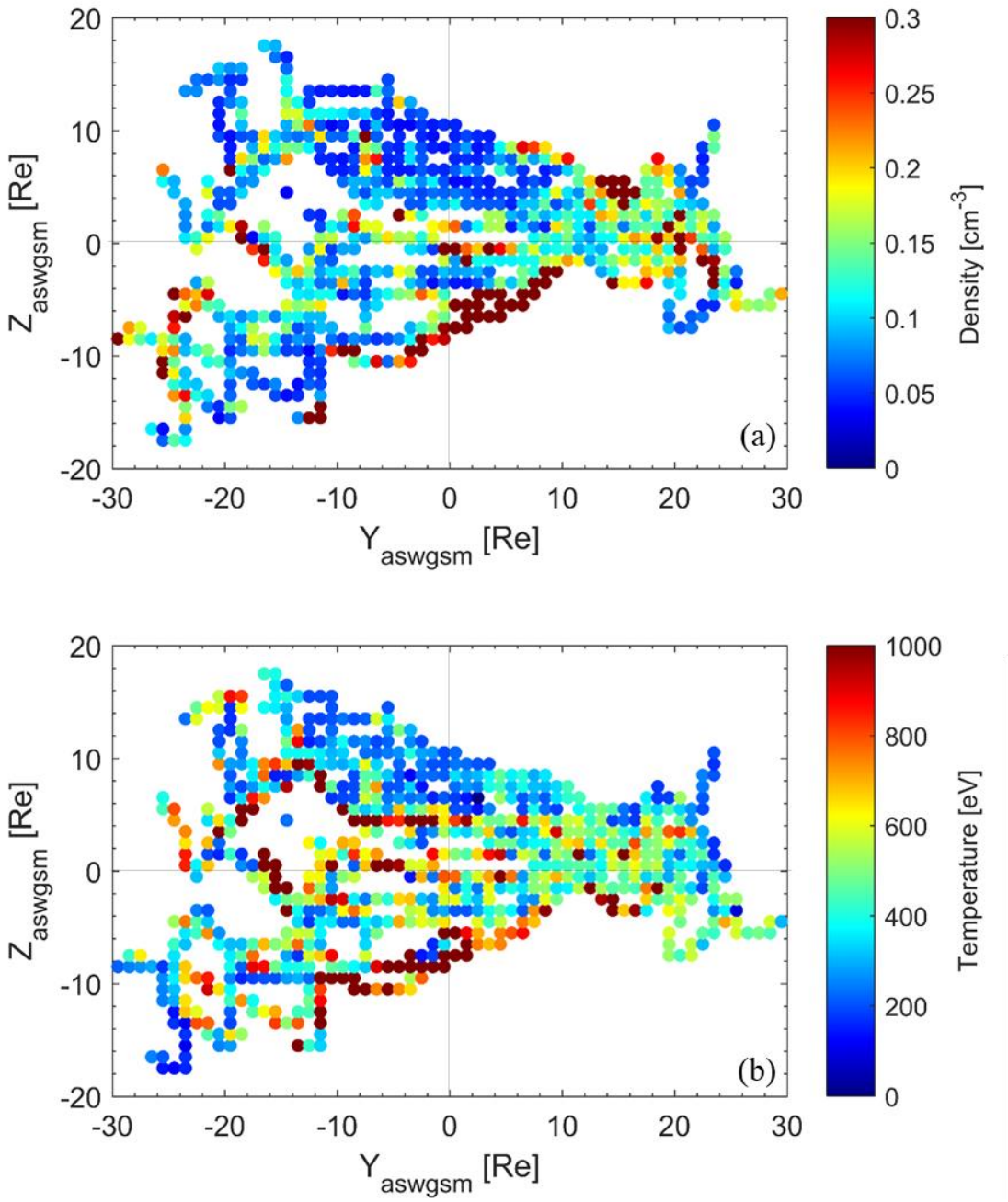

Figure 4.41 : The magnetotail plasma density (a) and temperature (b) configuration projected onto YZ-plane, orthogonal to Earth-Sun line. The Y- and Z- axes covers $60R_E$ and $40R_E$ distances creating 3:2 proportion since Y- and Z- axes have equal scales. The unequal coverage of dawn and dusk portions of the magnetotail is due to orbital parameters of the ARTEMIS probes. The dominantly crossed region, $\pm 7R_E$, is populated with plasma sheet particles. The current sheet where Bx=0 nT is marked with a solid, gray line as well as Y=0 R_E to differentiate the dawn, dusk and north, south portions of the magnetotail from each other. The dark red colors in the equally spaced contour map corresponds to 0.3 cm^{-3} and 1000 eV for the upper and lower figure, respectively.

Figure 4.42 shows the magnetotail plasma density (a) and temperature (b) configuration projected onto YBx-plane, orthogonal to Earth-Sun line. Bx- parameter

is used instead of Z-axis as a divider of the north and south magnetotail. The map seems fuller when Bx- is used instead of Z parameter. The plasma sheet region with denser and hotter plasma compared to boundary regions as well as lobes can be distinguished even by eye in the region of Bx= ±7nT. The region above 7nT (Bx>7nT) where the density and temperature parameters decrease, the magnetotail magnetic field vectors (see Figure 4.21) and the flow velocity vectors (see Figure 4.35) are unidirectional in the plane orthogonal to this plane either in the earthward or tailward direction in the central tail region with $|Y|<10R_E$.

There seems to be an asymmetry in the dawn-dusk direction in the density and temperature parameters. The increased density values are mainly observed in the dusk region whereas higher temperature values are encountered more in the dawn region. The asymmetries in the dawn-dusk direction have been studied in the solar wind-magnetosphere system as well, in which they found that higher densities are observed in the dawn section in the magnetosheath plasma. A review study by Walsh et al. (2014) summarize asymmetries in the dayside magnetosheath in the ion density and temperature in their Table 1. The increased density values are mainly observed in the dawn section up to a percent of 33. The same table also presents the elevated magnetosheath temperatures in the dawn section from 1% to 33%. The increased densities in the dawn region is noticeable in our findings as well. The authors root these asymmetries to various sources, e.g. foreshocks, asymmetric bow shock response to IMF direction, gradient drift etc. which will in return influence the geometry and the property of the magnetopause (Walsh et al., 2014). The gradient drift is also presented as the reason of the dawnside cooling during extended periods of northward IMF (Mata et al., 2014). The ions and electrons drift into the magnetosphere through the magnetopause from dawn and dusk sides, respectively and this entry nearly doubles during flank reconnection (northward IMF)(Walsh et al., 2014 and references therein). Another study by Wang et al (2006) proposes the increased density in the dawn flanks of the magnetosheath leads to increased density of cold component ions towards dawn in the magnetotail especially under northward IMF conditions. In return, creating the conditions for cold, dense plasma sheet during northward IMF. However, brief northward IMF conditions are not found to be enough for entry of cold, dense sheath plasma from reconnection at the flanks (Fujimoto et al., 1998; Mata et al., 2014). Figure 4.43 gives the density (on the left) and temperature (on the right)

distributions projected onto XY plane after sector separation. The contour maps for +IMF Bz (northward) and –IMF Bz (southward) sectors are presented over and under the dashed line, respectively. Figure 4.43a gives the density distribution for northward IMF sector and the higher densities are observed mainly in the dusk section. The coverage map in Figure 4.29a gives the number of observations gathered for northward IMF sector. The area within X= -56 R_E to -58 R_E and Y=0 R_E to 8 R_E as well as the region in the tailward of X=-63R_E and 3R_E>Y>0R_E has been briefly visited, therefore densities about 0.3 cm^{-3} are based on a few passes. Besides, the main reason of not experiencing increased densities in the dawn section is due to the fact that studied by Fujimoto et al. in 1998. Their one year earlier study in 1997 is one of the first studies that observed cold and dense plasma sheet during northward IMF sector (Fujimoto et al., 1997). ARTEMIS observations also show denser plasma in northward IMF sector compared to southward IMF however, higher temperatures can also be observed during northward IMF. The difference of our study is that we assign IMF sector information to magnetotail parameters after calculating solar wind time to travel that distance for each data point. This matching procedure, explained in detail in Section 2.3.1 ensures that magnetotail information belongs to one of the IMF sectors however, does not obligate that sector is a long interval. It can be even one-minute change of the IMF sector from another sector. Therefore, we do not have the information if the northward IMF is brief or prolonged for our ARTEMIS observations.

For southward IMF sector, the density seems to be more symmetric (see Figure 4.43c) as Wang et al (2006) showed in their study. They showed that the asymmetry in the density parameter fades in the southward IMF however; the asymmetry in the temperature stays the same as it is in our observations.

Another perspective is on the asymmetries created by the dynamic pressure, which will displace the magnetopause, creating increased thickness in the dawn section of the magnetopause (Sonnerup et al, 2008). As it is observed by ARTEMIS crossings and given in Section 3.3.

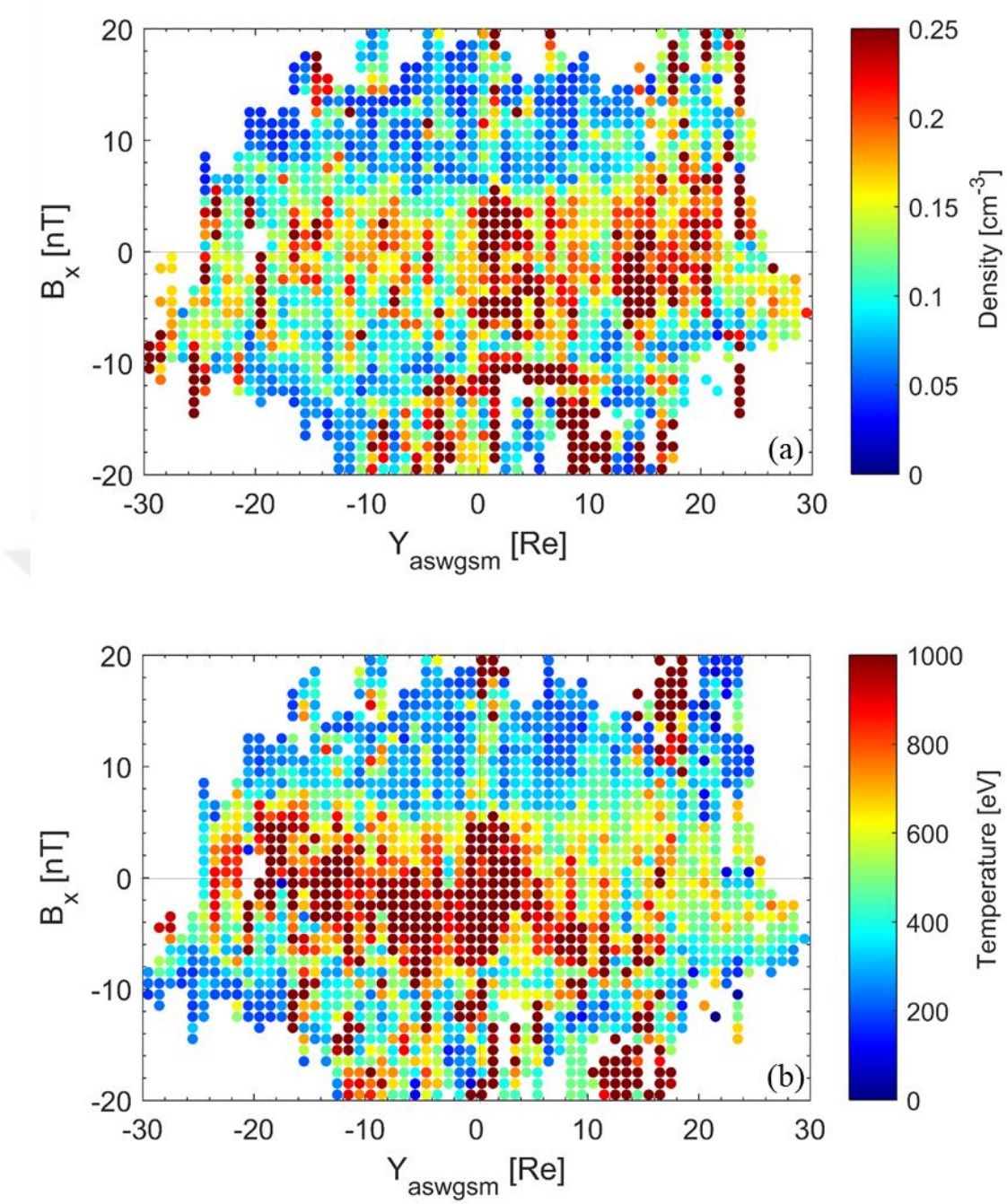

Figure 4.42 : The magnetotail plasma density (a) and temperature (b) configuration projected onto YBx-plane, orthogonal to Earth-Sun line. Bx- parameter is used instead of Z-axis as a divider of the north and south magnetotail. The current sheet where Bx=0 nT is marked with a solid, gray line as well as Y=0 R_E to differentiate the dawn, dusk and north, south portions of the magnetotail from each other. The dark red colors in the equally spaced contour map corresponds to 0.25 cm^{-3} and 1000 eV for the upper and lower figure, respectively.

The XZ- plane projections of the ARTEMIS density and temperature for northward and southward IMF are given in Figure 4.44. The density and temperature profiles for northward IMF is given in (a) and (b), whereas the density and temperature profiles for southward IMF are given in (c) and (d). For northward IMF the corresponding

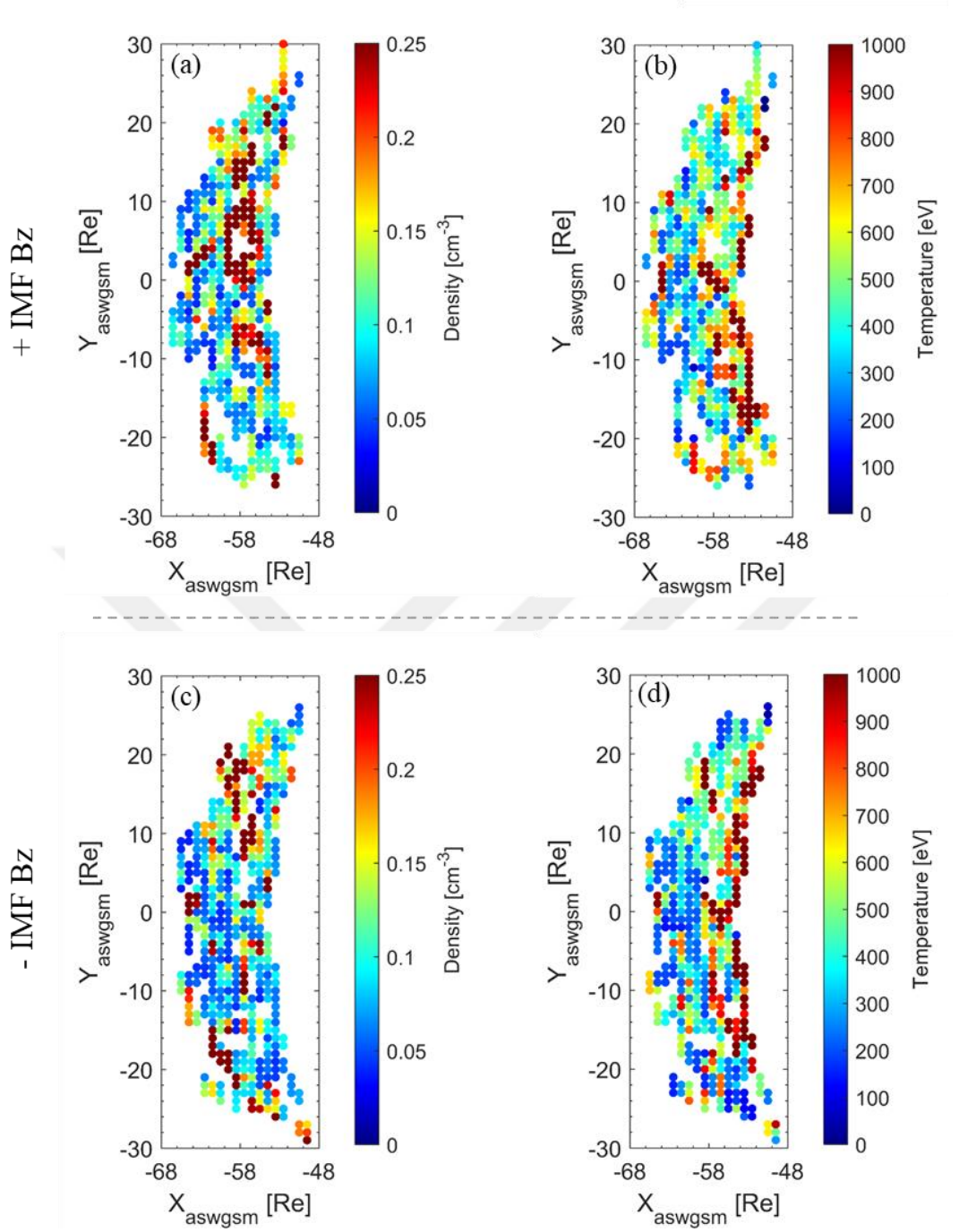

Figure 4.43 : The density (on the left) and temperature (on the right) distributions projected onto XY plane after sector separation. The contour maps for +IMF Bz (northward) and –IMF Bz (southward) sectors are presented over and under the dashed line, respectively. The density profile for northward IMF (a), the temperature profile for northward IMF (b), the density profile for southward IMF (c), and the temperature profile for southward IMF (d) are plotted onto XY plane. The colorbar scales from 0 (dark blue) to 0.25 cm^{-3} (dark red) for density and 0 (dark blue) to 1000eV (dark red) for temperature.

magnetic field vectors are given in Figure 4.16b. The thickening of the plasma sheet with decreased magnetic field magnitudes for northward IMF condition is seen as

expected from theory. The current sheet is sandwiched in between the plasma sheet as well as the central plasma sheet region. In Figure 4.44a, we can clearly see the current sheet on the move ($Z=\pm 10R_E$) in between the central plasma sheet with increased densities higher than 0.25 cm^{-3}. The region in between X= -58 R_E to -60 R_E and Z= -$5R_E$ to -$8R_E$ have similar plasma and magnetic field properties to the current sheet. This might be a formation of bifurcated current sheet as observed by Cluster (Asano et al., 2004). Asano and his colleagues draw a sketch of the expected bifurcated current sheet in their Figure 23 in which the magnetic field line direction, and flow structure resemble to our observations.

Figure 4.46 shows the density (on the left) and temperature (on the right) distributions projected onto YZ plane for +IMF Bz (northward) and –IMF Bz (southward) sectors over and under the dashed line. For the northward IMF sector, the density and temperature profiles are given in (a) and (b), and for the southward IMF sector, the density and temperature profiles are given in (c) and (d). The color bar scales from 0 (dark blue) to 0.25 cm^{-3} (dark red) for density and 0 (dark blue) to 1000eV (dark red) for temperature.

As mentioned earlier, for northward IMF sector main factor to look for is the dense, cold plasma compared to southward IMF sector after Fujimoto et al. (1997). Despite the insufficient observations in some regions some of which is due to low-inclination of the ARTEMIS orbit, we can detect increased density values in northward IMF sector and increased temperature values in southward sector, as expected from the fact that the magnetosphere is open to magnetosheath plasma, cold and dense, to enter during flank reconnection.

As an alternative way, we used Bx as a separator of the northern and southern part of the tail. Again, in Figure 4.48, the density and temperature profiles for northward IMF sector are given in (a) and (b), and the density and temperature profiles for the southward IMF sector are given in (c) and (d). These projections are made onto YBx-plane, and the resulting maps show the cold, dense plasma for northward IMF.

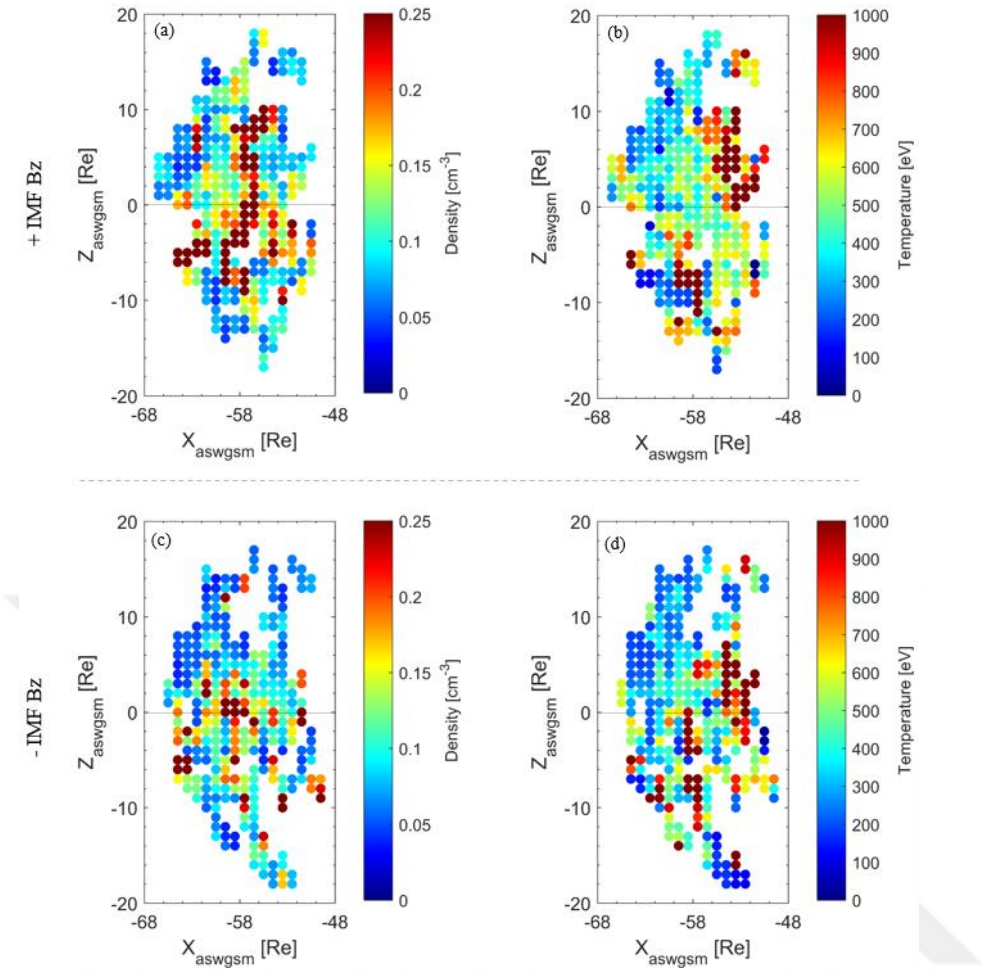

Figure 4.44 : The density (on the left) and temperature (on the right) distributions projected onto XZ plane after sector separation. The contour maps for +IMF Bz (northward) and –IMF Bz (southward) sectors are presented over and under the dashed line, respectively. The density profile for northward IMF (a), the temperature profile for northward IMF (b), the density profile for southward IMF (c), and the temperature profile for southward IMF (d) are plotted onto XZ plane. The colorbar scales from 0 (dark blue) to 0.25 cm^{-3} (dark red) for density and 0 (dark blue) to 1000 eV (dark red) for temperature.

As aforementioned, simulation results by Mata et al. (2014) showed that during long periods of northward IMF, dawn flank temperatures cools more than the dusk side. The authors associate this asymmetric cooling to the gradient drift. However, our observations show the otherwise; the dawn side of the magnetotail has more elevated temperatures compared to dusk side. This might be due to the fact that our observations are matched with IMF instantaneously. For instance, when IMF clock angle is calculated as it is directed northward with 1-minute resolution for a magnetotail data point, we do not concern about the interval or even 1-minute before or after the minute that our one magnetotail information is assigned to northward IMF sector.

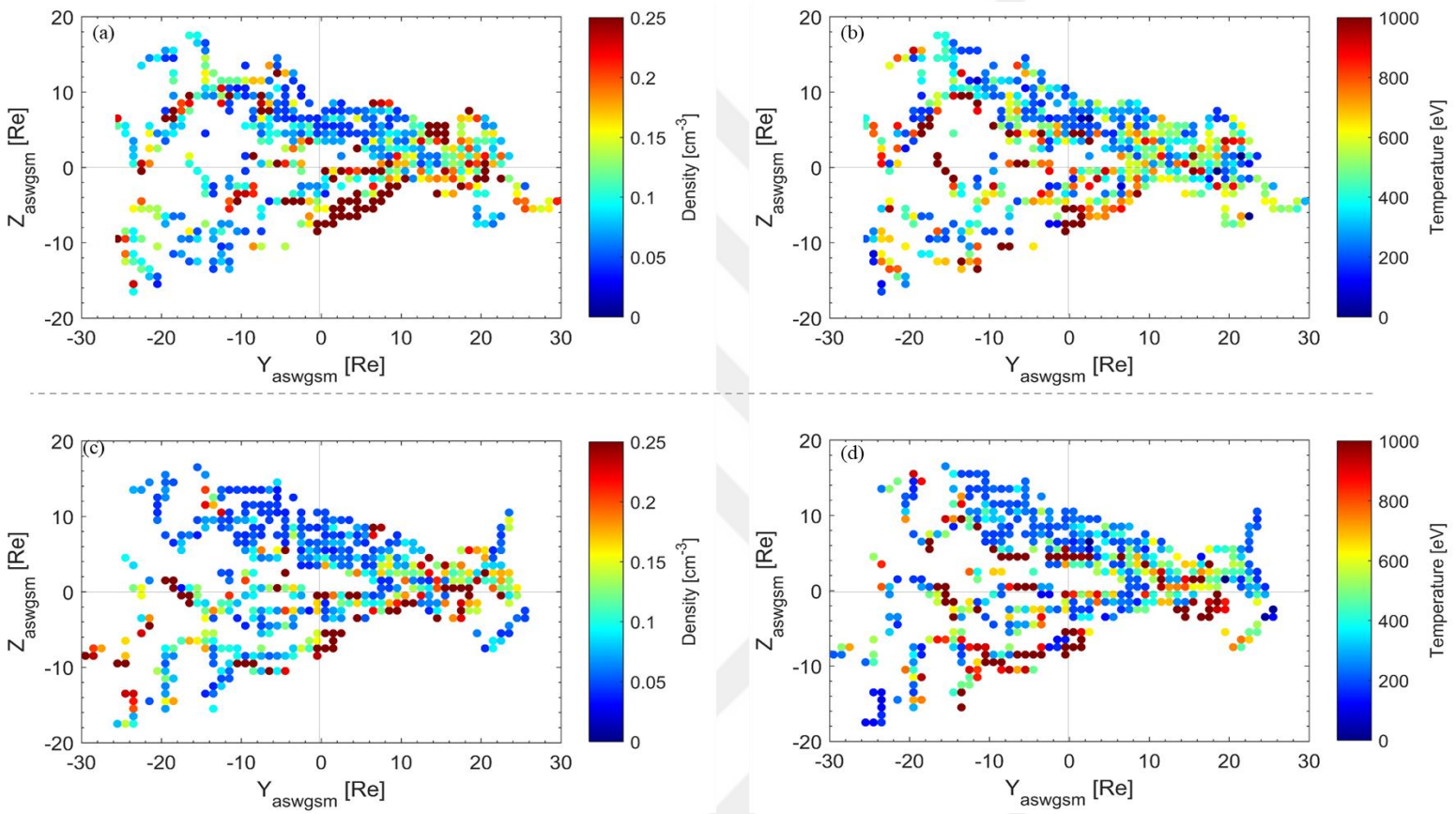

Figure 4.45 : The density (on the left) and temperature (on the right) distributions projected onto YZ plane after sector separation. The contour maps for +IMF Bz (northward) and –IMF Bz (southward) sectors are presented over and under the dashed line, respectively. The density profile for northward IMF (a), the temperature profile for northward IMF (b), the density profile for southward IMF (c), and the temperature profile for southward IMF (d) are plotted onto YZ plane. The color bar scales from 0 (dark blue) to 0.25 cm^{-3} (dark red) for density and 0 (dark blue) to 1000eV (dark red) for temperature.

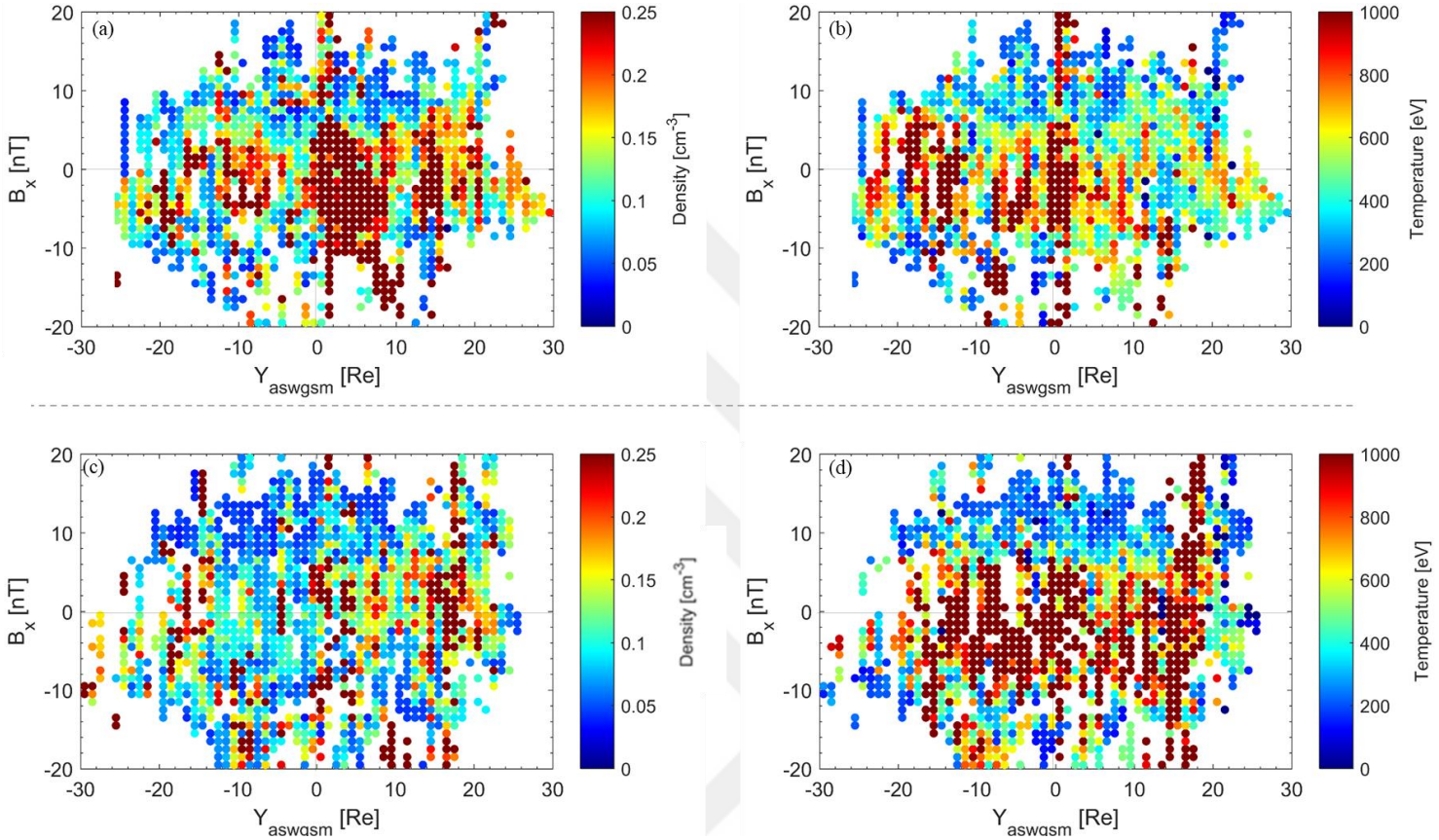

Figure 4.47 : The density (on the left) and temperature (on the right) distributions projected onto YBx plane after sector separation. The contour maps for +IMF Bz (northward) and –IMF Bz (southward) sectors are presented over and under the dashed line, respectively. The density profile for northward IMF (a), the temperature profile for northward IMF (b), the density profile for southward IMF (c), and the temperature profile for southward IMF (d) are plotted onto YBx plane. The color bar scales from 0 (dark blue) to 0.25 cm^{-3} (dark red) for density and 0 (dark blue) to 1000eV (dark red) for temperature.

The cooling of the magnetotail during northward IMF at -10 to -50 R_E distances is expected to mainly be effective in the region adjacent to boundary whereas the cooling of the center tail not as expressed as the outer regions (Tsyganenko and Mukai, 2003). The decrease in the temperature take place near magnetopause regions as well as the dusk region in our observations.

We studied the effect of IMF Bz in XY, XZ, YZ and XBx and YBx planes, now it is time to look for the effect of equatorial IMFs on the density and temperature profiles at lunar distances. The most significant IMF By effect takes place on the YZ- plane. Figure 4.49 is the same as Figure 4.46 but for positive and negative IMF By instead of positive and negative IMF Bz. YBx- plane projections are presented in Figure 4.50, same as Figure 4.48 but again +IMF By and –IMF By sectors are presented over and under the dashed line, respectively. In order to guide the eyes, Y=0, Z=0 and Bx=0 are marked with faint solid gray lines. The density and temperature profiles are given in (a) and (b) for positive IMF By, and in (c) and (d) for negative IMF By. The color bar scales from 0 (dark blue) to 0.25 cm^{-3} (dark red) for density and 0 (dark blue) to 1000eV (dark red) for temperature.

Figure 4.49a shows the increased density mainly in the south-dusk region, the expected increased density values in the north-dawn section is not as obvious as south dusk. This is due limited number of measurements during +IMF By, however, the coverage is much better in –IMF By since most of our observations fall into –IMF By sector. The denser and hotter regions for –IMF By sector, Figure 4.49c and Figure 4.49d, is north-dusk and south-dawn as expected from earlier observations.

Figure 4.50 gives the same effect projected onto YBx-plane, observations assigned to +IMF By sector, given in (a) and (b), are limited in number. Therefore, it is not easy to make inferences, even though temperature configuration shows that the regions adjacent to neutral line are hotter, and gets colder near plasma sheet boundary layer where Bx is about 8 nT. Temperature values rise again near magnetopause boundary. On the other hand, Figure 4.50c displays the density profile for –IMF By sector. Due to higher number of observations from that sector, the denser regions are located near the north-dusk and south-dawn regions where we expect merging occurs. Increased temperatures in south-dawn is observed as well as near neutral line.

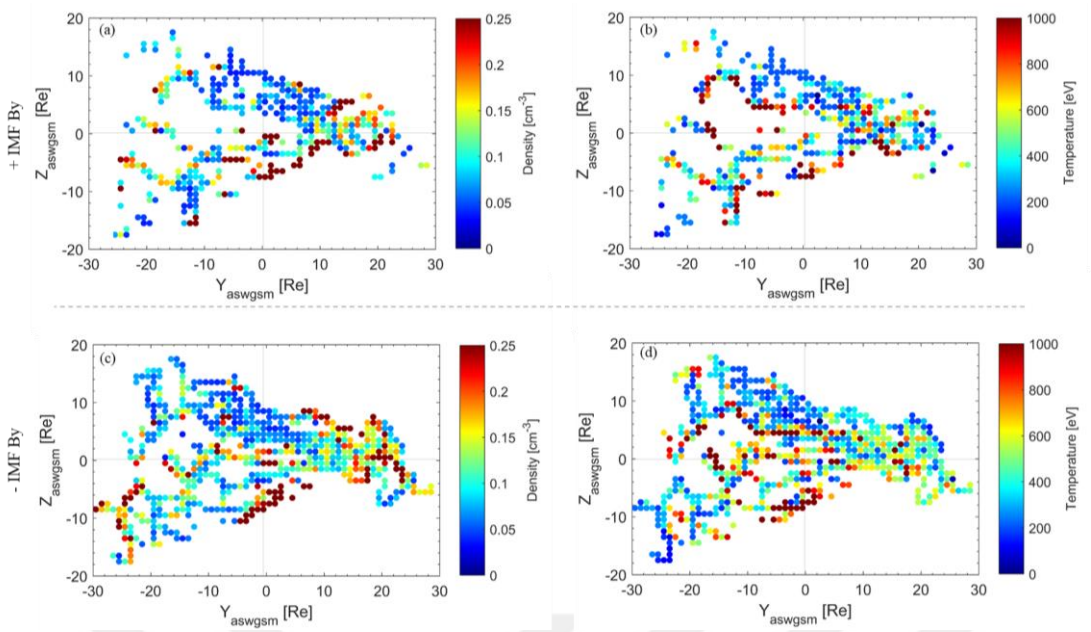

Figure 4.49 : The same as Figure 4.46 but for positive and negative IMF By instead of positive and negative IMF Bz. The density (on the left) and temperature (on the right) distributions projected onto YZ plane after sector separation. The contour maps for +IMF By and –IMF By sectors are presented over and under the dashed line, respectively. The density profile for +IMF By (a), the temperature profile for +IMF By (b), the density profile for – IMF By (c), and the temperature profile – IMF By (d) are plotted onto YZ plane. The color bar scales from 0 (dark blue) to 0.25 cm^{-3} (dark red) for density and 0 (dark blue) to 1000eV (dark red) for temperature.

In order to increase the data set, all IMF By assigned data is converted into positive IMF By sector. The rectification is applied to the magnetotail y- positions if they correspond to –IMF By sector such that sign of the y-positions are changed. Figure 4.51 gives the density and temperature configuration after rectification in the YZ plane in (a) and (b) and in the YBx- plane in (c) and (d). Here, all observations correspond to +IMF By sector in which we expect to see merging in the north-dawn and south-dusk regions.

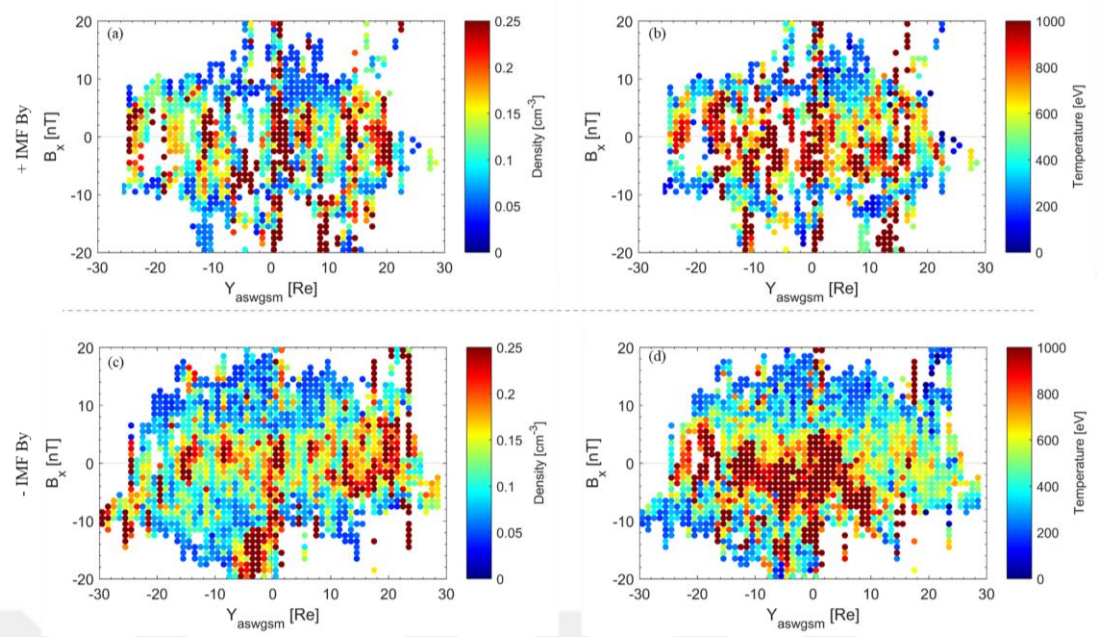

Figure 4.50 : The same as Figure 4.48 but for positive and negative IMF By instead of positive and negative IMF Bz. The density (on the left) and temperature (on the right) distributions projected onto YZ plane after sector separation. The contour maps for +IMF By and –IMF By sectors are presented over and under the dashed line, respectively. The density profile for + IMF By (a), the temperature profile for + IMF By (b), the density profile for – IMF By (c), and the temperature profile for – IMF By (d) are plotted onto YBx plane. The color bar scales from 0 (dark blue) to 0.25 cm^{-3} (dark red) for density and 0 (dark blue) to 1000eV (dark red) for temperature.

Figure 4.52 and Figure 4.54 displays the magnetotail magnetic pressure and plasma gas configuration projected onto XZ (a), YZ (b), and XY (c) planes. The same distributions are plotted onto XBx- (on the left) and YBx- (on the right) planes in Figure 4.53 and Figure 4.55. The color bar scales from 0 (dark blue) to 0.06 nPa (dark red). In Figure 4.53 and in Figure 4.55, we clearly see where the magnetic pressure and where the gas pressure is dominant. We can see from the magnetic pressure map in the XBx- and YBx- planes that the plasma sheet has a thickness of 7 R_E with depressed magnetic field values and plasma with higher density and temperature. The thickness seems to decrease in the central tail especially about Y=3R_E as expected from the theory.

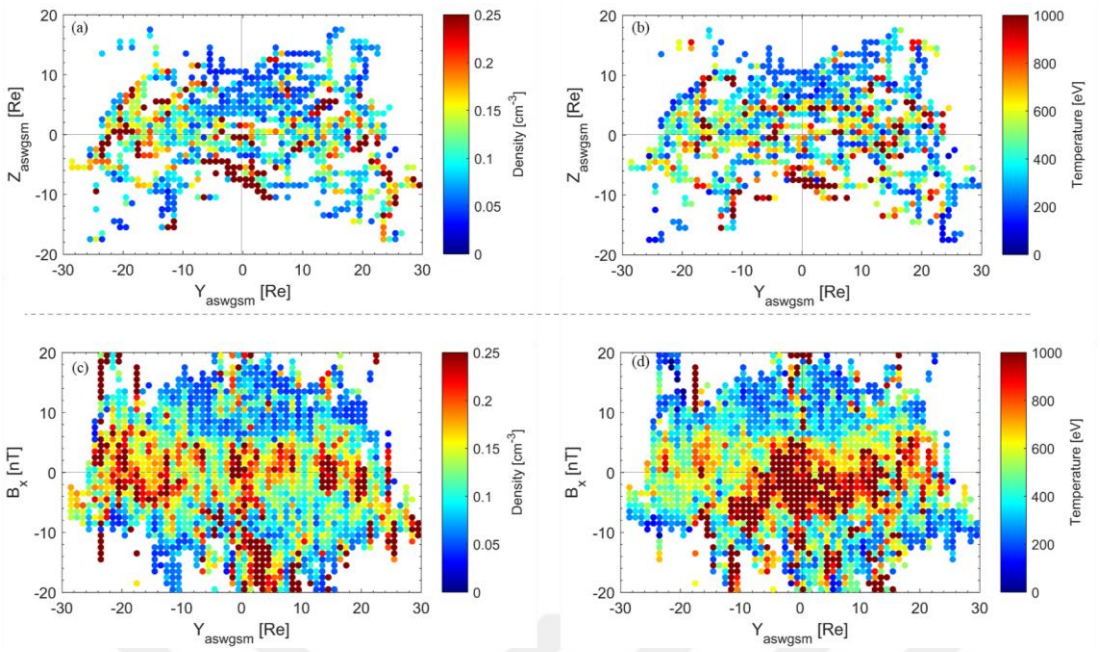

Figure 4.51 : The density (on the left) and temperature (on the right) distributions for positive and negative IMF By in Figure 4.50 are rectified here in which the magnetotail y positions are multiplied by -1 for negative IMF By sector and combined with the data set of positive IMF By sector. The contour maps for YZ and YBx planes are presented over and under the dashed line, respectively. The plots show the density profile to the rectified IMF By sector in YZ plane (a), the temperature profile for the rectified IMF By sector in YZ plane (b), the density profile to the rectified IMF By sector in YBx plane (c), and the temperature profile to the rectified IMF By sector in YBx plane (d). The colorbar scales from 0 (dark blue) to 0.25 cm^{-3} (dark red) for density and 0 (dark blue) to 1000eV (dark red) for temperature.

In order to understand the regimes of the plasma within the magnetotail, we will present scatter plots of density and temperature. Figure 4.56 presents the relation between the density and temperature for all magnetotail data. This plot shows that there is two populations with in the data, one of which has lower temperature values. This colder plasma region have temperatures less than 6eV and densities varying between $5x10^{-3}$ cm^{-3} to $5x10^{-1}$ cm^{-3}. The maximum density values, about $4.5cm^{-3}$, are encountered in the higher temperature population with the highest temperature values reaching nearly 10 keV.

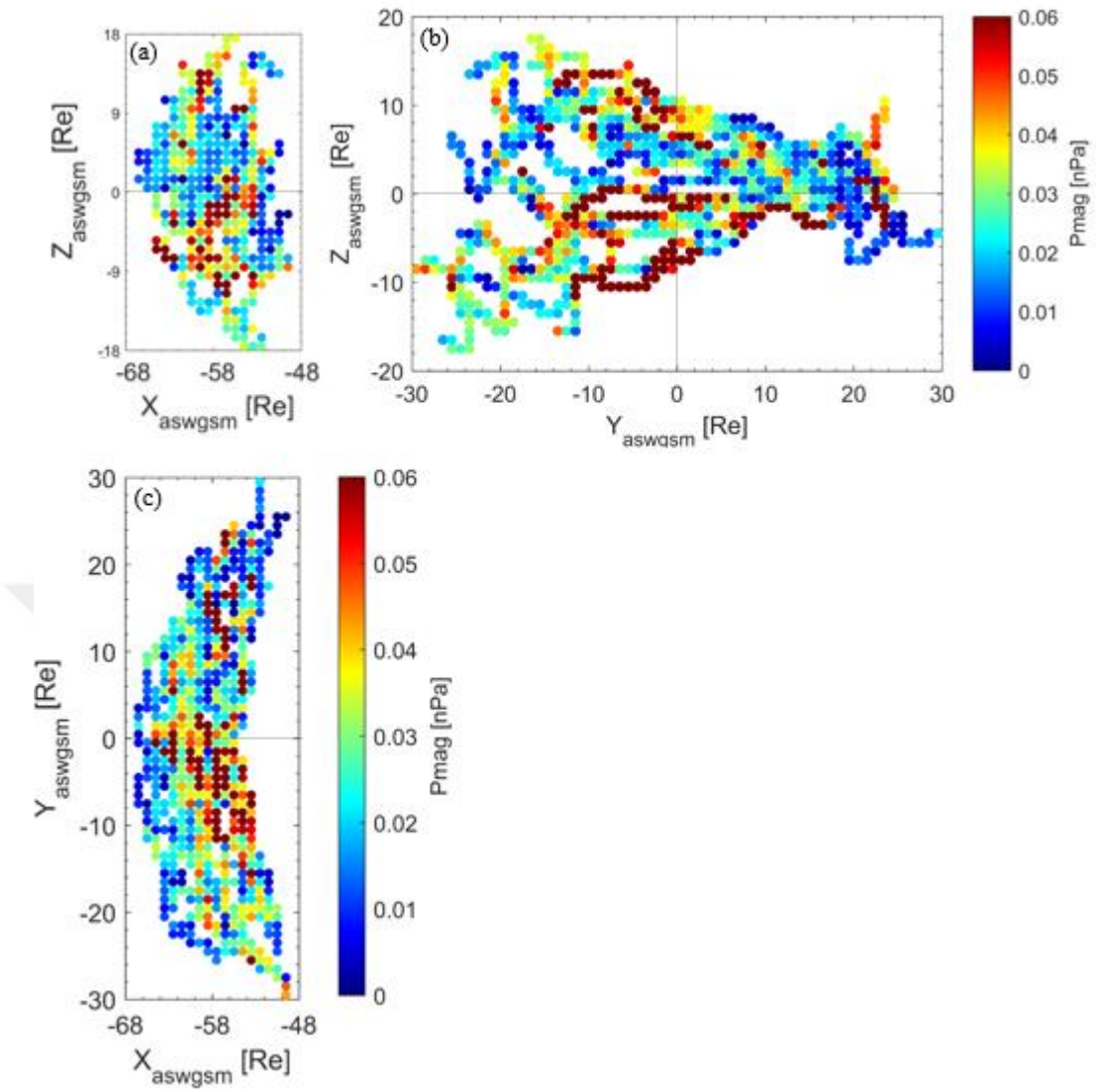

Figure 4.52 : The magnetotail magnetic pressure configuration projected onto XZ (a), YZ (b), and XY (c) planes. The colorbar scales from 0 (dark blue) to 0.06 nPa (dark red).

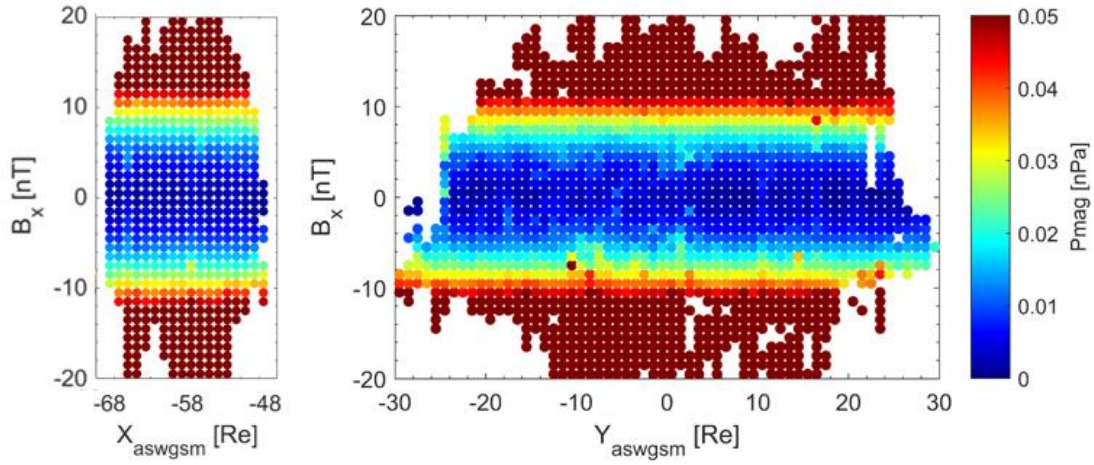

Figure 4.53 : The magnetotail magnetic pressure configuration projected onto XBx- (on the left) and YBx- (on the right) planes. The color bar scales from 0 (dark blue) to 0.05 nPa (dark red).

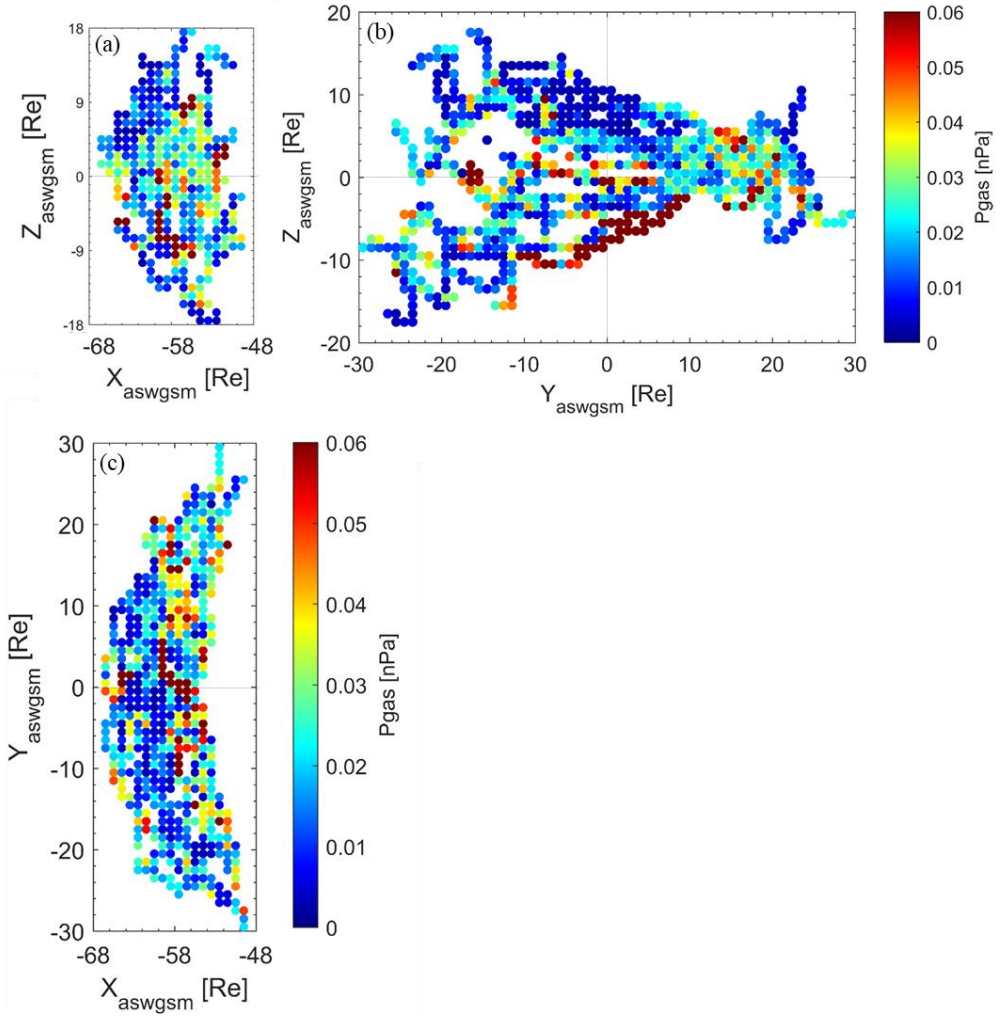

Figure 4.54 : The magnetotail gas pressure configuration projected onto XZ (a), YZ (b), and XY (c) planes. The color bar scales from 0 (dark blue) to 0.06 nPa (dark red).

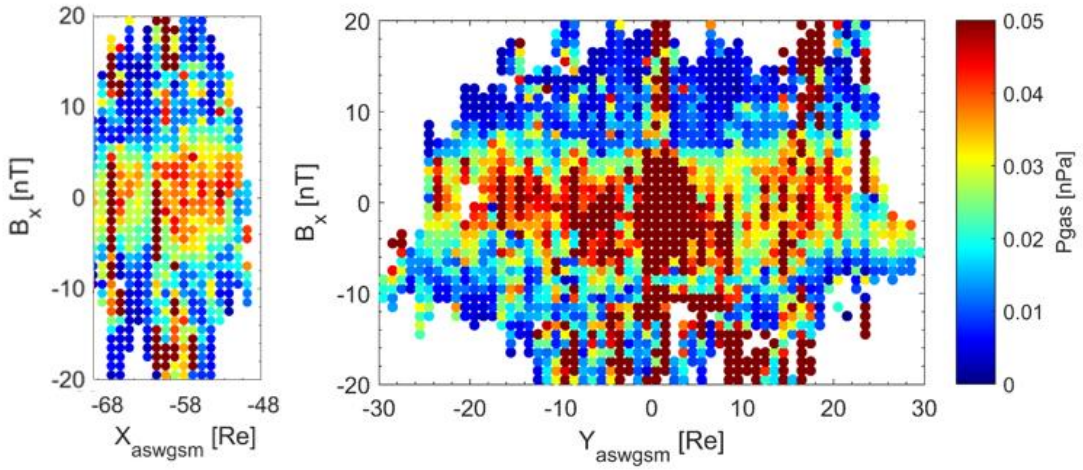

Figure 4.55 : The magnetotail gas pressure configuration projected onto XBx- (on the left) and YBx- (on the right) planes. The color bar scales from 0 (dark blue) to 0.05 nPa (dark red).

Figure 4.57 presents the same density, temperature relation for four IMF sectors, each having different colors. Northward IMF (+IMF Bz) sector is given on the upper left (in blue) whereas the southward IMF (–IMF Bz) sector is given on the upper right side (in purple). The equatorial IMFs are shown in the second row; westward IMF (+IMF By) sector on the lower left (in orange), and eastward IMF (–IMF By) sector on the lower right side (in yellow). When the IMF is northward, there is no reconnection on the dayside region. The plasma sheet density should therefore decrease. However, a very cold and dense plasma sheet is observed when the IMF is northward (Fujimoto et al., 1996, 1998; Terasawa et al., 1997). This is explained by the high latitude reconnection at the flanks enabling entry of the plasma with solar wind origin into the plasma sheet especially in the near Earth tail (Li et al., 2005). ARTEMIS observations shows that colder plasma is more likely to be encountered during northward IMF compared to the southward IMF conditions, see the first row of Figure 4.57. However, the density does not present the expected feature; denser plasma is more likely to be encountered in the southward IMF compared to northward IMF condition. This might be due to the fact that cold, dense plasma sheet studies are based on long term northward IMF conditions, longer than half an hour (Nagai et al., 1998; Li et al., 2005). Our observations on the other hand, are instantaneously synchronized with the IMF information. Therefore, the temperature not giving the expected response might be due to the nature of the methodology used in this study.

Another point is the rearrangement of the plasma populations; there are now three plasma populations appearing in the plots after IMF separation. The lower temperature population stays the same as it is in the Figure 4.56 however; a plasma population with temperature values higher than 1 keV seems to appear with density values changes mainly between 0.02-0.1 cm^{-3} with a maximum of 0.9 cm^{-3}. This group seems combined with the lower temperature group in the all data plot. The regions of these populations should be investigated deeply. The first step towards detailed investigation is presented in Section 4.4.4 in the figures from Figure 4.75 to Figure 4.72.

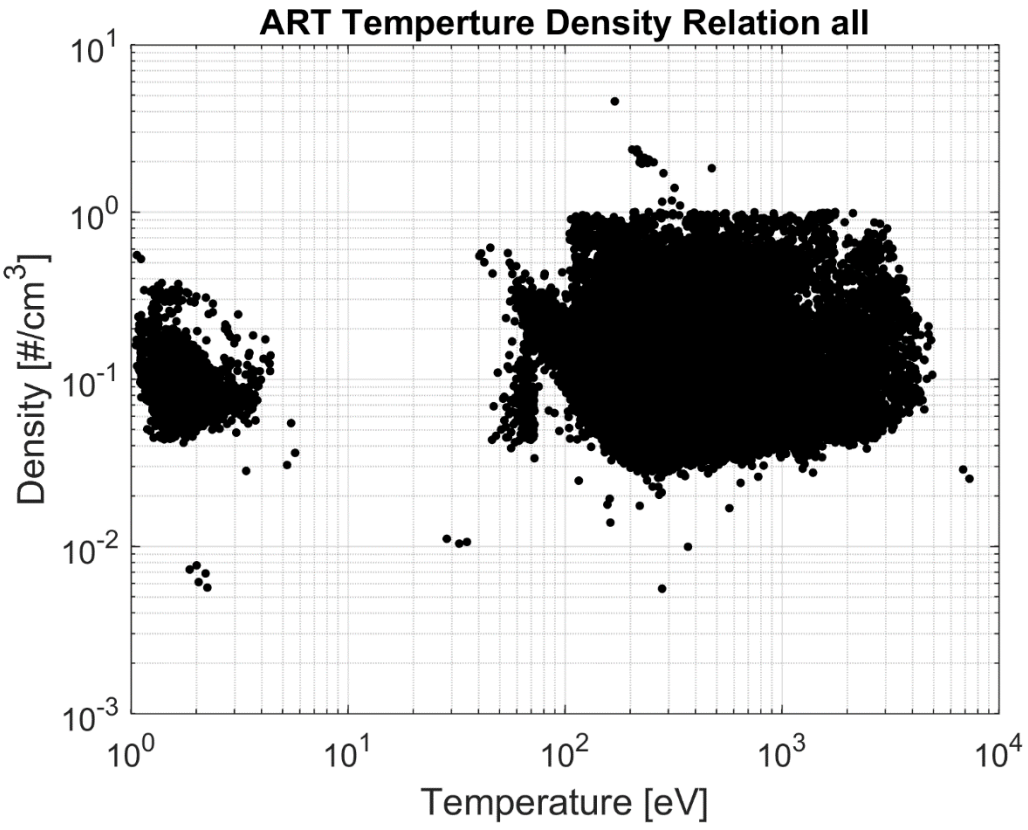

Figure 4.56 : The density, temperature relation for all IMF sectors plotted onto logarithmic scale axes.

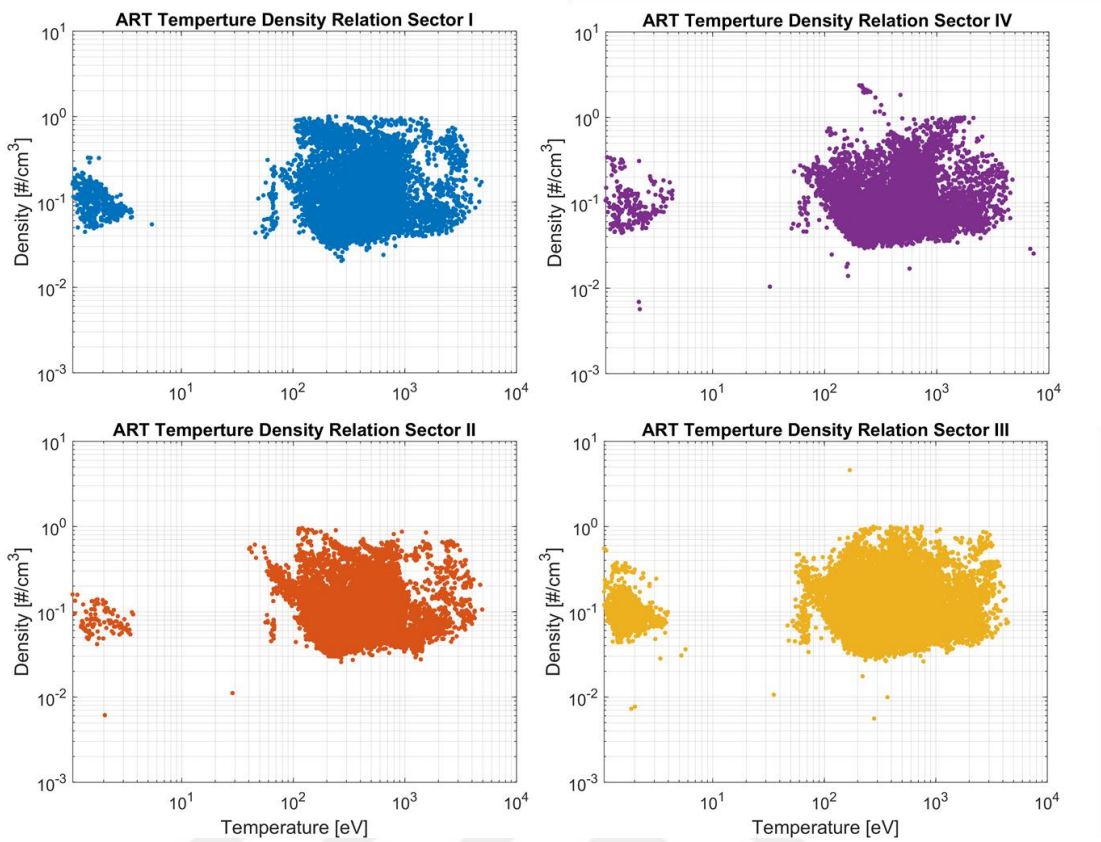

Figure 4.57 : The density, temperature relation for four IMF sectors: Northward IMF (+IMF Bz) sector on the upper left (in blue), southward IMF (–IMF Bz) sector on the upper right side (in purple), westward IMF (+IMF By) sector on the lower left (in orange), and eastward IMF (–IMF By) sector on the lower right side (in yellow).

4.4 Statistical Investigation of the Magnetotail Parameters

In this section, we plot histograms of the x-,y- and z- components of the magnetotail magnetic field and velocity parameters after sector separation. These plots will complement the results from the vector maps in Section 4.1 and Section 4.2. This part starts with the statistical investigation of the all observations; i.e. magnetic field, plasma flow, density and temperature, for the corresponding IMF direction. After the comparisons of the magnetotail response to the IMF polarity in the y- and z- direction, we separate the magnetotail observations into four tail quadrants in order to evaluate how the tail is affected by the direction of the dominant IMF sector.

4.4.1 Magnetic field components

The observations used to create the magnetic field vector maps given in Section 4.1 are studied statistically here in this Section.

We use 10 nT wide bins borders/edges at Bx= -30,-20,-10, 0, 10, 20, 30 nT for all sectors. We use 5 nT wide bins with edges at By and Bz= -15, -10, -5, 0, 5, 10, 15 nT for all sectors. Mean values of each panel is marked with a red line. In addition, mean and median values are given in the text box.

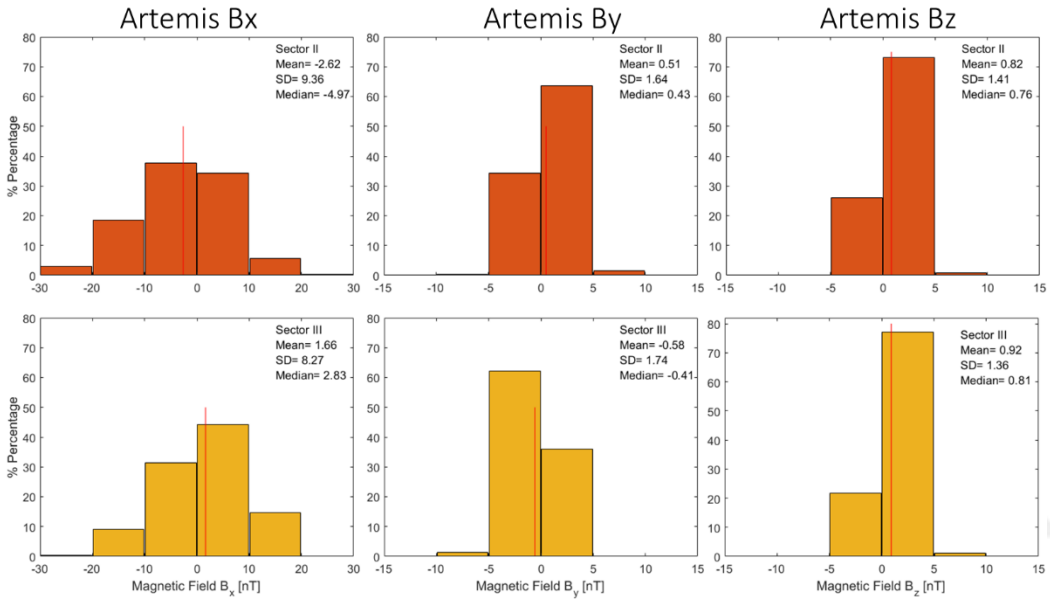

Figure 4.58 : Histograms of the percent occurrence distribution of the ARTEMIS magnetic field vector components Bx, By, and Bz, respectively for west-east IMFs. The plots in the first row, in orange color, corresponds to Westward IMF (+IMF By sector) and the plots in the second row, in yellow color, corresponds to Eastward IMF (–IMF By sector). Mean values are shown with a red line. The mean, standard deviation and median values are given in the right corner. For Bx, first column, 10 nT wide bins are used whereas for By and Bz, in second and third column, 5 nT wide bins are used.

Figure 4.58 gives the distribution of the magnetotail magnetic field components (Bx, By and Bz) when the IMF is either in positive y (upper part in orange color) or in negative y (below part in yellow color) direction. The main relation is expected to take place in the y-component of the ARTEMIS observations. The figure shows that when the IMF is dominant in the positive y-direction, the distribution of the magnetotail magnetic field lines are skewed towards positive, with a value of 0.51 nT. On the other hand, when IMF By is negative, the histogram shows that the magnetotail magnetic field lines in the y-direction are mainly negative with a mean value of -0.58nT. This

IMF By effect will be investigated deeply to look for any IMF By related asymmetries within the tail in Section 4.4.4 (see Figure 4.67).

Figure 4.59 gives the same distribution in the Figure 4.58 for the northward and southward IMF sectors instead of westward and eastward IMF sectors. The magnetotail magnetic field averages in the y-direction is nearly zero (-0.01 nT for northward and -0.17 nT for southward IMF). When compared with the equatorial IMF distributions in Figure 4.58, Figure 4.59 gives a distribution that is more symmetrical in y-direction.

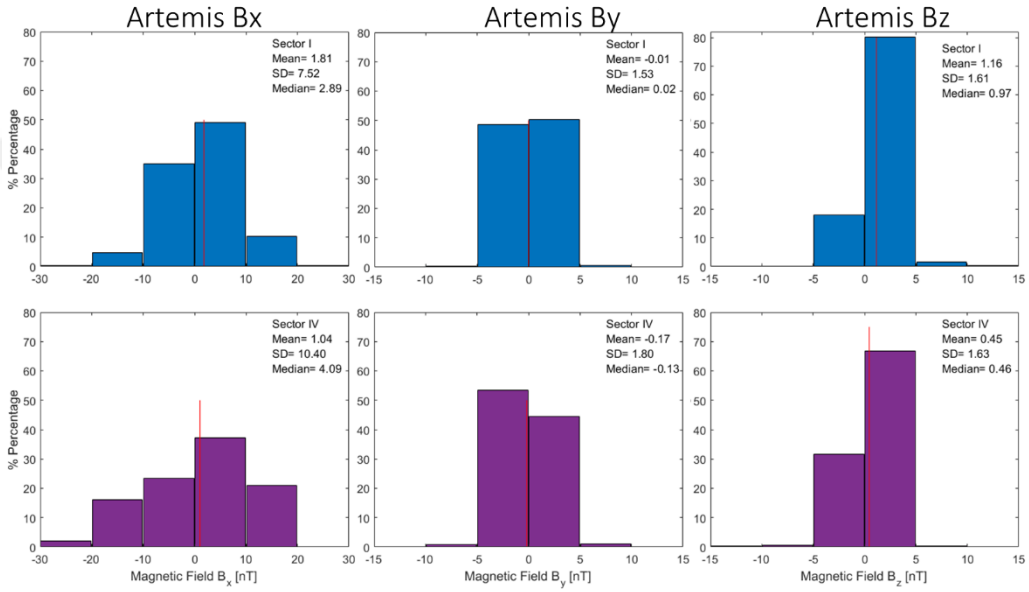

Figure 4.59 : Histograms of the percent occurrence distribution of the ARTEMIS magnetic field vector components Bx, By, and Bz, respectively for north-south IMFs. The plots in the first row, in blue color, corresponds to Northward IMF (+IMF Bz sector) and the plots in the second row, in purple color, corresponds to Southward IMF (–IMF Bz sector). Mean values are shown with a red line. The mean, standard deviation and median values are given in the right corner. For Bx, first column, 10 nT wide bins are used whereas for By and Bz, in second and third column, 5 nT wide bins are used.

The magnetotail Bz histogram for northward IMF sector skewed towards the positive with a mean value of 1.16 nT compared to the southward IMF sector with a mean value of 0.45 nT. The stronger northward directed field lines means tail is more dipolar during northward IMF, as expected whereas the weaker northward magnetotail field lines mean more stretched tail during southward IMF sector.

4.4.2 Plasma velocity components

The categorization of the magnetotail plasma according to its speed is a common way of investigating general features of the flow. One of the earliest paper in which the plasma characteristics are classified according to its velocity is the study by Hayakawa et al. (1982). They investigate flows by dividing them into three category; fast (|Vx|>300 km/s), medium (100 km/s <|Vx|<300 km/s) and slow (|Vx|<100 km/s) flow. They conclude that all slow flows, either earthward or tailward, can be seen in any region throughout the plasma sheet but mostly seen when IMF is northward. Using the same velocity limits, Nagai et al. (1998) discussed that fast tailward flows are associated with magnetic reconnection at X>-33Re. Studies by Nagai et al. (1994) and Nakamura et al. (1995) argued that bipolarity is a common feature for tailward flows in the tail beyond 50 R_E. Many studies such as Ohtani et al. (2004) uses the same criterion, V>300 km/s, as fast flow identifier but some other studies such as Baumjohann et al. (1990) and Angelopoulos et al. (1992, 1994) adopted the criterion |Vx|> 400 km/s for defining fast flows. Our results would not change significantly when we use other criterion values. With criterion of 300 km/s, we obtained 43 tailward flow events. Among these 43 tailward flows, the velocity becomes <-400 km/s for 42.

Baumjohann et al. (1990, 1991) showed that fast flows are bursty; i.e. flows have high speed enhancements in small time scales (Angelopoulos, 1992). Angelopoulos et al. (1994) defined their fast flows to be segments of continuous ion flow with magnitude V>100 km/s including at least one V> 400 km/s sample. In our classification method, we did not use continuity as a criterion. We examined all tailward and earthward flow events instantaneously and matched with concurrent interplanetary magnetic field data. Therefore, the nature of our methodology used in this study is not appropriate to investigate the bursty bulk flows.

Figure 4.60 shows all magnetotail plasma flow at lunar distance in three categories; slow, medium and fast. The first row shows the XZ-plane, and the second one showing the XY-plane. These rose graphs display both the number of events; axis scale is shown within circles and the direction of the flow. The main directions of the flow is written as northward, southward, tailward, earthward in the XZ- plane and duskward, dawnward, tailward, and earthward in the XY-plane.

Figure 4.60 shows that slow flows are dominant and fast flows are nearly rare. In XZ plane, tailward direction is the favored one especially in slow flows with the ratio of tailward to earthward flow about 3.5:1. In fast flows, tailward flow is still dominant (tailward to earthward flow ratio of about 1.8:1) but a slight southward tendency can also be observed. In XY plane, slow flows shows symmetricity in y- direction while presenting dominancy in the tailward direction. In fast flows, tailward and duskward flows seen more frequently. The dawn-dusk directed flows are nearly only seen with the slow flow condition.

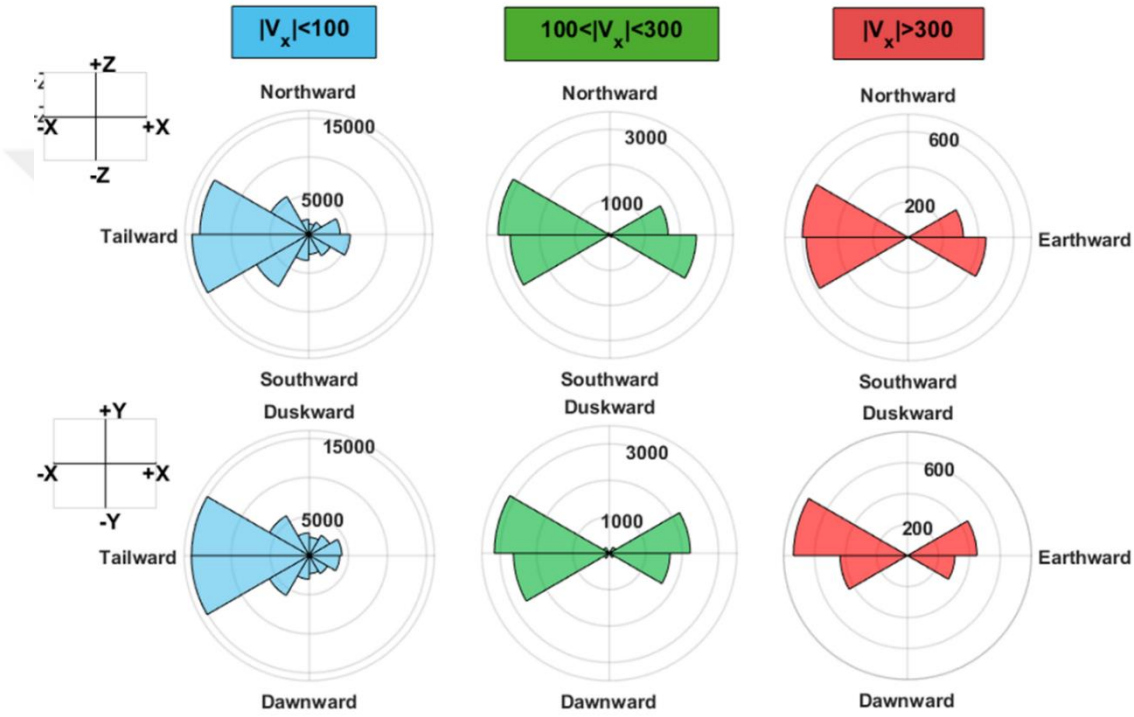

Figure 4.60 : All magnetotail plasma flow at lunar distance in XZ- (first row) and XY- (second row) plane. These rose graphs display both the number of events, axis scale is shown within circles and the direction of the flow, tailward/earthward directed flows are in left/right while northward/southward or duskward/dawnward flows in up/down. The flows are divided into three according to its speed; slow flow (|Vx|<100 km/s), medium flow (100 km/s <|Vx|<300 km/s) and fast flow (|Vx|>300 km/s).

Figure 4.61 shows the normal distribution fits of IMF Bz with respect to density for slow, medium and fast flows. Even if this data is not separated according to tail regions, i.e. PS, central PS, PSBL etc., higher velocity cases tend to occur with southward IMF cases in all parts of tail. There is a slight difference when slow and medium flow cases are compared.

The observations used to create the magnetotail flow maps given in Section 4.2 are studied statistically here. We use bins with 100 km/s wide higher values for Vx panels (±500 km/s) and 50 km/s wide bins with ±150 km/s limits at each end for Vy and Vz panels for all sectors.

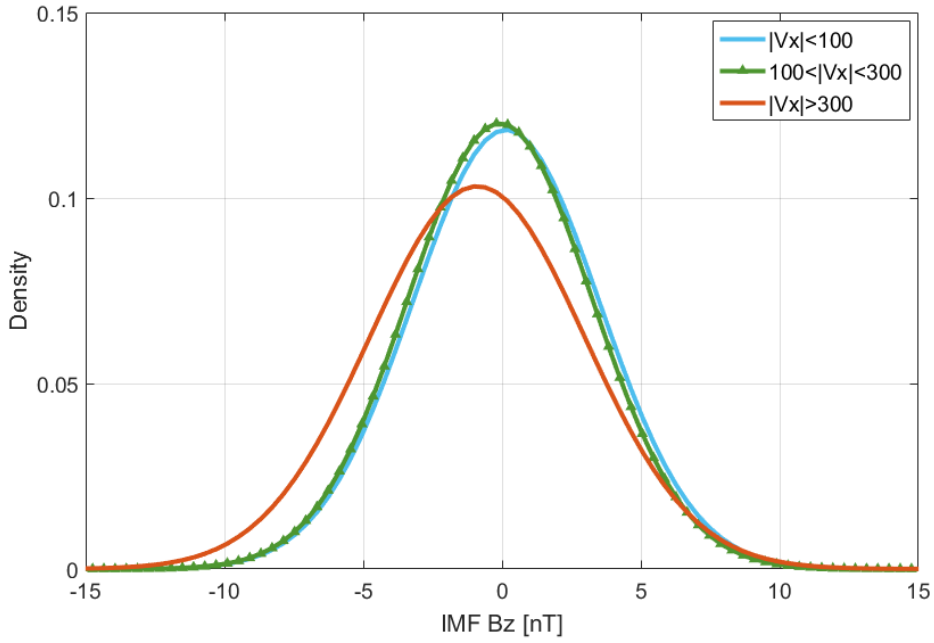

Figure 4.61 : Normal distribution fits of IMF Bz versus density categorized with respect to Vx. For slow flows (|Vx|<100 km/s) μ=0.14±0.01; for medium flows (100<|Vx|<300 km/s) : μ=-0.08±0.03 and for fast flows (|Vx|>300 km/s) μ =-0.90±0.09.

Figure 4.62 gives the distribution of the magnetotail plasma velocity components (Vx, Vy and Vz) when the IMF is either in positive y (+IMF By: upper part in orange color) or in negative y (–IMF By: below part in yellow color) direction. The mean, standard deviation and median values are given in the right corner. For Vx, first column, 100 km/sec wide bins are used within the range of ±500 km/sec whereas for Vy and Vz, in second and third column, 20 km/sec wide bins are used within the range of ±150 km/sec. The tendency of the flow direction to follow the direction of the dominant IMF direction can not be observed here. For both equatorial IMF, the flow in positive y-direction displays faster flows reaching nearly 150 km/sec. The distribution of the magnetotail plasma flow in the x-direction is nearly the same with mean Vx about -21.8 km/sec for +IMF By and -17.4 km/sec for –IMF By. The dominancy is the tailward flow can be observed for both sector.

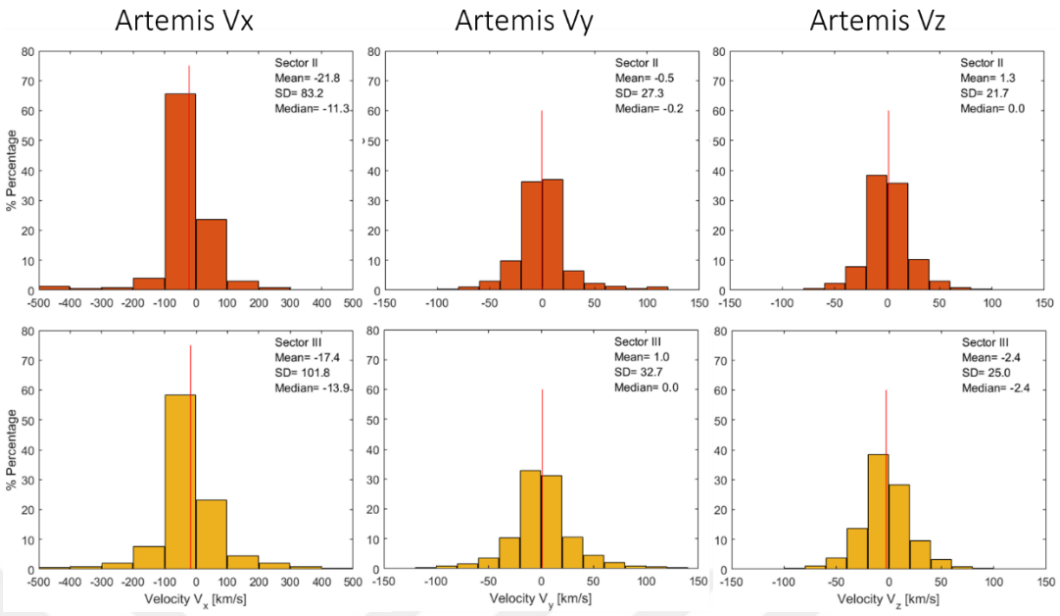

Figure 4.62 : Histograms of the percent occurrence distribution of the ARTEMIS plasma velocity vector components Vx, Vy, and Vz, respectively for east-west IMFs. The plots in the first row, in orange color, corresponds to Westward IMF (+IMF By sector) and the plots in the second row, in yellow color, corresponds to Eastward IMF (–IMF By sector). Mean values are shown with a red line. The mean, standard deviation and median values are given in the right corner. For Vx, first column, 100 km/sec wide bins are used within the range of ±500 km/sec whereas for Vy and Vz, in second and third column, 20 km/sec wide bins are used within the range of ±150 km/sec.

Figure 4.63 gives the same distribution in the Figure 4.62 for the northward and southward IMF sectors instead of westward and eastward IMF sectors for ARTEMIS plasma velocity vector components Vx, Vy, and Vz, respectively. The plots in the first row, in blue color, corresponds to Northward IMF (+IMF Bz sector) and the plots in the second row, in purple color, corresponds to Southward IMF (–IMF Bz sector). The increase in the magnitude of tailward flows can be observed during southward IMF sector with a mean value of -25.1 km/sec whereas the mean is about -7.1 km/sec for northward IMF sector.

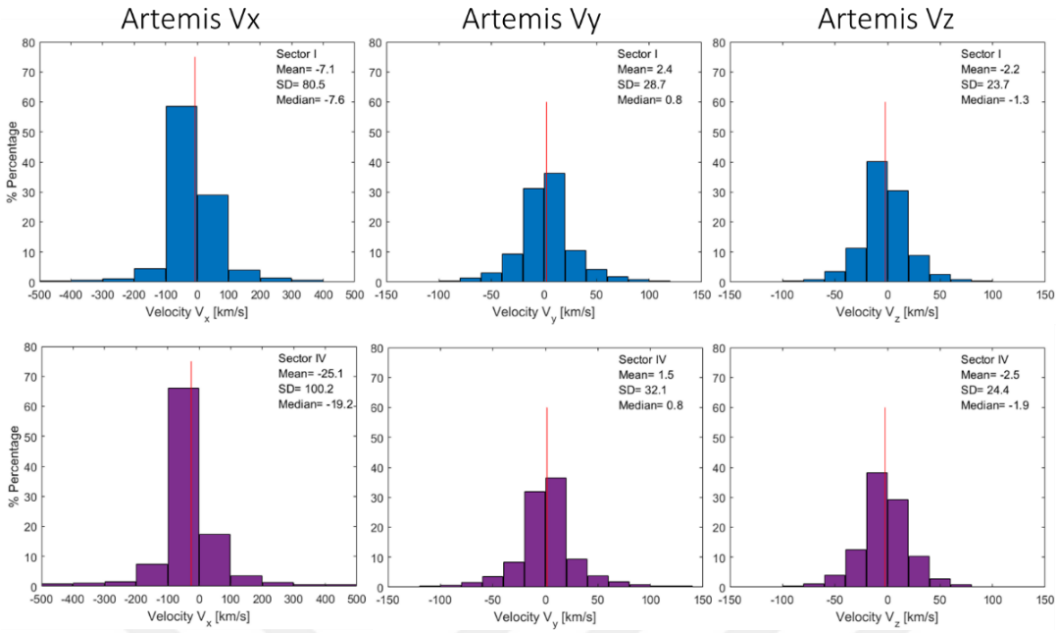

Figure 4.63 : Histograms of the percent occurrence distribution of the ARTEMIS plasma velocity vector components Vx, Vy, and Vz, respectively for north-south IMFs. The plots in the first row, in blue color, corresponds to Northward IMF (+IMF Bz sector) and the plots in the second row, in purple color, corresponds to Southward IMF (–IMF Bz sector). Mean values are shown with a red line. The mean, standard deviation and median values are given in the right corner. For Vx, first column, 100 km/sec wide bins are used within the range of ±500 km/sec whereas for Vy and Vz, in second and third column, 20 km/sec wide bins are used within the range of ±150 km/sec.

4.4.3 Plasma density and temperature parameters

In this section, we will investigate how density and temperature distributions change in response to the IMF direction. We do not expect to see a major change in the plasma parameters for the +IMF By and –IMF By sectors (Figure 4.64). From theory, we expect to see the change where the merging occurs. However, these plots are provided as a baseline before separating the magnetotail data according to the quadrants of the tail in Section 4.4.4 .

Figure 4.65 gives the percent occurrence distribution of the magnetotail plasma density in the left and plasma temperature in the right. The plots in the first row, in blue color, corresponds to northward IMF (+IMF Bz sector) and the plots in the second row, in purple color, corresponds to southward IMF (–IMF Bz sector). The cold, dense plasma theory can be tested using the distribution and the mean values, which shows that the density follows the theory whereas the temperature does not. The density of the plasma has a mean value of 0.16 cm^{-3} for northward and 0.12 cm^{-3} for southward IMF while

the temperature has a mean value of 525 eV for northward and 511 eV for southward IMF. The change in both the density and temperature parameters are not high however, a detailed investigation is needed for the plasma sheet region only.

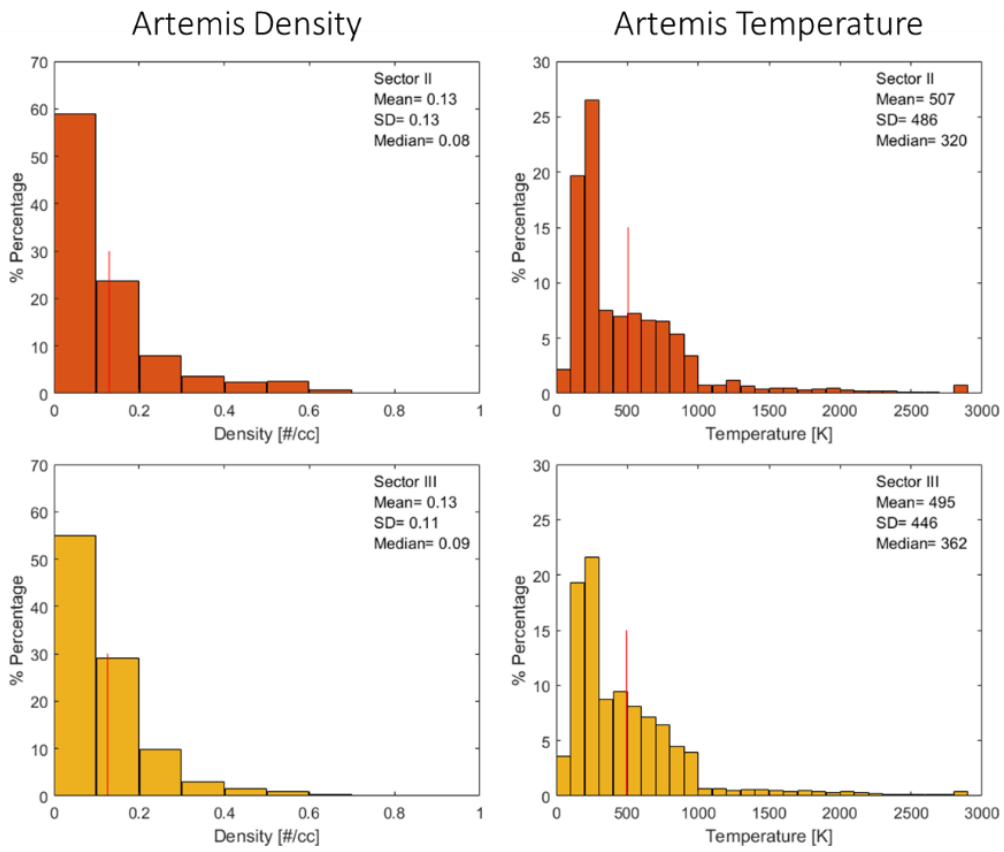

Figure 4.64 : Histograms of the percent occurrence distribution of the ARTEMIS plasma density in the left and plasma temperature in the right. The plots in the first row, in orange color, corresponds to Westward IMF (+IMF By sector) and the plots in the second row, in yellow color, corresponds to Eastward IMF (–IMF By sector). Mean values are shown with a red line. The mean, standard deviation and median values are given in the right corner. For density, 0.1 #/cm^3 wide bins are used up to 1 #/cm^3 whereas for temperature, 100 K wide bins are used up to 3000 K.

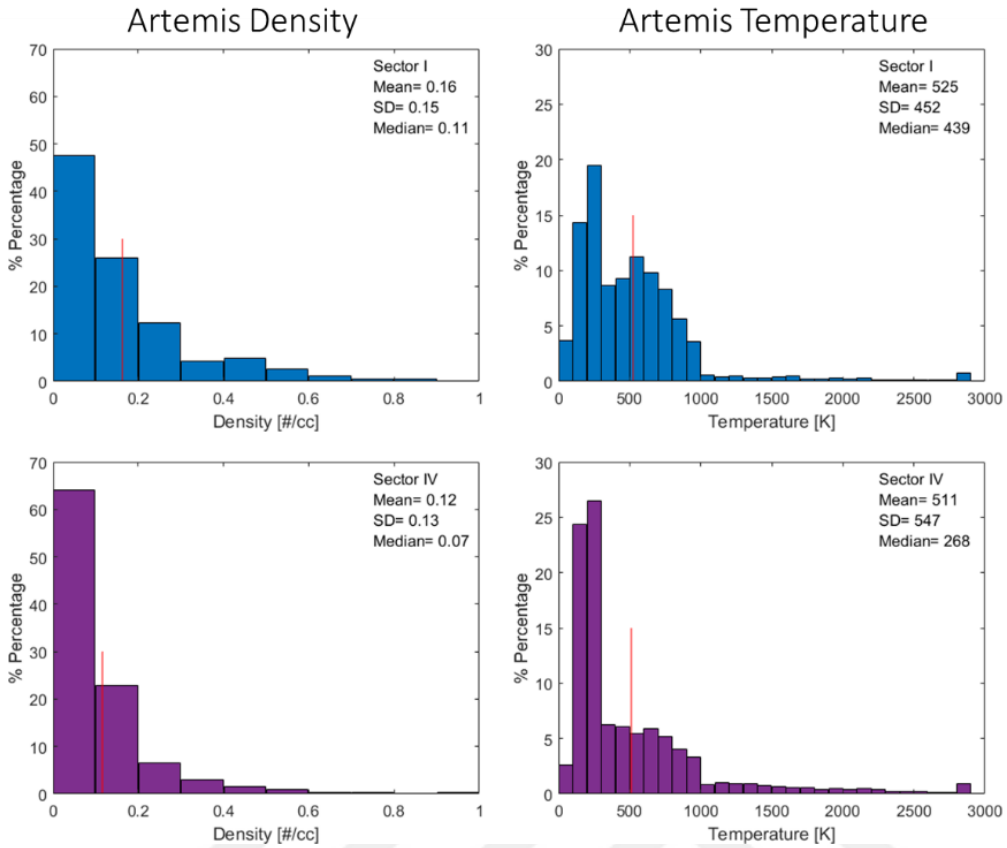

Figure 4.65 : Histograms of the percent occurrence distribution of the ARTEMIS plasma density in the left and plasma temperature in the right. The plots in the first row, in blue color, corresponds to Northward IMF (+IMF Bz sector) and the plots in the second row, in purple color, corresponds to Southward IMF (–IMF Bz sector). Mean values are shown with a red line. The mean, standard deviation and median values are given in the right corner. For density, 0.1 #/cm^3 wide bins are used up to 1 #/cm^3 whereas for temperature, 100 K wide bins are used up to 3000 K.

4.4.4 IMF effect on the magnetotail asymmetry

In this part, we will present the same histograms for the magnetotail magnetic field, plasma velocity, density and temperature for four IMF sectors after separating the magnetotail information according to its position on the tail. This is essential to reveal the effect of IMF By in which we expect to see effects on the preferred quadrants according to IMF By direction. In this section, the histograms, which correspond to equatorial IMFs, will be presented first. Then, northward-southward related effects will be given as a whole set.

Figure 4.66 shows how the separation of the magnetotail data is done into four quadrants. In the figure, the Earth and the Sun is on the left side. The position of the observation in the YZ- plane is evaluated such that, if;

- Y<0 and Z>0, the observation is taken from the north-dawn,
- Y>0 and Z>0, the observation is taken from the north-dusk,
- Y<0 and Z<0, the observation is taken from the south-dawn, and
- Y>0 and Z>0, the observation is taken from the south-dusk.

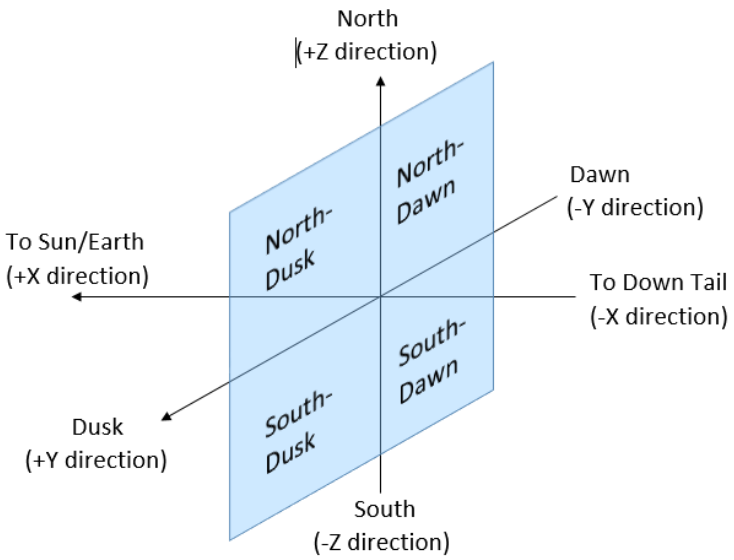

Figure 4.66 : The sketch shows the separation of the magnetotail data into four quadrants according to their position in the YZ- plane; north-dawn, north-dusk, south-dawn and south-dusk. X- direction is also plotted with +X directed sunward.

Figure 4.67 gives the histograms of the distribution of the magnetotail By in four quadrants of the magnetotail for westward IMF (+IMF By) sector on the left (in orange color) and for eastward IMF (–IMF By) sector on the right side (in yellow color). For +IMF By sector, we expect to see the effect of the interconnection of the magnetotail and magnetosheath field lines in the north-dusk and south-dawn regions. For positive IMF By sector the mean values in these quadrants (0.8 nT and 1.3 nT) are much higher than the other quadrants (-0.2nT and -0.2nT). For negative By sector, the north-dawn and south-dusk quadrants are the regions where the merging occurs and we expect to see the magnetotail magnetic field lines to gain a component in the dominant IMF By direction, in this case in negative y-direction. The mean values in the north-dawn and south-dusk quadrants are -0.7nT and -1.5nT whereas the mean values in the other two quadrants are 0 nT. The IMF By effect can be observed clearly after this separation.

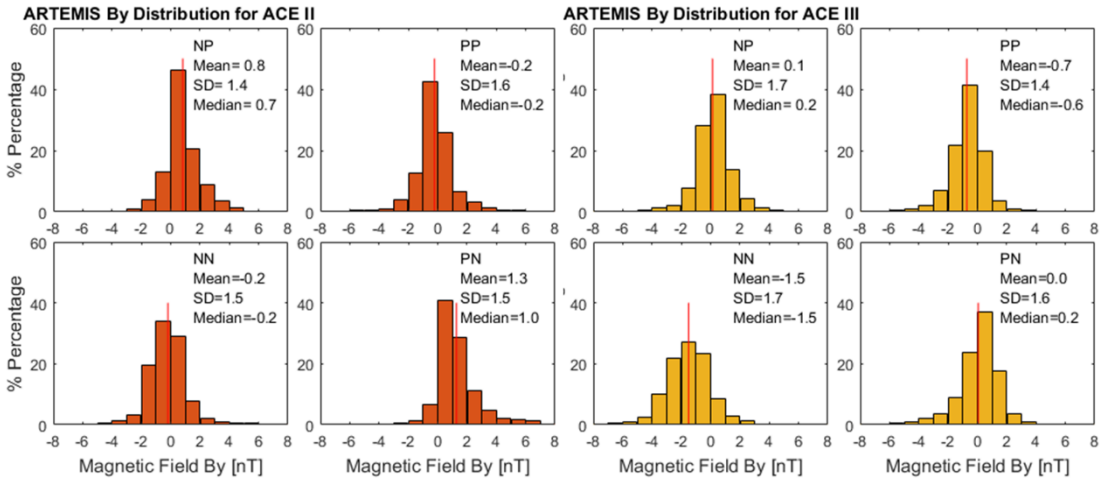

Figure 4.67 : Histograms of the distribution of the percent occurrence of ARTEMIS By in four quadrants of the magnetotail for westward IMF (+IMF By) sector on the left (orange colored histograms) and for eastward IMF (–IMF By) sector on the right side (yellow colored histograms). Mean values are shown with a red line. The mean, standard deviation and median values are given in the right corner.

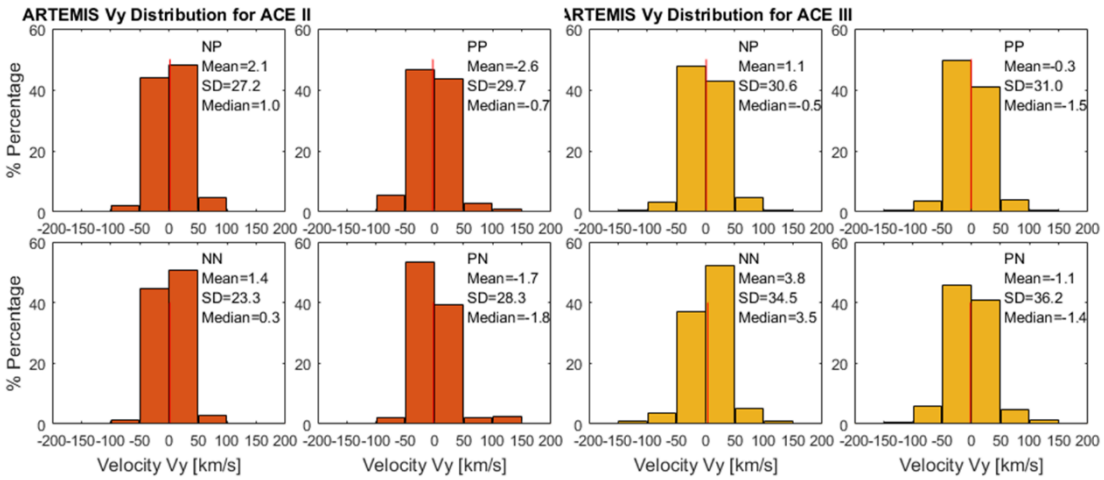

Figure 4.68 : Histograms of the distribution of the percent occurrence of ARTEMIS Vy in four quadrants of the magnetotail for westward IMF (+IMF By) sector on the left (orange colored histograms) and for eastward IMF (–IMF By) sector on the right side (yellow colored histograms). Mean values are shown with a red line. The mean, standard deviation and median values are given in the right corner.

When velocity flow maps are investigated, the magnetotail plasma flow, differing than the magnetic field lines, is expected to be directed towards the center of the tail. Therefore, the plasma flow in y-direction should point towards positive in the dusk regions and towards negative in the dawn regions. However, one can expect an increase of the flow velocity in the north-dusk quadrant (mean Vy= 2.1 km/sec) compared to south-dusk (mean Vy= 1.4 km/sec) and decrease in the strength of the velocity in the south-dawn quadrant (mean Vy= -1.7 km/sec) compared to north-dawn

(mean Vy= -2.5 km/sec) for +IMF By sector and vice versa for the –IMF By sector. Therefore from Figure 4.68, we can see that the magnetotail flows are also effected by the IMF By depending on the direction.

Figure 4.69 gives the distribution of the magnetotail plasma density, on the left, and temperature, on the right, in four quadrants for westward IMF (+IMF By) sector. The denser plasma is encountered in the preferred quadrants when the medians are compared. Since the mean values are too close to each other and the standard deviation values are high, mean values do not show the increased densities in the favored quadrants but the median values do with the medians of 0.08 cm^{-3} and 0.11cm^{-3} compared to 0.07 cm^{-3}. The temperature distributions shows that the colder plasma is observed in the quadrants where merging occurs for +IMF By sector and the magnetotail becomes open to the plasma originated from the solar wind. The means of the temperature in the north-dawn and south-dusk are 478 eV and 476 eV compared to 490eV and 584 eV in the north-dusk and south-dawn quadrants.

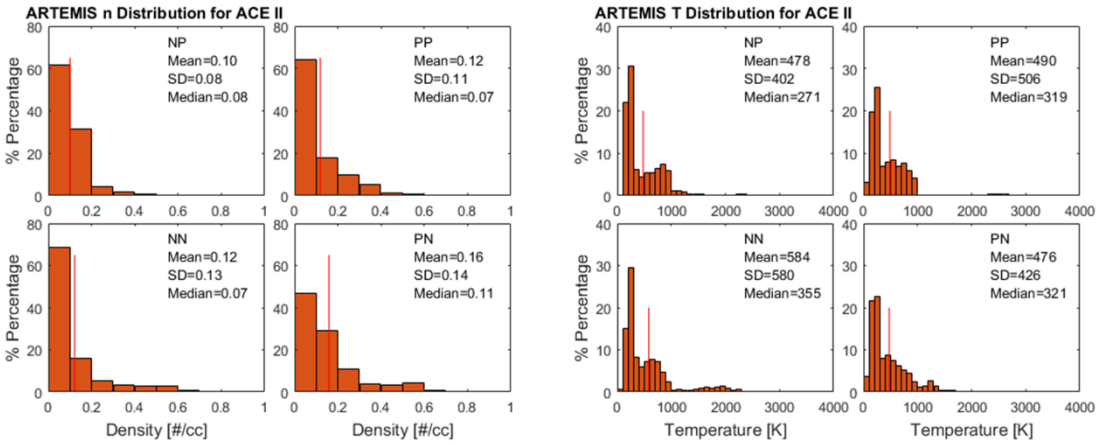

Figure 4.69 : Histograms of the distribution of the percent occurrence of ARTEMIS density, on the left, and temperature, on the right, in four quadrants of the magnetotail for westward IMF (+IMF By) sector. Mean values are shown with a red line. The mean, standard deviation and median values are given in the right corner.

This investigation is completed with a scatter plot of the relation between the density and temperature for +IMF By in Figure 4.70. The logarithmic scales are used in four quadrants in both axes. The colder plasma population is observed mainly in the north-dusk quadrant. The hot plasma (>1keV) is mainly observed in the south-dawn quadrant.

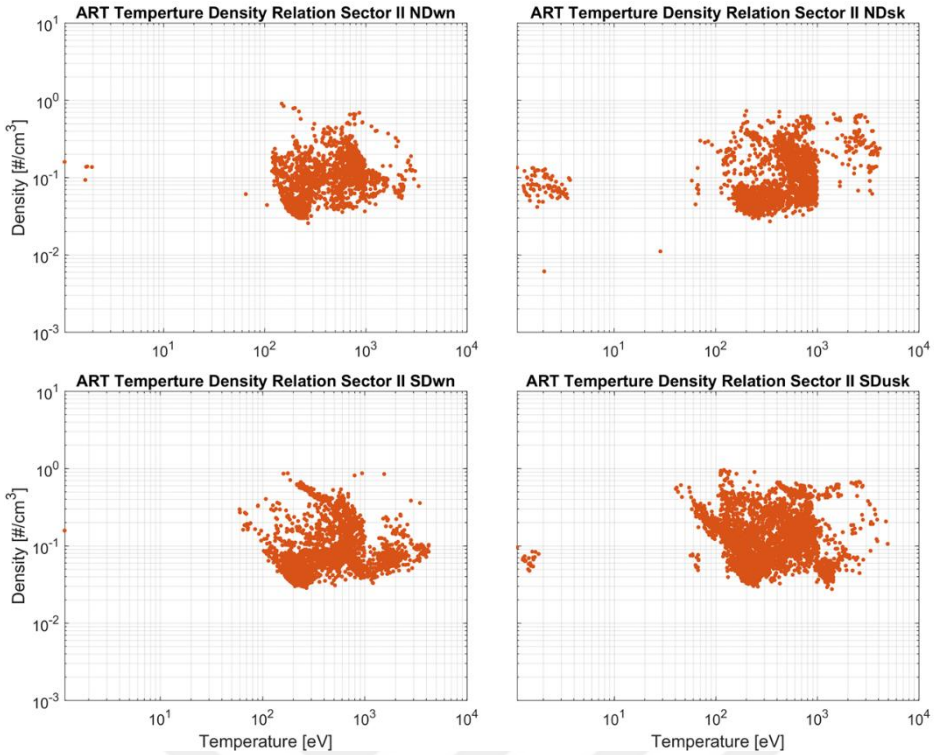

Figure 4.70 : Relationship between density (cm^{-3}) and temperature (eV) for westward IMF (+IMF By) sector in logarithmic scales for four quadrants of the magnetotail; north-dawn, north-dusk; south-dawn and south-dusk regions are given in the upper-left, upper-right, lower-left and lower-right, respectively.

The histograms of the distribution of the percent occurrence of the density and temperature distribution for –IMF By is presented in Figure 4.71. The highest mean density value of $0.16cm^{-3}$ is observed in the south-dusk region, which is not expected. However, the expected quadrants follow that value with 0.13 cm^{-3}. The temperature histograms has the same distribution with the density such that, the hottest mean value of 645eV observed in the south-dusk, followed by the south-dawn and north-dusk with 546 eV and 451 eV.

A scatter plot of the relation between the density and temperature for –IMF By (see Figure 4.72). The logarithmic scales are used in four quadrants in both axes. There are more observations gathered that corresponds to –IMF By. It is more likely to encounter the colder plasma population in all four quadrants in –IMF By sector compared to +IMF By sector. There are more hot plasma observations (>1keV) in the south-dawn

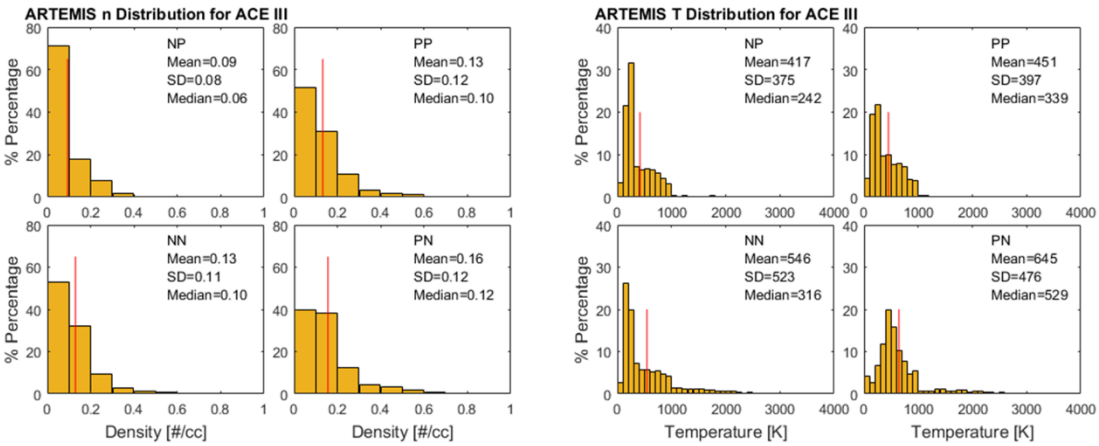

Figure 4.71 : Histograms of the distribution of the percent occurrence of ARTEMIS density, on the left, and temperature, on the right, for four quadrants of the magnetotail for eastward IMF (–IMF By) sector. Mean values are shown with a red line. The mean, standard deviation and median values are given in the right corner.

quadrant which we expect to see the IMF By effect. There is no clear results on the effects of the IMF By direction on the relationship between the density and the temperature.

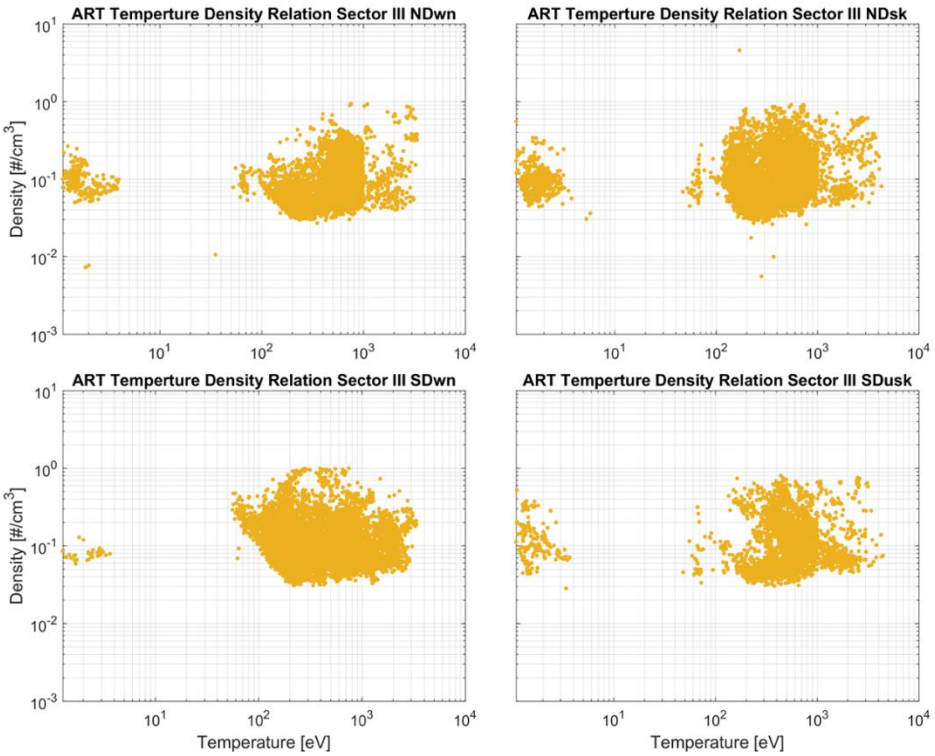

Figure 4.72 : Relationship between density (cm^{-3}) and temperature (eV) for eastward IMF (–IMF By) sector in logarithmic scales for four quadrants of the magnetotail; North-Dawn, North-Dusk; South-Dawn and South-Dusk regions are given in the upper-left, upper-right, lower-left and lower-right, respectively.

Figure 4.73 presents the ARTEMIS Bz in four quadrants of the magnetotail for northward IMF (+IMF Bz) sector on the left (blue) and for southward IMF (–IMF Bz) sector on the right side (purple). This figure shows stronger dipolar structure during the closed magnetosphere times, i.e. northward IMF sector. The increased magnetic field line vectors in the south regions are also encountered. For southward sector, the magnetotail shows more stretched magnetic field line distribution as expected from dayside reconnection and formation of distant neutral line in all quadrants.

Figure 4.74 gives the same distribution as in the Figure 4.73 for the z-component of the plasma flow. The flow direction is manly into the center of the tail. For northward IMF, the negative flow velocities in the north-dawn and south-dusk regions might be due to the fact that the –IMF By dominates even in the average case, which tilts the tail and now we see south tail in the northern (dawn) part of the tail and north tail in the southern (dusk) part of the tail.

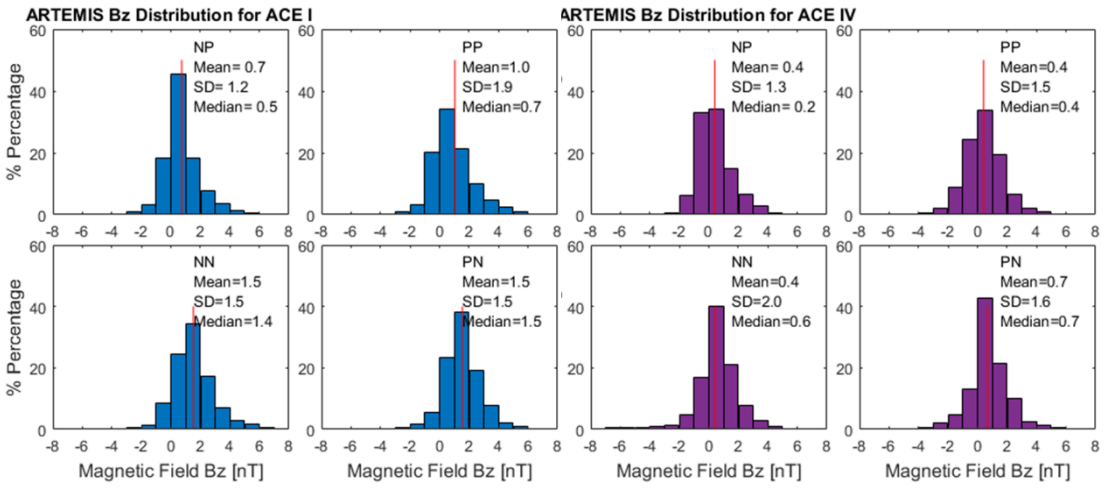

Figure 4.73 : Histograms of the distribution of the percent occurrence of ARTEMIS Bz in four quadrants of the magnetotail for northward IMF (+IMF Bz) sector on the left (blue colored histograms) and for southward IMF (–IMF Bz) sector on the right side (purple colored histograms). Mean values are shown with a red line. The mean, standard deviation and median values are given in the right corner.

Figure 4.75 shows the relationship between density (cm^{-3}) and temperature (eV) for northward IMF sector in logarithmic scaled axes for four quadrants of the magnetotail and the Figure 4.76 gives the same separation for the southward IMF. These figures will be beneficial to observe from which regions the ARTEMIS probes collect measurements. The cold plasma is mainly encountered in the north-dusk quadrant for independent of the IMF direction. The density is under 1cm-3 for the northward

IMFsector, however there are observations from the dusk region with higher density measurements during southward IMF.

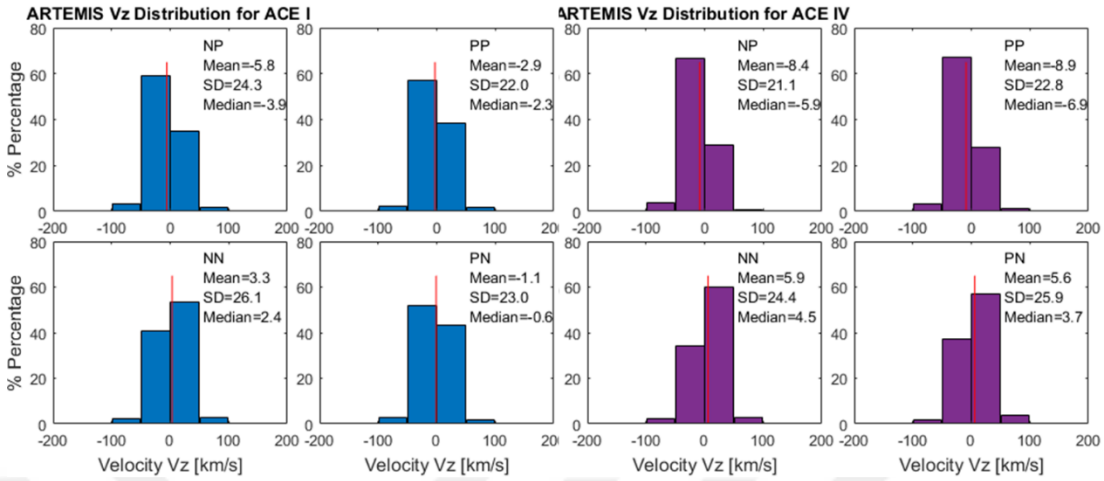

Figure 4.74 : Histograms of the distribution of the percent occurrence of ARTEMIS Vz in four quadrants of the magnetotail for northward IMF (+IMF Bz) sector on the left (blue colored histograms) and for southward IMF (–IMF Bz) sector on the right side (purple colored histograms). Mean values are shown with a red line. The mean, standard deviation and median values are given in the right corner.

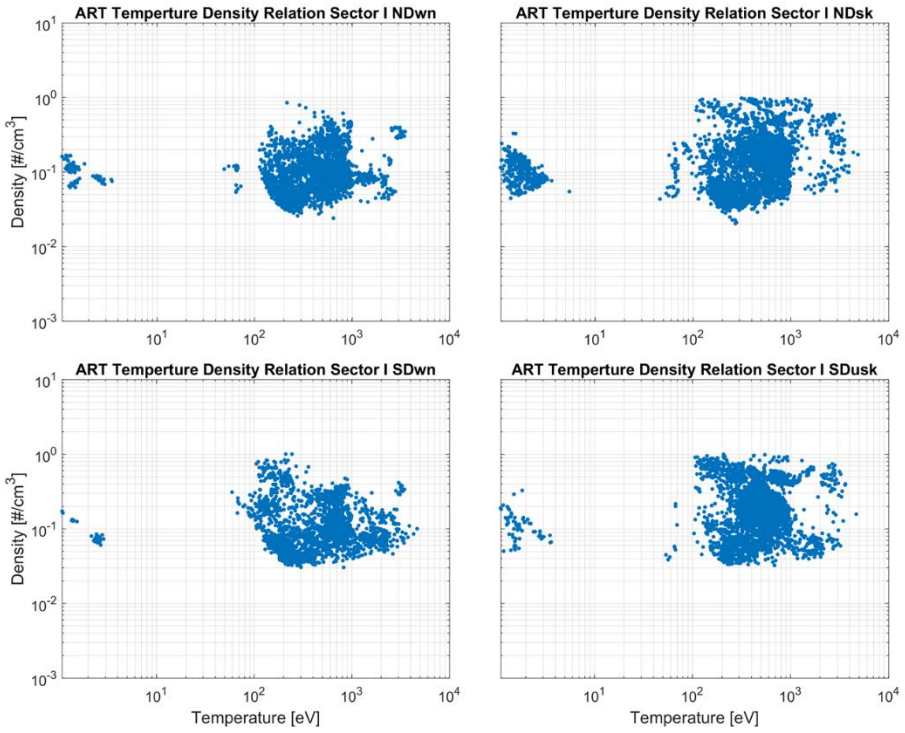

Figure 4.75 : Relationship between density (cm^{-3}) and temperature (eV) for northward IMF (+IMF Bz) sector in logarithmic scales for four quadrants of the magnetotail; north-dawn, north-dusk; south-dawn and south-dusk regions are given in the upper-left, upper-right, lower-left and lower-right, respectively.

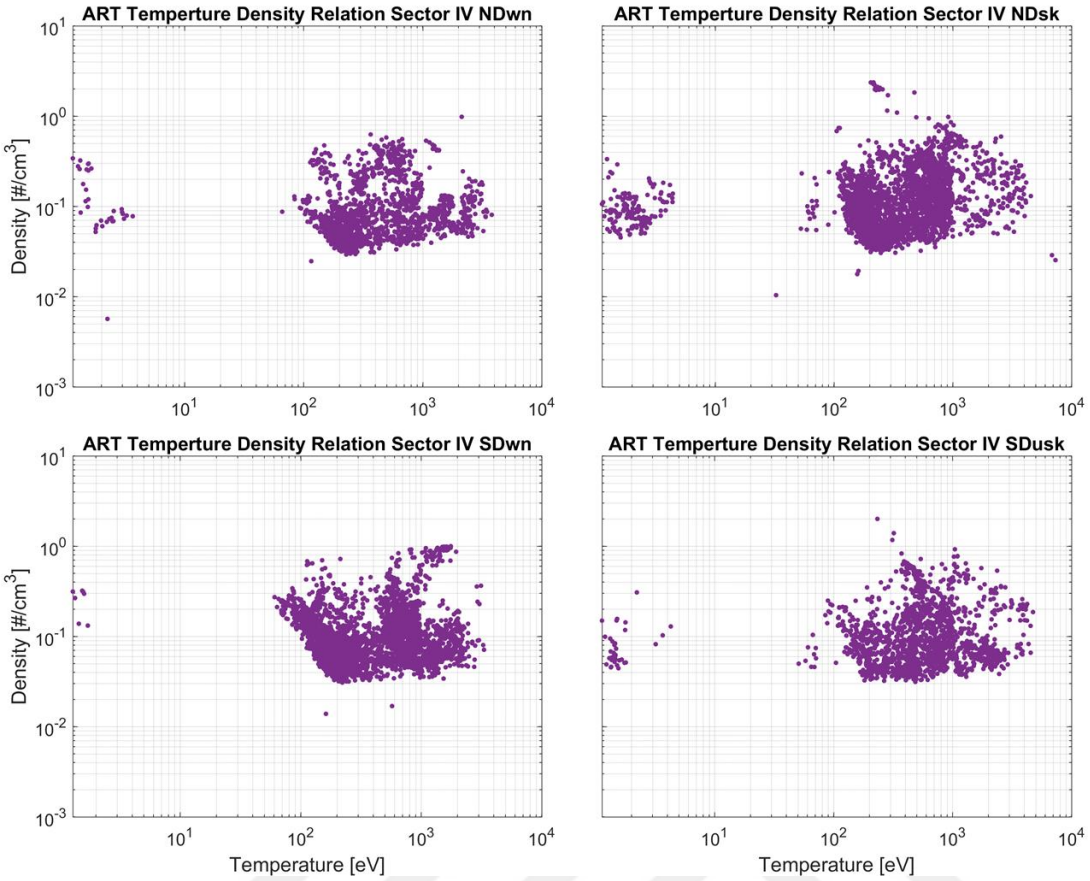

Figure 4.76 : Relationship between density (cm^{-3}) and temperature (eV) for southward IMF (–IMF Bz) sector in logarithmic scales for four quadrants of the magnetotail; north-dawn, north-dusk; south-dawn and south-dusk regions are given in the upper-left, upper-right, lower-left and lower-right, respectively.

4.5 Discussion

ARTEMIS probes crossing the magnetotail at the distance of Moon while orbiting around it and the spacecraft in pair collect continuous set of observations with the state of the art instrumentation at $\sim -60R_E$. We collected measurements from August 2011 to August 2013 from magnetometer and plasma instruments of the ARTEMIS probes as well as the solar wind monitor spacecraft, ACE, and WIND, at times. Based on magnetic field and plasma data obtained from lunar-orbiting ARTEMIS probes were studied for 18 magnetotail traversals. Our aim is to renew the information on magnetic field structure of the magnetotail at the distance of the Moon using high-resolution instruments of the ARTEMIS and present the plasma flow vectors of the magnetotail at lunar distances to the community. IMF effect is also investigated using sector separation. This vector based study is complemented with the statistical analysis of the ARTEMIS parameters. The followings are the results of this chapter.

1. The general structure of the magnetotail at lunar distances in XY plane is as expected. The magnetic field vectors are towards the Earth in the northern tail about 4 nT magnitude and away vectors in the southern tail with -8nT average. A maximum average of -20 nT is observed in the southern tail as well. The increased size of the vectors was observed during earlier studies based Explorer series. (Section 4.1.1)

2. In the XZ-plane projection of the magnetotail magnetic field lines shows the diamagnetic effect of the plasma sheet, which causes a decrease in the magnetic field magnitudes. The stretched dipolar field lines with an average of about 8 nT is found for $|Z|>7\ R_E$, whereas the $|B|_{ave}$ is 4 nT within $|Z|<7R_E$, where we expect to see plasma sheet. The results are similar to studies based on Explorer series. A gap seen in the coverage map results in a perturbation like effect on the general pattern in this view. Therefore, each vector map is attached with a corresponding coverage map. Bx parameter is also used instead of Z-coordinate since it is a common measure of the neutral sheet (Khurana et al., 1996). In the IMF sector separation, we observed increased thickness in the plasma sheet region during northward IMF sector with decreased magnetic field in the x-direction and increased magnetic field in the z-direction, $|Bx|_{ave}$= 0.2 nT, $|Bz|_{ave}$= 2.8 nT compared to $|Bx|_{ave}$= 15 nT, $|Bz|_{ave}$= 1.1 nT in southward IMF sector. The reason behind this is the fact that for southward IMF sector, the dayside reconnection results in the plasma sheet to thin, the magnetic field lines to be stretched and even a new neutral line to form at distant tail whereas a more dipolar magnetic field line structure is observed for closed magnetosphere condition, namely northward IMF sector. (Section 4.1.2)

3. The YZ plane view of the magnetic field lines show that the dipole effect is still dominant at lunar distances. When this plane projection is compared with the reference study at $-33R_E$ by Kaymaz et al. (1994), we could not identify nodes aligned with the Y=0 R_E axis and16 R_E apart in north-south direction as the reference study did instead the node like structure is encountered only in the northern tail at Y=-3 R_E and Bx=9 nT. The reason behind not observing south node is the ARTEMIS low-inclined trajectory. The shift in y-direction is because of the fact that the dominant interplanetary magnetic field is in –y direction, which results in the skewness of the nodes in counterclockwise

direction. When observations only corresponds to –IMF By sector are investigated, the node-like feature seems to rotate more in the –y direction at about Y=-7 R_E and Bx=10 nT. The +IMF By sector vector map shows the rotation in the clockwise direction, relocating the north node to Y=6 R_E and Bx= 9nT, as expected from theory as well as the reference study by Kaymaz et al.(1995).

The equatorial IMF effect is observed in the statistical analysis as well. All magnetotail respond as expected however, the effect seems to become more emphasized after quadrant separation. The dominant direction of the IMF By affect more in the favored quadrants due to penetration regions where magnetosheath and magnetospheric magnetic field lines merge (Sibeck et al., 1985). During –IMF By sector, the average magnetic field is negative throughout the tail with higher negative values in the south dawn (-1.5 nT) and north dusk (-0.7 nT) compared to other quadrants (-0.0 nT and -0.1 nT). Additionally, for +IMF By sector, the magnetotail magnetic field lines influenced more in the north-dawn and south-dusk regions with mean values of +0.8nT and +1.3nT compared to -0.2nT in the other two quadrants.

When northward and southward IMF sectors are compared in the same plane, the tail size is bigger for southward IMF than it is for northward IMF sector due to expansion of the tail after dayside reconnection. Because of increased number of temporal and spatial events like plasmoid passages and flux ropes during southward IMF, the general uniform pattern seems to be patchier for southward IMF sector. (Section 4.1.3, 4.4.4)

4. The flows are categorized into 3; fast flows ($|Vx|>300$ km/s), medium flows (100 km/s $<|Vx|<300$ km/s) and slow flows ($|Vx|<100$ km/s) following many other studies (Hayakawa et al., 1982; Nagai et al., 1998; Ohtani et al., 2004). The slow flows are dominant throughout the magnetotail as discussed by Hayakawa at al. (1982) and fast flows are nearly rare. The dawn-dusk directed flows are nearly only seen with the slow flow cases. The fast flows have a more tendency to occur with southward IMF sector, which is expected according to the reconnection theory. In addition, the histograms displays the increase in the magnitude of tailward flow velocity for southward IMF sector with a mean

value of -25.1 km/sec whereas the mean is -7.1 km/sec for northward IMF sector. (Section 4.4.2)

5. The plasma flow vector map drawn using all magnetotail observations in XY-plane shows that the velocity of the plasma flow in the plasma sheet region within $|Y|<10\ R_E$ (or near midnight sector (Y=0) is less than the flow near the magnetopause boundary. At about $X=-63\ R_E$, $|Y|<10\ R_E$, and $|Z|<10\ R_E$ there is a sudden increase in the tailward flow velocity which might be related to a neutral line formation in that region which needs to be investigated deeply before drawing any conclusions (Hones, 1979; Scholer et al.,, 1984). The number of these fast flows sourced from $-63\ R_E$ is increased during southward IMF. In addition, they can not be observed during northward oriented IMF instead they are replaced by earthward directed slow velocity vectors from that same region. Besides, fastest earthward flows are observed for northward IMF compared to all other sectors. When equatorial IMFs compared, there is a clear tendency to encounter higher flow velocities in the dusk region for positive IMF By condition and in the dawn region for negative IMF By condition. (Section 4.2.1)

6. The flow pattern shows a sporadic and disordered flow pattern when projected onto XZ- plane, therefore XBx- plane is also investigated. XBx- plane view of the plasma flow shows increased tailward flows as well as increased plasma sheet flows near the magnetopause boundary compared to flows in other regions. After IMF separation, higher flow velocities is observed in both directions, i.e. earthward and tailward, during southward IMF sector which can support the claim of encountering the distant neutral line in our observations. (Section 4.2.2)

7. In the YZ-plane, the slowest velocities are detected since the main plasma flow is in a plane orthogonal to this plane. The coverage in $|Z|<10\ R_E$, where the plasma sheet is likely to be, has substantial amount of information especially in the dusk region. The direction of the flow is toward the neutral sheet but it is irregular in the YZ-plane. The flow magnitudes increase towards the dawn/dusk flanks. In YBx- plane view of the magnetotail, flow shows the cross-tail current in the dawn to dusk direction with interrupted regions as it is seen in the study by Nakamura et al. (1994). (Section 4.2.3)

8. Three types of plasma populations are observed when density and temperature parameters are investigated after sector separation. The cold, dense plasma theory is tested for northward IMF (Fujimoto et al., 1997; Nagai et al., 1998). There is an increase in the possibility to observe cold plasma for northward sector however; the density parameter does not act as expected and the highest densities are observed in the southward IMF sector. This cold, dense plasma studies are based on prolonged northward IMF conditions. In this study, the IMF matching procedure, explained in detail in Section 2.3.1 ensures that magnetotail information belongs to one of the IMF sectors however, does not obligate that sector is a long interval. It can be even one-minute change of the IMF sector from another sector. Therefore, we do not have the information if the northward IMF is brief or prolonged for our ARTEMIS observations. Therefore, we test our observations if they catch that pattern but we also know that there is a possibility that they do not due to the nature of this study.

9. The cold, dense plasma theory is due to the high latitude reconnection at the flanks, which enables the entry of the plasma with solar wind origin into the plasma sheet especially in the near Earth tail during prolonged northward IMF (Fujimoto et al., 1997; Terasawa et al., 1997; Fujimoto et al., 1998; Nagai et al.,1998). The distributions and the mean values of our observations show that the density follows the theory whereas the temperature does not. The density of the plasma has a mean value of 0.16 cm^{-3} for northward and 0.12 cm^{-3} for southward IMF while the temperature has a mean value of 525 eV for northward and 511 eV for southward IMF. This might be due to the fact that cold, dense plasma sheet studies are based on long term northward IMF conditions, longer than half an hour (Nagai et al., 1998; Li et al., 2005). Our observations on the other hand, are instantaneously synchronized with the concurrent IMF information. Therefore, the temperature not giving the expected response might be due to the methodology used in this study.

10. The magnetic pressure and the gas pressure map shows where magnetic field or plasma parameters are dominant with about 0.06 nPa values. We can see from the magnetic pressure map that the plasma sheet has a thickness of 7 R_E with depressed magnetic field values and plasma with higher density and temperature. The thickness seems to decrease in the central tail with a little

skewness to $Y=3R_E$. This finding is relatable to the general plasma sheet expansion adjacent to the magnetopause boundary.

5. SUMMARY AND CONCLUSIONS

5.1 Summary and Conclusion

In this thesis study, we analyzed ARTEMIS magnetic field and plasma observations to determine and bring out the global structure and features of the magnetotail magnetic field, plasma flow morphology, plasma temperature, density, and pressure as well as the structure of the magnetotail boundary, the magnetopause, at the lunar distances, x=-60 Re. In addition, their variability in response to IMF orientation was investigated.

Following a literature work, terminology and fundamentals in Chapters 1 and 2, we presented results on the size, geometry and shape of the magnetotail boundary as well as the factors that affect the boundary motion under different IMF orientations and solar wind dynamic pressure in Chapter 3. In this part, processes for implementing criteria for the magnetopause location, electing and storing the magnetopause crossing positions out of two years of data, pairing ARTEMIS data with the concurrent IMF data from ACE and WIND, performing the most appropriate coordinate system and the methods to analyze the magnetopause crossing positions were described and discussed. In this respect, the aberration effects, dipole angle effects, and tail magnetopause flaring effects, separation by the IMF clock angle and IMF By and IMF Bz effects were extensively investigated and discussed. Comparisons with analytical models of magnetopause were presented. While our results verify the findings of some of the earlier works on the size and shape of the tail magnetopause, new results were obtained and demonstrated the effects of the IMF Bz and dynamic pressure involving physics and dynamics of the magnetotail at lunar distances. Below we highlight the results from case studies and statistical analysis of the magnetopause positions presented in this chapter.

1. At lunar distances, non-radial solar wind flow deviates the magnetotail by about 6^o on the average in the dawn-dusk direction and about 3^o out of the ecliptic plane. The largest total dawn-dusk and north-south aberration was

obtained to be 23.2^{o} and 11^{o} respectively. The magnetopause crossing positions should be transformed into the appropriate coordinate system for the correct interpretation of the distant tail boundary studies.

2. Based on the percent errors, the boundary of the magnetotail at lunar distances can be represented by a circle for all upstream conditions. A circular fit to magnetopause positions give a tail size with radius of 26.7 R_E with an RMS=4.94 R_E.

3. The tail size and the shape for different IMF clock angle sectors were hindered by the lack of high latitude boundary crossings. An elliptical boundary is reasonable for both east-west and north-south IMFs. The east-west IMF presents an oblate ellipse while the north-south IMF indicates a prolate ellipse. The shape of the tail is more circular (e=0.47) for IMF Bz sectors compared to IMF By sectors (e=0.72). The tail size and dimensions were found to be slightly larger for southward IMF compared to northward IMF, obtained approximately equal for northward and southward IMFs at this distance.

4. The magnetopause positions present a large scatter. While the average circular tail size is 26.3 R_E, the smallest (10 R_E) and the largest (39 R_E) tail dimensions were recorded. The smallest tail size was found to be associated with a strong northward IMF Bz and relatively large solar wind dynamic pressure. The largest tail size, on the other hand, corresponds to low solar wind dynamic pressure and a slightly southward IMF Bz.

5. Magnetopause models (the HB72, the PR96, the S97, the S98, the C02, and the L11) were compared with the all boundary crossings in the xR-plane at lunar distance. The models predicted the observed positions within a range of percent errors from 0.8 % to about ±6 %. Despite being the oldest, static the HB72 model gives the best prediction of the magnetopause boundary at lunar distances corresponding to all IMF and solar wind conditions. This is considered as the result of the tail magnetopause data from lunar distances that are included in the HB72. Results from three Shue et al. based empirical models (the S97, the S98, the C02) give similar magnetopause predictions with percent error varying from 1.2 to 2.9 %. While the L11 underestimates the

magnetopause size by about 7 % at lunar distance under the average solar wind conditions, the PR96 overestimates by about 6 %.

6. The model results were also compared for the uncommon upstream conditions corresponding to the smallest and largest magnetopause observations (10 R_E and 39 R_E). All models for these cases showed large deviations from the observed boundary. The closest prediction for the smallest boundary crossing position was obtained from the L11 model. For the largest magnetopause crossing, 39 R_E, on the other hand, the PR96 model gave the best prediction. The performance of the S97 model in predicting the magnetopause under unusual conditions was better than that of the S98 model. The HB72 model, on the other hand, showed the poorest prediction for the chosen cases. The percent errors were found to be larger under the unusually weak solar wind upstream conditions. The models were found to underestimate the tail flaring for the largest boundary crossing while they, except Lu et al. (2011), failed to represent the inward flaring in the case of the smallest boundary crossing. Tail size appears to be closely associated with the tail flaring which in turn related to the evolution of the magnetopause boundary from the subsolar point, through polar cusps at the terminator, and to the tail distances. These discrepancies or agreements indicate how the models may be improved at lunar distances.

7. Dependence of the magnetotail boundary size on the dynamic pressure and the direction of IMF Bz was investigated. In general, the decreasing tail boundary are seen to be associated with the increasing dynamic pressures. However, the dynamic pressure dependence shows two groups in the distribution of the magnetopause crossing points. Those with greater than 2 nPa showed large scatter with an average magnetopause size of about 26.5 R_E while those less than 2 nPa showed a decreasing magnetotail with increased pressure.

8. Similar results were also obtained for the dependence of the tail size on the strength of IMF Bz when IMF lies within the north-south clock angle sectors ($135 \leq |\theta| \leq 180$ and $0 \leq |\theta| \leq 45$). For both northward and southward IMF Bz, the tail size was found to decrease with the increasing strength of the northward or southward IMF Bz. The rate of decrease is slightly faster in case of southward IMF Bz.

9. Case 1 and Case 2 studies indicated that the final size of the magnetotail at lunar distances is a result of the balance between the dynamic pressure effects and IMF Bz effects. In that, compared to the nominal conditions, strong northward IMFs and large dynamic pressures resulted in the smallest tail size, while weak IMF Bz and weak dynamic pressures gave the largest tail size. It was shown that both parameters are important in determining the final size of the magnetotail at x=-60 R_E.

Inner regions of the magnetotail that are bounded by the magnetopause boundary at x=-60 R_E were investigated both statistically using histograms/bar plots under several external, IMF, conditions and also using vector and contour maps to understand the spatial variations of the magnetic field and plasma features within the magnetotail. Because of the orbital characteristics, the ARTEMIS probes, both P1 and P2, map the low latitudes of the magnetotail in the cross-sectional plane, and give a good opportunity to study the global characteristics of plasma sheet and its sub-regions neutral sheet and current sheet and extend/decline the results obtained in the near Earth distances and expand them to the plasma parameters. This was one of the main motivations in this study. In addition, a complete data set from solar wind monitors of ACE and WIND allow us to search for the IMF effects on the plasma sheet structure as well. In Chapters 4, the structure of the plasma sheet, both the magnetic field and plasma namely, velocity, density, temperature, and pressure were investigated in different planes (XY-, XZ-, YZ-) and under different IMF orientations using vector maps for velocity and contour maps for density, temperature and pressures. Both the magnetic field pressure and the plasma kinetic pressure were examined. To reveal the neutral sheet characteristics, both xz- and yz- planes as well as xBx- and yBx-planes were used. Chapter 4 presented the method analyses followed in the study of the inner structure of magnetotail, i.e. the plasma sheet. The creation of the vector and contour maps, binning strategy, separation to IMF clock angles and tail quadrants, statistical averages including moving averages were described in detail in this chapter. The vector maps were complemented with the statistical analysis to quantify features observed in Chapter 4. Even though the coverage of satellite throughout the plasma sheet is not evenly distributed, more data were present at dusk than at dawn, several gross characteristics of magnetic field and flow in the plasma sheet region were being

brought out. Comparisons with the available literature work including most recent ones were also presented in this Chapter.

IMF direction is the most important factor that controls the magnetotail's dynamics. The purpose in separating by IMF By was to see if the similar effects, such as the asymmetric distribution of the IMF related fields, seen in the near Earth magnetotail distances are evident and detectable throughout the plasma sheet region at lunar distances, how these effects appear at these distances, if similar effects were found in the flow and other plasma parameters, and compare the findings with those expected from theory and with earlier studies. Similarly, IMF Bz is the controlling factor for the storms/substorms to occur in near Earth tail at about x=-20 R_E and it is of great importance how the flow and plasma parameters respond to both northward and southward IMF Bz. These were investigated and discussed in Chapter 4 as well.

The results from the magnetic field observations in the magnetotail given in Section 4.1 are presented below.

1. The vectors maps of magnetic field in the YZ-plane indicates that the general topology of the magnetic field lines at x=-60 R_E is dipolar and the Earth's dipole is still dominant at lunar distances for all IMF orientations, though the field magnitude is weaker than near Earth distances as expected. While the magnetic field lines are purely directed in the z-direction at the central plane of the dawn-dusk direction, with slightly increased y-component towards dawn and dusk. The nodes where the magnetic field is zero in this plane and where the magnetic field is purely in the x-direction are not very distinctly apparent. The main reason for not being able to identify the nodes markedly is a result of the missing part of the magnetotail where the magnetic field lines flare in the north and south directions thus creating a one of weak magnetic field in this plane. However, there are hints of where the nodes may lie; fewer southward vectors and the region of weak magnetic field in the northern hemisphere of the tail and pure Bz field without any y-component. We call these signatures as the node-like regions which are visible only in the northern tail at about Y=-3 R_E and Bx=9 nT.
2. The XZ-plane projection of the magnetotail magnetic field vectors shows the region of weak magnetic field in the center of the magnetotail where the

tailward field lines of the southern hemisphere turn toward earthward field lines of the northern hemisphere. The region where magnetic fields is almost zero is identified as the neutral sheet which is embedded within the central part of the plasma sheet. The neutral sheet in the XZ-plane is found to be very wavy moving up and down of Z=0 line. In the X-Bx view of magnetic field, the motion of the neutral sheet is not seen. The plasma sheet in this view is very nicely revealed with the neutral sheet separating two oppositely directing magnetic field vectors in the north and south hemispheres of the magnetotail. The thickness of the plasma sheet in this view corresponding to all IMFs decreases as the tail distance increases away from the Earth.

3. The magnetic field strength ($|B|_{ave}$) within the plasma sheet denoted by $|Z|<7R_E$ is about 4 nT on the average while it is about 8 nT for $|Z|>7\ R_E$. These numbers are similar to those obtained by the Explorer series.

4. The magnetic field topology in the XY plane was given both for northern and southern magnetotail separately. These maps shows that the magnetic fields are away from the Earth in the southern hemisphere in the center of the tail (y~0) but slightly flare towards dawn and dusk and gains a slight y-component. The same is also observed for northern hemisphere but with magnetic field lines pointing toward the Earth. The average magnitude of the magnetic field strength in the northern tail is obtained as 4 nT and -8 nT in the southern tail. A maximum of -20 nT is observed in the southern tail as well. (Section 4.1.1)

5. The IMF By effects are revealed in the magnetic field vector maps as the tilt in the direction of the magnetic field vectors in the direction of IMF By, namely in the +y direction in the case of +IMF By and –y direction in the case of –IMF By. The histograms of the magnetic field for +IMF By and –IMF By clearly reflects the symmetric distribution of the By in the plasma sheet region. The histograms of By in the plasma sheet region are skewed toward +By for +IMF By and toward –By for –IMF By. The asymmetric distribution of the tail By within the plasma sheet can only occur as a result of the twisting of the magnetotail by the IMF By torque applied unevenly along the magnetopause boundary. This is the expected signature of the reconnection of the Earth's dipole field lines with IMF By. The By component in the expected plasma sheet quadrants, northern dawn and southern dusk for +IMF By and southern dawn

and northern dusk for –IMF By strengthens this expectation. For +IMF By sector, the average plasma sheet By in the north-dawn and south-dusk quadrants are +0.8nT and +1.3nT as compared to -0.2nT in the southern dawn and northern dusk quadrants. Similarly, during –IMF By sector, the average plasma sheet By is about -1.5 nT in the southern dawn and -0.7 nT northern dusk as compared to 0.0 nT and -0.1 nT in northern dawn and southern dusk quadrants. (Section 4.4.4)

6. Node-like features, as well, shift in the +y and –y direction during +IMF By and –IMF By respectively. They have been relocated at about Y=6 R_E for +IMF By and Y=-7 R_E for –IMF By and both at about |Bx|~9 nT. This shift, the tilt of the field lines, and the asymmetric distribution of plasma sheet By with respect to tail quadrants are consistent with the IMF By effects observed at the near Earth distances at x=-30Re (Kaymaz et al. 1995). These indicate that the tail responds the variations in IMF By as a whole and similar effects are also seen at lunar distances. (Section 4.1.3)
7. In the IMF sector separation, it is also observed that the plasma sheet thickens in the during the northward IMF sector with decreased magnetic field in the x-direction and increased magnetic field in the z-direction, $|Bx|_{ave}$= 0.2 nT, $|Bz|_{ave}$= 2.8 nT compared to $|Bx|_{ave}$= 15 nT, $|Bz|_{ave}$= 1.1 nT in southward IMF sector. (Section 4.1.2)
8. When northward and southward IMF sectors are compared in the same plane, the tail size is bigger for southward IMF than it is for northward IMF sector due to expansion of the tail following the magnetopause reconnection. Because of increased number of temporal and spatial events like plasmoid passages and flux ropes during southward IMF, the generally smooth pattern of plasma sheet seems to be patchier for southward IMF sector. (Section 4.1.3, 4.4.4)

The results from flow maps for all data and after IMF sector separation are summarized below:

1. The slow flows (|Vx|<100 km/s) are dominant throughout the magnetotail and fast flows (|Vx|>300 km/s) are very rare. The dawn-dusk directed flows are nearly only seen with the slow flow cases. The fast flows have a more tendency to occur with southward IMF sector, which is expected according to the

reconnection theory. In addition, the histograms display the increase in the magnitude of tailward flow velocity for southward IMF sector with a mean value of -25.1 km/sec whereas the mean is -7.1 km/sec for northward IMF sector. (Section 4.4.2)

2. The plasma flow vector maps for all IMF in the XY-plane shows that the velocity of the plasma flow in the plasma sheet region within $|Y|<10\ R_E$ (or near midnight sector (Y=0) is less than the flow near the magnetopause boundary. At about $X=-63\ R_E$, $|Y|<10\ R_E$, and $|Z|<10\ R_E$ there is a sudden increase in the tailward flow velocity which might be related to a distant neutral line formation in that region. The number of these tailward directed fast flows, seen around $-63\ R_E$ are increased during southward IMF. They are replaced by earthward directed slow velocity vectors from that same region during northward oriented IMF. The fastest earthward flows are observed for northward IMF compared to all other sectors. When equatorial IMFs compared, there is a tendency to encounter higher flow velocities in the dusk region near the boundary for positive IMF By condition and in the near-boundary-dawn region for negative IMF By condition. (Section 4.2.1)

3. The XBx- plane view of the plasma flow shows the plasma sheet region with slower flows within $|Y|<7R_E$ with higher coverage between $X=-53R_E$ to $-63R_E$. The flow velocities increased in the region outside the plasma sheet to near the magnetopause boundary region. After IMF separation, higher flow velocities are observed in both directions, i.e. earthward and tailward, during southward IMF sector which may indicate signatures of distant neutral line whereas slower flows are encountered in the northward IMF sector (Section 4.2.2)

4. In the YZ-plane, the slowest velocities are detected since the main plasma flow is in a plane orthogonal to this plane. The coverage in $|Z|<10\ R_E$, where the plasma sheet is likely to be, has substantial amount of information especially in the dusk region. The direction of the flow is toward the tail axis but it is irregular in the YZ-plane. The flow magnitudes increase towards the dawn/dusk flanks. In YBx- plane view of the magnetotail flow shows the cross-tail current in the dawn to dusk direction with interrupted regions as it is seen in the study by Nakamura et al. (1994). (Section 4.2.3)

Results from density and temperature maps are presented below.

5. The density is highest near midnight (Y=0) and falls off toward the dawn/dusk magnetopause boundary in the xy-view and the density profile tends to rise where the temperature falls.

6. Higher densities are observed near neutral line as well as the region at about X=-59 R_E and Z=-5 R_E to -8 R_E. The same region also seems to have elevated temperatures. The uniformity of the magnetic field vectors are interrupted in that region. This may be explained by the moving out of the current sheet about 8 R_E to the southern part of the tail. In Figure 4.44a, we can clearly see the current sheet on the move ($Z=\pm 10R_E$) in between the central plasma sheet with increased densities higher than 0.25 cm^{-3}.

7. When separated with respect to IMF direction, increased densities are observed in the north-dawn and south-dusk regions in +IMF By sector as seen in our magnetic field vector map findings, consistent with the theory.

8. ARTEMIS observations show two types populations for all IMF conditions: 1. cold plasma with temperatures less than 10 eV, 2. hot plasma with temperatures around 2000 eV. The densities for both plasma is about the same, on the order of 0.1 cc. However, when separated by IMF direction, a third population appears. For northward IMFs, the third population is seen with even higher temperatures greater than 1 keV on the order 2500 eV and lower densities on the average 0.7 cc. The distribution for northward IMFs is densely populated while southward IMF presents more scattered appearance. Additionally, the probability to encounter cold plasma is more in northward IMF than it is in southward IMF sector. The density of the plasma has a mean value of 0.16 cm^{-3} for northward and 0.12 cm^{-3} for southward IMF while the temperature has a mean value of 525 eV for northward and 511 eV for southward IMF.

9. The magnetic pressure and the gas pressure maps show where magnetic field or plasma parameters are dominant. A maximum of 0.06 nPa gas pressure is seen concentrated within the central plasma sheet and also at the plasma sheet boundaries (PSBL) which need further investigation. Both magnetic and gas pressure reach a maximum 0.06 nPa at the boundaries of plasma sheet with about 0.06 nPa values. We can see from the magnetic pressure map that the

plasma sheet has a thickness of 7 R_E after which the magnetic pressure increases sharply. The thickness of the plasma sheet region with weak magnetic field but higher plasma density and temperature seems to decrease in the central tail.

5.2 Future Work and Recommendations

Several additional work is still undergoing and can be proposed as further study based on the data in this thesis:

1. The very next thing we would like to do is to compare the flow vector maps, as well as other plasma parameters and magnetic field, with those from MHD models. This will enable us to understand and interpret the features seen in the vector maps as well as to see where and when the models fail or resemble the observations.
2. The magnetopause and bow shock crossings data used in this study can be integrated into the available analytical magnetopause models to improve their accuracy at mid-tail (x=-60 Re) distances or based on these data a new magnetotail boundary model may be suggested.
3. Increasing the magnetotail data will help to remove the data gaps in the vector maps and will help to improve the statistics presented in this thesis. We intend to expand our data coverage along with the data from the solar wind monitor so that especially the separation by IMF sectors will result in better statistics.
4. One of the studies that can be still pursued based on the data used in this thesis is to investigate the plasma sheet and its sub-regions such as neutral sheet, current sheet, and their magnetic field and plasma characteristics at x=-60 Re. Currently, the data coverage does not allow us to drive exact statistical conclusions. Expanding data set will give us to improve criteria to identify each region.
5. Investigation of flow and other plasma parameters accompanied with the magnetic field can be used to understand the earthward/tailward flows and the nature of the distant tail reconnection phenomena.

6. The substorms effects at lunar distances can be investigated in both magnetopause and magnetotail data. Currently, we considered the global structure of both regions in general. Case studies can help to understand the storm/substorm time of magnetotail at this distance.

Acknowledgement

I would like to thank the jury members of the Thesis Monitoring Commitee, Prof. Dr. Zafer ASLAN and Assist. Prof. Cuma YARIM for their valuable comments, critics, suggestions throughout this study. I would like to thank to Prof. Dr. K. Y. EKŞİ and Prof. Dr. A. ÖKTEN for accepting to be a jury member in my dissertation presentation.

Thank to the PIs of the instruments on board of ACE and ARTEMIS spacecraft.

Simulation results have been provided by the Community Coordinated Modeling Center at Goddard Space Flight Center through their public Runs on Request system (http://ccmc.gsfc.nasa.gov). The CCMC is a multi-agency partnership between NASA, AFMC, AFOSR, AFRL, AFWA, NOAA, NSF and ONR. The SWMF/BATS-R-US with RCM Model was developed by the Tamas Gombosi et al., Richard Wolf et al., Stanislav Sazykin et al., Gabor Toth et al. at the Center for Space Environment Modeling (CSEM) at the University of Michigan and especially Anna Chulaki from CCMC.

I gratefully acknowledge the funding received towards my PhD from Turkish Scientific and Technological Research Council, Project: 113Y213 and also the Istanbul Technical University Research Fund.

REFERENCES

Angelopoulos, V. (2009). *The THEMIS mission. In The THEMIS Mission* (pp. 5-34). Springer.

Angelopoulos, V., and StrangeWay, R. (2009). Space Plasma Physics: The Magnetosphere. Retrieved from http://www.igpp.ucla.edu/public /vassilis/ESS200C/Lectures9-11/Magnetosphere-Lectures_v1.pdf

Artemyev, A. V., Angelopoulos, V., Hietala, H., Runov, A., and Shinohara, I. (2017). Ion density and temperature profiles along (XGSM) and across (ZGSM) the magnetotail as observed by THEMIS, Geotail, and ARTEMIS. *Journal of Geophysical Research: Space Physics, 122*, 1590-1599.

Auster, H. U., Glassmeier, K. H., Magnes, W., Aydogar, O., Baumjohann, W., Constantinescu, D., . . . others. (2008). The THEMIS fluxgate magnetometer. *Space Science Reviews, 141*, 235-264.

Bame, S. J., Anderson, R. C., Asbridge, J. R., Baker, D. N., Feldman, W. C., Gosling, J. T., . . . Zwickl, R. D. (1983). Plasma regimes in the deep geomagnetic tail: ISEE 3. *Geophysical Research Letters, 10*, 912-915.

Baumjohann, W., and Treumann, R. A. (2012). Basic space plasma physics. World Scientific Publishing Company.

Behannon, K. W. (1968). Mapping of the earth's bow shock and magnetic tail by Explorer 33. *Journal of Geophysical Research, 73*, 907-930.

Behannon, K. W. (1970). Geometry of the geomagnetic tail. *Journal of Geophysical Research, 75*, 743-753.

Behannon, K. W., and Ness, N. F. (1966). Magnetic storms in the earth's magnetic tail. *Journal of Geophysical Research, 71*, 2327-2351.

Behannon, K. W., and Ness, N. F. (1968). Satellite studies of the Earth's magnetic tail. In Physics of the Magnetosphere (pp. 409-434). Springer.

Bellan, P. M. (2008). Fundamentals of plasma physics. Cambridge University Press.

Burke, W. J., and Reasoner, D. L. (1973). Observation of plasma flow in the neutral sheet at lunar distance during two magnetic bays. *Journal of Geophysical Research, 78*, 6790-6792.

Chapman, S., and Bartels, J. (1940). Geomagnetism (Vol. 2). Clarendon Press.

Chapman, S., and Ferraro, V. C. (1930). A new theory of magnetic storms. Nature, 126, 129.

Chapman, S., and Ferraro, V. C. (1931). ibid. 36171 (1931b). *Terrestrial Magnetism and Atmospheric Elec., 36*, 171.

Chapman, S., and Ferraro, V. C. (1940). The theory of the first phase of a geomagnetic storm. *Terrestrial Magnetism and Atmospheric Electricity, 45*, 245-268.

Chen, S.-H., Kivelson, M. G., Gosling, J. T., Walker, R. J., and Lazarus, A. J. (1993). Anomalous aspects of magnetosheath flow and of the shape and oscillations of the magnetopause during an interval of strongly northward interplanetary magnetic field. *Journal of Geophysical Research: Space Physics, 98*, 5727-5742.

Coroniti, F. V., and Kennel, C. F. (1972). Changes in magnetospheric configuration during the substorm growth phase. *Journal of Geophysical Research, 77*, 3361-3370.

Cowley, S. W. (1981). Asymmetry effects associated with the x-component of the IMF in a magnetically open magnetosphere. *Planetary and Space Science, 29*, 809-818.

Cowley, S. W. (1981). Magnetospheric asymmetries associated with the Y-component of the IMF. *Planetary and Space Science, 29*, 79-96.

Cowley, S. W. (1982). The causes of convection in the Earth's magnetosphere: A review of developments during the IMS. *Reviews of Geophysics, 20*, 531-565.

Culot, F. (n.d.). The Earth's Magnetosphere Plasma Boundaries.

Dmitriev, A. V., Chao, J. K., and Wu, D. J. (2003). Comparative study of bow shock models using Wind and Geotail observations. *Journal of Geophysical Research: Space Physics, 108*.

Dungey, J. W. (1961). Interplanetary magnetic field and the auroral zones. *Physical Review Letters, 6, 47*.

Eastwood, J. P., Hietala, H., Toth, G., Phan, T. D., and Fujimoto, M. (2015). What Controls the Structure and Dynamics of Earth's Magnetosphere? *Space Science Reviews, 188*, 251-286.

Eastwood, J. P., Nakamura, R., Turc, L., Mejnertsen, L., and Hesse, M. (2017). The scientific foundations of forecasting magnetospheric space weather. *Space Science Reviews, 212*, 1221-1252.

Eastwood, J. P., Phan, T. D., Fear, R. C., Sibeck, D. G., Angelopoulos, V., Øieroset, M., and Shay, M. A. (2012). Survival of flux transfer event (FTE) flux ropes far along the tail magnetopause. *Journal of Geophysical Research: Space Physics, 117*.

Fairfield, D. H. (1968). Average magnetic field configuration of the outer magnetosphere. *Journal of Geophysical Research, 73*, 7329-7338.

Fairfield, D. H. (1968). Simultaneous measurements on three satellites and the observation of the geomagnetic tail at 1000 RE. *Journal of Geophysical Research, 73*, 6179-6187.

Fairfield, D. H. (1971). Average and unusual locations of the Earth's magnetopause and bow shock. *Journal of Geophysical Research, 76*, 6700-6716.

Fairfield, D. H. (1992). On the structure of the distant magnetotail: ISEE 3. *Journal of Geophysical Research: Space Physics, 97*, 1403-1410.

Fairfield, D. H. (1993). Solar wind control of the distant magnetotail: ISEE 3. *Journal of Geophysical Research: Space Physics, 98*, 21265-21276.

Fairfield, D. H., and Ness, N. F. (1970). Configuration of the geomagnetic tail during substorms. *Journal of Geophysical Research, 75*, 7032-7047.

Fairfield, D. H., Hones Jr, E. W., and Meng, C.-I. (1981). Multiple crossings of a very thin plasma sheet in the earth's magnetotail. *Journal of Geophysical Research: Space Physics, 86*, 11189-11200.

Farrell, W. M., Desch, M. D., Ogilvie, K. W., Kaiser, M. L., and Goetz, K. (2003). The role of upper hybrid waves in magnetic reconnection. *Geophysical research letters, 30*.

Fedder, J. A., and Lyon, J. G. (1995). The Earth's magnetosphere is 165 RE long: Self-consistent currents, convection, magnetospheric structure, and processes for northward interplanetary magnetic field. *Journal of Geophysical Research: Space Physics, 100*, 3623-3635.

Frank, L. A. (1985). Plasmas in the Earth's magnetotail. *Space Science Reviews, 42*, 211-240.

Frey, H. U., Phan, T. D., Fuselier, S. A., and Mende, S. B. (2003). Continuous magnetic reconnection at Earth's magnetopause. *Nature, 426*, 533.

Gosling, J. T., Baker, D. N., Bame, S. J., Feldman, W. C., Zwickl, R. D., and Smith, E. J. (1985). North-south and dawn-dusk plasma asymmetries in the distant tail lobes: ISEE 3. *Journal of Geophysical Research: Space Physics, 90*, 6354-6360.

Gosling, J. T., Baker, D. N., Bame, S. J., Hones Jr, E. W., McComas, D. J., Zwickl, R. D., . . . Tsurutani, B. T. (1984). Plasma entry into the distant tail lobes: ISEE-3. *Geophysical Research Letters, 11*, 1078-1081.

Group, A. R. (n.d.). ARTEMIS. Retrieved from http://artemis.igpp.ucla.edu/index.shtml

Hammond, C. M., Kivelson, M. G., and Walker, R. J. (1994). Imaging the effect of dipole tilt on magnetotail boundaries. *Journal of Geophysical Research: Space Physics, 99*, 6079-6092.

Hapgood, M. A. (1992). Space physics coordinate transformations: A user guide. *Planetary and Space Science, 40*, 711-717.

Hardy, D. A., Freeman, J. W., and Hills, H. K. (1976). Plasma observations in the magnetotail. In Magnetospheric Particles and Fields (pp. 89-98). Springer.

Hardy, D. A., Hills, H. K., and Freeman, J. W. (1975). A new plasma regime in the distant geomagnetic tail. *Geophysical Research Letters, 2*, 169-172.

Hardy, D. A., Hills, H. K., and Freeman, J. W. (1979). Occurrence of the lobe plasma at lunar distance. *Journal of Geophysical Research: Space Physics, 84*, 72-78.

Hardy, D. A., Reiff, P. H., and Burke, W. J. (1979). Response of magnetotail plasma at lunar distance to changes in the interplanetary magnetic field, the solar wind plasma, and substorm activity. *Journal of Geophysical Research: Space Physics, 84*, 1382-1390.

Hasegawa, H., Maezawa, K., Mukai, T., and Saito, Y. (2002). Plasma entry across the distant tail magnetopause 1. Global properties and IMF dependence. *Journal of Geophysical Research: Space Physics, 107*.

Hayakawa, H., Nishida, A., Hones, E. W., and Bame, S. J. (1982). Statistical characteristics of plasma flow in the magnetotail. *Journal of Geophysical Research: Space Physics, 87*, 277-283.

Hietala, H., Artemyev, A. V., and Angelopoulos, V. (2017). Ion dynamics in magnetotail reconnection in the presence of density asymmetry. *Journal of Geophysical Research: Space Physics, 122*, 2010-2023.

Hill T., W. (1985). Flux loss from the geomagnetic tail. *Journal of Geophysical Research: Space Physics, 90*, 9897-9899. doi:10.1029/JA090iA10p09897

Hones Jr, E. W. (1985). Magnetic reconnection in the earth's magnetotail. *Australian journal of physics, 38*, 981-998.

Hones Jr, E. W., and Schindler, K. (1979). Magnetotail plasma flow during substorms: A survey with IMP 6 and IMP 8 satellites. *Journal of Geophysical Research: Space Physics, 84*, 7155-7169.

Howe, H. C. (1971). Explorer 33 and Explorer 35 plasma observations of the interaction region between the solar wind and the magnetic field of the earth.

Howe, H. C., and Binsack, J. H. (1972). Explorer 33 and 35 plasma observations of magnetosheath flow. *Journal of Geophysical Research, 77*, 3334-3344.

Howe, H. C., and Siscoe, G. L. (1972). Magnetopause motions at lunar distance determined from the Explorer 35 plasma experiment. *Journal of Geophysical Research, 77*, 6071-6086.

Huang, C. Y. (1987). Quadrennial review of the magnetotail. Reviews of Geophysics, 25, 529-540.

Huang, C. Y., Goertz, C. K., Frank, L. A., and Rostoker, G. (1989). Observational determination of the adiabatic index in the quiet time plasma sheet. *Geophysical research letters, 16*, 563-566.

Imber, S. M., Slavin, J. A., Auster, H. U., and Angelopoulos, V. (2011). A THEMIS survey of flux ropes and traveling compression regions: Location of the near-Earth reconnection site during solar minimum. *Journal of Geophysical Research: Space Physics, 116*.

J Rich, F., Reasoner, D. L., and Burke, W. J. (1973). Plasma sheet at lunar distance: Characteristics and interactions with the lunar surface. *Journal of Geophysical Research, 78*, 8097-8112.

Kallio, E., and Facskó, G. (2015). Properties of plasma near the Moon in the magnetotail. *Planetary and Space Science, 115*, 69-76.

Kaymaz, Z., Siscoe, G., & Luhmann, J. G. (1992). IMF draping around the geotail: IMP 8 observations. *Geophysical research letters, 19(8)*, 829-832.

Kaymaz, Z., Siscoe, G. L., Luhmann, J. G., Lepping, R. P., and Russell, C. T. (1994). Interplanetary magnetic field control of magnetotail magnetic

field geometry: IMP 8 observations. *Journal of Geophysical Research: Space Physics*, *99*, 11113-11126.

Kaymaz, Z., Siscoe, G. L., Tsyganenko, N. A., and Lepping, R. P. (1994). Magnetotail views at 33RE: IMP 8 magnetometer observations. *Journal of Geophysical Research: Space Physics*, *99*, 8705-8730.

Kaymaz, Z., Siscoe, G., Luhmann, J. G., Fedder, J. A., and Lyon, J. G. (1995). Interplanetary magnetic field control of magnetotail field: IMP 8 data and MHD model compared. *Journal of Geophysical Research: Space Physics*, *100(A9)*, 17163-17172.

Kessel, R. L., Chen, S.-H., Green, J. L., Fung, S. F., Boardsen, S. A., Tan, L. C., . . . Frank, L. A. (1996). Evidence of high-latitude reconnecting during northward IMF: Hawkeye observations. *Geophysical research letters*, *23*, 583-586.

Khurana, K. K., Walker, R. J., and Ogino, T. (1996). Magnetospheric convection in the presence of interplanetary magnetic field By: A conceptual model and simulations. *Journal of Geophysical Research: Space Physics*, *101*, 4907-4916.

Kivelson, M. G., Kivelson, M. G., and Russell, C. T. (1995). Introduction to space physics. Cambridge university press.

Koskinen, H. (2011). Physics of space storms: From the solar surface to the Earth. Springer Science and Business Media.

Lepping, R. P., Acũna, M. H., Burlaga, L. F., Farrell, W. M., Slavin, J. A., Schatten, K. H., . . . others. (1995). The WIND magnetic field investigation. *Space Science Reviews*, *71*, 207-229.

Li, W., Raeder, J., Dorelli, J., Øieroset, M., and Phan, T. D. (2005). Plasma sheet formation during long period of northward IMF. *Geophysical research letters*, *32*.

Lui, A. T. (1987). Magnetotail physics. Baltimore, MD, Johns Hopkins University Press, 1987, 445 p. For individual items see A88-46527 to A88-46569.

Maezawa, K., Hori, T., Mukai, T., Saito, Y., Yamamoto, T., Kokubun, S., and Nishida, A. (1997). Structure of the distant magnetotail and its dependence on the IMF By component: GEOTAIL observations. *Advances in Space Research*, *20*, 949-959.

Matzner, R. A. (2001). *Dictionary of Geophysics*, Astrophysics, and Astronomy. CRC Press. Retrieved from https://books.google.com.tr/books?id=eez38xjCYGkC

McComas, D. J., Bame, S. J., Barker, P., Feldman, W. C., Phillips, J. L., Riley, P., and Griffee, J. W. (1998). Solar wind electron proton alpha monitor (SWEPAM) for the Advanced Composition Explorer. *In The Advanced Composition Explorer Mission* (pp. 563-612). Springer.

McFadden, J. P., Carlson, C. W., Larson, D., Ludlam, M., Abiad, R., Elliott, B., . . . Angelopoulos, V. (2008). The THEMIS ESA plasma instrument and in-flight calibration. *Space Science Reviews*, *141*, 277-302.

Meng, C.-I., and Anderson, K. A. (1974). Magnetic field configuration in the magnetotail near 60 RE. *Journal of Geophysical Research, 79*, 5143-5153.

Meng, C.-I., and Mihalov, J. D. (1972). On the diamagnetic effect of the plasma sheet near 60 RE. *Journal of Geophysical Research, 77*, 4661-4669.

Mihalov, J. D., and Sonett, C. P. (1968). The cislunar geomagnetic tail gradient in 1967. *Journal of Geophysical Research, 73*, 6837-6841.

Mihalov, J. D., Colburn, D. S., and Sonett, C. P. (1970). Observations of magnetopause geometry and waves at the lunar distance. *Planetary and Space Science, 18*, 239-258.

Mitchell, D. G., Kutchko, F., Williams, D. J., Eastman, T. E., Frank, L. A., and Russell, C. T. (1987). An extended study of the low-latitude boundary layer on the dawn and dusk flanks of the magnetosphere. *Journal of Geophysical Research: Space Physics, 92*, 7394-7404.

Nagai, T., Fujimoto, M., Nakamura, R., Baumjohann, W., Ieda, A., Shinohara, I., . . . Mukai, T. (2005). Solar wind control of the radial distance of the magnetic reconnection site in the magnetotail. *Journal of Geophysical Research: Space Physics, 110*.

Nagai, T., Fujimoto, M., Saito, Y., Machida, S., Terasawa, T., Nakamura, R., . . . Kokubun, S. (1998). Structure and dynamics of magnetic reconnection for substorm onsets with Geotail observations. *Journal of Geophysical Research: Space Physics, 103*, 4419-4440.

Nakamura, R., Kokubun, S., Mukai, T., and Yamamoto, T. (1997). Changes in the distant tail configuration during geomagnetic storms. *Journal of Geophysical Research: Space Physics, 102*, 9587-9601.

Ness, N. F. (1969). The geomagnetic tail. Reviews of Geophysics, 7, 97-127.

Ness, N. F., Behannon, K. W., Cantarano, S. C., and Scearce, C. S. (1967). Observations of the earth's magnetic tail and neutral sheet at 510,000 kilometers by Explorer 33. *Journal of Geophysical Research, 72*, 927-933.

Ness, N. F., Behannon, K. W., Scearce, C. S., and Cantarano, S. C. (1967). Early results from the magnetic field experiment on lunar Explorer 35. *Journal of Geophysical Research, 72*, 5769-5778.

Nishida, A. (2000). The Earth's dynamic magnetotail. *Space Science Reviews, 91*, 507-577.

Ogilvie, K. W., Chornay, D. J., Fritzenreiter, R. J., Hunsaker, F., Keller, J., Lobell, J., . . . others. (1995). SWE, a comprehensive plasma instrument for the Wind spacecraft. *Space Science Reviews, 71*, 55-77.

Ohtani, S.-i. (2004). Flow bursts in the plasma sheet and auroral substorm onset: Observational constraints on connection between midtail and near-Earth substorm processes. *Space science reviews, 113*, 77-96.

Parker, E. N. (1958). Dynamics of the interplanetary gas and magnetic fields. *The Astrophysical Journal, 128*, 664.

Petrukovich, A. A., Baumjohann, W., Nakamura, R., Balogh, A., Mukai, T., Glassmeier, K.-H., . . . Klecker, B. (2003). Plasma sheet structure during strongly northward IMF. *Journal of Geophysical Research: Space Physics, 108.*

Pulkkinen, T. (2007). Space weather: terrestrial perspective. Living Reviews in Solar Physics, 4, 1.

Raeder, J., Walker, R. J., and Ashour-Abdalla, M. (1995). The structure of the distant geomagnetic tail during long periods of northward IMF. *Geophysical research letters, 22*, 349-352.

Reiff, P. H., and Reasoner, D. L. (1975). The magnetosheath electron population at lunar distance: General features. *Journal of Geophysical Research, 80*, 1232-1237.

Rich, F. J., Reasoner, D., and and Burke, W. (1973). Plasma sheet at lunar distance: Characteristics and interactions with lunar surface. *Journal of Geophysical Research*, 8097-8112.

Roelof, E. C., and Sibeck, D. G. (1993). Magnetopause shape as a bivariate function of interplanetary magnetic field Bz and solar wind dynamic pressure. *Journal of Geophysical Research: Space Physics, 98*, 21421-21450.

Russell, C. T. (1971). Geophysical coordinate transformations. Cosmic Electrodynamics, 2, 184-196.

Russell, C. T. (1972). The configuration of the magnetosphere. Critical problems of magnetospheric physics, (p. 1).

Russell, C. T., and Brody, K. I. (1967). Some remarks on the position and shape of the neutral sheet. *Journal of Geophysical Research, 72*, 6104-6106.

Russell, C. T., and Elphic, R. C. (1978). Initial ISEE magnetometer results: Magnetopause observations. *Space Science Reviews, 22*, 681-715.

Russell, C. T., Petrinec, S. M., Zhang, T. L., Song, P., and Kawano, H. (1997). The effect of foreshock on the motion of the dayside magnetopause. *Geophysical Research Letters, 24*, 1439-1441.

Scherer, K., Fichtner, H., Heber, B., and Mall, U. (2005). *Space Weather: The Physics Behind a Slogan.* Springer Berlin Heidelberg. Retrieved from https://books.google.com.tr/books?id=irHgIUtLi0gC

Scholer, M., Klecker, B., Hovestadt, D., Gloeckler, G., Ipavich, F. M., and Galvin, A. B. (1985). Energetic particle characteristics of magnetotail flux ropes. *Geophysical research letters, 12*, 191-194.

Sibeck D., G., Siscoe G., L., Slavin J., A., Smith E., J., Tsurutani B., T., and Bame S., J. (1985). Magnetic field properties of the distant magnetotail magnetopause and boundary layer. *Journal of Geophysical Research: Space Physics, 90*, 9561-9575. doi:10.1029/JA090iA10p09561

Sibeck, D. G., and Angelopoulos, V. (2008). THEMIS science objectives and mission phases. *Space Science Reviews, 141*, 35-59.

Sibeck, D. G., and Siscoe, G. L. (1984). Downstream properties of magnetic flux transfer events. *Journal of Geophysical Research: Space Physics, 89*, 10709-10715.

Sibeck, D. G., Angelopoulos, V., Brain, D. A., Delory, G. T., Eastwood, J. P., Farrell, W. M., . . . others. (2011). ARTEMIS science objectives. *In The ARTEMIS mission* (pp. 27-59). Springer.

Sibeck, D. G., Siscoe, G. L., Slavin, J. A., and Lepping, R. P. (1986). Major flattening of the distant geomagnetic tail. *Journal of Geophysical Research: Space Physics, 91*, 4223-4237.

Sibeck, D. G., Siscoe, G. L., Slavin, J. A., Smith, E. J., Bame, S. J., and Scarf, F. L. (1984). Magnetotail flux ropes. *Geophysical research letters, 11*, 1090-1093.

Sibeck, D. G., Siscoe, G. L., Slavin, J. A., Smith, E. J., Tsurutani, B. T., and Lepping, R. P. (1985). The distant magnetotail's response to a strong interplanetary magnetic field By: Twisting, flattening, and field line bending. *Journal of Geophysical Research: Space Physics, 90*, 4011-4019.

Siscoe, G., and Kaymaz, Z. (1999). Spatial relations of mantle and plasma sheet. *Journal of Geophysical Research: Space Physics, 104*, 14639-14646.

Slavin, J. A., Lepping, R. P., Gjerloev, J., Fairfield, D. H., Hesse, M., Owen, C. J., . . . Mukai, T. (2003). Geotail observations of magnetic flux ropes in the plasma sheet. *Journal of Geophysical Research: Space Physics, 108*.

Slavin, J. A., Smith, E. J., Sibeck, D. G., Baker, D. N., Zwickl, R. D., and Akasofu, S.-I. (1985). An ISEE 3 study of average and substorm conditions in the distant magnetotail. Journal of Geophysical Research: Space Physics, **90**, 10875-10895.

Slavin, J. A., Smith, M. F., Mazur, E. L., Baker, D. N., Hones, E. W., Iyemori, J. T., and Greenstadt, E. W. (1993). ISEE 3 observations of traveling compression regions in the Earth's magnetotail. *JGR Space Physics*.

Slavin, J. A., Tsurutani, B. T., Smith, E. J., Jones, D. E., and Sibeck, D. G. (1983). Average configuration of the distant (< 220 Re) magnetotail: Initial ISEE-3 magnetic field results. *Geophysical research letters, 10*, 973-976.

Smith, C. W., L'Heureux, J., Ness, N. F., Acuna, M. H., Burlaga, L. F., and Scheifele, J. (1998). The ACE magnetic fields experiment. *In The Advanced Composition Explorer Mission* (pp. 613-632). Springer.

Song, P., and Russell, C. T. (1992). Model of the formation of the low-latitude boundary layer for strongly northward interplanetary magnetic field. *Journal of Geophysical Research: Space Physics, 97*, 1411-1420.

Sonnerup, B. U., and Cahill Jr, L. J. (1967). Magnetopause structure and attitude from Explorer 12 observations. *Journal of Geophysical Research, 72*, 171-183.

Stern, D. P. (1975). The source of the electric field in the nightside magnetosphere.

Stone, E. C., Frandsen, A. M., Mewaldt, R. A., Christian, E. R., Margolies, D., Ormes, J. F., and Snow, F. (1998). The advanced composition explorer. *Space Science Reviews, 86*, 1-22.

Tsurutani, B. T., Jones, D. E., and Sibeck, D. G. (1984). The two-lobe structure of the distant (X≥ 200 Re) magnetotail. *Geophysical Research Letters, 11*, 1066-1069.

Tsurutani, B. T., Slavin, J. A., Smith, E. J., Okida, R., and Jones, D. E. (1984). Magnetic structure of the distant geotail from- 60 to- 220 Re: ISEE-3. *Geophysical research letters, 11*, 1-4.

Tsyganenko, N. (2008). GEOPACK 2008 Subroutines, Fact Sheet No 282.

Tsyganenko, N. A. (1998). Modeling of twisted/warped magnetospheric configurations using the general deformation method. *Journal of Geophysical Research: Space Physics, 103*, 23551-23563.

Tsyganenko, N. A., and Fairfield, D. H. (2004). Global shape of the magnetotail current sheet as derived from Geotail and Polar data. *Journal of Geophysical Research: Space Physics, 109*.

Walsh, A. P., Haaland, S., Forsyth, C., Keesee, A. M., Kissinger, J., Li, K., . . . others. (2017). Dawn-dusk asymmetries in the coupled solar wind-magnetosphere-ionosphere system: A review, 1701.04701.

Wang, C.-P., Lyons, L. R., Weygand, J. M., Nagai, T., and McEntire, R. W. (2006). Equatorial distributions of the plasma sheet ions, their electric and magnetic drifts, and magnetic fields under different interplanetary magnetic field Bz conditions. *Journal of Geophysical Research: Space Physics, 111*.

Wing, S., Newell, P. T., Sibeck, D. G., and Baker, K. B. (1995). A large statistical study of the entry of interplanetary magnetic field y-component into the magnetosphere. *Geophysical research letters, 22*, 2083-2086.

Zhao, S., Tian, A., Shi, Q., Xiao, C., Fu, S., Zong, Q., . . . others. (2016). Statistical study of magnetotail flux ropes near the lunar orbit. *Science China Technological Sciences, 59*, 1591-1596.

Zwickl, R. D., Baker, D. N., Bame, S. J., Feldman, W. C., Gosling, J. T., Hones, E. W., . . . Slavin, J. A. (1984). Evolution of the Earth's distant magnetotail: ISEE 3 electron plasma results. *Journal of Geophysical Research: Space Physics, 89*, 11007-11012.

APPENDICES

APPENDIX A: Maps and Diagrams

APPENDIX B : Flow Maps

APPENDIX A

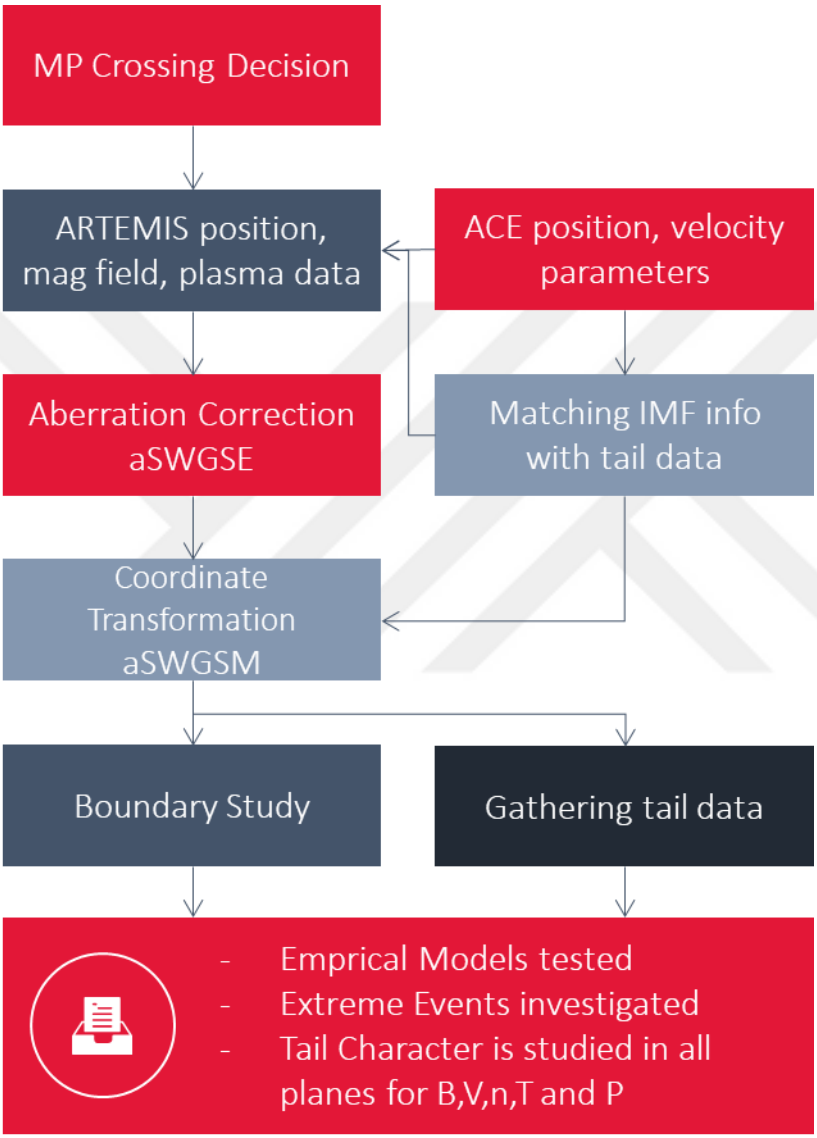

Figure A.1 : Flow diagram of the procedures used in the study.

APPENDIX B

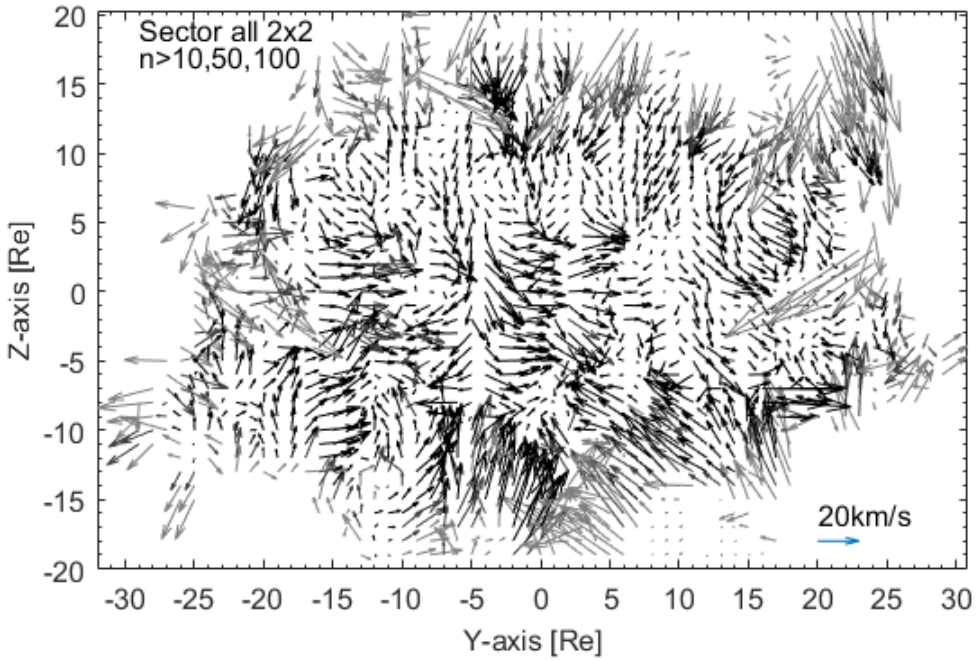

Figure B.1 : All ARTEMIS flow vectors in YBx- plane averaged in smaller bin size (2 R_E x 2 R_E bins) than presented within the text (6 R_E x 4 R_E bins). Bins with less than 100 observations are colored in light and dark grey.

This plot is presented here in Appendix to pinpoint that the bin size and the averaging procedure do not alter the physical behaviour of the flow. The chosen bin size is 0.5Rex0.5Re.

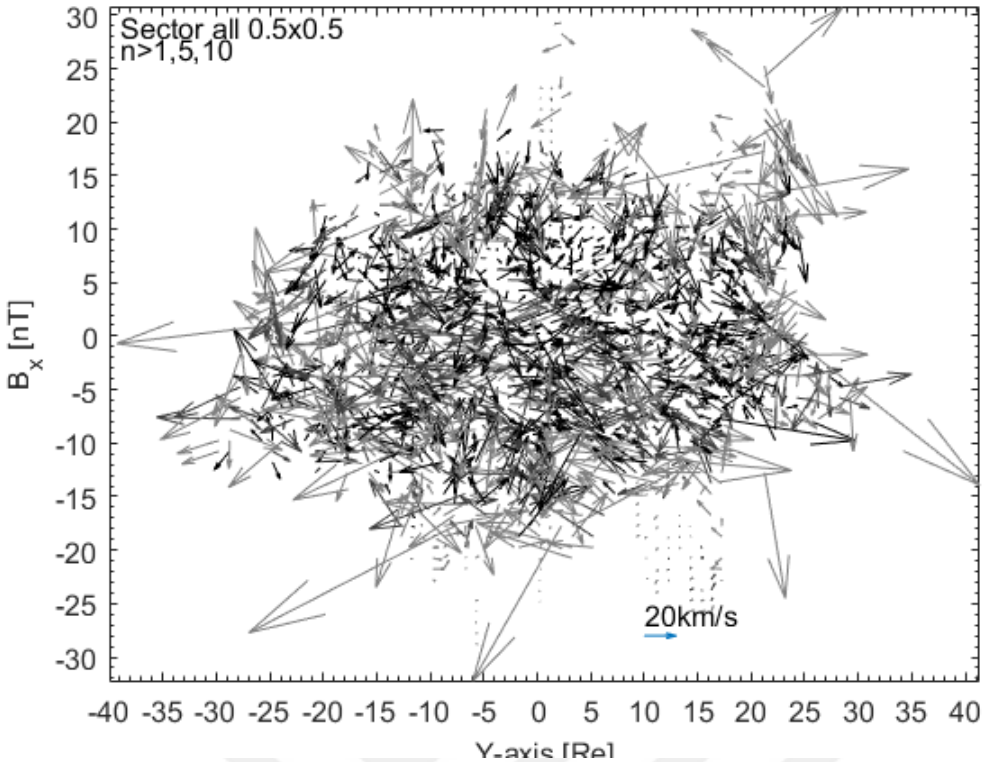

Figure B.2 : Every 10 magnetotail magnetic field data point is plotted onto YBx-plane for every crossing available.

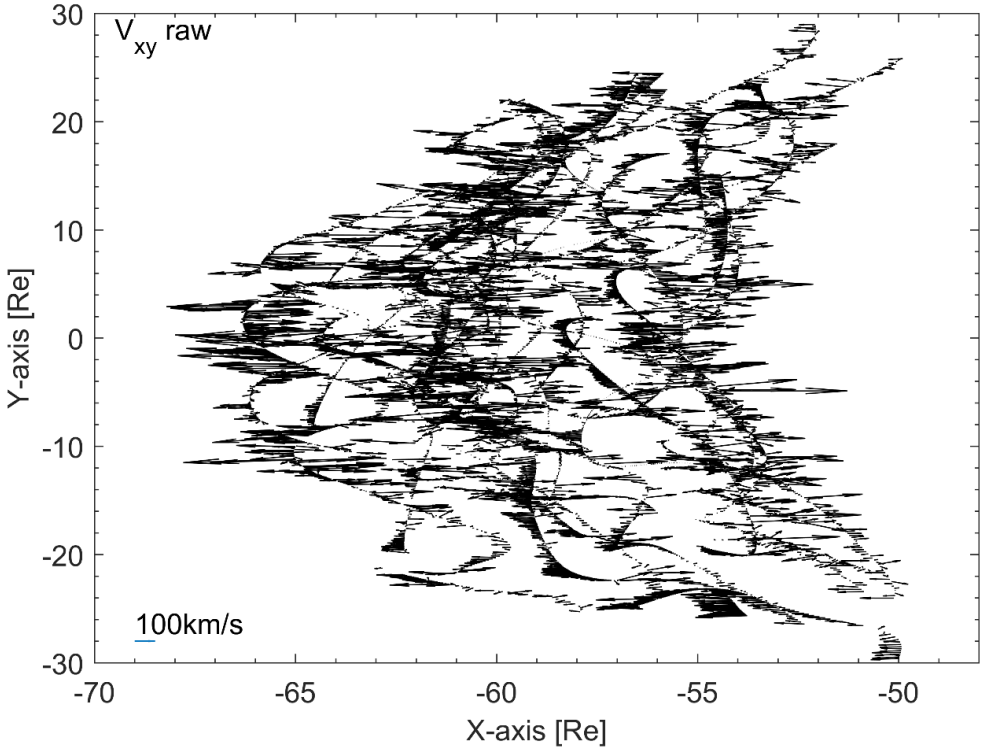

Figure B.3 : Every 10 magnetotail magnetic field data point is plotted onto XY-plane for every crossing available.

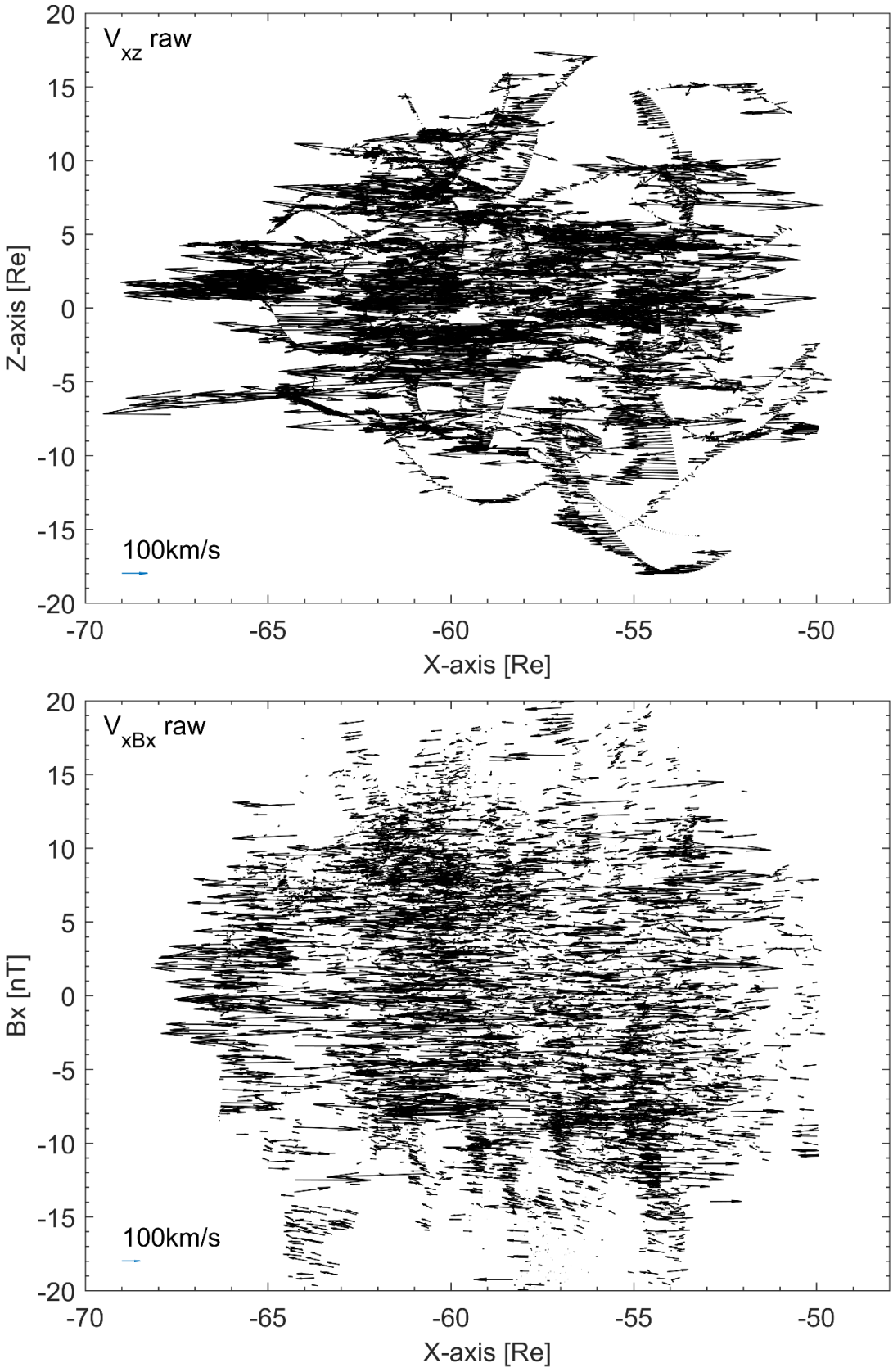

Figure B.4 : Every 10 magnetotail plasma flow data point is plotted onto XZ and XBx plane for every crossing available.

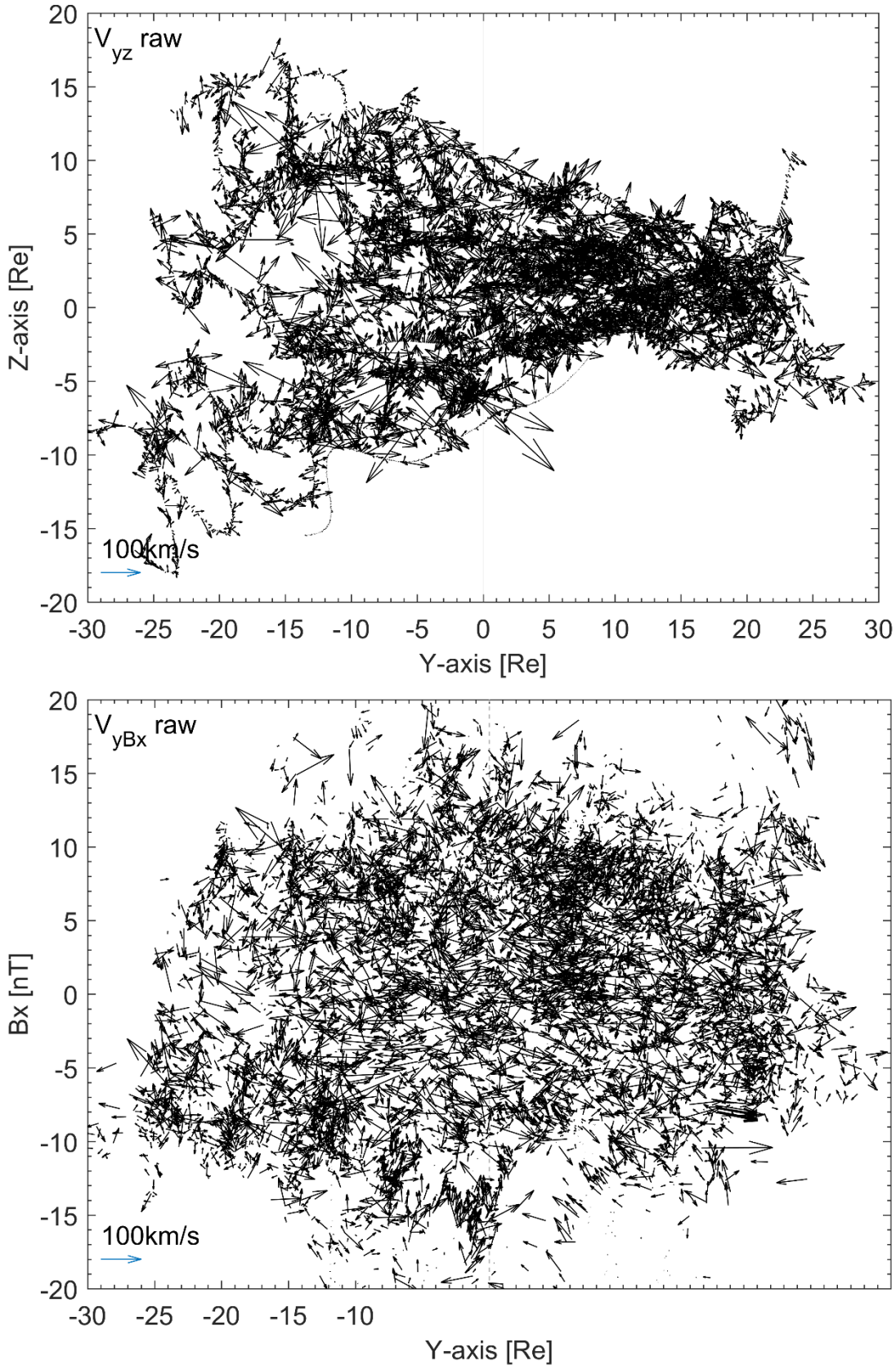

Figure B.5 : Every 10 magnetotail plasma flow data point is plotted onto YZ and YBx plane for every crossing available.

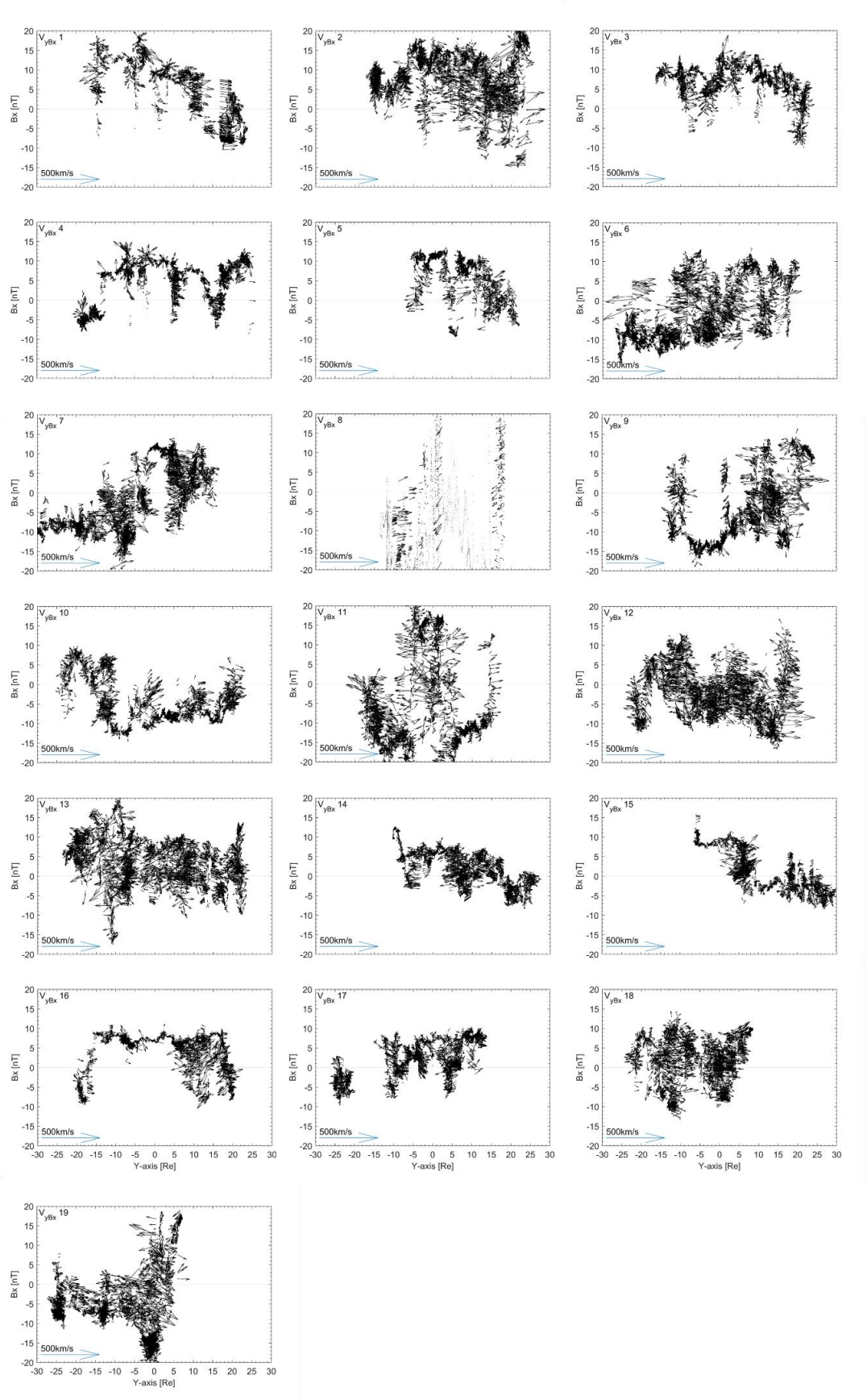

Figure B.6 : Every 19 crossing during one-and-a-half years that we collect magnetotail plasma flow measurements, plotted onto YBx plane.

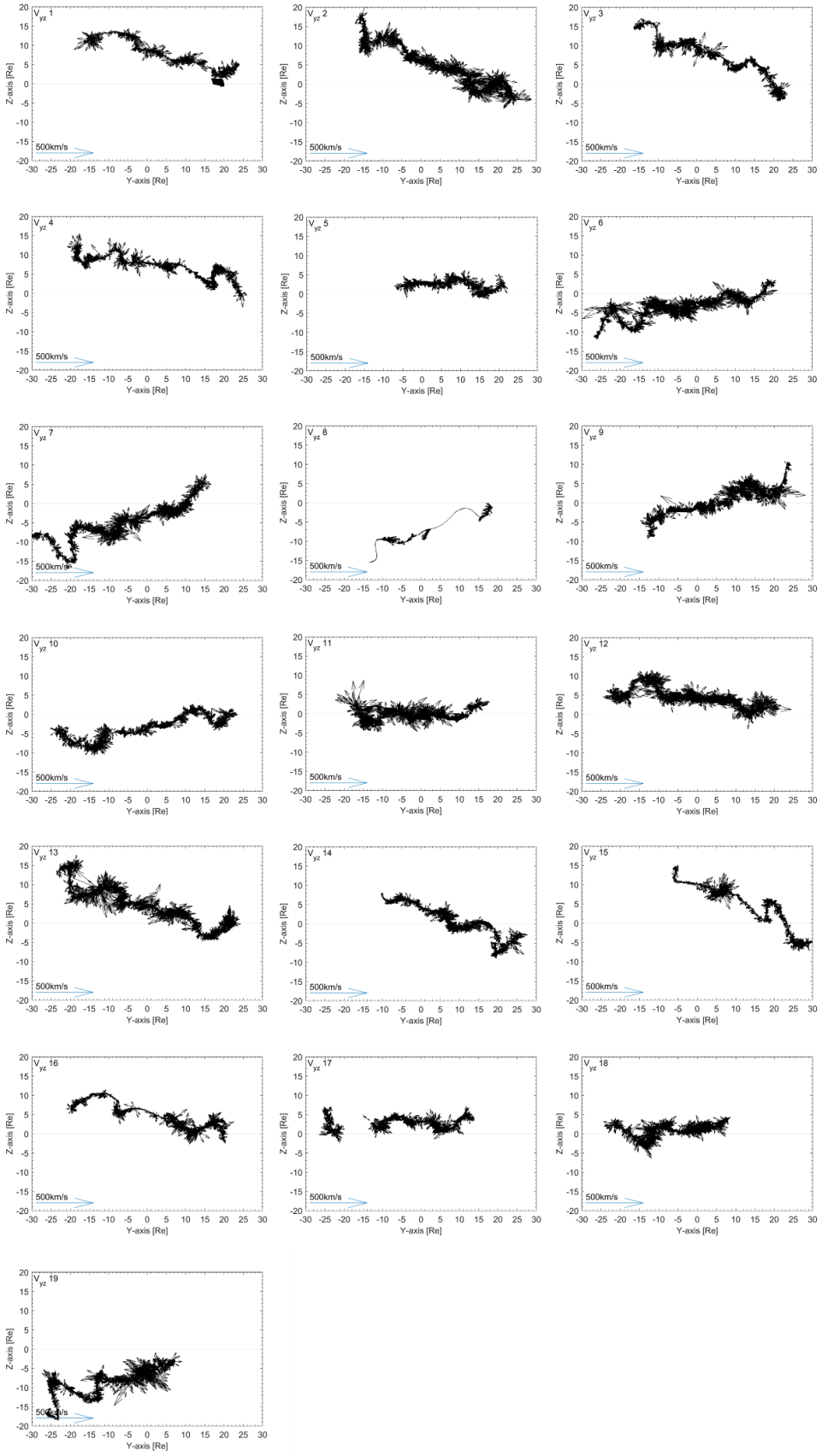

Figure B.7 : Every 19 crossing during one-and-a-half years that we collect magnetotail plasma flow measurements, plotted onto YZ- plane.

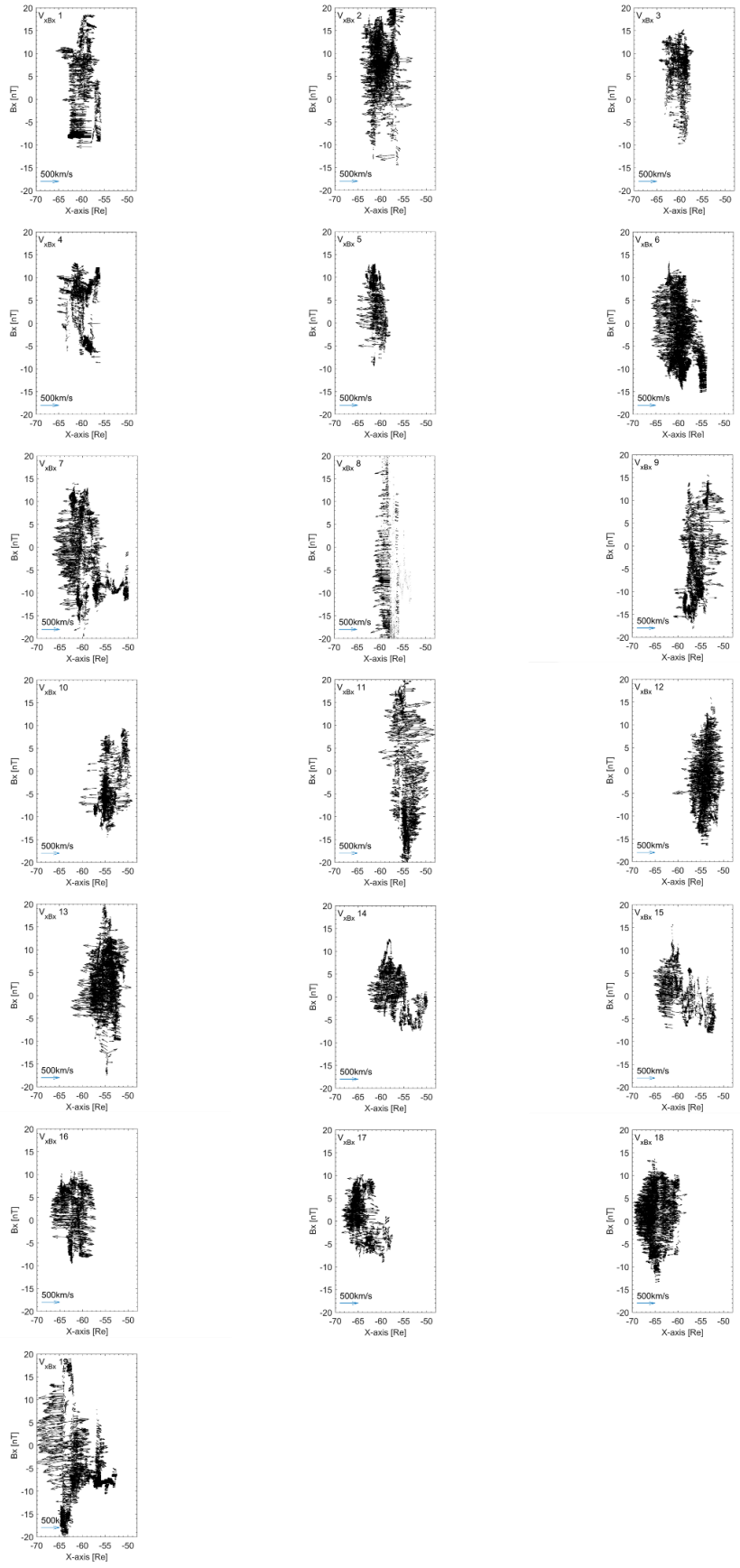

Figure B.8 : Every 19 crossing during one-and-a-half years that we collect magnetotail plasma flow measurements, plotted onto XBx- plane.

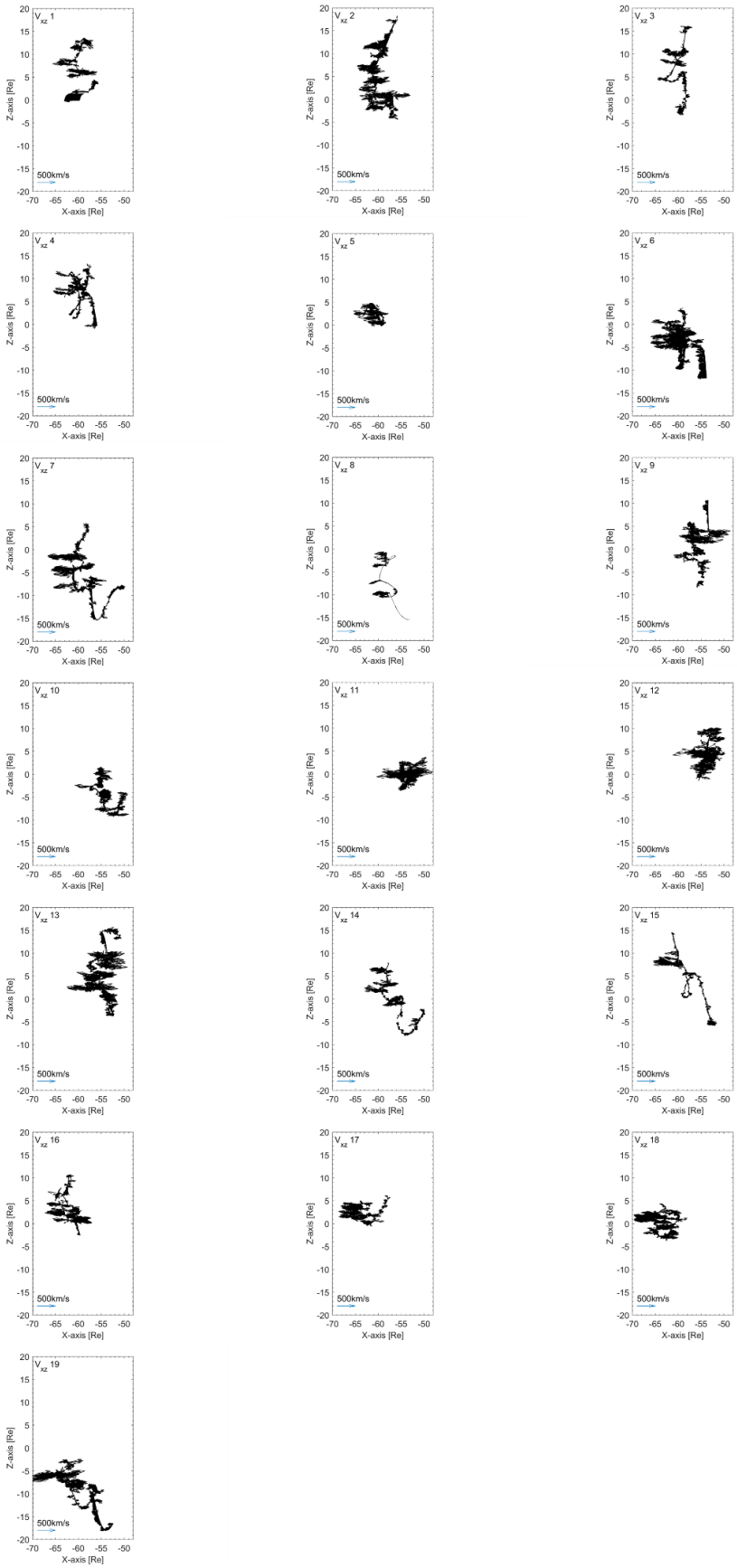

Figure B.9 : Every 19 crossing during one-and-a-half years that we collect magnetotail plasma flow measurements, plotted onto XZ- plane.

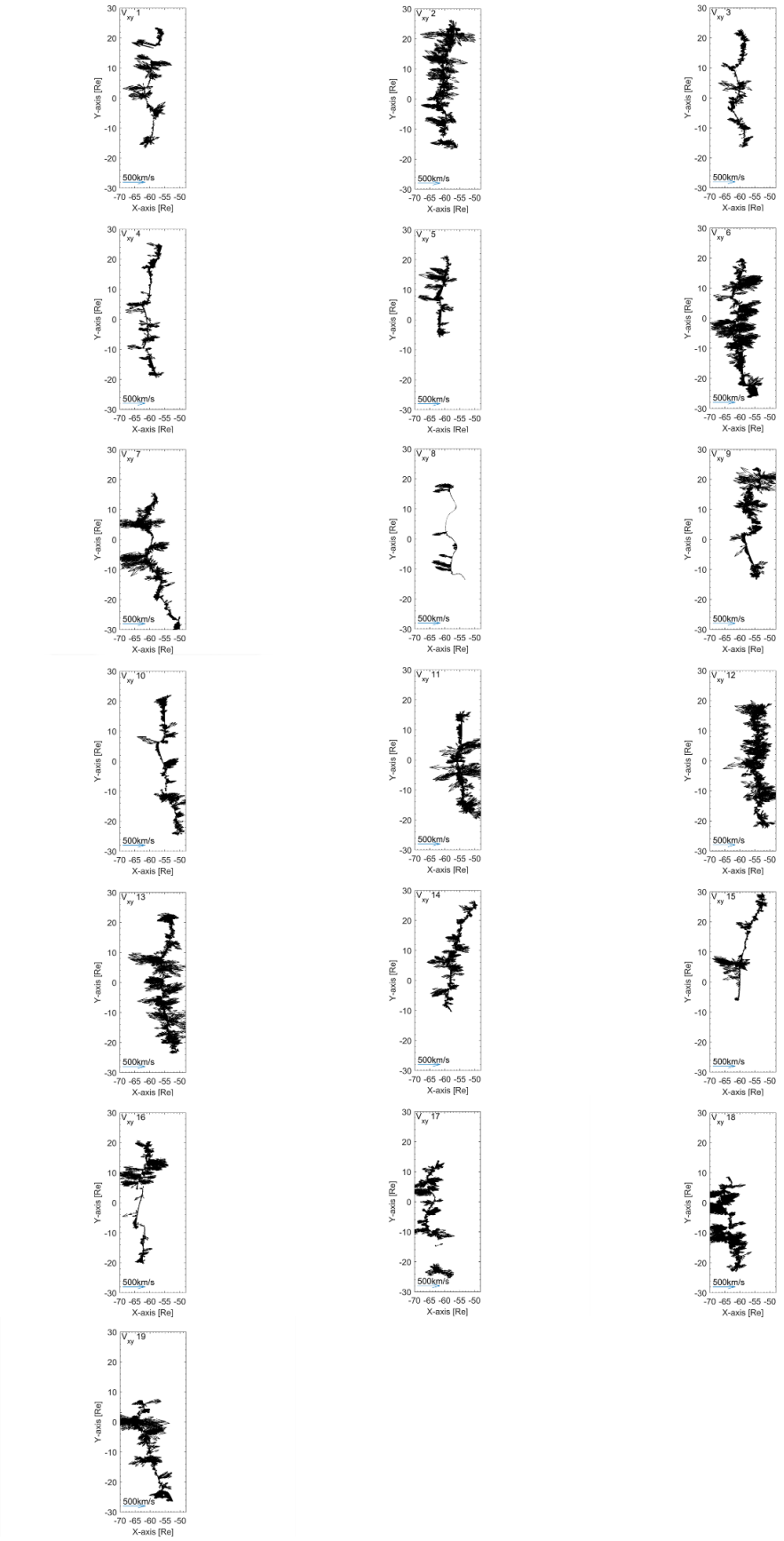

Figure B.10 : Every 19 crossing during one-and-a-half years that we collect magnetotail plasma flow measurements, plotted onto XY- plane.

CURRICULUM VITAE

Name Surname **:** İklim GENÇTÜRK AKAY

Place and Date of Birth **:** Üsküdar/İstanbul – 27/12/1985

E-Mail **:** gencturk@itu.edu.tr

EDUCATION

- **B.Sc.** **:**2007, Istanbul Technical University, Faculty of Aeronautics and Astronautics, Astronautical Engineering Department
- **M.Sc.** **:**2010, University of Texas at Austin, Cockrell School of Engineering, Aerospace Engineering Department
- **Ph.D.** **:**2019, Istanbul Technical University, Faculty of Aeronautics and Astronautics, Aeronautics and Astronautics Department

PROFESSIONAL EXPERIENCE AND REWARDS

- 2013 – 2016 Researcher , TUBITAK Project No: 113Y213 on Space Weather from the Moon to the Ionosphere
- 2013 – 2015 Researcher, ITU BAP Project on Determining Magnetotail Morphology at Lunar Distance Using ARTEMIS observations
- 2012 Project Team Member, TURKSAT-3USAT Project; a cubesat project developed in the Astronautics Department and funded by TURKSAT
- 2009 RASC-AL Competition, Graduate Team Member of The University of Texas at Austin, Conceptual level aerospace mission designed and presented during the conference
- 2008 Academic Project Fellowship from The Scientific and Technical Research Council of Turkey
- 2008 -2010 M.Sc. Scholarship from The Republic of Turkey, Ministry of National Education

- 2007 Honor Student, 3rd place in the graduating class of Astronautical Engineering Department
- 2004 – 2006 TUBITAK Space Technologies Research Institute; ROKETSAN Missiles Industries Inc.; Engineering Interships at ASKAM Truck Industries Inc.

PUBLICATIONS, PRESENTATIONS AND PATENTS ON THE THESIS

- **Gencturk Akay, I.,** Kaymaz, Z., and Sibeck, D. G. (2018, October). Magnetotail boundary crossings at lunar distances: ARTEMIS observations, Journal of Atmospheric and Solar-Terrestrial Physics 182, 45-60. (Publication)
- **Gencturk Akay, I.,** Kaymaz, Z., Sibeck, D. G. and V. Angelopoulos (2016, June 19-24). Velocity and Density Structure at Distant Tail in Response to IMF Variations, GEM Meeting (Poster Presentation)
- **Gencturk Akay, I,** Kaymaz, Z., Sibeck, D.G., Angelopoulos, V., Kuznetsova, M. (2015, December). Magnetic Field and Plasma Flow Structure at Lunar Distances, AGU Fall Meeting, (Poster Presentation)
- **Gencturk Akay, I.,** Kaymaz, Z., Sibeck, D. G. and V. Angelopoulos (2015, December). Artemis observations of Magnetotail Boundary Variations. ARTEMIS Meeting, Post-AGU (Presentation)
- **Gencturk Akay, Iklim, et al.** "Investigating magnetic field structure at moon distance: A single pass example." Recent Advances in Space Technologies (RAST), 2015 7th International Conference on. IEEE, 2015. (Presentation)
- **Gencturk Akay, I.,** Kaymaz, Z., and Sibeck, D. G. (2013, August). Structure of the Magnetopause at Lunar Distances. In IAGA, The XIIth Scientific Assembly
- **Gencturk Akay, I.,** Kaymaz, Z., and Sibeck, D. G. (2013, June). Magnetotail shape at lunar distances: ARTEMIS observations. In Recent Advances in Space Technologies (RAST), 2013 6th International Conference on (pp. 739-742). IEEE. (Presentation)
- **Gencturk Akay, I.,** Kaymaz, Z., and Sibeck, D. G. (2013, April). On the shape of the Geomagnetic Tail at Lunar distances: Preliminary Resuts from Artemis Observations. In EGU General Assembly Conference Abstracts (Vol. 15, p. 4060). Vienna, Austria. (Presentation)